CRANFIELD UNIVERSITY

Serena Zoppellari

Analytical Modeling of Rotating Stall and Surge

School of Engineering

Ph.D. Thesis

SCHOOL OF ENGINEERING
DEPARTMENT OF POWER AND PROPULSION

Full Time Ph.D.

Academic Year 2010 – 2014

Serena Zoppellari

Analytical Modeling of Rotating Stall and Surge

Supervisor: Dr V. Pachidis
Industrial Advisors: Mr A. Rowe, Mr S. Brown

March 2014

This report is submitted in partial fulfillment of the requirements for the degree of Doctorate of Philosophy

Executive summary

The life and performance of axial compressors are limited by the occurrence of instabilities such as rotating stall and surge. Indeed, in the course of the design phase a great effort is usually devoted to guarantee an adequate safety margin from the region of instabilities' onset. On the other hand, during its operating life, an axial compressor can be subjected to several conditions that can lead to the inception of stall and its dynamics. A few examples of possible stall causes, for the specific case of an axial compressor embedded in an aircraft engine, are inlet flow distortion, engine wear or shaft failure.

The shaft failure case can be seen as an exception, as a matter of fact, after this event surge is a desirable outcome since it can potentially decelerate the over-speeding turbine by reducing the mass flow passing through the engine. The possible occurrence of surge and stall should be predicted and controlled in order to avoid severe damage to the compressor and its surroundings. A lot of research has been carried out in the past years to understand the inception and development of stall to achieve the capability for predicting and controlling this severe phenomenon. Nonetheless, this problem is still not well understood and unpredictable outcomes are still a great concern for many axial compressor's applications.

The lack of knowledge in what concerns inception and development of stall and surge reflects in a lack of tools to investigate, predict and control these unstable phenomena. The tools available to study stall and surge events are still not highly reliable or they are very time consuming as 3D CFD simulations.

The doctoral research described herein, aimed at the investigation of the rotating stall phenomenon and the derivation of the compressor characteristic during this unstable condition. Following a detailed analysis of the tools and techniques available in the public domain and the identification of their limitations, the development of a FORTRAN through-flow tool was the methodology chosen. A distinctive feature of the developed tool is the independency from steady state characteristics which is a limitation for the majority of the available tools and its computational efficiency.

Particular attention was paid to capture various viscous flow features occuring during rotating stall through the selection and implementation of appropriate semi-empirical models and correlations. Different models for pressure loss, stall inceptions and stall cell growth/ speed were implemented and verified along with different triggering techniques to achieve a very close to reality simulation of the overall phenomenon, from stall inception to full development.

The final tool is a FORTRAN solver which offers the user the possibility to run it as a fully 2D Euler solver or as a Quasi-2D solver combined with a modified 'parallel compressors' technique that allows the correct modeling of asymmetric phenomena. The methodology implemented has proved promising since several simulations were run to test the tool adopting different compressor geometries. Verifications were performed in terms of overall compressor performance, with simulations in all the three possible operating regions (forward, stall and reverse flow), in order to verify the tool's capability in predicting the compressor characteristics. In terms of flow field, the ability to capture the right circumferential trends of the flow properties was checked through a comparison against 3D CFD simulations. The results obtained have demonstrated the ability of the tool to capture the real behavior of the flow across a compressor subjected to several different unstable conditions that can lead to the onset of phenomena such as rotating stall, classic and deep surge. Indeed, the tool has shown ability to tackle steady and transient phenomena characterized by asymmetric and axis-symmetric flow fields. This document provides several examples of investigations emphasizing the flexibility of the developed methodology. As a matter of fact, within this dissertation, many examples can be found on the effect of the plenum size, on the different transient phenomena experienced by the compressor when subjected to multiple regions of inlet distortion instead of a localized region of low or high flow, on the differences between temporary and stationary inlet disturbances and so on.

This document describes in detail the methodology, the implementation of the tool, its verification and possible applications and the recommended future work. The work was funded by Rolls-Royce plc and was carried out within the Rolls-Royce UTC in Performance Engineering at Cranfield as three-year Ph.D. program that started in October 2010.

Brief statement of contributions

The key contributions of this research are:

- Development and implementation of a methodology which allows the assessment of compressor transient performance under different operating conditions relying only on geometrical information. As a matter of fact, two CFD solvers (Quasi-2D Euler solver and a fully 2D Euler solver) combined into one tool were developed and used for the quick assessment of compressor transient performance under different operating conditions.
- Regarding the Quasi-2D Euler solver, the capability of capturing asymmetric flow fields relies on a modified 'parallel compressors' technique. In particular, a new mass redistribution technique was developed and implemented. The mass flow exchange was extended from the rotor-stator gap to each axial element with the exception of those elements located inside a blade row. The momentum in the axial and tangential direction along with the involved energy exchange was also introduced in the governing equations and compressibility was taken into account.
- A meticulous study of appropriate pressure loss and deviation models was carried out for each operating region (forward, stalled and reverse flow) in order to achieve reliability, accuracy and robustness. Different correlations from different researchers have been combined together to predict pressure loss and deviation across the three regions; three different models have been implemented to determined the inception of stall along with an appropriate logic to model the transition across all the three regions.
- Different stall triggering techniques have been investigated such as inlet flow distortion, throttle settings and axial force spikes. The developed tool was successfully adopted to investigate the effect of different pattern of temporary and stationary inlet flow distortion, the effect of plenum size, the capability of recovery from the stall condition, the derivation of the rotating stall characteristic etc.

To my parents Loris and Daniela

Acknowledgments

This is probably the most difficult part to write, since there are no words to properly express my infinite gratitude for having received the possibility of undertaking this research. These three years have changed me deeply from an academic and a personal point of view, providing me with maturity and skills that will help me in my future life. There are, of course, many people that played a role before and during this research.

I would like to thank, first of all my supervisor, Dr Pachidis, who supported and guided me through all the three years. I really admire your devotion and dedication to your work and students. For the possibility of working on this project, I would like to thank Rolls-Royce plc to have sponsored this research and in particular Arthur Rowe and Stephen Brown, my industrial supervisors, along with Richard Tunstall and Paul Hield for their invaluable technical contributions. I wish to express my gratitude also to Dr Macmanus and Dr Zachos for their useful technical advices.

My thought goes now to all the amazing people I have met in Cranfield, in particular I would like to thank Ahad, Nick&Claire, Domenico and Giuseppina. I really had lots of good time with you guys, our trips, dinners and night out in general will always remain in my memory. Thank you also for the technical help and the patience for listening to my complains. Many thanks also to Carlos for the technical discussions and moral support, to Kostantinos for the CFD's advices and life tips and Alejandro for the technical help with ANSYS CFX. My appreciation goes also to my M.Sc. students who collaborated with me during this doctoral research: Julie, Melody, David and Juan. I wish to extend my aknowledgements also to all the nice people who works and worked close to my office for the nice chats during lunch and tea breaks.

Shifting now to my old friends, I am indebted to Nada who is always available and has the right word to keep me on track and going on. Of all my old friends, I wish to thank in particular Elisa, Mauro and Elena from my hometown and my old friends from Padua, Giovanni and "Papi" who supported me from Italy believing in me more than myself and being proud of me. Thank you guys for being there despite the distance.

To conclude I would like to express my infinite gratitude to Marco for his help in my technical work, proofreading and for being there during my bad days. A very special thank goes to my parents Daniela and Loris and my grandfather who left me during my first year, for their moral support.

Contents

1 Introduction 1

1.1 Background 1

1.1.1 Compressor unstable behavior 2

1.1.2 Classification of rotating stall and surge 10

1.2 Aims and objectives 13

1.3 Thesis outline 14

2 Literature review 16

2.1 Axial compressor performance 16

2.1.1 Terminology and fundamentals of cascades aerodynamics . . 18

2.2 Compressor instabilities 19

2.2.1 Rotating stall and Surge features 20

2.2.1.1 Stall cell structure 20

2.2.1.2 A three-phase evolution 22

2.3 Numerical tools for the modeling of stall/surge 26

2.3.1 Through-flow VS 3D CFD 26

2.3.1.1 Losses and deviation in through-flow solvers 29

2.3.2 Grid-free methods VS grid-based methods 30

2.4 Compressor stall and surge models 32

2.4.1 The ’parallel compressors’ technique 33

2.4.1.1 A multiple segment ’parallel compressors’ model . 36

2.4.1.2 Circumferential and radial mass redistribution in the ’parallel compressors’ model 37

2.4.2 A lumped-volume approach 37

2.4.3 Quasi-1D and Quasi-2D Euler solvers 41

2.4.4 2D and 3D Euler solvers 43

2.5 Summary 46

3 Methodology **48**
3.1 Preliminary work . . . 49
3.1.0.1 The Lagrangian dilatation element method . . . 50
3.1.0.2 The finite difference Euler approach . . . 55
3.1.0.3 Lagrangian VS Euler . . . 58
3.2 Background to FENICE-PC . . . 59
3.2.1 The quasi-2D unsteady Euler solver . . . 59
3.2.1.1 Blade force and work exchange . . . 60
3.2.2 Boundary conditions, plenum and throttle modeling . . . 62
3.3 Modeling of a complete compressor map . . . 63
3.3.1 Forward flow . . . 64
3.3.2 Stalled flow . . . 69
3.3.3 Reverse flow . . . 77
3.4 Quasi-2D Unsteady Euler solver + 'Parallel compressors' . . . 79
3.4.1 Modified 'parallel compressors' theory . . . 79
3.4.2 Extension to the circumferential direction: FENICE-PC . . . 81
3.5 FENICE-2D . . . 83
3.6 FENICE tool general information . . . 84
3.6.1 Equations' integration scheme . . . 85
3.6.2 Inputs and outputs . . . 86
3.7 Summary . . . 89

4 Results and verification **90**
4.1 Lagrangian solver and Euler solver in comparison . . . 90
4.1.1 Verification . . . 90
4.2 Quasi-2D unsteady Euler solver . . . 97
4.2.1 Forward flow . . . 98
4.2.2 Stalled flow . . . 102
4.2.2.1 Influence of the time delay constant . . . 102
4.2.3 Reverse flow . . . 104
4.2.3.1 Influence of the plenum size . . . 106
4.2.3.2 Influence of the stall inception model . . . 107
4.3 Quasi-2D unsteady Euler + 'parallel compressors' (FENICE-PC) . . . 111
4.4 FENICE-2D verification . . . 119
4.4.1 Comparison between FENICE-2D and FENICE-PC (1 sector) 119
4.4.2 FENICE-2D and inlet distortion . . . 120
4.5 Verification against 3D CFD models . . . 124
4.6 FENICE-PC/2D Capabilities assessment . . . 144

5 Parametric study in the rotating stall region **149**
5.1 Inlet total pressure distortion 150
5.1.1 Effect of the amount of inlet total pressure distortion 150
5.1.2 Effect of the circumferential extent of the distorted region . . 152
5.1.3 Temporary and stationary distortion 156
5.2 Modeling of spike-type disturbance through axial force pulses 159
5.3 Derivation of the rotating stall characteristic 162

6 Conclusions and recommendations **167**
6.1 Summary 167
6.2 Conclusions 169
6.3 Recommendations for future work 171

References **173**

Bibliography **181**

Appendix A **187**

Appendix B **191**

List of Figures

1.1 Inviscid and viscous flow around a body [3]. 3
1.2 Flow separation [3]. 3
1.3 Boundary layer separation over a flat plate [32]. 4
1.4 Boundary layer separation over aerofoil [4]. 5
1.5 The stall inception in an axial compressor [65]. 6
1.6 Effects of different inlet distortions on the compressor performance [16]. 7
1.7 Two different transient behaviors after a shaft failure event [62]. . . . 8
1.8 Boeing 767-2B7/ER (US Airways) Netherlands 22 November 2005 [35]. 9
1.9 F-18C compressor surge during catapult launch - USS Nimitz 19 October 2009 [12]. 9
1.10 Rotating stall regimes [20]. 11
1.11 Possible rotating stall scenario [82]. 11
1.12 Examples of throttle curves on a compressor map [57]. 12

2.1 Typical axial compressor map [22]. 17
2.2 Schematic of a 2D linear cascade. 18
2.3 Blade geometrical details and sign convention. 19
2.4 Rotating stall and surge in comparison [57]. 20
2.5 Active and passive stall cell structure concepts [19]. 21
2.6 Axial motion of the flow inside the stall cell [19]. 21
2.7 Typical stall inception from modal waves [82]. 23
2.8 Example of spyke-type inception [72]. 24
2.9 Camp and Day criteria for determining the stall-inception type [72]. . 25
2.10 Tip-clearance spillage and back-flow [72]. 25
2.11 S1 and S2 stream surfaces for through-flow approaches [81]. 27
2.12 Pressure loss sources in a cascade [68]. 29
2.13 Stall cell blockage and its effect on the incoming flow [8]. 32
2.14 Basic 'parallel compressors' model for compressor response to circumferential total pressure distortion [47]. 33

2.15 Basic 'parallel compressors' model for compressor response to circumferential total temperature distortion [47]. 34
2.16 'Parallel compressors' approach applied to rotating stall studies [41]. . 35
2.17 Moore-Greitzer compressor model [80]. 38
2.18 Mechanical analogy of the Moore-Greitzer lumped-volume model [80]. 40
2.19 Transient response of a surge system to a pressure perturbation [57]. . 41
2.20 Mass flow redistribution induced by the stall region [82]. 46

3.1 Domain of the case-study [7]. 50
3.2 Elements motion during the integration [7]. 53
3.3 Characteristic waves for subsonic inlet and outlet. 57
3.4 Control volume for the calculation of the blade forces in a viscous flow field [65]. 60
3.5 Example of blade force and work exchange distribution adopted. . . . 62
3.6 Velocity triangles during forward flow and sign convention. 64
3.7 Typical trend of loss coefficient against incidence [6]. 67
3.8 Mach number effect on the pressure loss bucket [6]. 68
3.9 Off-design pressure loss coefficient against normalized incidence angle [6]. 69
3.10 Effect of split distortion, experimental obsevations carried out by Reid [61]. 72
3.11 First order time lag applied to the rotor incidence. 73
3.12 Moses and Thomason model 73
3.13 Regions of delay application 76
3.14 Velocity triangles during reverse flow and sign convention. 77
3.15 Basic concept of Longley's reverse flow model [46]. 78
3.16 'Parallel compressors' original concept [75]. 79
3.17 Model for the stall cell propagation mechanism. 80
3.18 'Parallel compressors' with cross flow. 81
3.19 Main program structure. 88

4.1 Lagrangian case study: straight duct with sudden change in cross section. 90
4.2 Comparison of steady solutions. 91
4.3 Propagation of the velocity disturbance from t=2s to t=2.4s (left to right and top to bottom). 93
4.4 Propagation of the temperature disturbance from t=2s to t=2.4s (left to right and top to bottom). 94

4.5 Propagation of the velocity disturbance predicted using the Lagrangian solver by Shen [66, 7]. 94
4.6 Propagation of the temperature disturbance predicted using the Lagrangian solver by Shen [66, 7]. 95
4.7 Time-wise sinusoidal cross section variation: (top graph) cross section of the middle of the duct against time, (bottom graph) axial distribution of the cross section respectively at zero, positive and negative indentation. 96
4.8 Propagation of a velocity disturbance produced by a sudden change in the cross section. 96
4.9 Propagation of a velocity disturbance produced by a sinusoidal time wise change in the cross section. 97
4.10 Cross section of the two/stage compressor NASA TP 1493 [76]. . . . 100
4.11 Comparison against experimental data of the predicted forward flow characteristic for the NASA TP 1493. 100
4.12 Cross sectional view of the compressor C106 [18]. 101
4.13 Comparison against experimental data of the predicted forward flow characteristic for the NASA TP 1493. 101
4.14 Influence of the delay parameter τ for a constant throttle setting. . . . 102
4.15 Total to static pressure rise versus rotor revolutions for different values of τ. 103
4.16 FENICE-PC (1 sector) prediction of the axis-symmetric rotating stall characteristic. 104
4.17 Comparison between the reverse flow characteristic predict by the Euler solver against the experimental one. 105
4.18 Sketch of the adopted configuration. 106
4.19 Influence of the plenum size beyond the surge line. 106
4.20 Plenum size effect on the frequency of oscillation: from rotating stall to deep surge. 107
4.21 Comparison of the three blade stall inception models for a plenum volume of 0.5 $m^3$and a throttle closure of 20%. 108
4.22 Comparison of the three blade stall inception models for a plenum volume of 1.0 m^3 and a throttle closure of 20%. 108
4.23 Comparison of the three blade stall inception models for a plenum volume of 1.5 m^3 and a throttle closure of 20%. 109
4.24 Comparison of the three blade stall inception models for a plenum volume of 2.0 m^3 and a throttle closure of 20%. 109

4.25 Comparison of the three blade stall inception models for a plenum volume of 2.5 m^3 and a throttle closure of 20%. 110
4.26 Plenum size investigation for the NASA TP 1493 compressor. 111
4.27 Clean operating points used as starting condition for inlet flow distortion investigations. 112
4.28 Compressor performance prediction for a total pressure drop of 2.5% and 5% imposed on half annulus adopting the original 'parallel compressors' approach. 113
4.29 Flow properties along the compressor obtained with the original 'parallel compressors' approach for the case of inlet total pressure drop of 2.5%. 114
4.30 Mass flow exchanges between clean and distorted sectors. Comparison Gap and Full cross prediction for a 2.5% total pressure drop on half annulus. 115
4.31 Static pressure trend along the axial direction for clean and distorted sectors. Comparison Gap and Full cross prediction for a 2.5% total pressure drop on half annulus. 116
4.32 Total pressure trend along the axial direction for clean and distorted sectors. Comparison Gap and Full cross prediction for a 2.5% total pressure drop on half annulus. 116
4.33 Compressor performance prediction for a total temperature increase of 2.5% and 5% on half annulus adopting the original 'parallel compressors' approach. 118
4.34 Effect of the amount of cross flow on the compressor performance. . 119
4.35 Circumferential discretization effect for an axis-symmetric stall. . . . 120
4.36 Comparison of compressor performance prediction with FENICE-PC no cross and FENICE-2D. 121
4.37 Comparison of the predictions obtained with all the different tool's set ups for the case of a 2.5% total pressure deficit on half annulus. (a) Comparison for different outlet conditions. (b) Effect of the circumferential resolution on the performance prediction of FENICE-2D. . . 121
4.38 Comparison between axial trends of the tangential velocity. (a) FENICE-PC no Cross and (b) FENICE-2D. 122
4.39 Comparison between axial trends of the tangential velocity. (a) FENICE-2D with a circumferential grid of 8 sectors, (b) FENICE-PC Full Cross with a C_{xflow} coefficient equal to 0.2. 122

4.40 Compressor performance prediction in the case of a total temperature increase of 2.5% on half annulus. 124
4.41 Convergent duct with total pressure distortion on a 90 degrees sector. 125
4.42 Contour of the tangential velocity obtained with ANSYS CFX. 127
4.43 Comparison of the circumferential trends of the tangential velocity. . . 127
4.44 Contour of the total pressure obtained with ANSYS CFX. 128
4.45 Comparison of the circumferential trend prediction of the total pressure. 128
4.46 Contour of the axial velocity obtained with ANSYS CFX. 129
4.47 Comparison of the circumferential trend prediction of the axial velocity. 129
4.48 Contour of the static pressure obtained with ANSYS CFX. 130
4.49 Comparison of the circumferential trend prediction for the static pressure. 130
4.50 Influence of the amount of mass flow exchange. 132
4.51 Experimental map of NASA Rotor 37. 133
4.52 Comparison of the predicted forward flow characteristic obtained with 3D CFD and FENICE-2D/PC against the experimental data for the NASA Rotor 37. 134
4.53 Rotor 37 3D domain adopted for the CFX simulations. 136
4.54 Circumferential trend of the axial velocity before and after the rotor for the case of total pressure distortion. 136
4.55 Circumferential trend of the total pressure before and after the rotor for the case of total pressure distortion. 137
4.56 Circumferential trend of the static pressure before and after the rotor for the case of total pressure distortion. 137
4.57 Circumferential trend of the total temperature before and after the rotor for the case of total pressure distortion. 138
4.58 Circumferential trend of the static temperature before and after the rotor for the case of total pressure distortion. 138
4.59 Circumferential trend of the axial velocity before and after the rotor for the case of total temperature distortion. 139
4.60 Circumferential trend of the total pressure before and after the rotor for the case of total temperature distortion. 140
4.61 Circumferential trend of the static pressure before and after the rotor for the case of total temperature distortion. 140
4.62 Circumferential trend of the total temperature before and after the rotor for the case of total temperature distortion. 141

4.63 Circumferential trend of the static temperature before and after the rotor for the case of total temperature distortion. 141
4.64 Overall compressor performance predictions for the case of total pressure distortion. 142
4.65 Overall compressor performance predictions for the case of total pressure distortion. 143
4.66 The differences behind FENICE-PC and FENICE-2D. 144
4.67 Comparison mass flow exchange: W_{cross} and G_1. 145
4.68 Comparison axial momentum exchange: Mom_{xcross} and G_2. 146
4.69 Comparison tangential momentum exchange: Mom_{tcross} and G_3. . . . 146
4.70 Comparison total enthalpy exchange: E_{cross} and G_4. 147

5.1 Effect of different amounts of total pressure distortion on a sector of 60 degrees and 90 degrees on the performance of the compressor C106. 151
5.2 Multiple regions of total pressure distortion. 152
5.3 Comparison between the effect of a 5% total pressure deficit distributed over a 60 degrees sectors against the effect of the same amount of distortion distributed over two 30 degrees opposite-facing sectors. . . . 153
5.4 Comparison between the effect of a stationary and a temporary three-region 5% total pressure deficit. 154
5.5 Flow coefficient traces at the IGV's inlet for a three-region stationary total pressure distortion. 155
5.6 Flow coefficient traces at the IGV's inlet for a three-region temporary total pressure distortion. 155
5.7 Temporary and stationary inlet total pressure distortion for the compressor C106. 157
5.8 Transient performance obtained combining a temporary distortion and a change in throttle settings. 157
5.9 Comparison of the transient performance for a stationary and a temporary inlet total pressure deficit for the NASA TP 1493. 158
5.10 Transient behavior of the total to static pressure rise coefficient for a temporary and a stationary case of inlet total pressure distortion for the compressor NASA TP 1493. 159
5.11 Positive axial force spike on the third rotor of the compressor C106. . 160
5.12 Negative axial force spike on the third rotor of the compressor C106. . 161
5.13 Flow coefficient traces at the inlet of the IGV for a negative spike of 1.05. 162
5.14 Flow coefficient traces at the inlet of the IGV for a negative spike of 1.2. 162

5.15 Rotating stall characteristic combining inlet total pressure distortion and throttle settings. 163
5.16 Time average of the compressor performance for three different throttle setting and stationary 5% total pressure distortion on a 60 degrees sector. 164
5.17 Rotating stall characteristic obtained combining inlet flow distortion and throttle changes. 164
5.18 Total to static pressure rise coefficient versus time with throttle settings highlighted. 165
5.19 Rotating stall characteristic obtained combining spikes and throttle changes. 166

Nomenclature

Roman

Symbols	**Descriptions**	**Units**
A	Cross section area, empirical factor Aungier model	m^2,-
a	Speed of sound	$\frac{m}{s^2}$
$\frac{a}{c}$	Location of the maximum thickness	%
B	Greitzer parameter, source terms conservative Euler equations	-,-
b	Blockage longley's model, exponent Aungier model	-,-
C	Coefficient	-
c	Chord	m
cp	Specific heat at constant pressure	$\frac{J}{kgK}$
cv	Specific heat at constant volume	$\frac{J}{kgK}$
D	Diffusion factor	-
dt	Time step	s
e	Exponent Aungier model	°
F	Force per unit lenght, axial fluxes conservative Euler equation	$\frac{N}{m}$
G	Greitzer parameter, tangential fluxes conservative Euler equations	-,-
H	Enthalpy	J
h	Element length	m

i	Incidence angle	$^{\circ}$
k	Loss coefficient moses and Thomason model	$-$
L	Length	m
M	Mach number	-
m	Slope parameter Aungier model	-
$\dot{m}$	Mass flow rate	$\frac{kg}{s}$
Mom	Momentum due to cross flow	$\frac{kg}{s^2}$
N	Rotational speed, number of stages, number of stall cells	$rpm,-$
$\bar{n}$	Normal vector	$-$
P	Pressure	Pa
Q	Generic variable	$-$
q	Exponent Aungier model	-
R	constant ideal gas, range of angles	$-,^{\circ}$
r	Meanline radius	m
S	Surfacethrough-flow methods, entropy, characteristic slope	$m^2,\frac{J}{K}$
T	Temperature	K
t	Blade thickness, time	m,s
th	Throttle settings	-
U	Blade speed, Euler conservative variable	$\frac{m}{s}$,-
V	Absolute velocity	$\frac{m}{s}$
W	Relative velocity, work per unit length	$\frac{m}{s},\frac{J}{m}$
X	Axial position Lagrangian elements	m
x	Cartesian x-axis	m
y	Cartesian y-axis	m
y_{plus}	Wall distance	-

z	Cartesian z-axis	m

Greek

Symbols	**Description**	**Units**
α	Absolute flow angle, angle of attack, axial area variation	$^\circ, ^\circ, -$
β	Relative flow angle, metal angle, throttle shape parameter	$^\circ, ^\circ, -$
γ	Stagger angle, isentropic expansion factor	$^\circ, -$
Δ	Finite difference, boundary correction lagrangian method	$-, -$
δ	Deviation angle, boundary layer thickness	$^\circ, m$
θ	Camber angle, circumferential direction, dilatation	$^\circ, ^\circ, \frac{m}{s^2}$
ν	Viscosity	$\frac{kg}{ms}$
ξ	Normilized incidence	-
π	Pi number, pressure ratio	$-, -$
ρ	Density	$\frac{kg}{m^3}$
σ	Solidity	-
τ	Time delay parameter	s
Φ	Velocity field	-
ϕ	flow coefficient	-
χ	Actual stage number	-
Ψ	Total to static pressure rise coefficient	-
Ω	Blade rotational speed	$\frac{rad}{s}$
$\bar{\omega}$	Pressure loss coefficient	-

Superscripts

Symbols	**Description**
’	Metal angle, non-dimensional value
$*$	Design value

0	Total property, free stream
cor	Corrector step MacCormark scheme
n	Generic time step
pre	Predictor step MacCormark scheme
Prov	Provisional variable

Subscripts

Symbols	**Description**
0	Zero camber
1,2,3,4	Index governing equations, number of sectors
1.0	Solidity equal to one
atm	Atmospheric condition
c	Compressor, negative stall limit
cell	Stall cell
cross	Cross flow
eff	Effective
eq	Equivalent
err	Error
ex	Exchange
gap	Space between turbo-components
H	Helmholtz
i	General index
in,out	Inlet/Outlet blade or domain
inst	Instantaneous
j	Index elements axial direction
l,r	Left, right

n,t	Normal and tangential force coefficients
p	Plenum
pc	Index circumferential direction
pr	Profile losses
rel	Relative value
REq.aero	Aerodynamic equivalent velocity ratio
REq.geom	Geometry-based equivalent velocity ratio
s	Secondary losses, positive stall limit
sh	Shock losses
ss	Steady-state
stage	Stage
t	Throttle, tangential direction
u	Unstalled
ws,wb	Normal vector surface, normal vector body
X	Damping coefficient
x	Axial direction
xflow	Cross flow coefficient

Acronyms

Symbols	**Description**
2D	Two-dimensional
3D	Three-dimensional
CFD	Computational Fluid Dynamic
CFL	Courant-Friedrichs-Lewy number
CN	Compressor followed by a con-di nozzle
CPN	Compressor followed by a plenum and a con-di nozzle

CPU	Central power unit
DLL	Dynamic-Link Library
FENICE	Fast Euler Numerical integrator for Compressor Evaluation
Full Cross	Cross flow evaluated at each axial element
Gap Cross	Cross flow evaluated at each axial element within rotor-stator gaps
IGV	Inlet Guide Vane
ODE	Ordinary Differential Equation
PC	Parallel Compressors
PDE	Partial Differential Equation
RANS	Reynolds-Averaged Navier-Stokes
SLC	Stream Line Curvature method
SVD	Singular Value Decomposition
TP	Technical report
VIS	Artificial viscosity

Chapter 1

Introduction

1.1 Background

The first axial flow compressor was built and patented in 1901 by Parson [36]. In the following years, compressors have evolved significantly in terms of design and materials. A lot of effort has been devoted in order to improve efficiency, increase the pressure ratio per stage and reduce the weight.

Axial flow compressors are, in fact, a primary component in several industrial and aerospace applications such as gas turbine for power generation, jet engines or pressurization systems. In most applications, compressors are coupled with turbines in order to produce torque or thrust. As many other devices, their operation is possible under certain conditions. Particularly, in turbo-machinery applications, safe and efficient operation of the compression system is imperative. To run a compressor as safely and efficiently as possible, preventing serious mechanical damage, flow instabilities such as rotating stall and surge must be avoided, or dealt with soon after their inception.

During the last 60 years many efforts have been made in order to understand the inception and evolution of rotating stall and surge. Although the knowledge and the capabilities for modeling and controlling the stall dynamics have improved enormously, there are still many lacks in the understanding. As a consequence there is lack of tools that allow the correct prediction of these types of events from onset to final state.

The a priori knowledge of the engine's behavior under different operating conditions is an important requirement to avoid or contain undesirable accidents. Indeed, experimental observations of modern high-speed multistage compressors during every possible operating condition are avoided due to the unreasonable cost and the damage involved. On the other hand, 3D CFD analysis, that represent a quite practical alternative, are very expensive in terms of time and computational power and not always accurate and trustworthy. Within this context, the work reported in this thesis finds its scope. This research was sponsored by Rolls-Royce plc and undertaken within the Shaft Over-speed/Failure Modeling group at the Cranfield University Technology Center (UTC). As a matter of fact, after the rare event of a gas generator shaft failure, rapid over-speed will occur as the power of the turbine is decoupled from its driven compressor. Under this condition it is likely for the compressor to surge. Although in other cases this operating condition should be avoided, in case of over-speed, surge is desirable. In fact, surge limits the mass flow across the turbine reducing the power available and therefore its speed.

There are several other events that can lead the compressor to experience stall or surge or both as it will become clearer hereafter. Therefore it is fundamental having a tool that can be easily applied to different scenarios and which allows a quick assessment of the transient compressor performance under different operating conditions.

1.1.1 Compressor unstable behavior

A compressor is considered stable if, after it is subjected to disturbances that alter its operating equilibrium, it is able to recover. Disturbances can have different origins and nature, they can be stationary or transient; a compressor is stable if after a transient disturbance the operating point goes back to the original one, or in case of stationary disturbances if the compressor finds a new stable point of equilibrium. As mentioned before, for a compressor in an aircraft engine or in an industrial gas-turbine there are several sources of disturbances, in some cases these can lead to the onset of instabilities. Compressor stability can be investigated under two perspectives: operational and aerodynamic stability. This work focuses mainly on the second type, since stall and surge are due to flow separation.

The inception of instabilities can be caused by different factors and their development as well depends on several aspects (not only geometrical features). In order to predict all the possible scenarios it is necessary to have a robust tool that allows the parametric analysis of different phenomena.

The physic behind flow separation inception

Before looking at the various events and features that can lead a compressor to stall, it is worthy to go back to the basic theory of airfoil stall and the role play by the boundary layers. It is common practice in aerodynamics to distinguish between viscous and inviscid flows, where viscous refers to those flows where “transport phenomena” such as mass diffusion, friction and thermal conduction take place, while the opposite applies to the term inviscid. In nature, there are not real inviscid flows, on the other hand, for high Reynolds numbers[1] this assumption can be made. For such flows, in fact, the influence of diffusion, friction and thermal conduction is limited to a very thin region close to the body and known as boundary layer. Figure 1.1 below sketches out the concept.

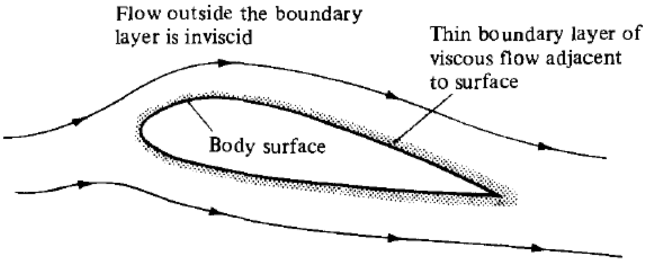

Figure 1.1: Inviscid and viscous flow around a body [3].

If the same airfoil of Figure 1.1 is inclined increasing the incidence angle of the flow, the boundary layer will separate from the suction surface of the body and form a large wake downstream as shown in Figure 1.2.

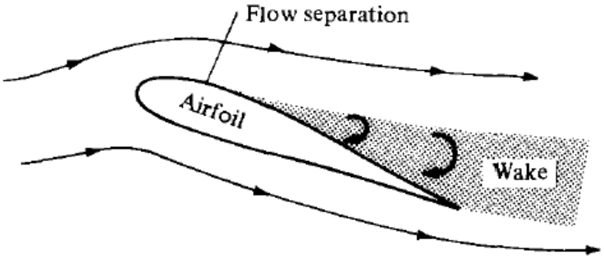

Figure 1.2: Flow separation [3].

To understand the phenomenon, it is necessary to take a closer look to the boundary layer and the flow within this region. If the plate in Figure 1.3 is taken into consideration, it is possible to observe that a boundary layer forms close to the surface once the flow encounters the leading edge of the plate. Close to the leading-edge the boundary layer thickness (δ) is very small but proceeding along the length of the plate the boundary layer becomes thicker as a larger amount of fluid slow down due to the friction. Indeed, close to the leading edge the flow is laminar while at a certain distance the critical value of Re is reached an the flow naturally transitions to turbulent flow.

---

[1] The Reynolds number represents the ratio between inertial and viscous forces.

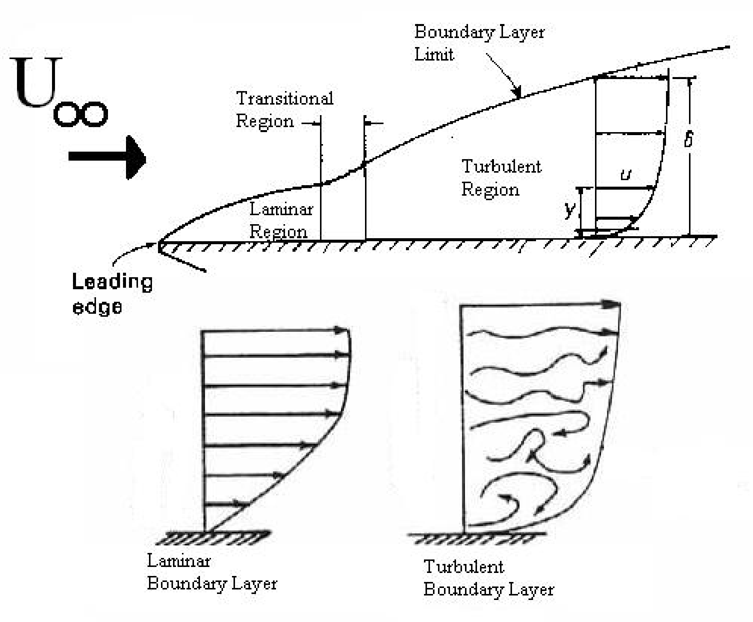

Figure 1.3: Boundary layer separation over a flat plate [32].

It is common practice to identify two major types of drag: skin friction drag due to the viscosity and the relative difference in velocity between different layers of the fluid, and pressure drag, which results from a difference in fluid pressure between the front and rear of the body. Figure 1.3 shows that in a turbulent boundary layer the flow velocity increases more rapidly as we move away from the wall compared to a laminar boundary layer. The steeper velocity gradient close to the wall therefore means that skin friction drag is higher for a turbulent boundary layer.

On the other hand pressure drag is greatly exacerbated by the boundary layer separation. When flow encounters an adverse pressure gradient (i.e. the fluid pressure increases in the flow direction as found after the point of maximum thickness in aerofoils) the flow has to work against the increase in pressure leading to momentum losses and decelerations in flow. As the flow speed in the boundary layer continues to decrease in the direction of the adverse pressure gradient, at some point the slowest moving fluid close to the wall will actually change direction, Figure 1.4. This is called boundary layer separation and leads to a larger wake of vortices forming behind the body.

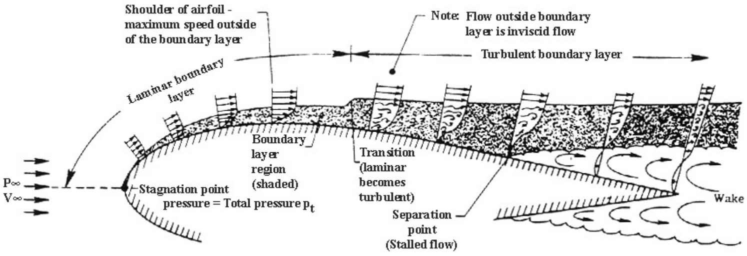

Figure 1.4: Boundary layer separation over aerofoil [4].

The fluid pressure in the vortex wake is much lower than in regions of attached flow close to the leading edge and this pressure difference will therefore push the body backwards. As described earlier the flow velocity in a turbulent boundary layer close to the wall is higher than in a laminar boundary layer. This initially higher fluid momentum means that flow separation occurs further downstream than for laminar flow, resulting in a narrower wake and thus less pressure drag. Skin friction drag is minimised by laminar flow and greatly worsened by turbulent flow while pressure drag is minimised by turbulent flow and greatly worsened by laminar flow. However, it is also clear that overall minimum drag is encountered for purely frictional drag with a laminar boundary layer.

Extending the described concept to a blade-row of an axial compressor, the onset of stall and surge becomes clearer. There are different types of events that can lead to the inception of stall as explained later in this section. Considering for instance, a generic phenomenon that produces a descrease in mass flow and therefore an increase in incidence angle, the sequence of events reported in Figure 1.5 can be observed. As first, a boundary layer separation inception may occur at a few blades, as sketched in Figure 1.5 (a). While the channel of these blades are occupied by low energetic stall cells, the rest of the blades operate at normal flow condition, however, at a different incidence angle, as shown in Figure 1.5 (b). Since the stall cells have blocked a portion of the cross sectional area, a redistribution of the mass flow in circumferential direction occurs, leading to a redistribution of the incidence angles. Based on the separation extent, the cells may partially occupy the tip and hub region, as well as the entire blade channels from hub to tip, as shown in Figure 1.5 (c). If these stall cells are located within rotor blades, they rotate with the corresponding frequency causing the compressor to operate in rotating stall mode. This operating mode is characterized by temporal fluctuations of the mass flow. Further reducing the mass flow may lead to a complete breakdown of the compressor operation that is called compressor surge. In this case, the compressor mass flow periodically oscillates between positive and negative.

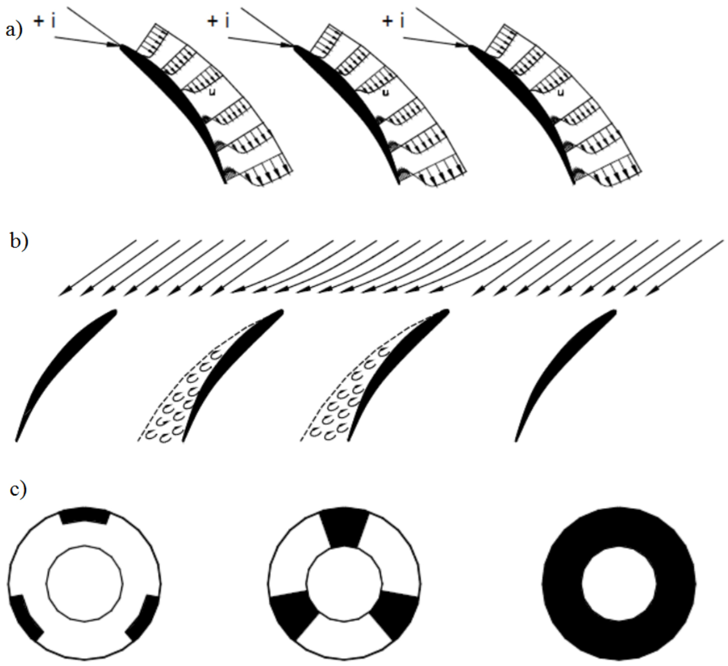

Figure 1.5: The stall inception in an axial compressor [65].

Events and compressor features that can affect the stall inception

During the operating life of an aircraft engine, several operating conditions can lead to the onset of stall and its dynamics:

- Inlet distortion/non-uniformity of the inflow due to inlet lip separation, hot gas ingestion, boundary layer separation etc;
- Engine wear that leads to changes of the tip clearances and coupling between rotor dynamics and tip clearances effect, mechanical vibrations;
- Shaft failure;
- Acceleration from idle to full power [57].

For instance, speaking about the first condition, it is very common for a compressor to be subjected to inlet distortion. Such distortion can occur naturally due to the unsatisfactory nature of the inlet or because of operational effects such as cross-wind into the engine intake. The inlet distortions are usually quite complex, therefore, in order to simplify the analysis of their effect, they are subdivided into distortions with circumferential extent or distortions with radial extent. It has been proved that circumferential distortions have a much stronger effect on the stability of the compressor especially if they act in the same direction of the rotor rotation (co-rotating distortion) [30, 49]. In most cases the distortion is transient hence it will have little or no effect, but in some circumstances the inlet distortion can be amplified leading to strong instabilities. Three types of inlet distortion are usually recognized: total pressure, total temperature and swirl; a combination of the mentioned distortions can also occur. Figure 1.6 clarifies the effect of different distortions on the turbo-machine; in brief the compressor performance is seriously penalized resulting in a drastically decrease of the surge margin.

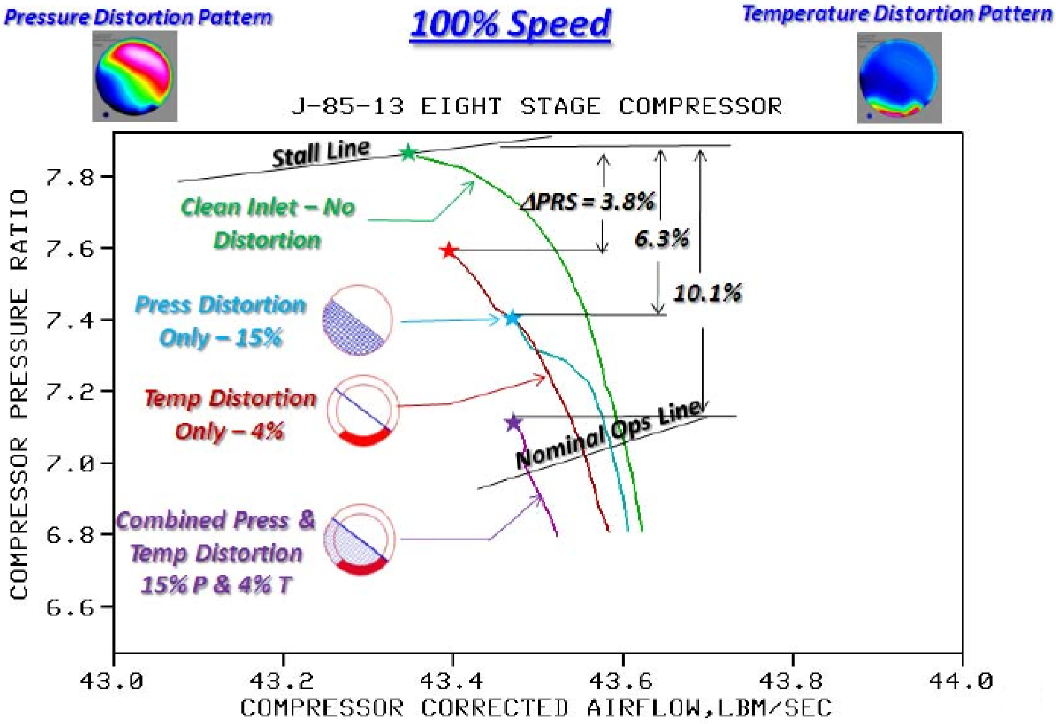

Figure 1.6: Effects of different inlet distortions on the compressor performance [16].

Another event that can occur and lead to stall inception, even if quite a rare scenario for a gas turbine, is the shaft failure. Indeed, after a shaft breakage, the turbine and the compressor are decoupled, if the engine is running at high power, the turbine will over-speed while the decoupled compressor will slow down. Unless surge occurs or fuel is shut off, the turbine's over-speed will end up in the burst of the turbine disc in a very short time, of the order of 100-200 milliseconds. Under this condition surge is therefore a desirable condition; the occurrence of this instability reduces the mass flow passing through the compressor controlling in this way the turbine over-speed [27].

The transient evolution of the flow after a shaft breakage is quite unknown and still unpredictable. For instance, the engine can surge, recover and surge again. The evolution and the final scenario is strongly dependent on the engine geometry, the particular failure and the role played by all the affected components.

An example of the variable nature of surge and rotating stall events is given in Figure 1.7. The graph, courtesy of Rolls-Royce plc, compares two engines rundown after a shaft-failure event. In both cases an initial surge due to the mechanical vibrations produced by the shaft's break occurs, but while the engine L4-3 settles in stall after the first surge and runs down, the engine L3-8A suddenly recovers from the first surge for then entering a second surge due to thermodynamic conditions and settling down [62].

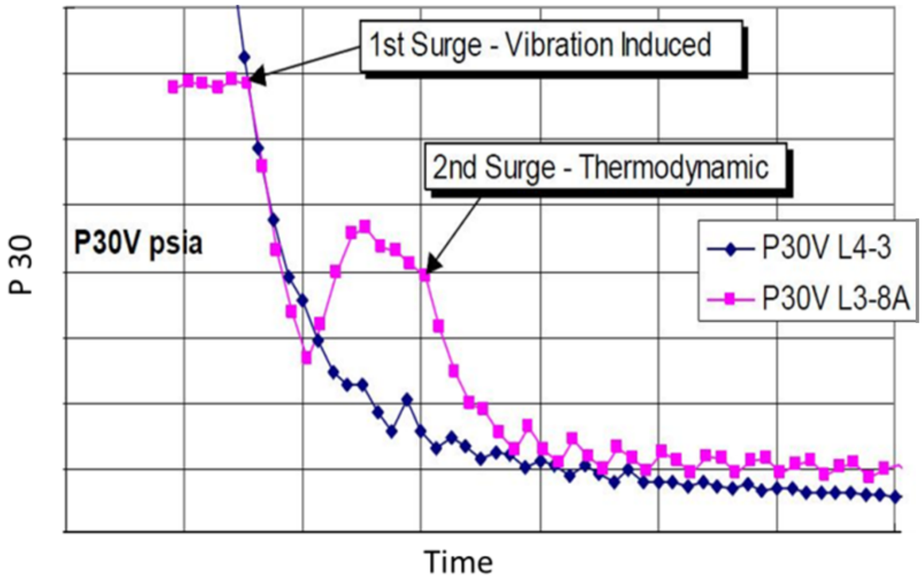

Figure 1.7: Two different transient behaviors after a shaft failure event [62].

Before introducing the various scenarios that can be observed during rotating stall and surge, two real and quite recent examples of surge events are discussed.

The first event reported in Figure 1.8 shows a surge event occurred to the US Airways Boeing 767 on the 22 of November 2005 during take-off at the Amsterdam-Schiphol airport. The photographer and other witnesses experienced 8 loud bangs followed by flames which are typical in compressor stall/surge episodes. In this particular occasion the event was not catastrophic, the pilots managed to return the aircraft safely on the ground.

Figure 1.8: Boeing 767-2B7/ER (US Airways) Netherlands 22 November 2005 [35].

Figure 1.9 shows a F-18C fully loaded with fuel and weapons experiencing a compressor surge during a catapult launch.

Figure 1.9: F-18C compressor surge during catapult launch - USS Nimitz 19 October 2009 [12].

Compressor surges are quite frequent on US aircraft carriers. As a matter of fact, during catapult launch, hot vapor is generated and can easily be ingested by the aircraft air intake thus creating a breakdown in the compression. The compressor, until recovery, is unable to absorb the momentary disturbance and to continue pushing the air against the already-compressed air behind it. As a consequence, the compressor experiences a momentary reversal of the air flow and a violent expulsion of previously compressed air out through the engine intake. The all event is usually associated with loud bangs from the engine and "back fires".

The compressor will usually recover to normal flow once the engine pressure ratio reduces to a level at which the compressor is capable of sustaining stable airflow. As emphasized by the sequence of pictures, the F-18C managed to complete its take-off. Indeed, carrier air wing airplanes cannot abort their take-off once started it. These kind of airplanes are, therefore, usually designed in order to be able to complete their take-off even with one engine momentarily out of order.

1.1.2 Classification of rotating stall and surge

Rotating stall and surge are two phenomena strictly linked, therefore they cannot be treated separately. The coupled nature of these phenomena has generated ambiguity in the terminology when referring to all the possible outcomes. This subsection aims to clarify the possible flow regimes during these unstable conditions and the terminology usually adopted and followed by the author through this work.

Talking about rotating stall, a first distinction is between part-span stall and full-span stall. In the case of part-span stall, as it is clear from the name itself, the stall cell, which is usually identified as a region of low flow, covers only a part of the span (during this regime , it is quite common to observe the stall cell located at the tip). On the other hand, when talking about full-span stall, the stall region covers the whole span from hub to shroud. The number of stall cells can also change. Figure 1.10 shows how the occurrence of one pattern instead of the other is also linked to the speed at which the surge limit is crossed. For instance at low speed operation part-span stall regimes are often observed while at higher speeds full-span stall is more common. In terms of transient characteristic, part-span stall is usually related to a progressive stall characteristic while full-span is more typical of an abrupt stall characteristic as shown in Figure 1.10.

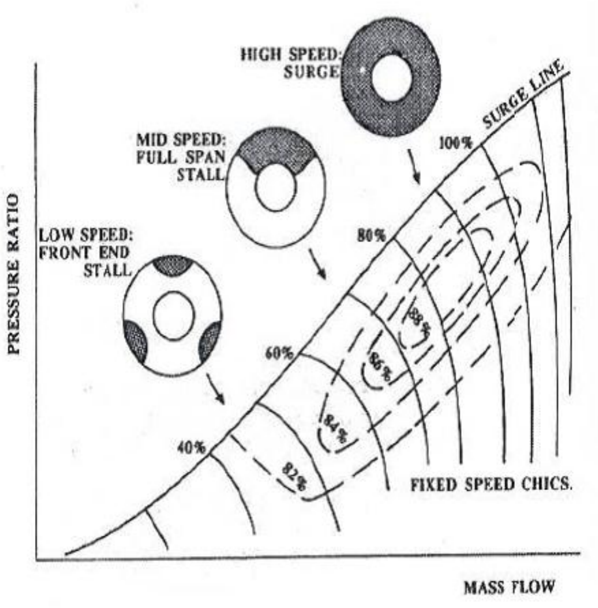

Figure 1.10: Rotating stall regimes [20].

Figure 1.11 sketches out three different types of characteristic. The first characteristic on the left, figure (a), is defined as progressive stall since it is characterized by a gradual reduction of total pressure rise after the inception of stall. At the onset of a progressive stall it is common to observe multiple cells but in the end full-span rotating stall will develop. The second characteristic, figure (b), is known as ’abrupt’ stall due to the steep jump between forward and stall chic. This behavior is usually linked to the presence of a single full span stall cell. The third characteristic is typical of the surge phenomenon which is described at the end of this section. Before shifting the focus on the surge event, it is important to remark that there are four other compressor’s features which play a role in determining the above mentioned outcomes.

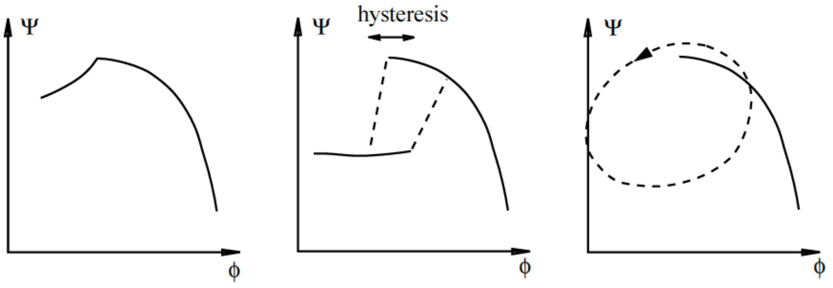

a) progressive stall b) 'abrupt' stall c) surge

Figure 1.11: Possible rotating stall scenario [82].

The first, worth to be mentioned, is the throttle curve (typical throttles curve are reported below in Figure 1.12 where K_t is a parameter used to change the throttle's slope), changing the slope of this characteristic is possible to obtained all the three stall characteristics described above. Indeed, a steeper throttle curve corresponds to a higher blockage which is one of the principal causes of stall onset.

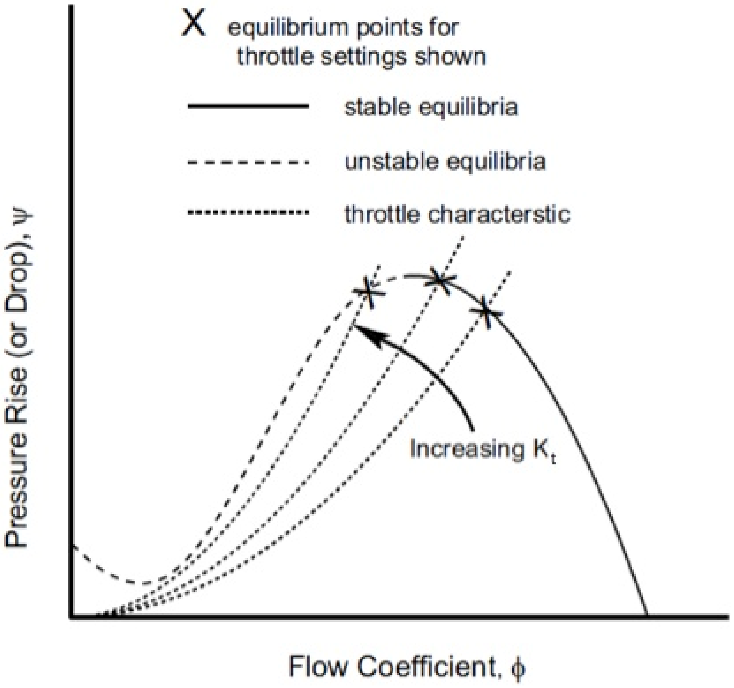

Figure 1.12: Examples of throttle curves on a compressor map [57].

There are then two geometrical features which have quite a strong impact on the occurrence of one pattern instead of the other: the number of stages and the hub to tip ratio. As a matter of fact, increasing the number of stages, the blockage increases, therefore it is more likely to have full-span at stall inception. Regarding the hub to tip ratio, generally, compressors with low hub to tip ratio exhibit part-span stall while compressors of moderate or high hub to tip ratio can develop part or full-span stall depending upon the blockage conditions. The fourth important feature in this context is the flow coefficient, usually defined as the ratio between the axial velocity and the blade speed. This parameter influences the slope of the compressor characteristic and therefore the amount of blockage; compressors with higher flow coefficients are more likely to manifest full-span stall due to the higher amount of blockage produced.

Shifting now the discussion to the surge phenomenon, surge is a dynamic instability, as explained in Section §2.2, that can produce severe damage to the compressor. Comparing it with rotating stall, the average flow across the annulus goes through oscillations of larger amplitudes with a lower frequency in the range from 3 to 10 Hz.

Surge is the most complex and varied condition of operation; it involves limit-cycle type oscillation of pressure rise and mass flow. Each cycle begins with rotating stall which produces a strong drop in the pressure rise follows by a rapid deceleration of the flow through the machine. When the pressure behind the compressor begins to pump the downstream collector up to full pressure again, the process repeats itself (hysteresis) [57].

A common practice is to distinguish between classic and deep surge; in both cases pressure and mass flow present a limit-cycle type of oscillation. The difference between classic and deep surge is due to the amplitude of the mentioned oscillation. Indeed during deep surge the mass flow through the compressor reverses and for a certain amount of time the engine discharges from both inlet and outlet.

1.2 Aims and objectives

The importance of designing a gas turbine that operates efficiently and safely, no matter which application is under discussion, has been mentioned along with the lack of knowledge on the rotating stall and surge phenomena. The necessity of having a tool able to predict the complete compressor map and in general to assess the transient behavior under different operating conditions satisfying requirements of accuracy, robustness and efficiency was also emphasized.

Although this project is undertaken within the Shaft-Over-speed/Failure Modeling group at Cranfield UTC, the variety of events which can promote the occurrence of rotating stall and surge, encouraged to develop a generic unsteady solver for the assessment and study of different compressor geometries subjected to various operating conditions.

Summarizing aims and objectives of this research, in order to succeed and achieve the final goal, the following steps were identified:

- Literature search on :
    - rotating stall and surge phenomena to identify the key features, similarities and differences;
    - compressor models and numerical techniques usually adopted to tackle these phenomena;
- Implementation of an unsteady solver able to satisfy the requirements reported as follows:
    - accuracy, robustness and efficiency;

  - geometrical information only as input;
  - capability of simulating/predicting transient performance of multistage axial compressors;

- Verification against experimental results and numerical results obtained through ANSYS CFX for different case scenarios (effect of stationary and temporary inlet flow distortion, spike-type disturbances etc.).

- Investigations of rotating stall key features: stall inception, compressor performance drop, influence of the plenum size, influence of the flow inertia, stall recovery capability, derivation of the rotating stall characteristic etc.

1.3 Thesis outline

This introductory chapter has already provided the reader with an overview on the research topic, highlighting aims and objectives, and with an initial notion of the methodology adopted. This section aims to provide the reader with a useful guideline to understand the mindset behind the all research.

The following chapter reports on the "Literature review" carried out by the author. Firstly, the reader is introduced to the axial compressor performance topic through a description of the compressor map which is the most straight forward way to represent and communicate information on compressor performance. A detailed review on the rotating stall and surge phenomena in terms of detection, inception and development is then provided. The last part of this chapter deals with computational fluid dynamic tools and methods that are usually adopted in this field together with the most well known compressor's through-flow models.

The third chapter deals with the methodology that was followed during this doctoral research to develop the unsteady solver under discussion. In particular, this chapter explains the path that led to the development of two versions of the tool; a Quasi-2D Euler solver that relies on the 'parallel compressors' technique to deal with asymmetric flow field (FENICE[2]-PC) and a 2D Euler solver (FENICE-2D). For both versions several details are provided on the computational approach adopted such as governing equations, source terms calculation, boundary conditions, etc. The core of this chapter consists on the description of how the modeling of the three regions of a compressor map was achieved providing details on different levels, from the sign conventions of the velocity triangles to semi-empirical correlations for pressure loss and deviations

---

[2] The name FENICE (/fe'nitʃe/), was inspired by the equivalent italian word for phoenix, the fabulous bird. FENICE stands for Fast Euler Numerical Integrator for Compressor Evaluation.

and the approach followed to achieve an asymmetric modeling capability. The last part of the methodology chapter describes the tool structure with useful information on how to set up and run the developed tool and post-process the obtained results. Chapters 4 and 5 present the results obtained during the verification and the parametric study performed with both versions of the tool emphasizing their pros and cons. The tool was , indeed, tested for different compressor geometries (NASA TP 1493, C106, Rotor 37) depending on the available experimental data and under different operating conditions. Conclusion and recommendations for future work follow in Chapter 6. Further details such as compressor geometries and information on tool's inputs and outputs can be found in the appendices.

Chapter 2

Literature review

This chapter reports on the literature search that was carried out during the doctoral research. Firstly, an overview of compressor performance is presented along with terminology and basic concepts of aerodynamics. The chapter then describes in detail the rotating stall and surge phenomena; in particular this chapter provides information on stall cell structure and stall inception. An important part of the literature review is also dedicated to the description of numerical techniques and models commonly adopted to assess the behavior of the compressor when subjected to rotating stall and/or surge.

2.1 Axial compressor performance

When dealing with axial compressor performance it is common practice to take into consideration the compressor map. In fact, each compressor has a characteristic map that describes its performance at design and off-design conditions. A typical example of high-speed axial compressor map is shown in Figure 2.1. The map shows the relationship between the four parameters commonly adopted to describe compressor operation: pressure ratio; rotational speed; mass flow; and efficiency. These parameters are usually considered non-dimensional or corrected to allow an easier comparison between different compressors. As illustrated below, these kinds of maps typically display the variation of total pressure ratio as a function of non-dimensional mass flow at a series of constant non-dimensional speed lines. The efficiency can be found in a separated graph or, as in this particular case, reported directly on the compressor map through “islands”.

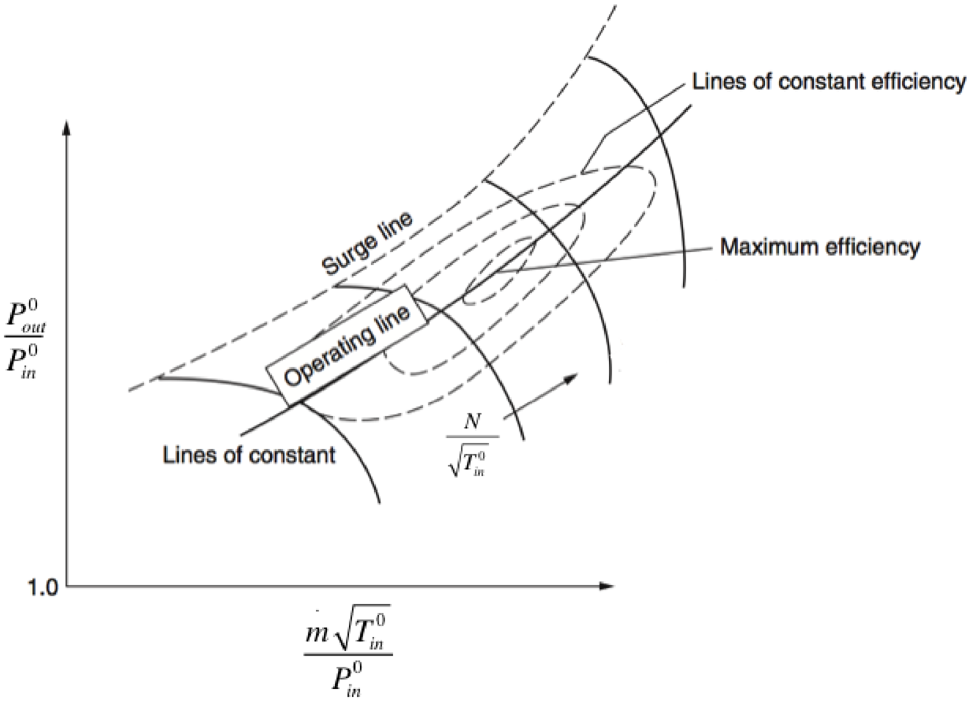

Figure 2.1: Typical axial compressor map [22].

The most important features, which it is worthy mentioning, are the limits of safe operation. Considering, for instance, a certain speed line on the map, increasing the pressure ratio, the operating point will move upward and eventually it will reach the surge line. The blades of the compressor will stall entering a zone of unstable operation. Vice versa, increasing the mass flow, the point moves downward on the same speed line approaching a zone referred to as “stone wall” or choke. While at choke the machine has reached its maximum mass flow, the surge limit is far more important since it can lead to a catastrophic scenario and therefore its occurrence should be avoided. Surge consists on the reversal of flow and is a complete breakdown of the continuous steady flow through the whole compressor. Surge leads to mechanical damage due to the large fluctuations of flow and therefore strong changes in the direction of the thrust forces [60]. Rotating stall as introduced in the previous chapter, is another transient phenomenon that can be encounter beyond the surge line. The latter is less severe than the former, on the other hand one can lead to the other and vice versa. A more complete and detailed description of the phenomena occurring beyond the surge line is provided in detail in Section §2.2.

2.1.1 Terminology and fundamentals of cascades aerodynamics

At this point, before starting a detail discussion on compressor instabilities, it is worthwhile providing a clear description of the terminology adopted when referring to the blade geometry (see Figure 2.2 and Figure 2.3) and some fundamentals on cascades aerodynamics. Henceforward, this document is coherent with the terminology described in this subsection.

Considering the simple cascade sketched out in Figure 2.2, basically a straight duct with a row of blades moving with velocity U in the tangential direction, it is common practice to switch from the absolute to the relative frame of reference in order to simplify the assessment of compressor performance.

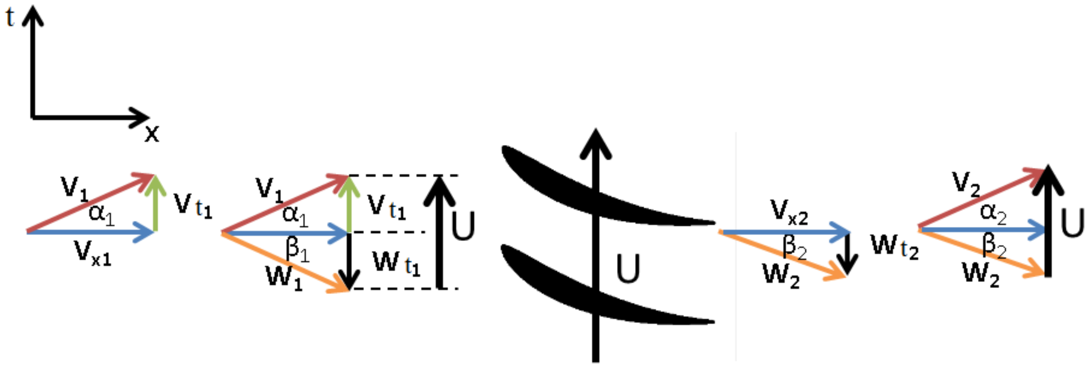

Figure 2.2: Schematic of a 2D linear cascade.

The absolute velocities and flow angles are usually expressed as V_i and α_i, while the relative velocities and flow angles are commonly expressed as W_i and β_i. The relation between absolute and relative frame or vice versa, is provided by the below vector sum:

$$\overline{W} = \overline{V} - \overline{U} \tag{2.1}$$

Figure 2.3 provides further geometrical information of the blade. Considering Figure 2.3, the chord (c) is the distance between the leading and trailing edge of the airfoil. The blade angles ($\beta_1^{'}$ and $\beta_2^{'}$), also known as blade metal angles, are the angles between the axial direction and the line tangent to the camber line at the leading and trailing edges. The difference between the inlet relative angle (β_1) and the blade inlet metal angle ($\beta_1^{'}$) is defined as incidence (i) while the difference between the exit relative flow angle (β_2) and the blade exit metal angle ($\beta_2^{'}$) is known as deviation angle (δ). The angle formed by the chord line and the axial direction is referred as stagger angle (γ).

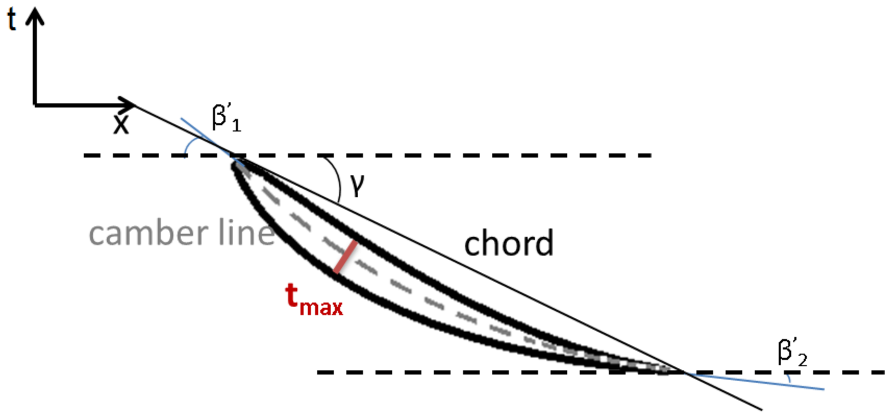

Figure 2.3: Blade geometrical details and sign convention.

Two other blade features, which always appear in pressure loss and deviation correlations, are the maximum thickness between the pressure and suction surface (t_{max}) and its location along the chord ($\frac{a}{c}$ usually expressed in percentage i.e. 0.5 corresponds to half chord).

2.2 Compressor instabilities

Beyond the surge line, as already anticipated, it is noteworthy to identify two main instabilities: rotating stall and surge. These two phenomena were originally treated separately, but it is now recognized that they are strictly connected. Both phenomena can seriously damage the compression system, due to an increase in the temperature of blades and an off-design distribution of stresses [21, 63, 25, 29]. At the same time rotating stall and surge present quite different features, this section aims to highlight the main differences. From a macroscopic point of view, Figure 2.4 sketches out the major differences; rotating stall is a circumferential perturbation characterized by the oscillation of one or more stall cells in the circumferential direction with a velocity lower than the shaft speed (typically 20-60% of shaft speed). The oscillation frequency is high, around 50-100Hz but it does not compromise the axial direction. In contrast during surge, the whole compressor system oscillates in the axial direction, the flow is reversed and the oscillation frequency is around 3-10Hz [30].

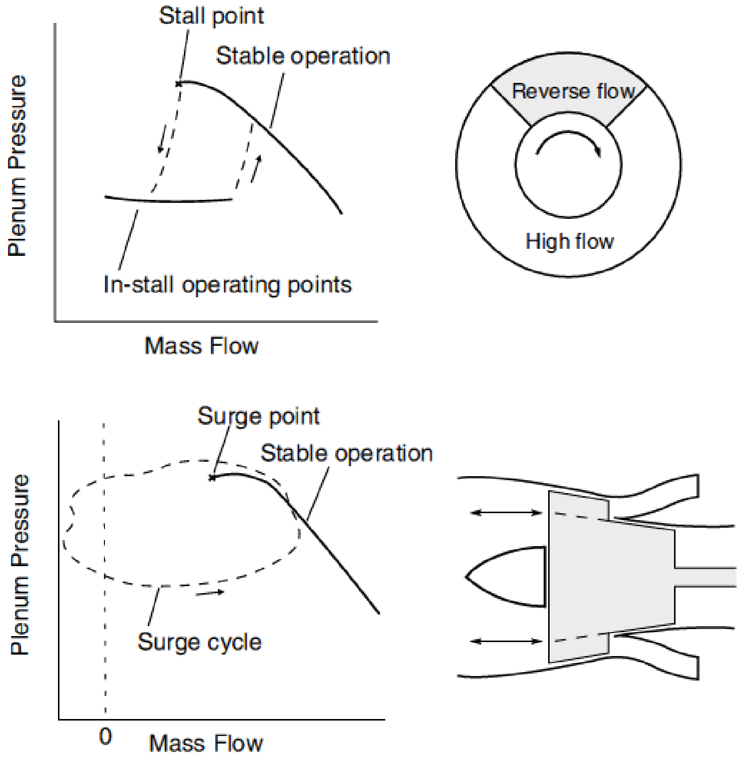

Figure 2.4: Rotating stall and surge in comparison [57].

2.2.1 Rotating stall and Surge features

2.2.1.1 Stall cell structure

The stall cell is usually identified as a region of low or zero flow which rotates around the annulus. This rotational motion around the annulus is better described in Section §2.4 by Emmons' theory [24]. This subsection focus on the stall cell structure; on this regard mainly two different concepts can be find in the literature.

Initially the stall cell was considered as a passive or inactive region of fluid which extends axially as a wake of a bluff body, which means no interaction occurs between the unstalled and stalled flow and an helical twist can be observed along the axial direction [25]. The passive stall cell model was then proved inconsistent by experimental observations, the absence of the helical trend and the presence of high tangential velocities led to the development of the active stall cell structure model [55]. A sketch of both concepts is reported in Figure 2.5.

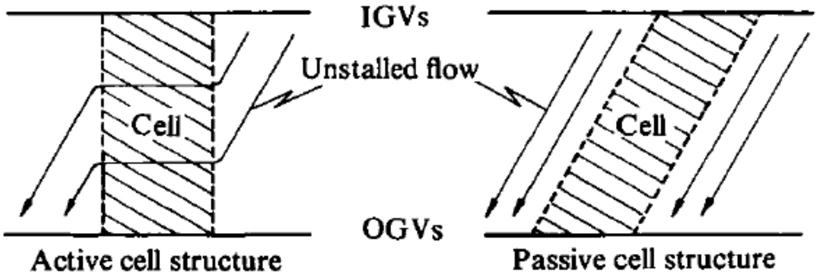

Figure 2.5: Active and passive stall cell structure concepts [19].

Considering Figure 2.5, in the active model the unstalled flow can rotate faster than the stall cell itself, therefore fluid will have to cross the stall region to preserve continuity in the tangential direction [19]. In terms of flow within a stall cell, a certain amount of fluid moves axially through the blade row; this axial motion is usually studied considering the flow behind the rotor where the tangential component is smaller. Figure 2.6 reported below is only a sketch, but it provides a clear idea of how the flow behaves inside the stall region. Indeed the stall cell can be divided into two parts which are identified as forward and reversed flow.

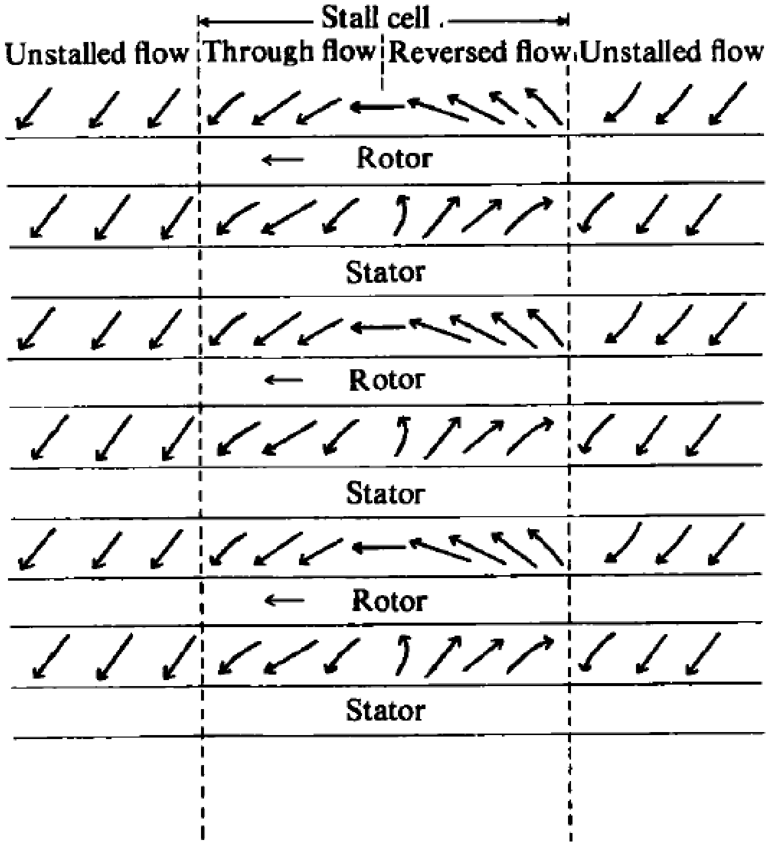

Figure 2.6: Axial motion of the flow inside the stall cell [19].

Day and Cumpsty also linked the extent of the forward and reverse part with the design flow coefficient; for low values of the flow design coefficient they observed a complete absence of reverse flow. For an high flow design coefficient, the flow is reverse almost over the entire cell. Assuming the flow inside the stall region as zero, positive or negative only, is quite simplistic; on the other hand due to the complexity of the flow and the necessity of having simple tools to deal with this phenomenon, simplifications are usually introduced (see for instance pressure loss models and deviation correlation in Chapter 3).

2.2.1.2 A three-phase evolution

In order to prevent or control the development of these instabilities, it is important to detect and understand the flow field behavior that usually precedes their occurrence. The whole phenomenon is commonly divided into three stages: inception, development and final flow pattern [72, 82]. During the first stage, inception, the flow becomes unstable, a disturbance appears and grows until stall or surge behaviors are fully developed. For some compressors, this stage can be quite extended, up to hundred of rotor revolutions during which disturbances of infinitesimal amplitude that grows linearly can be observed (modal type). In other cases the inception stage is much faster; it takes only few rotor revolutions (spike type). A better description of these two types of inceptions is going to follow below. The inception stage is usually the object of major focus for instability modeling and prediction. The second stage, development, is in fact less important since it represents all the processes that lead to final flow pattern and it varies from one compressor to the other. Indeed, the final flow pattern of one compressor can be an intermediate stage of another one.

Stall inception: modal-type and spike-type disturbances

There are mainly two paths that lead to fully developed rotating stall:

- Growth of modal perturbations characterized by long wavelength, they are 2D disturbances;

- Growth of spike perturbations characterized by small circumferential extent (order of one to several blade pitches), they are 3D and they spread circumferentially and radially.

Modal-type disturbances can be thought as small sinusoidal velocity fluctuations that rotate around the annulus at a steady speed (20%-50% of shaft speed) [72, 69, 57]. They are considered reversible, in fact, they can be created or suppressed changing the throttle settings. If the conditions allow the growth of these perturbations, these waves grow into a fully developed rotating stall without any sharp change in amplitude or phase. These perturbations can influence the stall cell's formation but they are not a necessary pre-requisite.

A modal wave penetrates axially the whole compressor, therefore the detection of these disturbances can be performed by sensors at any location along the axial direction. A typical example of modal-type disturbances is shown in Figure 2.7. Figure 2.7 is a quite common type of plots when dealing with compressor instabilities; on the y-axis the flow coefficient is reported for different circumferential positions against time, which is expressed for convenience in rotor revolutions. These kind of representations of the flow field provide information on the circumferential propagation of the disturbance and therefore on its rotational speed. Figure 2.7 describes the particular case of a modal inception, as a matter of fact, modal waves rotating at almost half of the shaft speed can be observed few rotor revolutions before the appearance of the stall cell. Linear stability analysis is usually sufficient to properly describe this type of inception (see Moore and Greitzer model section 2.4.2).

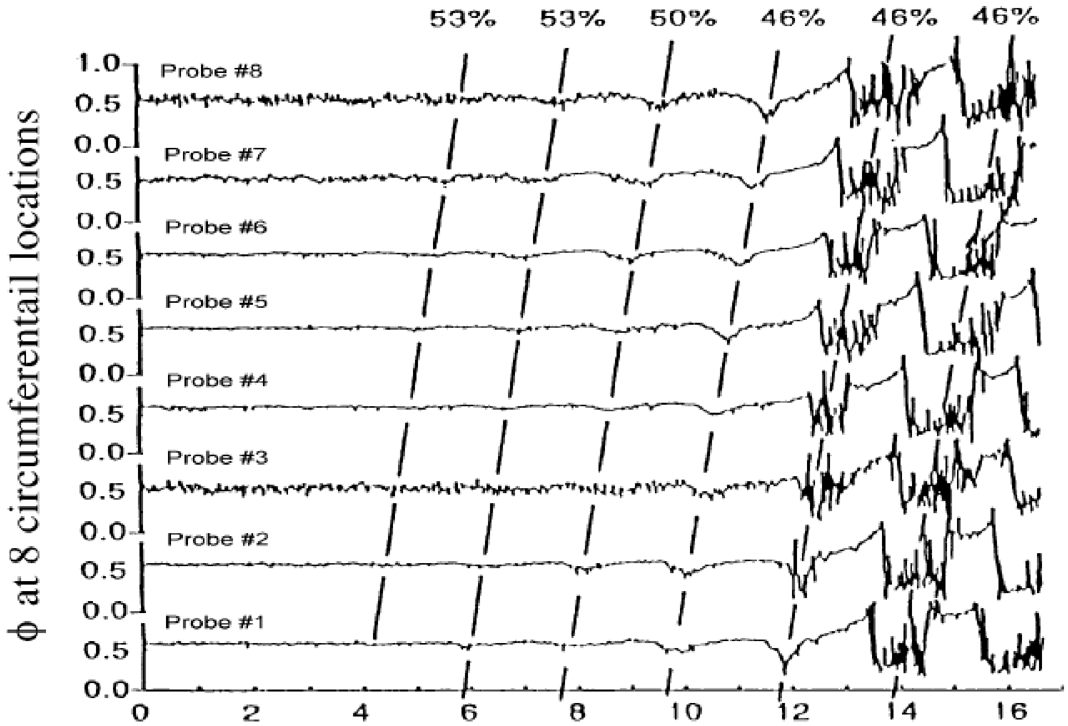

Figure 2.7: Typical stall inception from modal waves [82].

The second type of perturbation is commonly known as "spike" due to its spike-like appearance, an example is provided in Figure 2.8 . This disturbance is generated by the stalling of a particular blade row. In fact, a spike can be described as a local disturbance with a short extent in the circumferential direction which propagates quickly around the annulus (70% of rotor speed). Comparing Figure 2.7 and Figure 2.8, it is clear how a spike-type inception is not preceded by observable waves and at onset the disturbance rotates at a much higher rotational speed. In general, if the spike enters a region of high flow it can be suppressed, otherwise, it will leave the local low flow when it has grown enough and its speed has decreased.

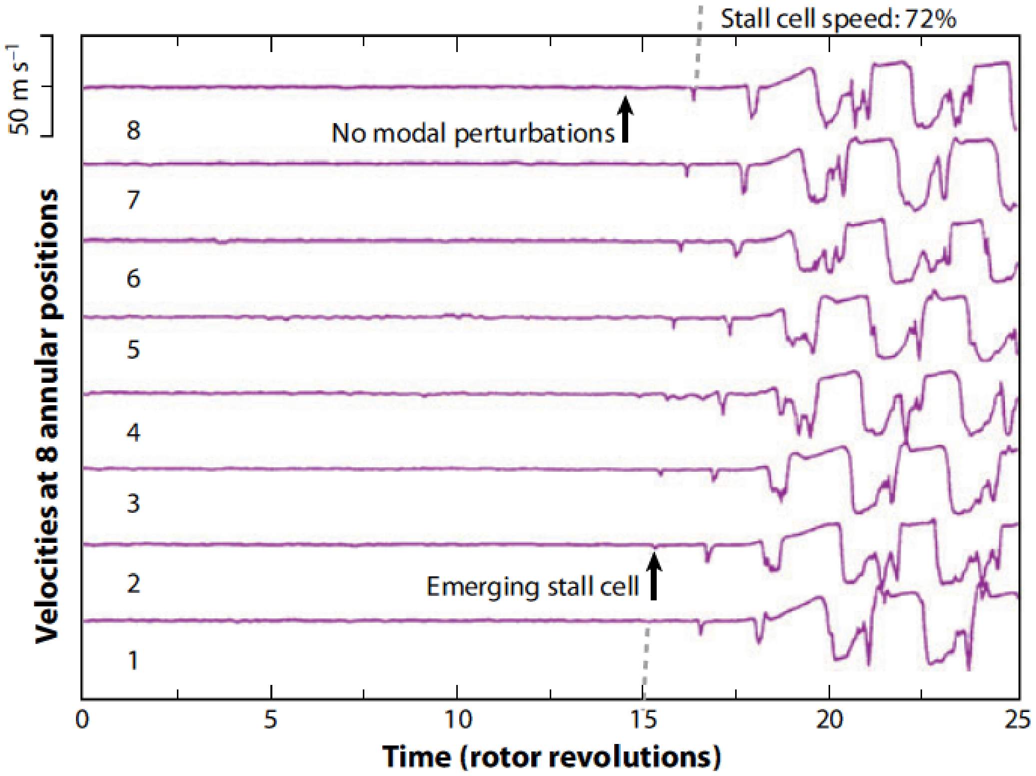

Figure 2.8: Example of spyke-type inception [72].

Comparing modal wave and spikes, these last grow into a stall cell more rapidly and locating them in the compressor characteristic, they are usually observed on the negative slope of the curve as represented in Figure 2.9. This observation led Camp and Day [10] to propose a criterion to define the stall inception type. The Camp and Day's criterion is based on a combination of characteristic slope and the occurrence of the critical rotor incidence. Referring to Figure 2.9, if this critical value of incidence is reached before the peak of the compressor map, the inception will occur through spike-type otherwise a modal-type disturbance will appear. However, this critical value changes with rotor stagger or compressor design. Simpson and Longley [69] proposed a tip-loading criterion. Another criterion proposed by Vo [78][77], states that a compressor will present spike-type stall onset, if a compressor stage experiences the two following conditions while operating close to the peak of the characteristic on the negative slope part [72] (see Figure 2.10):

- Backflow of tip-clearance: fluid from adjacent blade passages at the trailing edge passage;

- Spillage of tip-clearance: fluid ahead of the blade's leading edge;

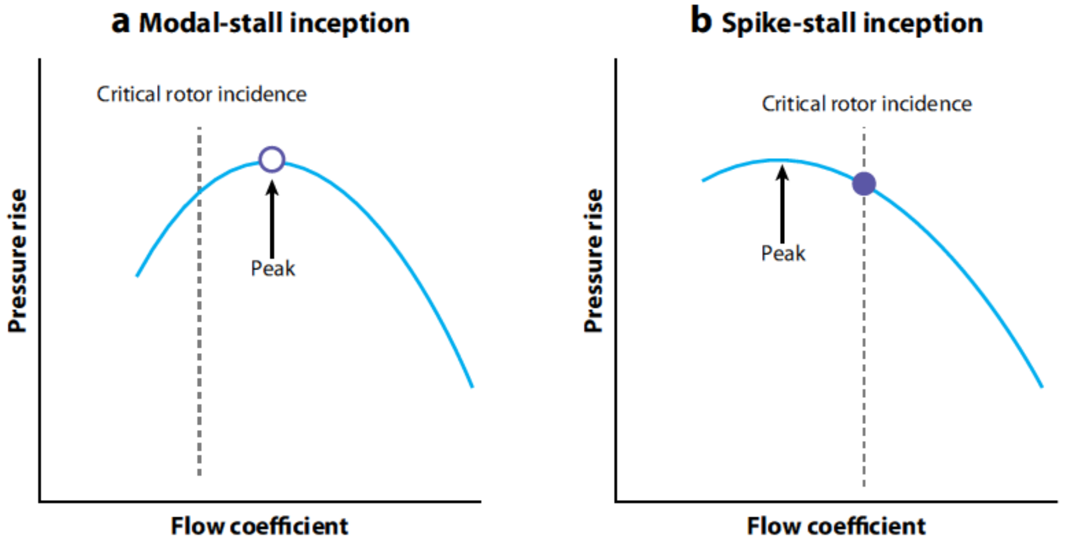

Figure 2.9: Camp and Day criteria for determining the stall-inception type [72].

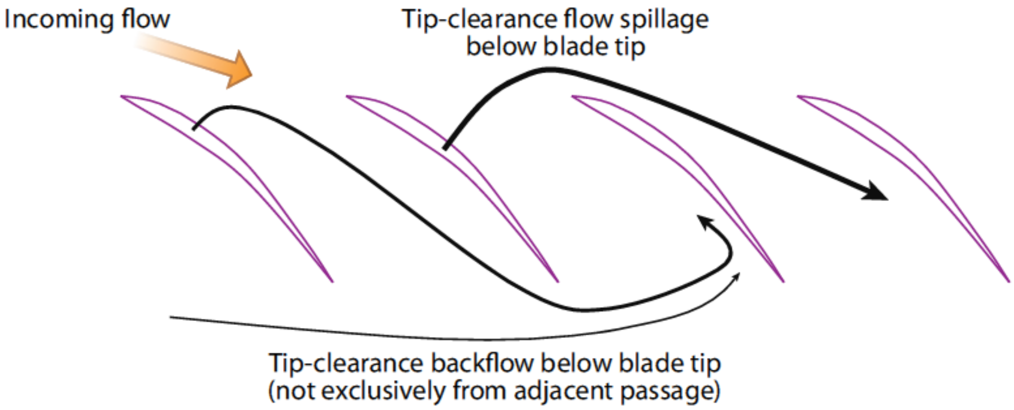

Figure 2.10: Tip-clearance spillage and back-flow [72].

Location of stall inception

The position of stall inception in a compressor depends on several aspects, for instance considering two compressors with the same overall geometry; the stall inception will likely be at the rotor hub if the compressor is characterized by small tip clearance or at the rotor tip if it is designed with larger clearance. This difference in the inception position relies on the blockage caused by the end-wall boundary layers or better by the combination of the end-wall and blade boundary layers. In case of small tip clearances the blockage near the hub is larger therefore the first unsteadiness leading to stall occurs near the hub. From experimental data, it is also known that changes in tip clearance can modify the type of stall inception (see 2.2.1.2) [52]. The knowledge of the interaction between clearance vortex, tip-clerance spillage and tip-clerance backflow with the end-wall boundary layer and their influence on the aerodynamic stability of axial compressor has not stopped to the identification of stall inception. Several researcher has investigated the possibility of using tip-injections or special case-treatments to increase the momentum of the flow and therefore stop or delay the stall inception as reported for instance by [79].

2.3 Numerical tools for the modeling of stall/surge

This section describes the different approaches and models that are and have been used to tackle unsteady flow phenomena such as those under investigation and provides few brief descriptions of well known compressor models. Looking at the modeling techniques currently available, three major categories/approaches can be recognized:

- Detailed flow observation: earlier works were mainly experimental; nowadays this kind of research continues trying to achieve better and more reliable measurements.

- Stall detection methods: this kind of approach tries to detect pre-stall or better an indication that the flow is less stable, near stall onset.

- Stall control and modeling: they often are considered like detection methods, they detect stall inception and try to control its development.

Modeling of compressor dynamics plays a fundamental role in all of the above mentioned attempts [57].

2.3.1 Through-flow VS 3D CFD

In terms of computational power/efficiency, accuracy and reliability, an investigation into the computational methods available was performed and it is described in this subsection. Before describing the most popular computational methods, the following two subcategories can be distinguished:

- 1D/2D simulation: through-flow methods;

- 3D simulation: CFD tools like Fluent and ANSYS CFX.

Generally, 3D simulations provide certainly the most reliable results; on the other hand the computational time and power required are major limits to their use. Through-flow methods can be fast, reliable and they can easily deal with machines having a large number of blade rows. In the literature there are several through-flow methods available, but the common basic idea is the decomposition of 3D flow field into two 2D flows (see Figure 2.11):

- 2D axis-symmetric meridional flow on the S2–surface (hub to shroud);

- 2D flow on the S1-surface between two adjacent blades.

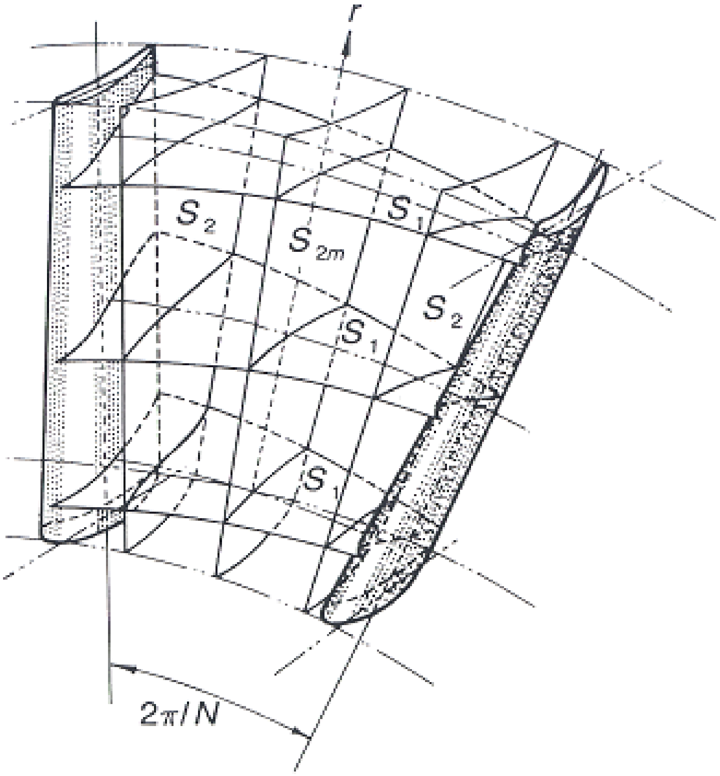

Figure 2.11: S1 and S2 stream surfaces for through-flow approaches [81].

Over the years, two different kinds of through-flow methods have been developed, the quasi-3D, through the coupling of the two 2D flows described above and the 2D axis-symmetric S2 approach with profile loss and turning calculated from empirical correlations (almost 100 times faster than the quasi-3D) [59]. In this subsection only few through-flow methods are going to be mentioned, focusing the attention on the more common ones. Generally speaking about this class of methods, they provide the velocity fields and thermodynamic properties at defined locations inside the flow path of a turbo-machine. Through the years, several through-flow methods have been developed in order to better take into account more features of the flow. These methods are based on several assumptions, an important one is the consideration of the relative flow at the inlet and outlet of each blade row as steady, allowing a locally 2D treatment of the flow. Moreover each method adopts specific simplifications to treat different features of the flow.

Mean line method: the axial compressor channel and other flow properties as velocity, temperature, pressure are calculated along a mean line defined inside the flow path. The adoption of only one stramline and therefore the assumption of uniform flow in the radial and circumferential direction requires the use of empirical correlations to estimate losses and other 3D flow features [34].

Radial equilibrium method: the analysis is performed on the meridional plane that containes the axis of rotation. The radial discretization allows the determination of the flow properties at different points along the radial direction. The flow properties are determined combining conservation laws and empirical correlations.

Streamline curvature method (SLC) [5]: it is a meridional through-flow analysis, the annulus is subdivided into a certain number of stream-tubes separated by stream-surfaces. An important assumption is that there is no mass flow across stream-surfaces. The calculations are performed on computational nodes defined by the intersections of the streamlines and the blade edges. The procedure is iterative, initially the streamline positions are guessed, so at each iteration, they are repositioned until their position remains constant and all the flow properties can be calculated. A considerable source of problems is, indeed, the calculation of the curvature and the repositioning of the stream surfaces. In the literature several techniques are available to simplify this process. Other limitations of this technique can be encountered in the modeling of transonic flow and regions of low/zero flow. All the losses and the 3D effects are implemented using empirical models and correlations.

Finite element method: this numerical technique is based either on eliminating the differential equations completely (steady state) or transforming the PDEs (partial differential equations) into ODEs (ordinary differential equations) that are then integrated using standard techniques such as Runge-Kutta [64].

The accuracy of through-flow methods relies mostly on the choices made for the modeling of features such as:

- Deviation model;
- Loss model;
- Model of radial distribution of losses and deviation;
- Spanwise mixing model;
- Endwall boundary layer model.

A brief introduction on losses and deviation models for trhough-flow solvers is provided in the next subsection.

2.3.1.1 Losses and deviation in through-flow solvers

From the analysis of the flow through a cascade, it is possible to appreciate that there are several sources of loss as sketched out in Figure 2.12. The figure also emphasizes the complexity of the flow field and its highly 3D behavior.

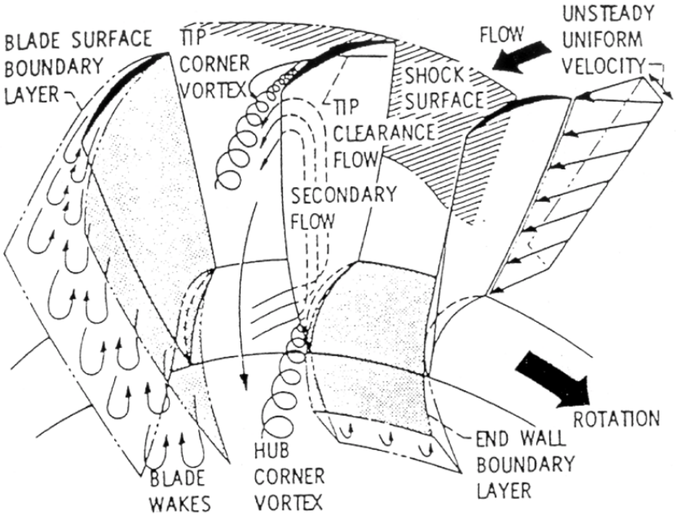

Figure 2.12: Pressure loss sources in a cascade [68].

Loss and deviation correlations which are used to estimate the entropy generation and the fluid turning due to the presence of blades are usually based on linear cascades experimental observations along with strong assumptions and simplifications. The pressure loss ($\bar{\omega}$) is generally defined as a non-dimensional ratio of the difference between inlet total pressure and exit total pressure to the inlet dynamic pressure, as reported by the equation below.

$$\bar{\omega} = \frac{P^0_{in} - P^0_{out}}{P^0_{in} - P_{out}} \tag{2.2}$$

As previously mentioned, Figure 2.12 sketches out different sources of pressure loss; indeed, an increase in entropy can be due to shocks, boundary layers, secondary flows, mixing as well as various combinations of them. There are several models and correlations available in the public domain to estimate the pressure loss coefficient. On the other hand all the methods are strongly dependent on semi-empirical coefficients which need to be calibrated for each specific geometry. The common practice in combining all the different sources, is to assume linearity and estimate the total loss coefficient as a sum of each individual loss term.

$$\bar{\omega} \cong \bar{\omega}_{sh} + \bar{\omega}_{pr} + \bar{\omega}_{s} \tag{2.3}$$

Where $\bar{\omega}_{sh}$ refers to the loss due to shocks, $\bar{\omega}_{pr}$is the profile pressure loss due to boundary layers and $\bar{\omega}_{s}$ represents the loss due to secondary flow effects.

The deviation angle, as mentioned above in this section, is the difference between the blade angle from the trailing edge and the exit flow angle. The deviation is mainly an inviscid phenomenon due to the divergence of the stream lines from the suction surface in a diffusing flow. In the case of highly loaded blades, an additional contribution to this phenomenon is provided by the thickening of the boundary layer on the suction surface [37].

Section §3.3 in Chapter 3 provides all the correlations adopted to estimate the deviation angle for each operating region. At this point, it is worthy underlining that deviation, as seen for the pressure loss coefficient, is determined using correlations which were derived analyzing experimental data from 2D cascades. Factors and empirical coefficients are therefore used to account for different blade profiles, mach number effects, design and off-design conditions.

2.3.2 Grid-free methods VS grid-based methods

Grid-free or meshless methods represent the next generation of computational methods [50, 38, 44]. The interest in their development is guided by the desire of solving problems with: free surfaces, deformable boundaries, moving interfaces, large deformations, complex geometries and mesh adaptivity. These kinds of methods are usually classified into three sub-categories:

- Methods based on the strong form formulation of the governing equations;
- Methods based on the weak form formulation of the governing equations;
- Particle methods.

The first type is simple to implement, computationally efficient and can be defined as truly meshless. On the other hand it is not very accurate and it is often unstable. For the second type, stability and accuracy are excellent but a background mesh is necessary for the integration. To the third group belongs the most famous meshless method, the SPH (Smoothed-Particle Hydrodynamics). It is similar to the methods based on the weak form but it is stable for many problems and the accuracy depends on the choice of the smoothing function. The equations used to describe fluid flow are the well known Navier-Stokes equations. Their solution is usually achieved applying some numerical techniques; in fact their exact solution is not always possible.

More common techniques are finite difference methods, finite volume methods and finite elements methods. All these techniques rely heavily on the quality of the discretization of the domain. Therefore a first disadvantage is the application of these methods to problem with complex geometries. A second problem is that they can be subjected to nonphysical numerical diffusion. Numerical diffusion is a problem that affects especially advection-dominated problems and comes from the numerical discretization. Terms like $(\partial^2 V_x)/\left(\partial x^2\right)$and $(a\Delta x/2) \cdot (1-\nu)$ act as viscous terms, numerical dissipation and artificial viscosity. Although such artificial viscosity compromises the accuracy of the solution, it is very important to improve its stability. In fact, flow problems with very strong gradients, such as shock waves are particularly sensitive and usually required addition of artificial viscosity. Meshless methods lack of numerical diffusion and need addition of artificial viscosity to handle discontinuities in the flow. In terms of benefits and drawbacks for both methods the following can be stated:

- Meshless approach: it is difficult to obtain clouds of points for stable and accurate computations (2D and 3D problems). They lack a discrete conservation property, they are often computationally expensive due to the requirement of a bigger storage in comparison with other common methods. The boundaries treatment is sometimes tricky. On the other hand they do not need a grid which could be very time consuming in case of complex geometries, they are more accurate and they can better handle problems with moving boundaries or free surfaces.

- Grid-based approach: they require an effort for the construction of a proper computational grid; task that can be very time consuming especially if the problem under investigation is characterized by deformable boundaries, large deformations and others features such as those listed at the beginning of this section. As advantages they can deal with flow discontinuities since they are subjected to numerical dissipation, they require a smaller storage of information (reciprocal) and the equations adopted are in the conservative form.

2.4 Compressor stall and surge models

In the past few years several attempts to model stall and surge have been made; this section briefly describes the models that the author has considered as fundamental to acquire the necessary knowledge on modeling techniques and develop the tool under discussion.

A first physical explanation of the circumferential propagation of the stall region was provided by Emmons [24]. The mechanism is shown in Figure 2.13 and its explanation is quite intuitive. The stall cell itself represents a blockage for the incoming flow which tries to circumnavigate the low flow region. This redistribution of the flow increases the incidence angles ahead of the stall cell moving direction and decreases those behind the stall cell region (see Figure 2.13). Therefore on one side the flow is forced to stall, while on the other side it is forced to recover from stalled condition. A more physically-based description comes from Cumpsty and Greitzer who linked the rotational speed of the stall cell with the balance between the unsteady inertial effects of relative and stationary components [82].

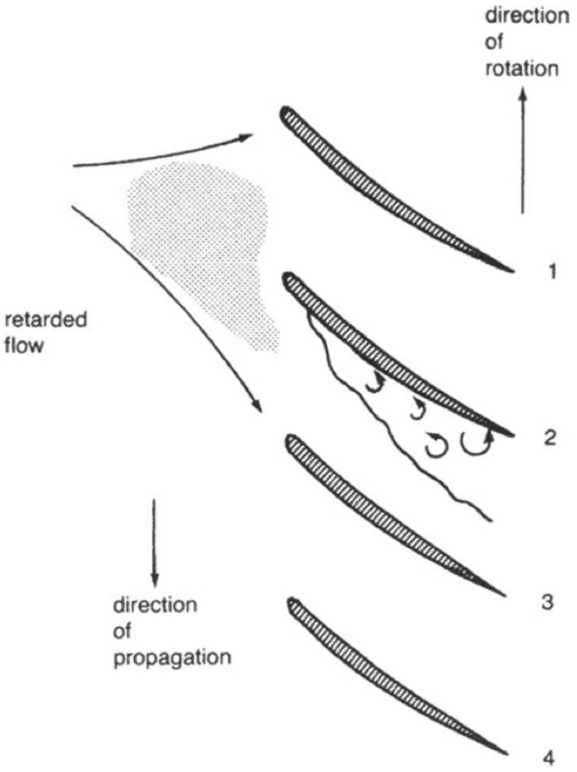

Figure 2.13: Stall cell blockage and its effect on the incoming flow [8].

2.4.1 The 'parallel compressors' technique

The idea of modeling the compressor system as a combination of two compressors working in parallel was first suggested by Pearson and McKenzie [58] in order to examine the effect of inlet total pressure distortion on the compressor system.

Figure 2.15 provides a visual description of the 'parallel compressors' technique; the case sketched out is a generic step change in inlet total pressure with an extent which covers half compressor.

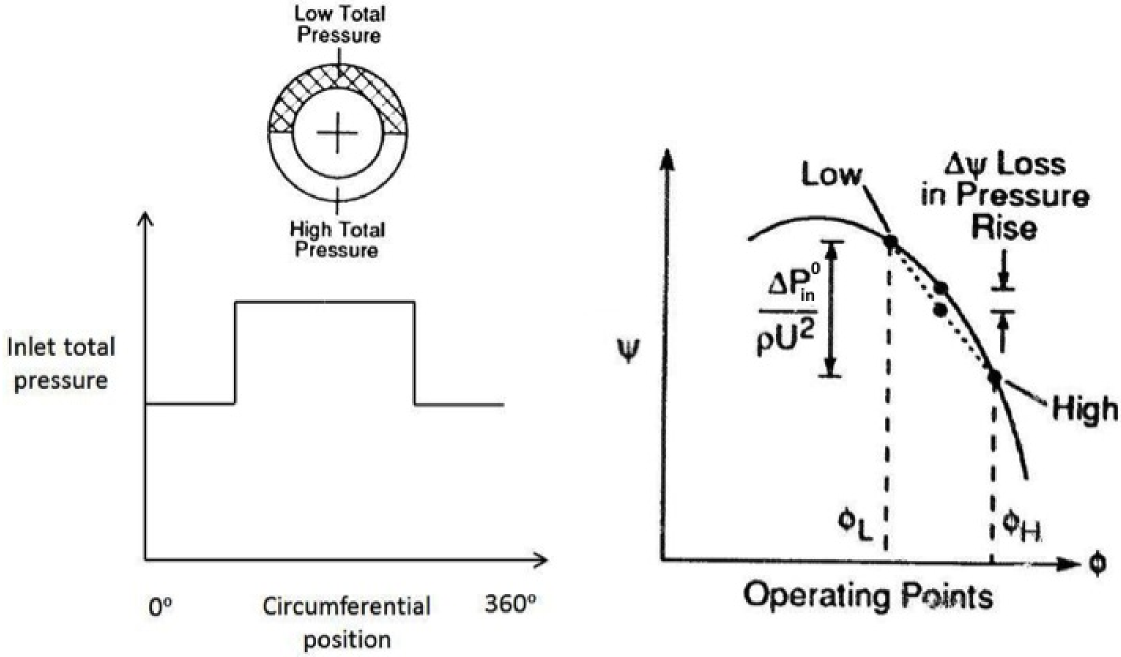

Figure 2.14: Basic 'parallel compressors' model for compressor response to circumferential total pressure distortion [47].

The flow field in the duct upstream of the compressor can be thought as composed by two streams with different, but uniform, total pressures. Under these circumstances, the 'parallel compressors' theory considers the compression system as divided into two imaginary compressors working in parallel, each one handling one of the two streams. The basic assumptions behind this methodology are the following:

- Each of the parallel compressors operates on the same non-dimensional characteristic, which corresponds to that measured on the whole compressor with completely uniform inlet conditions.

- Both compressors exhaust to a common uniform exit static pressure.
- Negligible circumferential cross flows, from one of the streams to the other, exist within the compressor.

The overall compressor performance is then determined by averaging the compressor performance of both parallel compressors. Indeed, for each parallel compressor, an individual operating point is calculated as shown in Figure 2.15. Both operating points are on the same speed line since both streams have the same inlet total temperature. The distorted compressor, subjected to a lower inlet total pressure, operates at a higher pressure rise and therefore lower mass flow; vice versa occurs for the clean parallel compressor. Considering Figure 2.14 from a stability point of view, although the mean operating point may be far from the clean inlet surge line, the 'parallel compressors' theory is quite conservative and considers the whole system as unstable when the low-total pressure region reaches the uniform flow (undistorted) stability limit.

This methodology, in a similar manner, can be applied to the investigation of the effect of circumferential total temperature distortion on compressor performance. Considering again a compressor system with half annulus operating at a higher inlet total temperature, the two parallel compressors operate at two different corrected speeds, while delivering the same pressure ratio, as indicated in Figure 2.15.

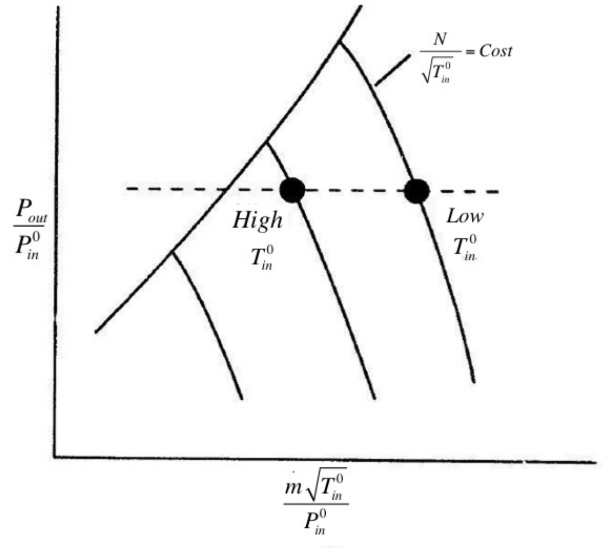

Figure 2.15: Basic 'parallel compressors' model for compressor response to circumferential total temperature distortion [47].

Again the distorted compressor operates closer to the surge line, determining a decrease in surge margin for the whole system as seen before for the total pressure case.

The 'parallel compressors' approach was also adopted in the past as a quick tool to estimate the compressor characteristic in rotating stall. Day, Greitzer and Cumpsty were the first to adopt the 'parallel compressors' technique to quantify rotating stall performance. The origin of this idea is due to experimental observations. Indeed a compressor operating in rotating stall presents two distinct regions around the annulus; one region operating at high flow while the remaining part is operating at low or reverse flow [41]. In the light of experimental observations that showed both the stalled and unstalled flows exhausted at the same average static pressure, they modeled the compression system as two separate compressors: one stalled and one unstalled.

Another two important assumptions regard the inlet average total pressure and the exit average static pressure which are assumed to be the same for both stalled and unstalled regions.

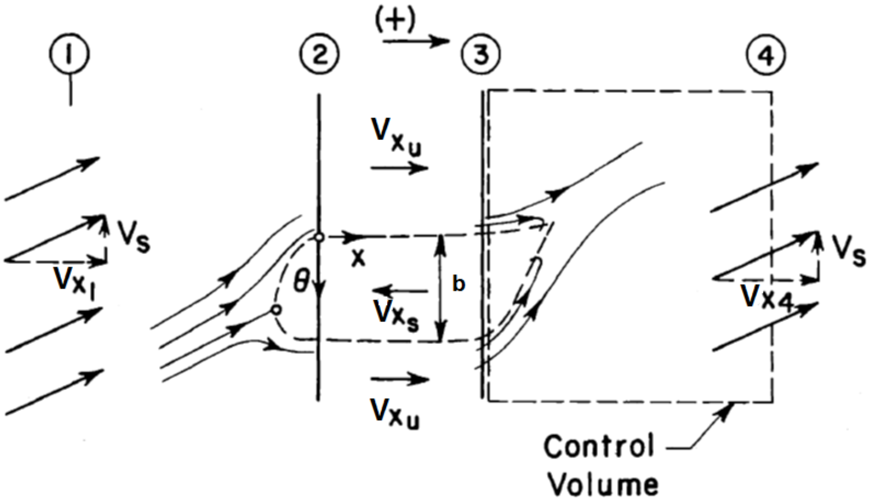

Reference frame relative to stall cell.

Let b = fraction of annulus occupied by stall cell

1-b = fraction of annulus occupied by unstalled flow

V_{x_u} = unstalled axial velocity

V_{x_s} = stalled and reversed axial velocity

Figure 2.16: 'Parallel compressors' approach applied to rotating stall studies [41].

Considering the control volume represented in Figure 2.16 and applying the axial momentum and the mass conservation equations together with the assumptions previously described, the total to static pressure rise can be obtained as :

$$\psi = \psi_u(\phi_u) + (1-b)\phi_u^2 - \alpha\phi_s^2 - \phi^2 \tag{2.4}$$

Where ψ_u is the forward flow characteristic (total to static pressure rise), b represents the fraction of the annulus occupied by the stall cell (see Figure 2.16) while ϕ_u

and ϕ_s are respectively the unstalled and reverse flow coefficient.

Necessary inputs for this methodology are the compressor characteristics in forward and reverse flow, the stall cell size and the throttle setting. A very strong limitation of this methodology already appears in the required inputs. Stall cell size and throttle settings are, in fact, not independent quantities in a real compressor.

While 'parallel compressors' theory provides a simple calculation procedure for predicting circumferential distortion effects, there exists a basic lack of agreement with a large amount of experimental data on distortion attenuation and loss in surge margin. As a result, a considerable research effort has been made to refine and improve the basic form of the 'parallel compressors' theory. Some modeling techniques concentrate on avoiding some of the assumptions required whereas other approaches incorporate new features and modifications. At this stage, only a brief overview is provided, further details regarding these modifications to the original theory are described in section 3.4.1 as part of the methodology followed in this work.

2.4.1.1 A multiple segment 'parallel compressors' model

A first important modification to the basic 'parallel compressors' approach is the concept of multiple parallel segments introduced by Mazzawy [51] in 1977. In the multiple-segment 'parallel compressors' model, the compressor annulus is discretized into more than two parallel compressors allowing a better circumferential resolution. In fact, by using multiple parallel segments, a more detailed definition of the circumferential flow field is achieved and more complex distorted flow patterns can be investigated. Another important concept, in contrast with the classic 'parallel compressors' theory, promoted by Mazzawy regards the distorted overall compressor performance. Mazzawy stated that the compressor performance of each individual distorted circumferential sector can be different from the compressor performance obtained considering the same sector as operating undistorted but with the same distorted boundary condition. Therefore, the calculation of the performance of the individual parallel segment, cannot rely on information regarding uniform flow operation. In the previous section, the fact that the parallel compressors are considered as discharging to the same uniform exit static pressure was highlighted as one of the basic assumptions. Greitzer and Griswold [31] describe in details when this assumption holds true. The uniform exit static pressure is a correct assumption provided that the compressor is treated as an isolated component, that is, the compressor is viewed as operating in a duct with long upstream and downstream sections of constant area. However, compressors are integrated in systems characterized by much more complex geometrical features. In the multiple-segment 'parallel compressors' model, the uniform exit static pressure assumption is avoided, the exit static pressure at the outlet of each parallel segment can be specified independently. Moreover this model accounts for the circumferential displacement of the distorted region due to the presence of rotors and stators and the unsteady flow effects which play an important role in the determination of the surge margin.

2.4.1.2 Circumferential and radial mass redistribution in the 'parallel compressors' model

Another important modification to the classic 'parallel compressors' theory, introduced first by Kimzey [40] and then extended by Steeken [71], regards the mass flow redistribution in the circumferential and radial direction. As previously seen in this section, the classic 'parallel compressors' theory neglects the circumferential flow redistribution. The classic 'parallel compressors' theory assumes that there is no fluid flow across parallel sections. Starting from a fully 3D solver, Kimzey simplified the equations, introducing special source terms to avoid the integration in the radial and circumferential direction. In Kimzey's model, the compressor is divided in control volumes, which are conceptually similar to parallel compressors. These compressor elements are assumed to be in radial and circumferential equilibrium with the adjacent control volumes when the compressor is operating with uniform flow. In case of distortion, the radial and circumferential flows are different from zero. Bearing in mind aim and objectives of this research, particular attention was given by the author to the circumferential mass redistribution technique. On this regard, more details on this special treatment are provided in Section §4.2. On the other hand, it is important to mention that Kimzey's model relies on an orifice flow analogy to evaluate the cross flow between parallel compressors neglecting the momentum and energy exchanges. A similar modification was applied also by Steenken [71]. However, Steenken's model accounts also for the circumferential and radial momentum and energy variations due to the mass redistribution. Another difference between Kimzey and Steeken is that while the former allows cross flow only in the rotor stator gap, the latter evaluates the cross flow for each turbo-component. Testing this methodology Steeken proved that the mass redistribution plays quite an important role especially for a compressor system without inlet guide vanes.

2.4.2 A lumped-volume approach

A very well-known lumped-volume compressor model for dynamic analysis was developed by Moore and Greitzer. By definition, a lumped-volume approach implies the simplification of the whole system into discrete entities. This kind of models are valid until the characteristic length of the phenomenon under investigation is greater than the length of the discrete entities. These approaches are substituted with more general models such as the distributed element model when different length-scales are involved. Although this kind of approach was not considered suitable for this project, it is worthwhile analyzing this simple model since it unfolds an interesting link between the mathematical representation and the real physical phenomenon. First of all, the compression system adopted in the Moore–Greitzer model is constituted by five elements: inlet duct (A), compressor (B), exit duct (C), plenum (D) and throttle (E). Figure 2.17 shows this schematic compressor system where $\phi(\theta,t)$ is the flow coefficient, that is the non-dimensional value of the axial velocity while the $\psi(t)$ is the non-dimensional pressure rise in the plenum. In this lumped parameter model, the compressor is substituted by an actuator disk and a duct of length L_c. The actuator disk is basically the representation of the blade row as a plane across which the continuity of mass flow is guaranteed while discontinuous trends are allowed for total pressure and circumferential velocity. The compressor duct discharge in a large plenum which communicates with the atmosphere through a throttle. The throttle, as for the compressor, is modeled as a combination of an actuator disk, a duct of length L_t and area A_t.

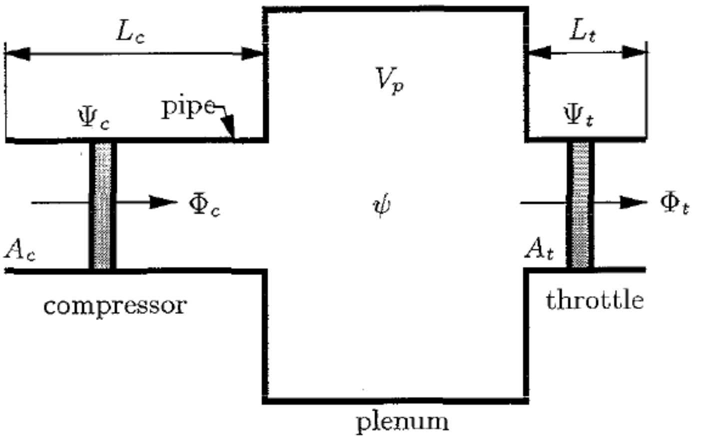

Figure 2.17: Moore-Greitzer compressor model [80].

Behind this methodology there are several important assumptions; as first the flow in the ducts is considered as incompressible and one-dimensional which holds true for systems with low inlet Mach numbers and small pressure rises compared to the ambient pressure. The pressure in the plenum is considered uniform and the compression process isentropic. The velocity inside the plenum is considered negligible and the throttle is modeled as a quasi-steady device through the parabolic relation of equation (2.5).

$$\psi_t = \left(\frac{A_c}{A_t}\right)^2 \phi_t^2 \tag{2.5}$$

The unsteady behavior of the compressor is taken into account with a first order time lag law and the rotational speed is considered constant allowing in this way the use of a single compressor characteristic.

Keeping in mind the above mentioned assumptions and applying the momentum equation to the flow in the compressor and throttle duct along with the mass conservation to the flow across the plenum a set of four coupled non linear differential equations can be derived. The equations in dimensionless form appear as:

$$\frac{d\phi_c}{dt} = B(\psi_c - \psi) \tag{2.6}$$

$$\frac{d\phi_t}{dt} = \frac{B}{G}(\psi - \psi_t) \tag{2.7}$$

$$\frac{d\psi}{dt} = \frac{1}{B}(\phi_c - \phi_t) \tag{2.8}$$

$$\frac{d\psi_c}{dt} = \frac{1}{\tau}(\psi_{c,ss} - \psi_c) \tag{2.9}$$

where B, G and τ are three dimensionless system parameters defined as:

$$B = \frac{U}{2a}\sqrt{\frac{V_p}{A_c L_c}} \tag{2.10}$$

$$G = \frac{L_c A_c}{L_c A_t} \tag{2.11}$$

$$\tau = \frac{2\pi r N_{cell}}{U} \tag{2.12}$$

The B-parameter, also known as Greitzer stability parameter is well known and usually adopted as a quantitative measure to predict the behavior of compression system subsequent to the stall inception. Indeed, a critical value of B can be defined above which the compressor will exhibit surge, whereas a rotating stall behavior will be observed for lower values of B. A physical interpretation of this parameter was also provided by Greitzer, in fact, re-writing the B parameter as :

$$B = \frac{\frac{1}{2}\rho U^2 A_c}{\rho \omega_H U L_c A_c} \tag{2.13}$$

It is clear that B is the ratio between pressure and inertial forces in the compressor duct. The numerator being proportional to the magnitude of the pressure difference across the duct, it is linked with the acceleration of the fluid in the duct. For what concerns the denumerator, it represents the inertial forces in the compressor duct due to local fluid accelerations. In practice, larger mass flow variations are likely to occur increasing the driving force, therefore there will be a tendency to surge increasing the plenum volume which appears at the numerator of equation (2.10). Although the B parameter appears very powerful it is not widely applicable since the critical value changes from one compressor to the other.

The G-parameter compares the inertia of the fluid flow across the throttle and the inertia of the flow across the compressor, while τ is a time lag parameter that accounts for the time needed to achieve full development of rotating stall.

Assuming G small and τ negligible, the set of equation (2.6)-(2.9) can be reduced to:

$$\frac{d\phi_c}{dt} = B\left(\psi_c - \psi\right) \tag{2.14}$$

$$\frac{d\psi}{dt} = \frac{1}{B}\left(\phi_c - \phi_t\right) \tag{2.15}$$

where ψ_c equals $\psi_{c,ss}$ and ψ_t is equal to ψ.

The Moore and Greitzer lumped-volume approach is well known also for the mass-spring-damper system analogy. A graphical explanation is provided by Figure 2.18.

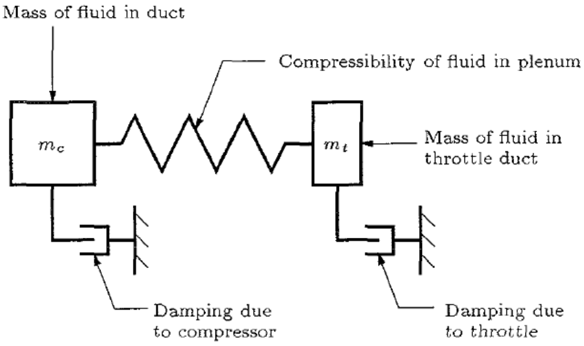

Figure 2.18: Mechanical analogy of the Moore-Greitzer lumped-volume model [80].

In this analogy, the incompressible fluid in the compressor and throttle duct is represented respectively by the mass m_c and m_t while the compressibility of the fluid in the plenum is equivalent to a spring. In this analogy the displacement of m_c and m_t corresponds to the axial displacement of the fluid in the ducts while the spring force resembles the plenum pressure rise ψ. From a stability perspective, writing the characteristic equation of the system:

$$s^2 + \left[\frac{a^2 Lc}{V pAc} \left(\frac{1}{\frac{d\triangle P_t}{d\dot{m}_t}} \right) - \left(\frac{d\triangle P_c}{d\dot{m}_c} \right) \right] \frac{A_c}{L_c} s + \omega_H^2 \left[1 - \frac{\left(\frac{d\triangle P_c}{d\dot{m}_c} \right)}{\left(\frac{d\triangle P_t}{d\dot{m}_t} \right)} \right] = 0 \qquad (2.16)$$

where the term $\frac{d\triangle P_t}{d\dot{m}_t}$ is the slope of the throttle characteristic and $\frac{d\triangle P_c}{d\dot{m}_c}$ is the slope of the compressor characteristic.

Since $\frac{d\triangle P_t}{d\dot{m}_t}$ is always positive the portion of the compressor map with negative slope is always stable. The system becomes unstable near $\frac{d\triangle P_c}{d\dot{m}_c} = 0$. In this analogy the linearized transient behavior of the compressor near surge is governed by the B parameter, previously defined by equation (2.10), as the ratio of compliance to inertia in the system and can be easily identified inside equation (2.16) . For a large B parameter (soft spring), the compression system experiences large mass flow fluctuations and small variations of plenum pressure. In the case of small B parameter (stiff spring) there are strong variations of plenum pressure but small changes in mass flow, as described in Figure 2.19.

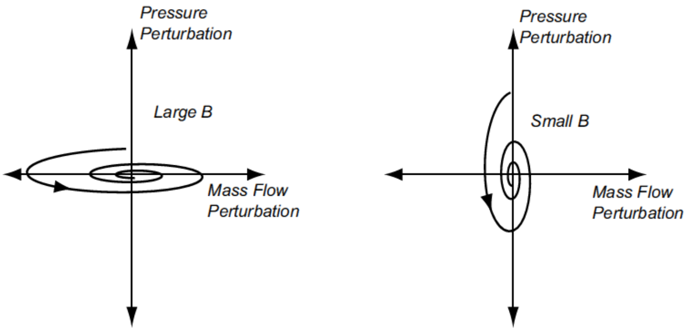

Figure 2.19: Transient response of a surge system to a pressure perturbation [57].

2.4.3 Quasi-1D and Quasi-2D Euler solvers

A one-dimensional tool

When searching the public domain for tools which allow the modeling of stall and surge, and a quick assessment of their effect on compressor performance, several reports on tools which adopt a quasi-1D approach are found [33, 17, 1]. The core of the methodology in all these tools is represented by the Euler equations and the approach followed for the derivation of the necessary source terms.

Most of these quasi-1D solvers rely on steady state characteristics for the extraction of blade forces and work exchange and apply first order time lag law to account for the inertia of flow during unsteady conditions. A generic example of first order time lag is given by equation (2.17) and it is usually applied to the calculation of the axial blade force.

$$\tau\frac{\partial Q}{\partial t} = Q_{ss} - Q \tag{2.17}$$

where Q is the quantity of interest while τ is the time constant and depends on the flow convection time through the blade passage.

An upgraded version of this type of tools is what is usually defined as quasi-2D [1]. The major difference is that the velocity field is now due to two velocity components, axial and tangential. The basic assumption behind this kind of solvers is that the tangential component changes only axially, or better it is circumferentially uniform for each axial location. The system of Euler equations for a quasi-2D is reported below:

$$\frac{\partial}{\partial t}\begin{bmatrix}\rho A\\ \rho V_x A\\ \rho V_t A\\ \rho E^0 A\end{bmatrix} + \frac{\partial}{\partial x}\begin{bmatrix}\rho V_x A\\ \rho V_x^2 A + PA\\ \rho V_x V_t A\\ V_x A\left(\rho E^0 + P\right)\end{bmatrix} = \begin{bmatrix}0\\ P\frac{\partial A}{\partial x} + F_x\\ F_t\\ F_t \Omega r\end{bmatrix} \tag{2.18}$$

Equation (2.18) is adopted in bladed regions, in case of a duct the source terms F_x, F_t and $F_t\Omega r$ which refer to the presence of blades are set to zero.

The integration of the tangential velocity and the adoption of semi-empirical models and correlations for pressure loss, deviation and other 3D flow features, allows the calculation of the velocity triangles and therefore the derivation of blade forces and work exchange. The accuracy and reliability of these tools are limited by the choice of the semi-empirical models and correlations and by the assumption of an axis-symmetric flow field which becomes unrealistic especially for phenomena as rotating stall or inlet distortion.

DYNTECC and the meanline-code

The combination of the quasi-2D, often addressed also as meanline solver, with the 'parallel compressors' technique is a clever strategy adopted by some researchers (see for instance the transient solver DYNTECC) [16, 26], to improve the circumferential resolution. A modified 'parallel compressors' technique allowing mass flow exchange between parallel compressors enhances the quasi-2D solver with the capability of simulating asymmetric flow phenomena.

To the author's knowledge, this methodology has only being used to study the effect of different inlet distortions such as bulk swirl, total pressure and total temperature for operating condition on the forward flow characteristic up to the stall inception.

An example of application can be found in Cousins et al [16], the treatment implemented to allow the cross flow between the parallel compressors was first introduced by Kimzey [40], to overcome the over-prediction of compressor performance typical of the original 'parallel compressors' theory without having to solve the 3D Euler equations. A more detailed discussion on this methodology is reported in the next chapter since a part of the present work was inspired by this modeling technique.

2.4.4 2D and 3D Euler solvers

A typical 2D Euler solver is the one developed by Longley [13, 14]. The main purpose of his analysis was to understand the development of flow field disturbances rather than predicting precisely the stall inception. Being aware that the best representation would require an unsteady Navier-Stokes calculation able to solve length scales down to the boundary layers, and that this task was beyond the available computational power, he developed a 2D model. The model was restricted to the simulation of unsteady moderate to long length scales compressible flow. Therefore short length scale and part-span stall could not be simulated. In this model the inlet duct, inter-blade row gaps and the exit duct are simulated using a 2D time accurate Euler solver for which the well known equations are reported below:

$$\frac{\partial}{\partial t}\begin{bmatrix}\rho \\ \rho V_x \\ \rho V_t \\ \rho E\end{bmatrix}+\frac{\partial}{\partial x}\begin{bmatrix}\rho V_x \\ \rho V_x^2+P \\ \rho V_x V_t \\ V_x(\rho E+P)\end{bmatrix}+\frac{\partial}{\partial y}\begin{bmatrix}\rho V_t \\ \rho V_x V_t \\ \rho V_t^2+P \\ V_t(\rho E+P)\end{bmatrix}=0 \tag{2.19}$$

Concerning the bladed regions, instead of using the historic actuator disk where the blade row has zero axial length or the semi-actuator disk, where the axial length is taken into account throughout a one-dimensional passage without flow turning in it, he adopted a modified actuator disk. With this last model, the flow is allowed to vary continuously through the blade row as it does in reality. The equations of motion for a rotor blade row with velocity U are reported below:

$$\frac{\partial}{\partial t}\begin{bmatrix}\rho \\ \rho V_x \\ \rho V_t \\ \rho E\end{bmatrix}+\frac{\partial}{\partial x}\begin{bmatrix}\rho V_x \\ \rho V_x^2+P \\ \rho V_x V_t \\ V_x(\rho E+P)\end{bmatrix}+\frac{\partial}{\partial y}\begin{bmatrix}\rho U \\ \rho V_x U \\ \rho V_t U \\ \rho E U\end{bmatrix}=\begin{bmatrix}0 \\ F_x-F_y tan\beta \\ F_y \\ UF_y\end{bmatrix} \tag{2.20}$$

Three equations are associated with the usual one-dimensional passage, while the extra equation comes from the flow turning effect due to the body force. To take into account the unsteady behavior of blade row during non steady flow, that is, changes in the inlet flow conditions at the blade row are not immediately reflected in the blade row exit, again a simple first order time lag equation, equation (2.17), was introduced.

In his simulations Longley applied the lag law to the blade row circulation and the blade row pressure loss. For what concerns the downstream plenum and throttle, the former is considered throughout a volume with uniform flow properties and the throttle as a specified exit flow area.

The numerical integration is performed applying the equations to a finite volume representation and the time integration is undertaken by using a two-step Runge-Kutta scheme. Moreover, to simulate the unsteadiness found within a compressor, a random noise was added at each time step to the blade row loss and circulation parameters, while for the boundary conditions, a non reflecting approach was adopted.

This section continues with the description of a more recent model developed by Longley, based on the blockage mixing method [46]. The basic idea of this second model is to use the blockage mixing mechanism to generate the high rate of entropy production expected in “steady” reverse flow. The blockage of the jet-wake structure can be defined in a general form through the definition of momentum of the flow as the ratio between the momentum of non-uniform flow over the momentum of uniform flow.

The main effect of the short length-scales is the increased momentum and kinetic energy carried by the flow. To take into account these effects Longley derived the following equations for 3D compressible flow adding the blockage variable b(x,t).

$$\frac{\partial}{\partial t}\begin{bmatrix}\rho\\ \rho V_x\\ \rho V_t\\ \rho W\\ \rho E^0\end{bmatrix}+\frac{\partial}{\partial x}\begin{bmatrix}\rho V_x\\ \rho b V_x^2+P\\ \rho b V_x V_t\\ \rho b V_t W\\ V_x H^0\end{bmatrix}+\frac{\partial}{\partial y}\begin{bmatrix}\rho V_t\\ \rho b V_t V_x\\ \rho b V_t^2+P\\ \rho b V_t W\\ \rho V_t H^0\end{bmatrix}+\frac{\partial}{\partial z}\begin{bmatrix}\rho W\\ \rho b W V_x\\ \rho b W V_t\\ \rho b W^2+P\\ \rho W H^0\end{bmatrix}=\begin{bmatrix}0\\ F_x\\ F_y\\ F_z\\ 0\end{bmatrix} \tag{2.21}$$

$$\begin{aligned}\frac{\partial}{\partial t}\left(\frac{1}{2}\rho(b-1)V_x^2\right)+\frac{1}{2}(b-1)^2V_x^2\nabla\cdot(\rho V_x)+ & \\ +\left(\frac{b-1}{b}\right)(\rho V_x\cdot\nabla)\left(\frac{1}{2}V_x^2b^2\right) &= -V_xF-\rho T\frac{DS}{Dt}\end{aligned} \tag{2.22}$$

The last equation, reported above, is the blockage transport equation that governs the development of the excess kinetic energy per unit volume. To apply this method to the simulation of a whole compression system, a model for the blade passage is required. For the blade passage Longley adopted again the concept of the body force. In this case the major constraint was that the body force has to produce the required change in tangential momentum and entropy generation. He used steady-state estimates of viscous losses and flow turning together with models for the effects of non-steady flow. The numerical integration of the above reported equations was carried on applying non-reflecting boundary condition to the total flow properties and flow angle at the inlet of the computational domain. The computational domain is attached to a large exit volume (plenum) with a throttle at the outlet. At the interface between plenum and computational domain, energy and mass conservation are applied together with non-reflecting boundary conditions based on the static pressure within the exit volume; a radial equilibrium is also specified through the tangential velocity of the flow leaving the computational domain. Concluding, with this second solver, Longley managed to achieve fully compressible simulations and to include the effect of 3D short length-scale effects. On the other hand, the exact procedure for the determination of the blade forces and the transition from high to low flow operation has not been reported in detail and it seems to be quite arbitrarily performed.

Another quite well known example of 3D solver based on the inviscid Euler equations is the one developed by Gong [82]. This tool has the capability of modeling the inception and development of unsteady flow phenomena caused by non-uniform loading around the annulus, radial and circumferential non-uniformity of inlet total conditions and so on. Particular attention was devoted to the inception of stall through short wavelength disturbances and the assessment of the influence of some key design characteristic such as the length of the rotor-stator gap. As seen previously in this section for Longley's model, Gong's model relies on the concept of body force to account for the presence of blades; an important assumption behind his methodology is that each blade row is considered consistent of an infinite number of blades, reducing in this way the computational resources required for solving the flow field.

Concerning the derivation of the above mentioned body forces, steady state characteristic are adopted together with a first order time lag law as seen in previous sections to account for the inertia of the flow. Particular care is devoted to the distribution of the axial and tangential blade force in order to avoid un-physical oscillations; indeed Gong suggests a kind of sinusoidal distribution which zeros at leading and trailing edge allowing a smooth transition between bladed and un-bladed regions.

Only a couple of models, within those described in this section, have attempted the modeling of short-wavelength disturbances, better known as spikes. Spike-type stall inception is on the other hand very common in low and high speed compressors. From an experimental point of view, through the years several techniques have been adopted to detect spike. Some of them are listed below:

- Cross-correlation of spatially adjacent signals;

- Travelling wave energy analysis: the wave energy is calculated from the difference between positive-frequency and negative-frequency power spectra;

- Windowed space-time correlation based on a scalar metric created using unsteady surface pressure around the annulus.

The experimental observation has revealed some key features on the nature of these disturbances and led to the determination of a couple of guidelines for their modeling.

Generally speaking, to simulate spike stall inception, a model should take into account:

- The flow redistribution within rotor-stator gap of the stage where the short-length perturbation is located;

- Redistribution of the flow within a blade row.

The two concepts listed above are better represented in Figure 2.20.

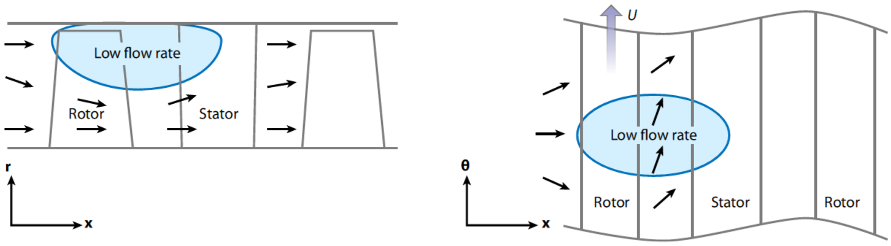

Figure 2.20: Mass flow redistribution induced by the stall region [82].

2.5 Summary

A literature research encompassing different aspects of the rotating stall/surge phenomenon has been reported in this chapter. The literature search focused mainly on identifying the key features of these instabilities, that is, all the features that need to be model in order to simulate the real phenomenon as more accurately as possible. Numerical methods, tools, semi-empirical model and correlations developed through the years to investigate the rotating stall/surge phenomenon and its effects on the turbomachine performance have been broadly reviewed. Exscluding the 3D CFD based on the Navier-Stokes equation, which provide the best representation of the flow field at the expense of computational efficiency, the chapter has also highlighted how most of the tools available in the public domain rely on steady-state characteristic for the derivation of the blade force and work imparted by the blades to the flow. There is therefore a need for robust tools capable of tackling transient phenomena as rotating stall and surge without requiring exceptional amounts of computational time and power and relying geometrical information as only input.

Concluding there are few important concepts/messages that are worth highlighting and that the author considered as guidelines in the development of its own tool:

- Rotating stall and surge are very complex transient phenomena that completely disrupt the flow field; 3D flow features characterized by short-wave length disturbances can occur together with long-wave length disturbances.
- During rotating stall the presence of a rotating region of low flow induces an asymmetric flow pattern that does not appear during a surge cycle; the latter can instead be considered and therefore modeled as an axis-symmetric phenomenon.
- The best representation of the flow field would be obtained with an unsteady 3D Navier-Stokes simulation that becomes computationally very heavy for multi-stage high-speed compressors.
- Modeling key features such as blockage, mass redistribution, losses and other flow features in time and space is extremely important to get a representation of the flow field as closer to reality as possible.

The next chapter describes in details the methodology followed, from the numerical techniques selected for the integration of the governing equations to the semi-empirical models implemented, to the treatment of the different key features discussed within this chapter.

Chapter 3

Methodology

This research focused on developing a fast and robust CFD tool that is able to simulate the steady-state and transient performance of multistage axial compressors. As mentioned above, it is important to be able to assess the compressor performance under rotating stall operating conditions satisfying at the same time requirements such as accuracy, robustness and efficiency in terms of CPU time. In the context of this work, a wide literature search on compressor performance simulation models and numerical methods was carried out and this led to the choice of an unsteady through-flow approach.

The tool described in this document, was developed following two slightly different paths; a quasi-2D Euler solver, which leans on the ‘parallel compressors’ technique to model asymmetric flow fields (named by the author as FENICE-PC), and a 2D Euler solver (named by the author as FENICE-2D). This chapter describes in details equations, models and correlations, integration schemes, implemented for both versions emphasizing their major differences. A comparison in terms of solvers’ capabilities is presented in the results section.

The present chapter is divided into several sections which describe step by step the implementation of the final tool.

Desired tool features

The literature review, on the computational methods currently available to model the rotating stall phenomenon, provided some important guidelines for the development and implementation of the final software. The prime goal was to develop a tool that could tackle transient asymmetric phenomena in multistage axial compressors, requiring only information on the compressor geometry. Therefore, in order to achieve this goal, during the development and implementation the author focused on the following main requirements:

- Capability of tracking the transient behavior of the flow in all three possible regions of operation (forward flow, reverse and rotating stall);
- Capability of dealing with subsonic and supersonic flow;
- Accuracy of the performance prediction which depends on the modeling of losses and blade deviation for all three operating regions;
- Capability of modeling asymmetric phenomena (disturbances' propagation around the annulus);
- Low computational time and power required.

Simplifications/assumptions

As already mentioned in the introductory part of this document, the flow field during a rotating stall or surge event is completely disrupted and therefore very complex, characterized by several 3D flow features. Through-flow solvers usually account for these features through semi-empirical models or correlations derived from experimental observations. The tool developed follows the same philosophy, and therefore is 'limited' by the same assumptions and simplifications which apply to any through-flow calculation:

• Blade losses and deviation are accounted through semi-empirical models and correlations (their assumptions are reported in section Section §3.3);

• Stall cell growth is taken into consideration through a first order time lag law;

• An infinite number of blades is assumed avoiding in this way the necessity of modeling each blade and therefore the requirement of solving the flow field inside each blade passage, the latter would notably increase the computational time;

• The body-force concept is adopted to model the presence of blades;

• The flow is considered radially uniform which implies the limitation of modeling full-span rotating stall;

• In terms of velocity triangles, mixed conditions are neglected; in other words, the flow across a blade row or blade row segment (depending on the circumferential discretization) can be in forward or reverse flow only.

3.1 Preliminary work

The first step towards the implementation of the final tool was the implementation of an unsteady solver for compressible flows. In this contest, an unsteady quasi-1D solver was implemented following two different approaches: a Lagrangian dilatation element method and a common finite difference method. The reason behind the implementation and comparison of two different techniques to solve the transient behaviour of the flow was the need to indetify the most suitable approach in terms of robustness and efficiency. This section describes the basic concepts behind both methods highlighting the guiding factors that led to the selection of the more common finite difference approach. The prime task was in fact the development of a robust and efficient unsteady solver able to deal with unsteady compressible flow in a tube characterized by cross section variations in time and space.

In order to implement the Lagrangian dilatation element method (Lagrangian code), the author followed the algorithm developed by Shen and Bernard [66, 7].

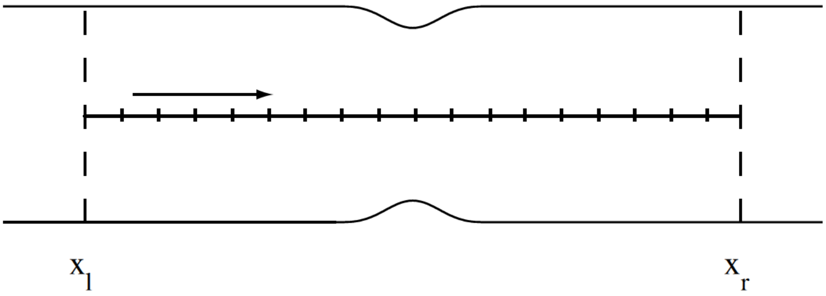

Figure 3.1: Domain of the case-study [7].

Figure 3.1 displays the case-study selected, as in the work of Shen, the domain is subdivided into a certain number of elements that are considered as Lagrangian particles. The elements are convected with the local fluid while their properties, like dilatation, temperature and volume are changed with time. The Lagrangian governing equations are integrated throughout a second order Runge-Kutta scheme. At each time step the elements move toward the outflow boundary, but the whole coverage of the domain is ensured through a re-sizing procedure as described at the end of this section. The following subsection describes in details the implementation of this technique.

3.1.0.1 The Lagrangian dilatation element method

The flow properties are assumed to vary only in the axial direction (x) and in time (t); the cross section variation in the streamwise direction is relatively small to allow the one-dimensionality assumption.

From a control volume analysis the following three equations can be derived:

1. Mass conservation:

$$\frac{\partial \rho}{\partial t} + V_x \frac{\partial \rho}{\partial x} = -\rho \left(\theta + V_x \alpha\right) \tag{3.1}$$

where θ is the dilatation and it is defined as $\frac{\partial V_x}{\partial x}$, while α represents the cross section variation in the axial direction and is therefore expressed as $\frac{\partial A}{\partial x}$.

2. Momentum balance:
$$\frac{\partial V_x}{\partial t}+V_x\frac{\partial V_x}{\partial x}=-\frac{1}{\rho}\frac{\partial P}{\partial x} \tag{3.2}$$
which can be written in terms of dilatation as:
$$\frac{\partial \theta}{\partial t}+V_x\frac{\partial \theta}{\partial x}=-\theta^2-\frac{\partial}{\partial x}\left(\frac{1}{\rho}\frac{\partial P}{\partial x}\right) \tag{3.3}$$

3. Energy balance:
$$\frac{\partial E}{\partial t}+V_x\frac{\partial E}{\partial x}=-\frac{P}{\rho}\left(\theta+V_x\alpha\right) \tag{3.4}$$

To complete the flow description and close the system of equations, the well-known equation of state for perfect gas is introduced allowing the energy to be expressed in terms of temperature:

$$P=\rho RT \tag{3.5}$$

$$E=c_vT \tag{3.6}$$

All the flow properties are then non-dimensionalized respect to the following reference properties:

- P^0, ρ^0, T^0 upstream equilibrium conditions (total quantities);
- $a^0=\sqrt{\gamma RT^0}$ speed of sound;
- $\sqrt{A^0}$ area of the upstream constant region.

The final set of governing equations consists on:

1. Dilatation :
$$\frac{\partial \theta}{\partial t}+V_x\frac{\partial \theta}{\partial x}=-\theta^2-\frac{1}{\gamma-1}\frac{\partial^2 T}{\partial x^2} \tag{3.7}$$

2. Temperature:
$$\frac{\partial T}{\partial t}+V_x\frac{\partial T}{\partial x}=-\left(\gamma-1\right)T\left(\theta+V_x\alpha\right) \tag{3.8}$$

along with two equations to account for the movement and distortion of the computational elements:

1. Position of the element along the axial direction:

$$\frac{\partial X}{\partial t}+V_x\frac{\partial X}{\partial x}=V_x \tag{3.9}$$

2. Length of the element:

$$\frac{\partial h}{\partial t}+V_x\frac{\partial h}{\partial x}=h\theta \tag{3.10}$$

The velocity field is evaluated summing the contribution of each element under the assumption of uniform distribution of dilation over each element.

Therefore the i-th element contributes to the velocity field ($\Phi(x)$) as:

$$\Phi_i\left(x\right)=\begin{cases}-h_i\theta_i/2 & x\leq X_i-h_i/2\\ \theta_i\left(x-X_i\right) & \mid x-X_i\mid<h_i/2\\ h_i\theta_i/2 & x\geq X_i+h_i/2\end{cases} \tag{3.11}$$

In the evaluation of the velocity field, since this approach is based on the mesheless concept, it is necessary to deal with new elements entering the computational domain and old ones leaving it. The dilatation outside the computational domain needs to be taken into account. This method relies on the wave properties to recover the effect of the dilatation that passes outside the computational domain.

The final equation adopted to calculate the velocity field is:

$$V_x\left(x\right)=V_x^0+\frac{1}{2}\triangle_l+\sum\Phi_i(x)-\frac{1}{2}\triangle_r \tag{3.12}$$

where V_x^0 is the far field velocity and $\triangle_{r/l}$ are corrections to account for the dilatation entering and leaving the domain at every time step.

The set of equations described above is then integrated adopting a two-step Runge-Kutta method as previously mentioned, before each step, boundary conditions and the second order derivative of T needs to be evaluated. For the second order derivative of the static temperature (T) a local weighted least-square fit of a fourth degree polynomial was adopted. The two steps of time integration are briefly explained below.

For the first time step (^{Prov}) the domain is discretized into N elements and all the properties are initialized with uniform conditions.

$$X_i^{Prov}=X_i^n+dtV_{xi}^n \tag{3.13}$$

$$\theta_i^{Prov}=\theta_i^n-dt\left(\left(\theta_i^n\right)^2+\frac{1}{\gamma-1}\frac{\partial^2 T_i^n}{\partial x^2}\right) \tag{3.14}$$

$$T_i^{Prov} = T_i^n - dt\,(\gamma - 1)\,T_i^n\,(\theta_i^n + V_{xi}^{\ n}\alpha_i^n) \tag{3.15}$$

$$h_i^{Prov} = h_i^n + dt h_i^n \theta_i^n \tag{3.16}$$

Before proceeding to the next time step, the dilation that has exited the computational domain and the boundary conditions need to be updated; the right boundary correction is calculated as:

$$\triangle_r^{Prov} = \triangle_r^n + \left(dt\sqrt{T_r^n}\right)\theta^{Prov}\,|_{x=(x_r+V_{xr}^n dt+\sqrt{T_r^n}dt/2)} \tag{3.17}$$

where $dt\sqrt{T_r^n}$ is the size of the gap between the end of the N^{th} element and the characteristic that left from x_r at time t_n as described in Figure 3.2. A similar procedure is performed for the left boundary.

$$\triangle_l^{Prov} = \triangle_l^n + \left(dt\sqrt{T_l^n}\right)\theta^{Prov}\,|_{x=(x_l+V_{xl}^n dt-\sqrt{T_l^n}dt/2)} \tag{3.18}$$

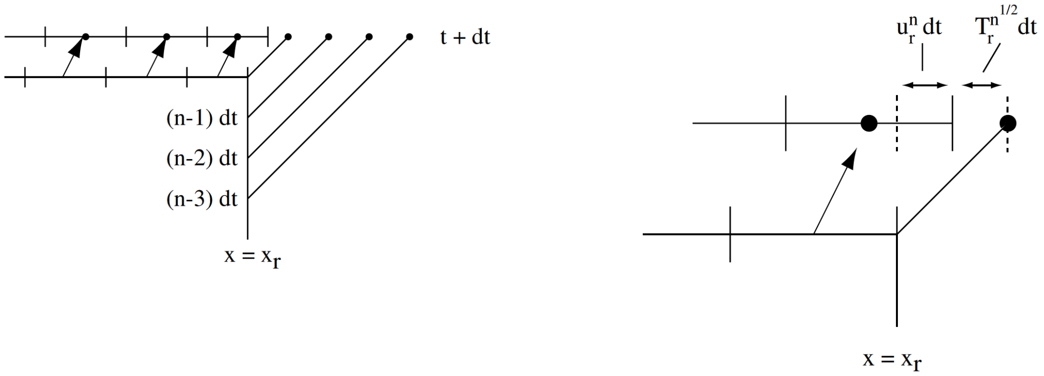

Figure 3.2: Elements motion during the integration [7].

The required values of θ^{Prov} are calculated interpolating the dilatation values inside and outside the domain. For the dilatation outside the domain a simple finite difference approximation is applied:

$$\theta_l^{n+1,k} \approx \frac{V_{xl}^{\ k} - V_{xl}^{\ k-1}}{\triangle x_l^{n+1,k}} \tag{3.19}$$

$$\theta_r^{n+1,k} \approx \frac{V_{xr}^{\ k-1} - V_{xr}^{\ k}}{\triangle x_r^{n+1,k}}$$

For $x = x_r$ and $x = x_l$ the velocity is calculated using equation (3.12) while the temperature is computed with:

$$T_r = \left(1 + \left(V_{xr} - V_x^0\right)(\gamma - 1)/2\right)^2 \tag{3.20}$$

$$T_l = \left(1 - \left(V_{xl} - V_x^0\right)(\gamma - 1)/2\right)^2$$

Using the equations (3.17), (3.18) and (3.12) to get the provisional velocity, the second step of the Runge-Kutta integration can be computed:

$$X_i^{n+1} = X_i^n + dt\left(V_{x_i}^n + V_{x_i}^{Prov}\right)/2 \tag{3.21}$$

$$\theta_i^{n+1} = \theta_i^n - dt\left(\left((\theta_i^n)^2 + (\theta_i^*)^2\right)/2 + \frac{1}{\gamma - 1}\left(\frac{\partial^2 T_i^n}{\partial x^2} + \frac{\partial^2 T_i^{Prov}}{\partial x^2}\right)/2\right) \tag{3.22}$$

$$T_i^{n+1} = T_i^n - dt(\gamma - 1)\left(T_i^n\left(\theta_i^n + V_{x_i}^n \alpha_i^n\right) + T_i^{Prov}\left(\theta_i^{Prov} + V_{x_i}^{Prov} \alpha_i^{Prov}\right)\right)/2 \tag{3.23}$$

$$h_i^{n+1} = h_i^n + dt\left(h_i^n \theta_i^n + h_i^{Prov} \theta_i^{Prov}\right)/2 \tag{3.24}$$

To complete the time integration step, new $\triangle_{r/l}^{n+1}$ need to be calculated and boundary conditions need to be applied adjusting lengths and positions of the elements closest to inlet and outlet. As previously seen, for the provisional values $\triangle_{r/l}^{Prov}$, the $\triangle_{r/l}^{n+1}$are calculated adding to those of the previous time step the amount of dilatation filling the region between the boundaries and the characteristics that moved out during dt.

$$\triangle_r^{n+1} = \triangle_r^n + \left(dt\sqrt{T_r^n}\right)\theta^{n+1}\mid_{x=(x_r+V_{x_r}^n dt+\sqrt{T_r^n}dt/2)} + \left(dtV_{x_r}^n\right)\theta^{n+1}\mid_{x=(x_r+V_{x_r}^n dt/2)} \tag{3.25}$$

$$\triangle_l^{n+1} = \triangle_l^n + \left(dt\sqrt{T_l^n}\right)\theta^{n+1}\mid_{x=(x_l+V_{x_l}^n dt-\sqrt{T_l^n}dt/2)} - \left(dtV_{x_l}^n\right)\theta^{n+1}\mid_{x=(x_l+V_{x_l}^n dt/2)} \tag{3.26}$$

$V_{x_r}^{n+1}, V_{x_l}^{n+1}, T_r^{n+1}$and $T_l^{n+1}$are updated with equation (3.12) and (3.20), for what concerns the dilatation term, this is updated preserving the total integrated dilatation:

$$\left[\theta_N^{n+1} h_N^{n+1}\right]_{new} = \left[\theta_N^{n+1} h_N^{n+1}\right]_{old} - \left(dtV_{x_r}^n\right)\theta^{n+1}\mid_{x=(x_r+V_{x_r}^n dt/2)} \tag{3.27}$$

$$\left[\theta_1^{n+1} h_1^{n+1}\right]_{new} = \left[\theta_1^{n+1} h_1^{n+1}\right]_{old} + \left(dtV_{xl}^{\,n}\right)\theta^{n+1}\,|_{x=(x_l+V_{xl}^{\,n}dt/2)} \tag{3.28}$$

The length and position of both, inlet and outlet elements, need to be adjusted periodically, since after each time step the element at inlet grows while the element at the outlet shrinks. As a criterion, the element at inlet is subdivided into two when its length is bigger than $3/2\bar{h}$ (with $\bar{h}$ is the average length of all the axial elements) while the outlet element is merged with the one preceding it once its length is less than $\bar{h}/2$. The above described procedure is repeated iteratively until convergence.

3.1.0.2 The finite difference Euler approach

The same fluid dynamic problem (Figure 4.1) was tackled using the finite difference approach [2]. In particular, with this technique the tube is discretized with a certain number of elements that is fixed throughout the iterations. The time integration is performed using the MacCormarck's technique, a second order method based on the predictor-corrector scheme. For the spatial derivatives the second order central differences are implemented. This section describes in details the implemented equations, the adopted boundary conditions, and the integration technique. The equations that follows are the common Euler equations for a quasi-1D problem as reported below.

$$\frac{\partial}{\partial t}\begin{bmatrix} \rho' A' \\ \rho' A' V_x' \\ \rho' A'\left(\frac{T'}{\gamma-1}+\frac{\gamma}{2}V_x'^2\right) \end{bmatrix} = -\frac{\partial}{\partial x}\begin{bmatrix} \rho' V_x' A' \\ \rho' A' V_x'^2 + \frac{1}{\gamma}P' A' \\ \rho' V_x' A'\left(\frac{T}{\gamma-1}' + \frac{\gamma}{2}V_x'^2\right) + P' A' V_x' \end{bmatrix} + \begin{bmatrix} 0 \\ \frac{1}{\gamma}P'\frac{\partial A'}{\partial x} \\ 0 \end{bmatrix} \tag{3.29}$$

As for the Lagrangian case all the properties were non-dimensionalized (') with respect to the same reference values. It is recognized that the conservative form of these equations is more robust and suitable for integration purposes [2], therefore the equations implemented in the solver appear as:

$$\frac{\partial}{\partial t}\begin{bmatrix} U_1 \\ U_2 \\ U_3 \end{bmatrix} = -\frac{\partial}{\partial x}\begin{bmatrix} F_1 \\ F_2 \\ F_3 \end{bmatrix} + \begin{bmatrix} 0 \\ B_2 \\ 0 \end{bmatrix} \tag{3.30}$$

where

$$
\begin{aligned}
U_1 &= \rho' A' \\
U_2 &= \rho' A' V_x' \\
U_3 &= \rho' A' \left(\tfrac{T'}{\gamma - 1} + \tfrac{\gamma}{2} u'^2 \right) \\
F_1 &= \rho' u' A' \\
F_2 &= \rho' A' u'^2 + \tfrac{1}{\gamma} p' A' \\
F_3 &= \rho' u' A' \left(\tfrac{T}{\gamma - 1}' + \tfrac{\gamma}{2} u'^2 \right) + p' A' u' \\
B_2 &= \tfrac{1}{\gamma} p' \tfrac{(\partial A')}{\partial x}
\end{aligned}
\tag{3.31}
$$

The time integration is performed using the second order MacCormark's scheme. This technique is an explicit predictor-corrector method and it is extensively used in CFD investigations for its simplicity and robustness. Before starting the integration, all the properties are initialized with constant values or using a previous converged solution. The properties are then non-dimensionalized using the reference values as previously mentioned. The predictor step is then calculated using forward difference for the spatial integration. An example for the mass conservation equation is reported below:

$$\frac{\partial}{\partial t}[U_1(j)]^{pre} = -\left[\frac{F_1(j+1) - F_1(j)}{x(j+1) - x(j)} \right] \tag{3.32}$$

With this first value, a provisional solution is calculated:

$$U_1^{Prov}(j) = U_1(j)^t + dt \frac{\partial}{\partial t}[U_1(j)]^{pre} \tag{3.33}$$

The fluxes, F, need to be recalculated with the provisional values before proceeding to the corrector step, while boundary values are not updated at this time. The corrector step adopts rearward difference, as before an example is provided for the mass conservation equation:

$$\frac{\partial}{\partial t}[U_1(j)]^{cor} = -\left[\frac{F_1(j) - F_1(j-1)}{x(j) - x(j-1)} \right] \tag{3.34}$$

The final value of each conservative property is then determined averaging the time derivatives estimated during predictor and corrector step:

$$U_1(j)^{t+1} = U_1(j)^t + \frac{dt}{2} \left(\frac{\partial}{\partial t}[U_1(j)]^{pre} + \frac{\partial}{\partial t}[U_1(j)]^{cor} \right) \tag{3.35}$$

An additional term known as artificial viscosity is also added to equation (3.33) and (3.35) to better capture phenomena which involves strong gradients of pressure or temperature such as shock waves. The artificial viscosity is calculated for each equation and for each element. As an example, the equation adopted to determine the artificial viscosity for the mass balance is given below:

$$VIS_1(j) = C_X \mid \frac{(P(j+1) - 2P(j) + P(j-1))}{(P(j+1) + 2P(j) + P(j-1))} \mid (U_1(j+1) - 2U_1(j) + U_1(j-1)) \tag{3.36}$$

where Cx is a damping factor usually fixed at the value of 0.5 [2]

At the end of the corrector step, the boundary conditions need to be applied, the new fluxes need to be calculated along with the primitive variable as well as the minimum dt in order to respect the CFL number (Courant-Friedrichs-Lewy condition) as reported at the end of this subsection by equation (3.38).

The boundary conditions are treated on the basis of the characteristic waves that travel outside or inside the domain. For a quasi-one dimensional case, there are two characteristic slopes that need to be calculated at inlet and outlet. The slopes of the characteristics are calculated as follows:

$$\begin{aligned} S_{lc} &= V_x^{'} - a^{'} \\ S_{rc} &= V_x^{'} + a^{'} \end{aligned} \tag{3.37}$$

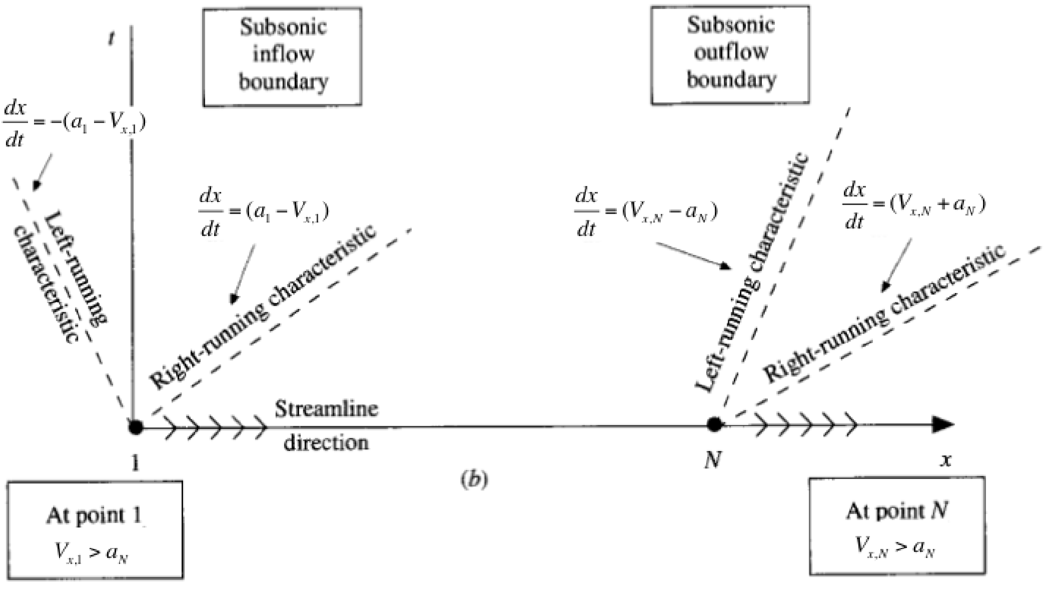

Figure 3.3: Characteristic waves for subsonic inlet and outlet.

Figure 3.3 above shows a typical case of subsonic inlet and subsonic outlet. Considering the inlet, there is one characteristic going out of the domain and one entering;

the streamlines are as well entering the domain. In this case, two values need to be imposed and one has to be free to float. This last value is usually linearly extrapolated using the values inside the domain.

Considering the outlet, one characteristic and the streamlines are going downstream while one characteristic is entering the domain. For this second case, two values are extrapolated from inside the domain but one value needs to be imposed. Usually density and velocity are extrapolated while the temperature is calculated from the density and the imposed outlet static pressure.

Following this procedure, at every time step the slope of the three characteristics is calculated at inlet and outlet of the domain and the boundary conditions are consequently applied to the conservative variables as reported below:

SUBSONIC INLET:

- Linear extrapolation of the velocity;
- Imposition of total pressure and temperature;

SUBSONIC OUTLET:

- Linear extrapolation of U1 and U2;
- Imposition of the exit static pressure;

SUPERSONIC INLET:

- Linear extrapolation of U1, U2 and U3;

SUPERSONIC OUTLET:

- Linear extrapolation of U1, U2 and U3.

The correct *dt* is evaluated before starting the new time step adopting the following equation and imposing a CFL number which does not exceed unity (MacCormark is in fact an explicit scheme). An appropriate time step value is calculated for each element, the final *dt* selected satisfies the condition of minimum. The physical explanation behind this concept is that a small enough time step has to be selected to capture the fastest traveling waves.

$$dt = CFL \frac{\triangle x}{a+V} \tag{3.38}$$

3.1.0.3 Lagrangian VS Euler

The major differences between the two approaches are in terms of speed of iteration, storage requirements and the possibility of handling discontinuities. As it is described in the work of Shen [7, 66], the Lagrangian dilatation method cannot handle the presence of discontinuities in the flow. He suggested that a simple way to fix this deficiency could be the addition of an artificial viscous term. The main drawback of this simple solution appears in the necessity of an accurate tuning of the viscosity and in discontinuous results that are greatly smeared. In Chapter 4, a comparison of the results obtained with both versions of the code is reported. Both codes were tested in terms of accuracy of the converged solution, computational time and required storage. After several tests and analysis of drawbacks and advantages, it was found that the dilatation element method requires more computational time to reach the steady solution and it appears to be less accurate compared to the finite difference approach. For the mentioned reasons, the finite difference method was selected.

3.2 Background to FENICE-PC

The knowledge acquired modeling the unsteady compressible flow in a simple duct with variable cross section provided the ground for the development of FENICE-PC. Indeed, FENICE-PC was developed combining a quasi-2D unsteady Euler solver with a ‘parallel compressors’ approach. At first, the quasi-2D unsteady solver was developed and implemented into FORTRAN.

3.2.1 The quasi-2D unsteady Euler solver

The core of the tool is represented by the Euler equations and in particular by the source terms used to model features such as the axial change of the cross section, the presence of rotors and stators, mean-line radius changes and so on. The equations implemented are reported below:

- Mass conservation equation:

$$\frac{\partial}{\partial t}(\rho A) = -\frac{\partial}{\partial x}(\rho V_x A) \tag{3.39}$$

- Axial momentum conservation equation:

$$\frac{\partial}{\partial t}(\rho V_x A) = -\frac{\partial}{\partial x}\left(\rho V_x^2 A + PA\right) + \left(\frac{\rho V_t^2 A}{r}\frac{\partial r}{\partial x} + P\frac{\partial A}{\partial x} + F_x\right) \tag{3.40}$$

- Tangential momentum conservation equation:

$$\frac{\partial}{\partial t}(\rho V_t A) = -\frac{\partial}{\partial x}(\rho V_x V_t A) + \left(-\frac{\rho V_x V_t A}{r}\frac{\partial r}{\partial x} + F_t\right) \tag{3.41}$$

- Energy conservation equation:

$$\frac{\partial}{\partial t}\left(\rho E^0 A\right) = -\frac{\partial}{\partial x}\left(\rho V_x H^0 A\right) + (W_{ex}) \tag{3.42}$$

In the tool, the equations have been implemented using their conservative form for robustness purposes as previously explained. Each equation is written in terms of conservative variables U, fluxes F and source terms B as shown by equation (3.43).

$$\frac{\partial}{\partial t}\begin{bmatrix} U_1 \\ U_2 \\ U_3 \\ U_4 \end{bmatrix} = -\frac{\partial}{\partial x}\begin{bmatrix} F_1 \\ F_2 \\ F_3 \\ F_4 \end{bmatrix} + \begin{bmatrix} B_1 \\ B_2 \\ B_3 \\ B_4 \end{bmatrix} \tag{3.43}$$

Where $U_1 = \rho A$, $F_1 = \rho V_x A$ and so on.

3.2.1.1 Blade force and work exchange

The equation used to determine the blade force is derived from the momentum balance in a linear cascade.

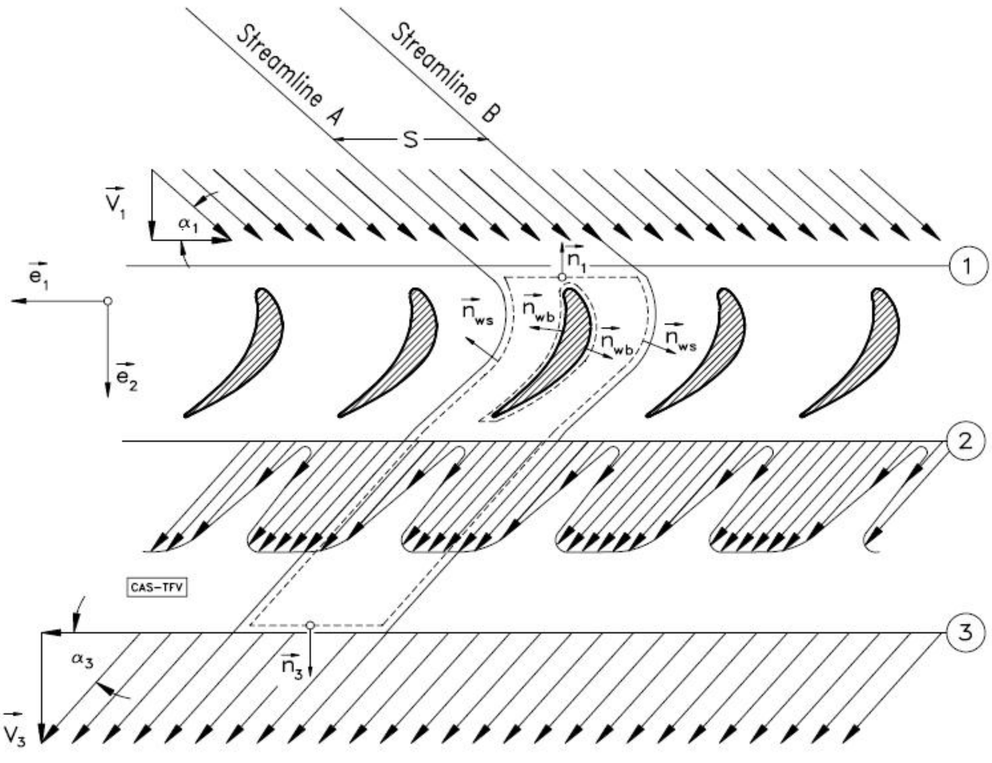

Figure 3.4: Control volume for the calculation of the blade forces in a viscous flow field [65].

The axial force per unit length source term is determined as:

$$F_x = \frac{(\dot{m}\,(V_{xout} - V_{xin}) + (P_{out} - P_{in})\overline{A})}{c_x} \tag{3.44}$$

where:

$\dot{m}$: is the mass flow across a blade row;

V_x: is the axial velocity;

P: is the static pressure;

c_x: blade axial length;

$\overline{A}$: is the average cross section of a stream-tube and is calculated as:

$$\overline{A} = \pi \left(\frac{\Delta R_{in}^2 + \triangle R_{out}^2}{2} \right) \tag{3.45}$$

with $\triangle R$ distance between tip and hub calculated orthogonally to the engine axis. The main contribution in terms of axial force, comes from the difference in static pressure, the axial velocity contribution is almost negligible especially at steady state condition. The axial blade force as well as the following source terms are divided by the axial chord since, these terms are then distributed over the elements inside each blade row.

Torque per unit length for a stationary blade:

$$F_t r = \frac{\dot{m}\,(V_{tout} r_{out} - V_{tin} r_{in})}{c_x} \tag{3.46}$$

where:

$\dot{m}$, c_x :as above;

r: mean radius;

V_t: absolute tangential velocity.

The same expression applies to a rotor blade with relative velocities adopted in the place of absolute ones.

Work exchange per unit length:

$$W_{ex} = \frac{\dot{m}\,(W_{tout} r_{out} - W_{tin} r_{in})\,\Omega}{c_x} \tag{3.47}$$

$\dot{m}$, x: as above;

W_t: relative tangential velocity;

Ω: rotational speed.

The axial/tangential blade force and the work exchange are respectively inserted in the momentum and energy equation as shown above in equation (3.40), (3.41) and (3.42).

The blade force and work exchange calculated as explained above are in fact distributed over the elements inside each blade row. Figure 3.5 shows a typical distribution of blade force and work exchange. Although, initially a constant distribution was tested, a sinusoidal distribution was finally adopted in order to guarantee a smooth transition from un-bladed to bladed regions and vice versa. Gong [82] suggested a similar distribution in order to reduce numerical oscillations.

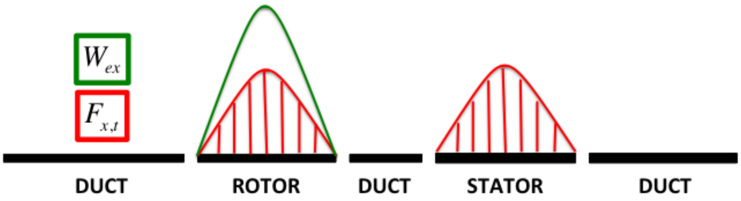

Figure 3.5: Example of blade force and work exchange distribution adopted.

3.2.2 Boundary conditions, plenum and throttle modeling

In terms of boundary conditions, the same concept described in section 3.1.0.2, is applied for the quasi-2D solver. Depending on the slope of the characteristic waves, for a subsonic inlet and a subsonic outlet, total pressure, total temperature and flow direction are applied at the inlet of the domain, while static pressure is applied at the outlet. In case of supersonic flow all the properties are linearly extrapolated from inside the domain.

In order to investigate the behavior of a compressor during surge or rotating stall, it is important to properly simulate a plenum and a throttle. These two components can be modeled in terms of cross section variations and therefore integrated in time and space; as an alternative, they can be represented through few equations reducing in this way the integration's time. The alternative method adopted in this work, considers the plenum as a component with a user-specified volume, while the throttle is modeled as a con-di nozzle with a user-specified throat area.

The choked nozzle condition is checked at each time step and the boundary conditions are then obtained through the following calculations.

- At first a check is performed to verify if the nozzle is choked, considering the pressure ratio between plenum and the ambient conditions (atmospheric) and determining the Mach number:

$$M_t = \begin{cases} \sqrt{\frac{2}{\gamma-1}\left(\left(\frac{P_p}{P_{atm}}\right)^{\frac{\gamma-1}{\gamma}}-1\right)} & \frac{P_p}{P_{atm}} \leq \left(\frac{\gamma+1}{2}\right)^{\left(\frac{\gamma}{\gamma-1}\right)} \\ 1 & \frac{P_p}{P_{atm}} > \left(\frac{\gamma+1}{2}\right)^{\left(\frac{\gamma}{\gamma-1}\right)} \end{cases} \tag{3.48}$$

- Having determined the Mach number at the nozzle throat, the mass flow across the throttle can be calculated with the following equation. A_t is a user-defined parameter which can also be modified during a simulation.

$$m_t = \sqrt{\rho P_p \gamma} A_t \frac{M_t}{\left(1 + \frac{\gamma-1}{2} M_t^2\right)^{\frac{\gamma+1}{2(\gamma-1)}}} \tag{3.49}$$

- The pressure inside the plenum and the density are then determined through a four steps Runge-Kutta integration as shown below:

$$RT1 = \frac{1}{V_p}\left(m_p - m_t\right) \tag{3.50}$$

$$RT2 = \frac{\gamma P_p}{\rho_p V_p}\left(m_p - m_t\right)$$

$$\begin{aligned}
\rho_p^{(0)} &= \rho_p^{(n)} \\
P_p^{(0)} &= P_p^{(n)} \\
\rho_p^{(1)} &= \rho_p^{(0)} + \tfrac{1}{4} \triangle t RT1^{(0)} \\
P_p^{(1)} &= P_p^{(0)} + \tfrac{1}{4} \triangle t RT2^{(0)} \\
\rho_p^{(2)} &= \rho_p^{(1)} + \tfrac{1}{3} \triangle t RT1^{(1)} \\
P_p^{(2)} &= P_p^{(1)} + \tfrac{1}{3} \triangle t RT2^{(1)} \\
\rho_p^{(3)} &= \rho_p^{(2)} + \tfrac{1}{2} \triangle t RT1^{(2)} \\
P_p^{(3)} &= P_p^{(2)} + \tfrac{1}{2} \triangle t RT2^{(2)} \\
\rho_p^{(n+1)} &= \rho_p^{(3)} + \triangle t RT1^{(3)} \\
P_p^{(n+1)} &= P_p^{(3)} + \triangle t RT2^{(3)}
\end{aligned}$$

3.3 Modeling of a complete compressor map

As already pointed out in the introductory chapter of this document, a complete compressor map consists of three different operating regions: forward, stalled and reverse flow.

This section provides information on the velocity triangles calculation and semi-empirical models/correlations chosen and implemented in order to predict the correct body forces over the three different regions.

3.3.1 Forward flow

Velocity triangles

In forward flow operating condition the velocity triangles at inlet and outlet of a rotor and a stator appear as shown in Figure 3.6. All the calculations are performed being consistent with the sign convention reported at the bottom left of the figure below.

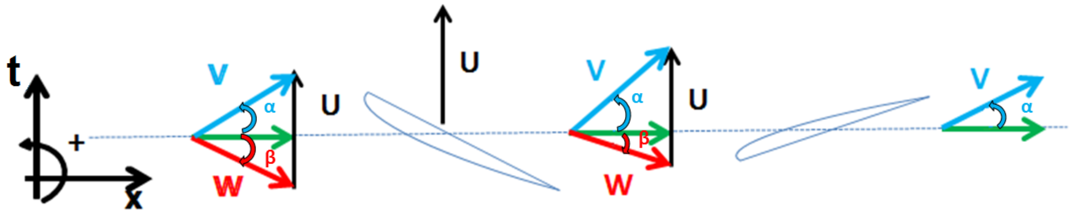

Figure 3.6: Velocity triangles during forward flow and sign convention.

Pressure loss coefficient and deviation in this region are provided by a collection of correlations derived by Aungier [6]. A detailed description of these correlations is provided below in this section. In addition it is important to highlight the fact that all the empirical models presented in this chapter are extensions of models derived from experimental observation of 2D cascades. It is well known that a large amount of experimental work in this context was carried out by NACA. The correlations presented below are therefore adaptation of the original correlations in order to account for different blade profiles, design and off-design conditions.

Deviation model

Aungier suggested three slightly different procedures in order to predict the deviation angle during the forward flow operating condition. This subsection described the procedure implemented in the solver.

As previously mentioned all these correlations need to be adapted to account for different blade profiles; to obtain the design angle of attack, two corrector factors need to be calculated. A shape corrector factor (K_{sh}) for which Aungier suggests three possible values: 1.0 for NACA profiles, 1.1 for C4-series and 0.7 for double-circular-arc; and a thickness corrector factor which can be derived either graphically in Johnsen and Bullock [39] or with the following equation:

$$K_{t,i} = \left(10\left(\frac{t_{max}}{c}\right)\right)^{q} \tag{3.51}$$

where the exponent q, that is a function of the ratio between maximum blade thickness and chord, is determined as:

$$q = \frac{0.28}{\left[0.1 + \left(\frac{t_{max}}{c}\right)^{0.3}\right]} \tag{3.52}$$

The design angle of attack can then be calculated along with the design incidence angle as shown below:

$$\alpha^* = \left[3.6 K_{sh} K_{t,i} + 0.3532\theta \left(\frac{a}{c}\right)^{0.25}\right] \sigma^e \tag{3.53}$$

$$e = 0.65 - 0.002\theta \tag{3.54}$$

$$i^* = \alpha^* + \gamma - \beta_1^{'} \tag{3.55}$$

where $\frac{a}{c}$ is the location of the point of maximum camber. Combining all the above calculations, it is possible to assess the inlet flow angle which corresponds to the situation of minimum loss. The minimum loss inlet flow angle is determined as:

$$\beta_1^* = \beta_1^{'} + i^* \tag{3.56}$$

All the calculations related to the inlet of the blade row have been described. The following calculations regard the procedure applied to the outlet of the blade row and the determination of the deviation angle. A thickness corrector factor for the deviation angle is defined using the following equation:

$$K_{t,\delta} = 6.25 \left(\frac{t_{max}}{c}\right) + 37.5 \left(\frac{t_{max}}{c}\right)^2 \tag{3.57}$$

The next step involves the calculation of the deviation angle for a zero camber blade. Similarly to the case of the thickness corrector factor, the deviation angle for a zero camber blade could be derived either graphically from Johnsen and Bullock or with the correlation reported below.

$$(\delta_0^*)_{1.0} = 0.01\sigma |\beta_1^*| + \left[0.74\sigma^{1.9} + 3\sigma\right] \left(\frac{|\beta_1^*|}{90}\right)^{(1.67+1.09\sigma)} \tag{3.58}$$

The design deviation angle can then be determined with equation (3.63) once the slope parameter *m* has been corrected to account for values of solidity different from 1.0 following the set of equations reported below.

$$x = \frac{|\beta_1^*|}{100} \tag{3.59}$$

$$m_{1.0} = 0.17 - 0.0333x + 0.333x^2 \tag{3.60}$$

$$b = 0.9625 - 0.17x - 0.85x^3 \tag{3.61}$$

$$m = \frac{m_{1.0}}{\sigma^b} \tag{3.62}$$

$$\delta^* = K_{sh} K_{t,\delta} \left(\delta_0^*\right)_{1.0} + m\theta \tag{3.63}$$

As for the inlet flow angle the outlet flow angle for minimum loss is determined as a function of the outlet metal angle with equation (3.63).

$$\beta_2^* = \beta_2' + \delta^* \tag{3.64}$$

In order to properly model off-design conditions a correction based on the axial velocity and the incidence angle has to be implemented as shown below by equation (3.65) and equation (3.66).

$$\left(\frac{\partial \delta}{\partial i}\right)^* = \left[1 + \left(\sigma + 0.25\sigma^4\right)\left(\frac{|\beta_2^*|}{53}\right)^{2.5}\right] / e^{(3.1\sigma)} \tag{3.65}$$

$$\delta = \delta^* + \left(\frac{\partial \delta}{\partial i}\right)^* (i - i^*) + 10\left(1 - \frac{W_{m2}}{W_{m1}}\right) \tag{3.66}$$

Pressure loss model

Similarly to what has been described for the deviation angle, Aungier describes the procedure for deriving the pressure loss coefficient starting from the condition of minimum loss. Therefore the starting point is the definition of the design profile loss coefficient which is based on the knowledge of the design diffusion factor. For the calculation of the latter, the equation provided by the NASA TP 1493 [76] was adopted:

$$D^* = 1 - \frac{V_2}{V_1} + \left[\frac{r_2 V_{t2} - r_1 V_{t1}}{(r_2 + r_1)\,\sigma V_1}\right] \tag{3.67}$$

Once the design diffusion factor is calculated, the design profile loss coefficient can be determined using the following equation:

$$\bar{\omega}^* = (factor + K_1(K_2 + A_1 D^* + A_2 D^*))\frac{2\sigma}{cos(\beta_2^*)} \tag{3.68}$$

where K_1, A_1 and A_2 are determined curve-fitting data available in [76], while K_2 and the $factor$ are provided below:

$$K_2 = 1 + \left(\frac{s}{h}\right) cos(\beta_2^*) \tag{3.69}$$

$$factor = \begin{cases} -0.0105 & stator \\ -0.001 & rotor \end{cases} \tag{3.70}$$

Figure 3.7 sketches out the typical trend of loss coefficient with incidence; as it is clear observing the graph, the loss coefficient tends to be almost constant over a range of incidence angles around the value of the design incidence angle. The range of low loss operation is usually limited by two angles known as positive (i_s) and negative (i_c) stall incidence angles.

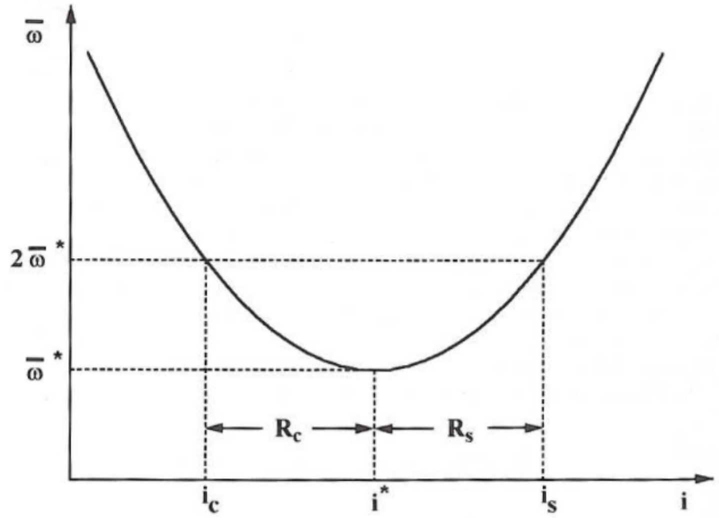

Figure 3.7: Typical trend of loss coefficient against incidence [6].

To determine these two incidence angles, an iterative procedure based on the secant method was implemented to solve the set of equations reported below.

$$\alpha^* = \alpha_c + 9 - \left[1 - \left(\frac{30}{\beta_{1c}}\right)^{0.48}\right] \frac{|\theta|}{4.176} \tag{3.71}$$

$$\beta_{1c} = \alpha_c + \gamma \tag{3.72}$$

$$\alpha^* = \alpha_s + 10.3 - \left[2.92 - \left(\frac{\beta_{1s}}{15.6}\right)\right] \frac{|\theta|}{8.2} \tag{3.73}$$

$$\beta_{1s} = \alpha_s + \gamma \tag{3.74}$$

Once identified the negative and positive stall angles of attack, the negative and positive range can be calculated together with negative and positive stall incidence angles.

$$R_c = \alpha^* - \alpha_c = i^* - i_c \tag{3.75}$$

$$R_s = \alpha_s - \alpha^* = i_s - i^* \tag{3.76}$$

The correlations described so far was derived from observation of experiments performed with low-speed cascade; in order to correctly apply these models to a real high speed compressor, additional corrections are necessary. For instance, considering Figure 3.8, it can be appreciated how increasing the Mach number, the parabolic curve tends to shift and reduce in amplitude.

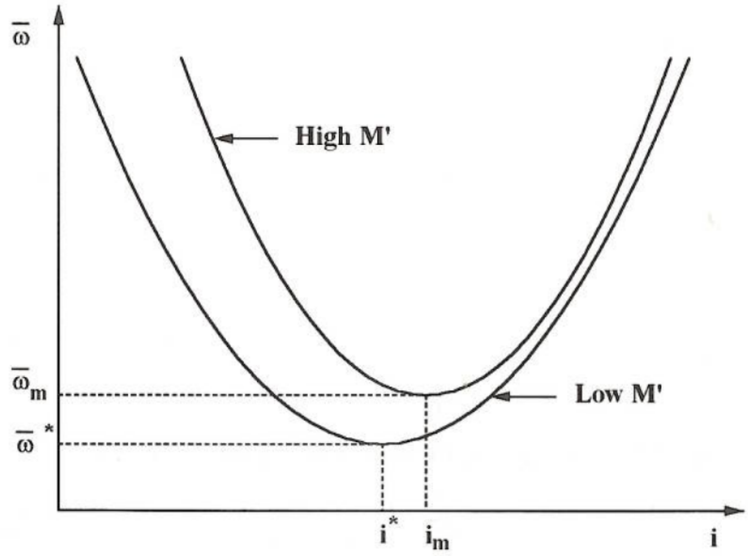

Figure 3.8: Mach number effect on the pressure loss bucket [6].

Aungier suggests the following correlations to account for the effect of the Mach number:

$$i_c = i^* - \frac{R_c}{\left(1 + 0.5M_{in}^3\right)} \tag{3.77}$$

$$i_s = i^* + \frac{R_s}{(1 + 0.5(K_{sh}M_{in})^3)} \tag{3.78}$$

Combining equation (3.75), (3.76), (3.77) and (3.78) the “minimum loss” incidence angle and the respective “minimum loss” profile loss coefficient are defined as:

$$i_m = i_c + \frac{(i_s - i_c)R_c}{R_c + R_s} \tag{3.79}$$

$$\bar{\omega}_m = \bar{\omega}^* \left[1 + \frac{(i_m - i^*)^2}{R_s^2}\right] \tag{3.80}$$

The off-design loss coefficient is finally obtained from the "minimum loss" coefficient through a correction based on the normalized incidence angle parameter (ξ) defined as:

$$\xi = \begin{cases} \frac{i-i_m}{i_s-i_m} & i \geqslant i_m \\ \frac{i-i_m}{i_m-i_c} & i < i_m \end{cases} \tag{3.81}$$

$$\bar{\omega} = \bar{\omega}_s + \bar{\omega}_m(1-\xi^2) \quad -2 \leqslant \xi \leqslant 1 \tag{3.82}$$

$$\bar{\omega} = \bar{\omega}_s + \bar{\omega}_m[5-4(\xi+2)] \quad \xi < -2 \tag{3.83}$$

$$\bar{\omega} = \bar{\omega}_s + \bar{\omega}_m[2+2(\xi-1)] \quad \xi > 1 \tag{3.84}$$

Figure 3.9 describes graphically the above equation for the off-design pressure loss coefficient.

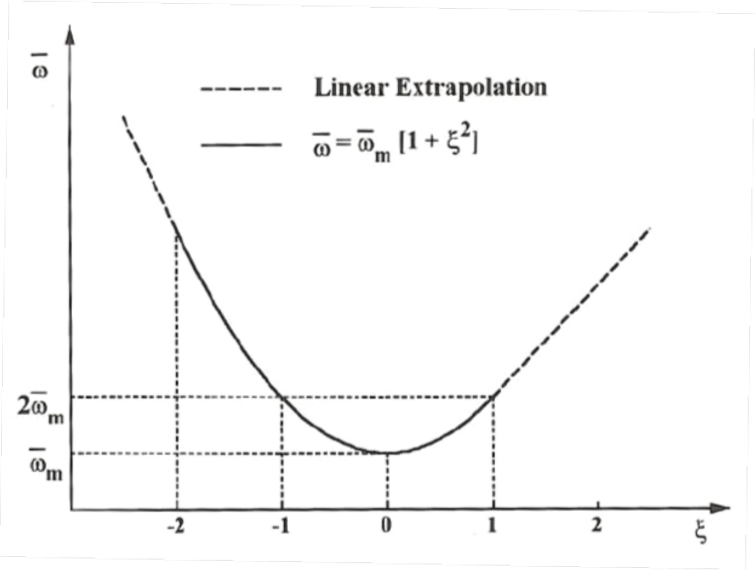

Figure 3.9: Off-design pressure loss coefficient against normalized incidence angle [6].

3.3.2 Stalled flow

Velocity triangles During stall, the flow field is completely disrupted, therefore a specific representation of velocity triangles in this unstable operating region cannot be provided. In this particular region the calculations performed are the same shown in forward flow and reverse flow, in the sense that for each blade a check is performed in terms of direction of the axial velocity to decide which calculation is more appropriate, "forward" or "reverse".

Stall cell model

Another important part of this research involves the modeling of a rotating stall cell. In order to account for the presence of a stall cell there are mainly five important aspects that need to be modeled:

- Blade stall inception;
- Pressure loss across a stalled blade row;
- Deviation angle at the outlet of a stalled blade row;
- Rotation of the stall cell around the annulus and stall cell growth;
- Blockage induced by the stall cell and circumferential mass redistribution.

Blade stall inception

The switching from forward flow viscous correlations to stalled flow viscous correlations is handled by a stall inception model. The user can utilize three possible stall criteria: one that is based on the flow coefficient at stall, one that is based on incidence angle, or Aungier's correlations [6]. For all three techniques, the check is performed at each blade. Chapter 4 presents the different results obtained choosing one model or another. In general the flow coefficient criterion, relying on a priori knowledge of the forward flow characteristic, is the most precise and straight forward one since it does not require any calibration to capture the correct stall inception point. On the other hand, this method is not suitable during preliminary design. The incidence method relies on a very simple correlation suggested by O'Brien [56] and comes from observations of experimental data by Yocum [83], Hynes and Longley [48]. In fact, from experimental observations it was found that the flow on an isolated blade starts to separate when the incidence angle exceeds 8 degrees; while a stage in a multistage compressor is instead able to remain unstalled at a much lower flow thanks to the pumping action of the downstream stages. The incidence which determines the stall condition is defined as:

$$i_{stall} = 8 + \frac{N - \varkappa}{N - 1} \triangle i \tag{3.85}$$

Where N is the number of stages and $\varkappa$ is the position of the stage within the compressor. The $\triangle i$ account for the difference between stall incidence of the first stage and the actual incidence of the stage under consideration.

Aungier's model is based on a comparison between an aerodynamic ($W_{(REq.aero)}$) and a geometry-based equivalent velocity ratio ($W_{(REq.geom)}$). The passage is considered stalled if the following condition is satisfied:

$$W_{(REq.aero)} < W_{(REq.geom)} \tag{3.86}$$

where the aerodynamic equivalent velocity ratio is determined as:

$$W_{(REq.aero)} = \sqrt{\frac{P^0_{2,rel} - P_2}{P^0_1 - P_1}} \tag{3.87}$$

and the geometry-based equivalent velocity ratio as:

$$W_{(REq.geom)} = \frac{([0.15 + 11(\frac{t_{max}}{c})]/[0.25 + 10(\frac{t_{max}}{c})])}{(1 + 0.4[\theta\sigma/2\sin(\theta/2)\cos\gamma]^{0.65})} \tag{3.88}$$

A slightly different version for the geometry equivalent velocity ratio is reported below. This second equation is used when the equivalent diffusion factor D_{eq} is greater than 2.2.

$$W_{(REq.geom)} = \frac{((\frac{2.2}{D_{eq}})^{0.6}[0.15 + 11(\frac{t_{max}}{c})]/[0.25 + 10(\frac{t_{max}}{c})])}{(1 + 0.4[\theta\sigma/2\sin(\theta/2)\cos\gamma]^{0.65})} \tag{3.89}$$

Rotor stall delay model

The label “rotor stall delay model” refers to a feature that was added to the developed tool almost at the end of the research, in order to account for the inertia of the flow when dealing with inlet flow distortion. The feature is presented here, after the stall inception model since it is linked with the incidence criterion presented above.

The concept of the rotor stall delay can easily be described considering a specific compressor geometry and three different patterns of inlet flow distortion. Figure 3.10 sketches out the concept; considering that the overall extent and the intensity of the distortion is the same for all the three cases, it is clear that the most severe effect in terms of loss of surge margin is produced by a distortion concentrated on one larger sector. The onset and development of stall or surge for a certain blade passage, depends on the time spent by the same blade passage in the low pressure region. Basically, a rotating blade needs a certain amount of time to adapt to a different operating condition. Splitting the distorted region into smaller ones might avoid the inception of stall considering fixed throttle settings.

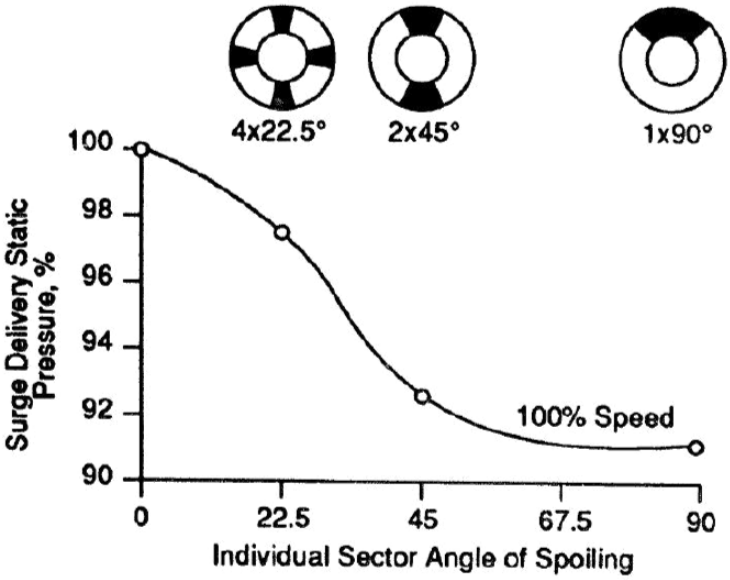

Figure 3.10: Effect of split distortion, experimental obsevations carried out by Reid [61].

The rotor stall delay model takes into account the time needed by the blade to adapt to the low pressure region in terms of incidence angle. Therefore it was implemented in order to be used along with the incidence stall inception criterion.

Without this modification, a blade entering in the low pressure region, would be subjected to an abrupt increase of incidence angle; the rotor stall delay retards the blade response applying a first order time lag law to the incidence angle. The effect of the first order time lag is shown in Figure 3.11 below. From an implementation perspective, the equation used in the solver is equation (3.90) where i_{inst} is the incidence that would be felt by the blade neglecting the flow inertia while i_{eff} is the effective incidence which is then used to decide if the blade is stalled or not.

$$i_{eff} = i_{eff} + (i_{inst} - i_{eff})(1 - e^{\frac{\frac{-\triangle\theta}{\Omega}}{\tau}}) \tag{3.90}$$

The time constant τ is usually inferred from blade geometry and flow properties as reported by Lecht [43].

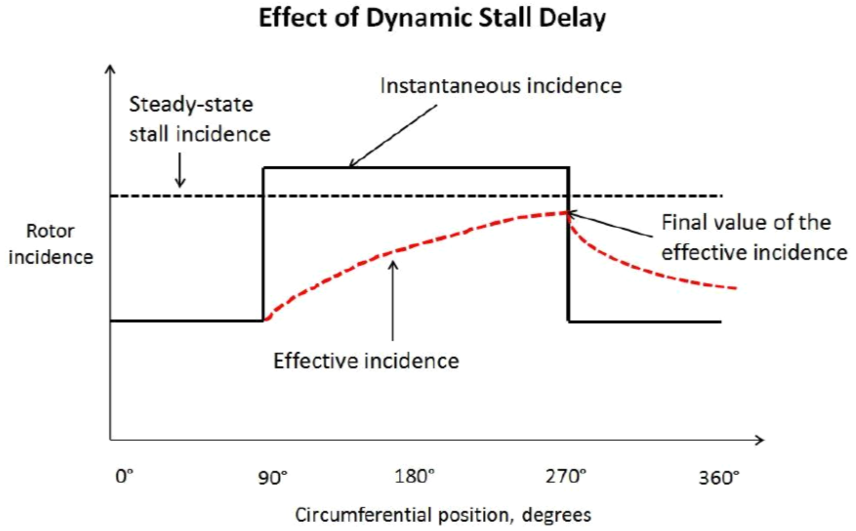

Figure 3.11: First order time lag applied to the rotor incidence.

Pressure loss models

Due to the complexity of the flow field in the rotating stall region, the models available to account for the pressure losses that occur are very few. The model selected for this tool is the one that is most commonly used, the Moses and Thomason model [54].

This model is an approximation for fully stalled cascade characteristics; therefore a more accurate pressure loss prediction is reached as the through-flow tends to zero.

Considering Figure 3.12, the flow is assumed separated from the leading-edge and the trailing-edge is considered as the combination of a zone with essentially zero velocity and a region with velocity V_2. Moreover, the blade forces are considered parallel and normal to the chord line.

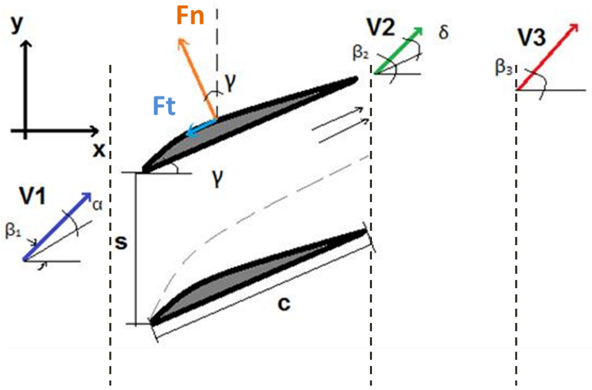

Figure 3.12: Moses and Thomason model

Deriving the momentum equation for the control volume of Figure 3.12, the following two equations can be found:

$$C_n = \frac{F_n}{\left(\rho\frac{V_1^2 c}{2}\right)} = \frac{2}{\sigma}cos\beta_1(sin\alpha - \frac{V_2}{V_1}sin\delta) + \left(\frac{P_2 - P_1}{\rho\frac{V_1^2}{2}}\right)\frac{sin\gamma}{\sigma} \tag{3.91}$$

$$C_t = \frac{F_t}{\left(\rho\frac{V_1^2 c}{2}\right)} = \frac{2}{\sigma}cos\beta_1(\frac{V_2}{V_1}cos\delta - cos\alpha) + \left(\frac{P_2 - P_1}{\rho\frac{V_1^2}{2}}\right)\frac{cos\gamma}{\sigma} \tag{3.92}$$

For closely spaced blades, the deviation angle can be considered almost zero. The actual flow at the trailing-edge is considered uniform therefore the losses due to the mixing are taken into account introducing a relative total pressure loss factor k.

$$\frac{P_2 - P_1}{\left(\rho\frac{V_1^2}{2}\right)} = 1 - (1+k)\frac{V_2^2}{V_1^2} \tag{3.93}$$

Again from the assumption of fully mixed, uniform flow at station 3, the flow angle can be determined from the mass flow rate and the momentum along the y-direction while the fully mixed pressure can be found from the mass flow rate and the momentum along the x-direction.

$$tan\beta_3 = \frac{V_2 sin\beta_2}{V_1 cos\beta_1} \tag{3.94}$$

$$\frac{P_2 - P_3}{\left(\rho\frac{V_1^2}{2}\right)} = 2cos\beta_1(cos\beta_1 - \frac{V_2}{V_1}cos\beta_2) \tag{3.95}$$

Concluding, the loss coefficient is defined from equation (3.93) and equation (3.95) as:

$$\bar{\omega} = \frac{P_1^0 - P_3^0}{\left(\rho\frac{V_1^2}{2}\right)} = (1+k)\frac{V_2^2}{V_1^2} + 2cos\beta_1(cos\beta_1 - \frac{V_2}{V_1}cos\beta_2) - \frac{cos^2\beta_1}{cos^2\beta_3} \tag{3.96}$$

Where k is approximated by:

$$k = 0.15\sigma/cos\beta_1 \tag{3.97}$$

Deviation model

The original Moses and Thomason model assumes that the jet leaves the blade parallel to the stagger which translates in zero deviation. This assumption is known to be quite simplistic, as an alternative, the author implemented Tauveron's correlation [73].

$$\beta_2(\chi) = \beta_2'(\chi) - \frac{\chi - 1}{N_{stage} - 1}(\beta_2'(\chi) - \gamma(\chi)) \tag{3.98}$$

Where N_{stage} is the number of stages, χ is the position of the stage and β_2' is the blade metal angle.

The author is aware that the above correlation is extremely trivial and does not model properly the real behavior of the flow. During this doctoral research some work was carried out in collaboration with an M.Sc. student [53] in order to developed a correlation which accounts for the real flow physic of the stall phenomenon. In particular, the work made use of 2D and 3D CFD simulations of a multistage cascade in order to derive a new correlation that links the deviation angle also to the incidence angle and not only to the position of the blade in the cascade. However, due to time constrain, only steady CFD simulations were carried out adopting the C106 compressor geometry. For this reasons the results obtained during the mentioned campaign did not allow the derivation of a satisfying deviation model and therefore they are not reported in this work. For further information on this topic, the reader may refer to Molinero [53]. Although the campaign of 2D and 3D CFD simulations did not lead to the development of a satisfying deviation model, this strategy could provide an accurate deviation correlation. Indeed, the author believes that collecting enough data for different compressor geometries and for incidence angles in a range which covers the region between stall inception to fully developed stall, it would be possible to derive a correlation for the deviation angle more representative of the reality.

Stall cell growth

A very important assumption behind the modified Euler solver and the models implemented for the rotating stall condition is the consideration of the flow being axis-symmetric and fully separated. Therefore, when the solution switches from normal forward to stalled flow it is necessary to account for the inertia of the flow and the stall cell growth. This feature is taken into account introducing a first order time lag law in the calculation of the axial blade force as shown in the equation below. The constant τ represents the time necessary for the stall cell to grow until it occupies the whole annulus.

$$\tau\frac{\partial F}{\partial t}+F=F_{ss} \tag{3.99}$$

The effect of the τ parameter is better described in section 4.2.2.1. For the application of this delay, a check is carried out on the flow coefficient of each blade. Figure 3.13 shows the region of the compressor map where τ is applied, for the recovery part (which means for a blade row or blade row segment that is moving from lower flow coefficients to higher ones), as emphasized by the graph, the delay is applied on a larger region. The extent of the “stalling part” and of the “recovery part” can be calibrated for each geometry. For this project the author referred to the values of flow coefficient suggested also by Adam [1, 23] for the compressor C106. For this particular compressor the “stalling part” covers the region from the flow coefficient at stall inception to a flow coefficient which is slightly less than zero (-0.09 in order to be in steady reverse flow when the lag is removed). For the “ recovery part”, the delay is applied from a flow coefficient of -0.09 till a flow coefficient which is equal to the stall inception flow coefficient (which depends on the geometry adopted) plus a factor.

For all the results reported in Chapter 4 and Chapter 5 the added factor was 0.1 slightly larger than what suggested by [23] since a smoother transition between stall and forward condition was observed.

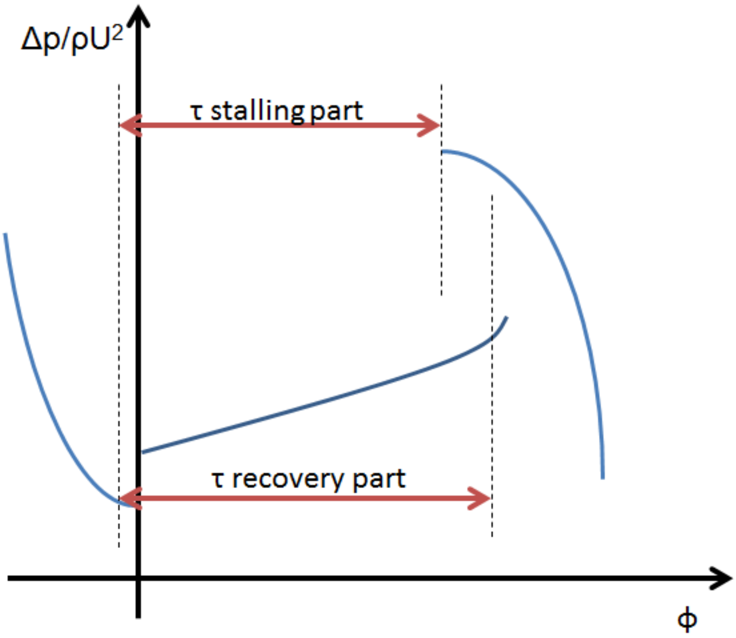

Figure 3.13: Regions of delay application

Blockage and circumferential mass redistribution

One of the peculiar features of rotating stall is the blockage induced by the stall cell and the consequent circumferential mass redistribution that causes the stall cell rotation around the annulus. In order to improve the tool's capability to model asymmetric phenomena, a modified 'parallel compressors' technique was implemented. The reason behind implementing this technique was the desire to provide a better representation of the real phenomenon (see Section §3.4).

3.3.3 Reverse flow

A complete compressor map consists of three operating regions, known as: forward, stalled and reverse flow. As already highlighted in the introduction, rotating stall and surge are strictly linked and they cannot be treated separately. Therefore, to develop a fully functional tool, it is important to be able to model also the reverse flow condition.

Velocity triangles

During steady reverse flow the velocity triangles appear as those shown in Figure 3.14. As it is shown in the picture, the sign convention adopted during this regime is the same one adopted during forward flow. The major differences are that both absolute and relative velocities change "plane" when passing through a blade row and all flow angles (inlet and outlet) are higher than 90 degrees.

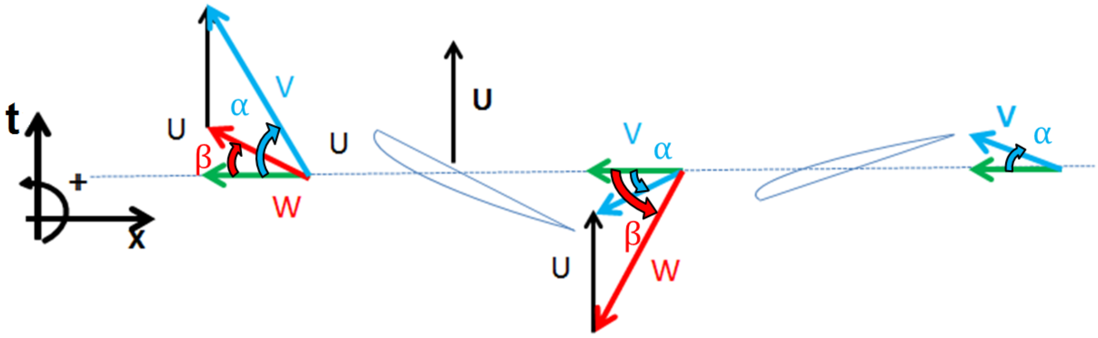

Figure 3.14: Velocity triangles during reverse flow and sign convention.

Pressure loss model To predict the pressure loss occurring during this condition, three possible models have been taken into consideration: Koff [41], Longley [46] and Moses and Thomason [54]. All these models have similar assumptions and range of applicability. This subsection describes Longley's model which was selected and implemented since it is the one more frequently used for this specific application, as found in several recent publications [1, 23, 46].

As in the case of stalled flow, these models consider the flow as steady, incompressible and fully separated. The jet is again considered leaving the blade with zero deviation, and the blades are considered as flat plates.

Figure 3.15 sketches out the concept of this model.

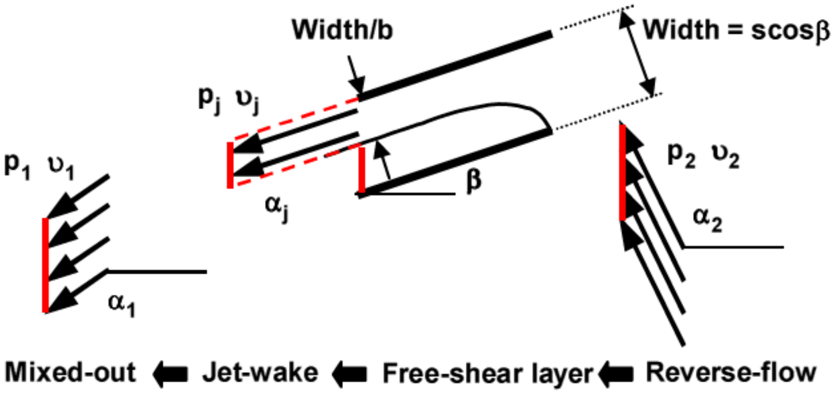

Figure 3.15: Basic concept of Longley's reverse flow model [46].

The blockage (b) due to the flow separation is calculated considering the conservation of mass flow and momentum, parallel to the plate and ignoring the skin friction.

$$b = 1 + |(sin(\alpha_2 - \beta))/(cos(\alpha_2))| \tag{3.100}$$

The pressure loss is then determined considering a complete mixing-out of the jet-wake. For the calculation of the total pressure loss coefficient Longley suggests two possible expressions depending on two basic assumptions:

- Constant pressure mixing:

$$\bar{\omega} = \frac{\triangle P^0}{1/2 \rho U^2} = (b^2 - 1)\,(cos(\alpha_2))^2 \tag{3.101}$$

- Constant area mixing:

$$\bar{\omega} = \frac{\Delta P^0}{1/2 \rho U^2} = (b-1)^2 (cos(\alpha_2))^2 \tag{3.102}$$

Both expressions are available for the user, since during the verification of the reverse flow model negligible differences were found adopting one or the other expression (see also Longley [46]).

3.4 Quasi-2D Unsteady Euler solver + 'Parallel compressors'

The second chapter of this document describes extensively the rotating stall phenomenon. One of its peculiar features is the blockage induced by the stall cell and the consequent circumferential mass redistribution that causes the stall cell rotation around the annulus.

In order to improve the tool's capability of modeling asymmetric phenomena such the one under study, a modified 'parallel compressors' techniques was implemented. The driving aim behind this technique was the desire of providing a better representation of the real phenomenon. During rotating stall, the flow is highly asymmetric, the blockage due to the stalled region produces a circumferential redistribution of the mass flow.

3.4.1 Modified 'parallel compressors' theory

As seen in section 2.4.1, the 'parallel compressors' approach is usually more commonly applied in the study of inlet flow distortion. The rationale of this method is the subdivision of the whole annulus into a certain number of independent virtual compressor's segments. Each parallel compressor is operating at the same rotational speed discharging to the same plenum (same exit static pressure). What changes is the inlet condition of each sector [16, 26, 42].

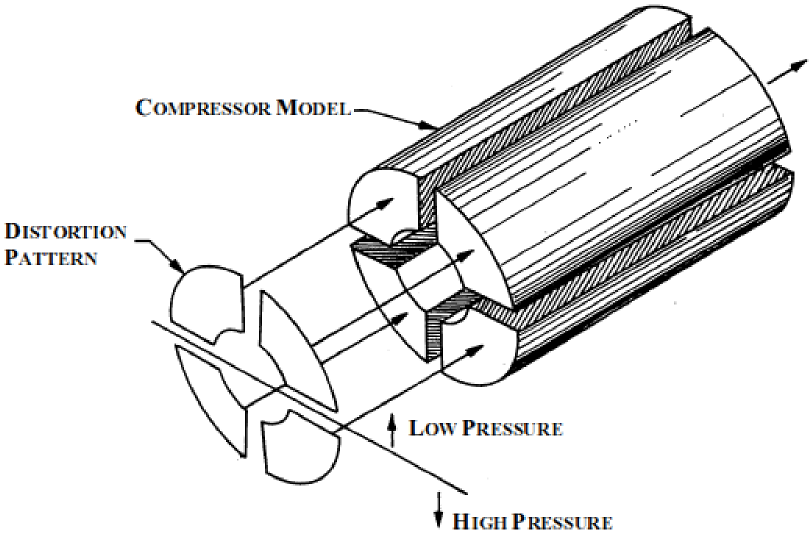

Figure 3.16: 'Parallel compressors' original concept [75].

The imposition of a unique exit static pressure implies the assumption of uniform exit flow conditions. Under these conditions the clean sectors have to operate at higher mass flows and lower pressure ratio in order to match the imposed exit static pressure while compensating for the distorted sectors.

In Chapter 2, section 2.4.1 has already provided a detailed description of the 'parallel compressors' technique. Besides, section 2.4.1 underlines the limitations as well as some of the modifications introduced to overcome these limitations and to provide a more realistic description of the physical phenomenon.

Taking into account the case of total pressure distortion as a relevant example, a circumferential redistribution of mass flow is usually observed. A similar phenomenon is caused by the presence of a rotating stall cell. As mentioned by section 2.4.1.2, a first attempt to model the circumferential and radial mass flow redistribution was provided by Kimzey [40].

Kimzey, indeed, suggested to model the mass flow redistribution through an orifice flow analogy; the mass flow exchange is considered to occur exclusively in the rotor-stator gap due to the difference in static pressure of two adjacent segments. The cross flow is estimated with equation (3.103) reported below, assuming the flow as incompressible and neglecting energy and momentum exchanges.

$$\dot{m}_{cross} = C_{xflow} A_{gap} \sqrt{2\rho \left(P_{high} - P_{low}\right)} \tag{3.103}$$

Where C_{xflow} is analogous to the orifice coefficient, A_{gap} is the cross section of the gap.

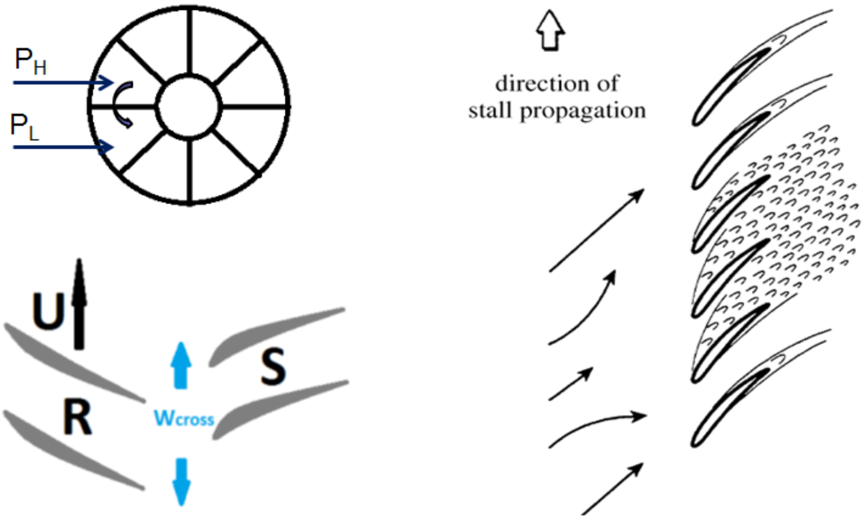

Figure 3.17: Model for the stall cell propagation mechanism.

3.4.2 Extension to the circumferential direction: FENICE-PC

The extension of the developed quasi-2D Euler solver was performed applying a modified 'parallel compressors' technique.

An initial attempt was carried out adopting a slightly different version of the Kimzey's approach. Basically, the mass flow exchange between parallel segments was determined using the equation provided before, equation (3.103). An additional term representing the energy exchange due to the cross flow was also introduced. As for Kimzey's model, compressibility effects and momentum exchanges were neglected. However, the methodology proved to be unable to deal with large amount of cross flow, showing important convergence problems.

A second attempt involving the revision of this methodology in order to account for compressibility as well as axial/circumferential momentum and energy exchanges was carried out and proved successful.

The improved 'parallel compressors' technique finally adopted in FENICE-PC is represented by the calculation of the four source terms introduced in equations (3.39)-(3.42), as shown below by equation (3.104).

$$\frac{\partial}{\partial t}\begin{bmatrix}\rho A\\ \rho V_x A\\ \rho V_t A\\ \rho E^0 A\end{bmatrix} = -\frac{\partial}{\partial x}\begin{bmatrix}\rho V_x A\\ \rho V_x^2 A + PA\\ \rho V_x V_t A\\ \rho V_x A H^0\end{bmatrix} + \begin{bmatrix}\dot{m}_{cross}\\ \frac{\rho V_t^2 A}{r}\frac{\partial r}{\partial x} + P\frac{\partial A}{\partial x} + F_x + Mom_{xcross}\\ -\frac{\rho V_x V_t A}{r}\frac{\partial r}{\partial x} + F_t + Mom_{tcross}\\ W_{ex} + E_{cross}\end{bmatrix} \tag{3.104}$$

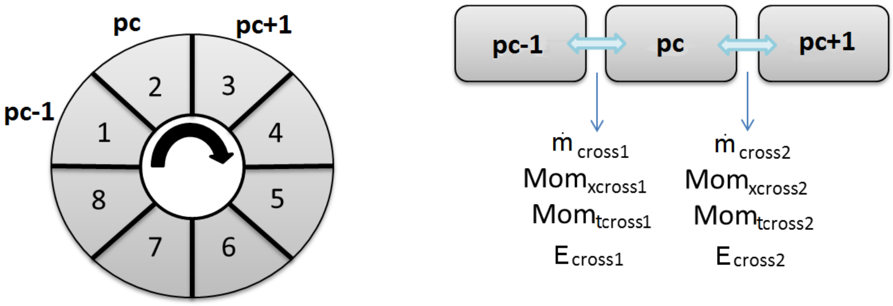

Figure 3.18: 'Parallel compressors' with cross flow.

A first important modification introduced to the Kimzey's model is that the evaluation of the mass flow exchange is performed for each axial element; in fact, for each axial element the procedure which is going to follow, is carried out.

The system of equations which has to be solved to determine the source terms corresponds to the basic normal shock wave equations and it is reported below.

$$\rho_1 V_{t1} = \rho_2 V_{t2} \tag{3.105}$$

$$P_1 - P_2 = \rho_2 V_{t2}^2 - \rho_1 V_{t1}^2 \tag{3.106}$$

$$cp_1 T_1 + \frac{V_{t1}^2}{2} = cp_2 T_2 + \frac{V_{t2}^2}{2} \tag{3.107}$$

$$P = \rho R T \tag{3.108}$$

Where the subscripts “1” and “2” refers to two adjacent circumferential positions, that is, a generic “pc” and “pc+1” as shown in Figure 3.18.

In order to solve the above system, two main assumptions need to be introduced:

- The cross flow can be visualized as a small packet of air which departs from the elements at high static pressure to reach the element at lower static pressure. The element at higher static pressure is therefore considered as a reservoir which practically translates in nullifying V_{t1}. As a consequence, the first equation, equation (3.105), is removed.
- The packet of air which travels from “1” to “2” is established from the difference in the static pressure field. It is therefore correct to use the subscripts “1” and “2” when referring to the static pressure of the two adjacent elements. On the other hand ρ_2, T_2 and V_{t2} should be addressed as ρ_{cross}, T_{cross} and V_{cross} since these terms do not correspond to the flow properties of the main flow of “2”. From a visual point of view, the “cross” terms refer to the flow flowing in an imaginary pipe connecting two adjacent elements.

With these assumptions in mind, the system of equations can be rewritten in the following more convenient form:

$$P_1 - P_2 = \rho_{cross} V_{cross}^2 \tag{3.109}$$

$$cpT_1 = cpT_{cross} + \frac{V_{cross}^2}{2} \tag{3.110}$$

$$P_2 = \rho_{cross} R T_{cross} \tag{3.111}$$

The solution of the system provides the values of ρ_{cross}, T_{cross} and V_{cross} which are then used to determine the source terms of equation (3.104).

$$\dot{m}_{cross} = C_{xflow}\rho_{cross}V_{cross}A_{gap} \tag{3.112}$$

where A_{gap} is actually the thickness ($\triangle R$) in order to be dimensionally consistent.

$$Mom_{xcross} = \dot{m}_{cross}V_{x1} \tag{3.113}$$

$$Mom_{tcross} = \dot{m}_{cross}\left(V_{t1} \pm V_{cross}\right) \tag{3.114}$$

$$E_{cross} = \dot{m}_{cross}cp_1T_1^0 \tag{3.115}$$

The sign of V_{cross} is considered positive when the cross flow occurs in the same direction of the compressor rotation (which is considered always as the positive direction of the reference system). Moreover, the term $\dot{m}_{cross}$ is positive for the segment which is receiving mass flow and negative for the one which is giving. Therefore a parallel segment receiving mass flow against the positive direction of the reference system will have a positive $\dot{m}_{cross}$ but will loose tangential momentum.

The final source terms that are introduced in the Euler equations, equation (3.104), are obtained for each element of each parallel segment applying the procedure described above two times in order to account for the contributions in terms of cross flow of the two neighboring parallel compressors.

3.5 FENICE-2D

During the verification, the developed FENICE-PC has proved to be able of tackling unsteady/steady phenomena characterized by axis-symmetric and asymmetric flow fields within certain limitations. Indeed, for all the tested compressor geometries, limitations in increasing the circumferential discretization were observed along with a unrealistic transient behaviour in the rotating stall region (further information in this regard is provided in Chapter 4 and Chapter 5). To overcome the limitations encountered with FENICE-PC and assess also differences in accuracy, robustness and computational time, a second fully-2D approach was implemented.

The governing equations for FENICE-2D are listed below [67, 15, 14]. The equations are written in the cylindrical form and in the stationary frame. The body force technique, already adopted with FENICE-PC, was used to model the presence of blades with the assumption that each blade row consists of an infinite number of blades. This assumption was necessary since an important requirement of this tool was the computational efficiency which would be lost if the flow field within each blade passage was to be tackled.

- Duct

$$\frac{\partial}{\partial t}\begin{bmatrix} \rho A \\ \rho A V_x \\ \rho A V_t \\ \rho A E^0 \end{bmatrix} = -\frac{\partial}{\partial x}\begin{bmatrix} \rho V_x A \\ \rho A V_x^2 + PA \\ \rho A V_t V_x \\ \rho V_x A H^0 \end{bmatrix} - \frac{1}{r}\frac{\partial}{\partial \theta}\begin{bmatrix} \rho V_t A \\ \rho V_t V_x A \\ \rho V_t^2 A + PA \\ \rho V_t A H^0 \end{bmatrix} + \begin{bmatrix} 0 \\ \frac{\rho V_t^2 A}{r}\frac{\partial r}{\partial x} + p\frac{(\partial A)}{\partial x} \\ -\frac{\rho V_x V_t A}{r}\frac{\partial r}{\partial x} \\ 0 \end{bmatrix} \tag{3.116}$$

- Rotor

$$\frac{\partial}{\partial t}\begin{bmatrix} \rho A \\ \rho A V_x \\ \rho A V_t \\ \rho A E^0 \end{bmatrix} = -\frac{\partial}{\partial x}\begin{bmatrix} \rho V_x A \\ \rho A V_x^2 + PA \\ \rho A V_t V_x \\ \rho V_x A H^0 \end{bmatrix} - \frac{1}{r}\frac{\partial}{\partial \theta}\begin{bmatrix} \Omega \rho A \\ \Omega \rho V_x A \\ \Omega \rho V_t A \\ \Omega \rho A E^0 \end{bmatrix} + \begin{bmatrix} 0 \\ \frac{\rho V_t^2 A}{r}\frac{\partial r}{\partial x} + P\frac{(\partial A)}{\partial x} + F_x \\ -\frac{\rho V_x V_t A}{r}\frac{\partial r}{\partial x} + F_t \\ W_{ex} \end{bmatrix} \tag{3.117}$$

- Stator

$$\frac{\partial}{\partial t}\begin{bmatrix} \rho A \\ \rho A V_x \\ \rho A V_t \\ \rho A E^0 \end{bmatrix} = -\frac{\partial}{\partial x}\begin{bmatrix} \rho V_x A \\ \rho A V_x^2 + PA \\ \rho A V_t V_x \\ \rho V_x A H^0 \end{bmatrix} - \frac{1}{r}\frac{\partial}{\partial \theta}\begin{bmatrix} 0 \end{bmatrix} + \begin{bmatrix} 0 \\ \frac{\rho V_t^2 A}{r}\frac{\partial r}{\partial x} + p\frac{(\partial A)}{\partial x} + F_x \\ -\frac{\rho V_x V_t A}{r}\frac{\partial r}{\partial x} + F_t \\ 0 \end{bmatrix} \tag{3.118}$$

The calculation of the correct time step, previously obtained with equation (3.38), was modified to account for the circumferential direction as shown below.

$$dt_{max} = C\frac{\triangle x \triangle \theta}{|V_x|\triangle \theta + |V_t|\triangle x + a\sqrt{\triangle x^2 + \triangle \theta^2}} \tag{3.119}$$

Similarly to what is described in section 3.1.0.2 for the axial direction, a term of artificial viscosity triggered by gradients in static pressure in the circumferential direction was introduced.

3.6 FENICE tool general information

The tool described so far can be used adopting different set ups. Firstly, the circumferential discretization can be set to 1, reducing the solver to a quasi-2D tool which solves the tangential momentum considering the tangential velocity field as axis-symmetric; increasing the circumferential number of elements the user can decide to run the tool as a real 2D solver (FENICE-2D) or as a quasi-2D+'parallel compressors' (FENICE-PC). The latter offers also the possibility to account for the mass flow exchange in the rotor-stator gap (Gap Cross) or everywhere (Full Cross). In terms of compressor geometry, several geometries are implemented and they are identified through a compressor name. Each compressor's geometry can be run adopting one of the three following configuration types:

- C: compressor only, first and last components are “DUCT”;
- CN: compressor followed by a con-di nozzle;
- CPN: compressor followed by a plenum and a con-di nozzle.

3.6.1 Equations' integration scheme

The tool offers the user the choice between two time integration schemes: a 2^{nd} order MacCormark scheme and a 4^{th} order Runge-Kutta one. All the results presented in Chapter 4 and Chapter 5 were obtained with the MacCormark scheme which is faster being a second order scheme. An explanation of the MacCormark technique has been already provided in section 3.1.0.2, therefore this subsection is dedicated to the Runge-Kutta scheme. The description in this subsection applies to FENICE-PC; the derivation of the equations for FENICE-2D is straight forward and therefore not reported. For both integration techniques the spatial derivative adopts a finite difference approach.

Runge-Kutta 4^{th} order The Runge-Kutta 4th order, as the MacCormarck scheme, is a very well known explicit method. Before starting the integration, all the properties need to be initialized with constant values or using a previous converged solution as for the MacCormark scheme.

The integrated values for each conservative variable are then obtained following the procedure reported below:

- Calculation time derivative: forward differences are adopted for odd 'Ks' while rearward differences are used for even 'Ks'.

$$\frac{\partial}{\partial t}[U_1(j,pc)]^K = -\frac{F_1(j+1,pc)-F_1(j,pc)}{x(j+1,pc)-x(j,pc)} + \dot{m}_{cross}(j,pc) \tag{3.120}$$

- Calculation provisional values for the first two steps (K=1 and K=2)

$$U_1^K(j,pc) = U_1^t(j,pc) + \frac{\triangle t}{2}\frac{\partial}{\partial t}[U_1(j,pc)]^K + VIS1(j,pc) \tag{3.121}$$

- Calculation provisional values for the third step (K=3)

$$U_1^K(j,pc) = U_1^t(j,pc) + \triangle t\frac{\partial}{\partial t}[U_1(j,pc)]^K + VIS1(j,pc) \tag{3.122}$$

- Calculation for the last step (K=4)

$$\begin{aligned} U_1^4(j,pc) &= U_1^t(j,pc) + \frac{\triangle t}{6}\left(\frac{\partial}{\partial t}[U_1(j,pc)]^1 + \frac{\partial}{\partial t}[U_1(j,pc)]^4\right) + \\ &+ \frac{\triangle t}{3}\left(\frac{\partial}{\partial t}[U_1(j,pc)]^2 + \frac{\partial}{\partial t}[U_1(j,pc)]^3\right) + VIS1(j,pc) \end{aligned} \tag{3.123}$$

$$U_1^{t+1}(j,pc) = U_1^4(j,pc) \tag{3.124}$$

where $VIS1(j,pc)$ is the artificial viscosity, defined as already seen in section 3.1.0.2 with equation (3.36). After each 'K-step', the boundary conditions are applied following the characteristics' slopes as already described for the MacCormark scheme and the updated fluxes are calculated.

3.6.2 Inputs and outputs

A user-friendly interface (GUI) for this solver has not been developed yet, therefore during the implementation the author tried to minimize the required inputs. All the information, in terms of inputs and outputs, is exchanged between the tool and the user through .TXT files. A detailed list with descriptions of each term is reported in Appendix A.

At this stage, it is worth mentioning that there are only two input files: one that contains all the information to set up the simulation (such as number of total time steps, axial and circumferential number of nodes and so on) and one that is needed to initialize the flow variables with a previous converged solution.

In terms of output files, the user should be aware that the action of writing the .TXT files while performing the simulation is computationally expensive. On the other hand, saving throughout a simulation is suggested during the debugging phase. In this regards, a variable is available to set up the time step between the "savings".

Convergence check In the input file with the settings for the simulation it is possible to set a maximum number of iterations (Nstep), on the other hand the integration stops when convergence is reached. The subroutine "Convergence_check" which is called at the end of each time step, decides if the solution is converged with a mass flow based criterion. At steady condition, the mass flow conservation has to be respected through all the compressor; a check is therefore performed at each axial plane. The maximum error accepted can be adjusted by the user. For all the cases presented in the next two chapter, the tolerance was set up at $6 * 10^{-3}$.

Tool's structure FENICE-PC/2D consists of almost 60 subroutines counting also the DLLs implemented for some calculations. Therefore the description of each subroutine is out of the purpose of this work. On the other hand the structure of the main program is quite important to understand the order of the calculations. Figure 3.19 provides a simple flow chart of the main program clarifying the order of the calculations described previously in this chapter. As indicated by the legend, the blue blocks correspond to calculations performed in the main program while the green blocks refer to the calling of other subroutines. The red and orange boxes identify respectively the time loop for the time integration and the loop for the circumferential discretization.

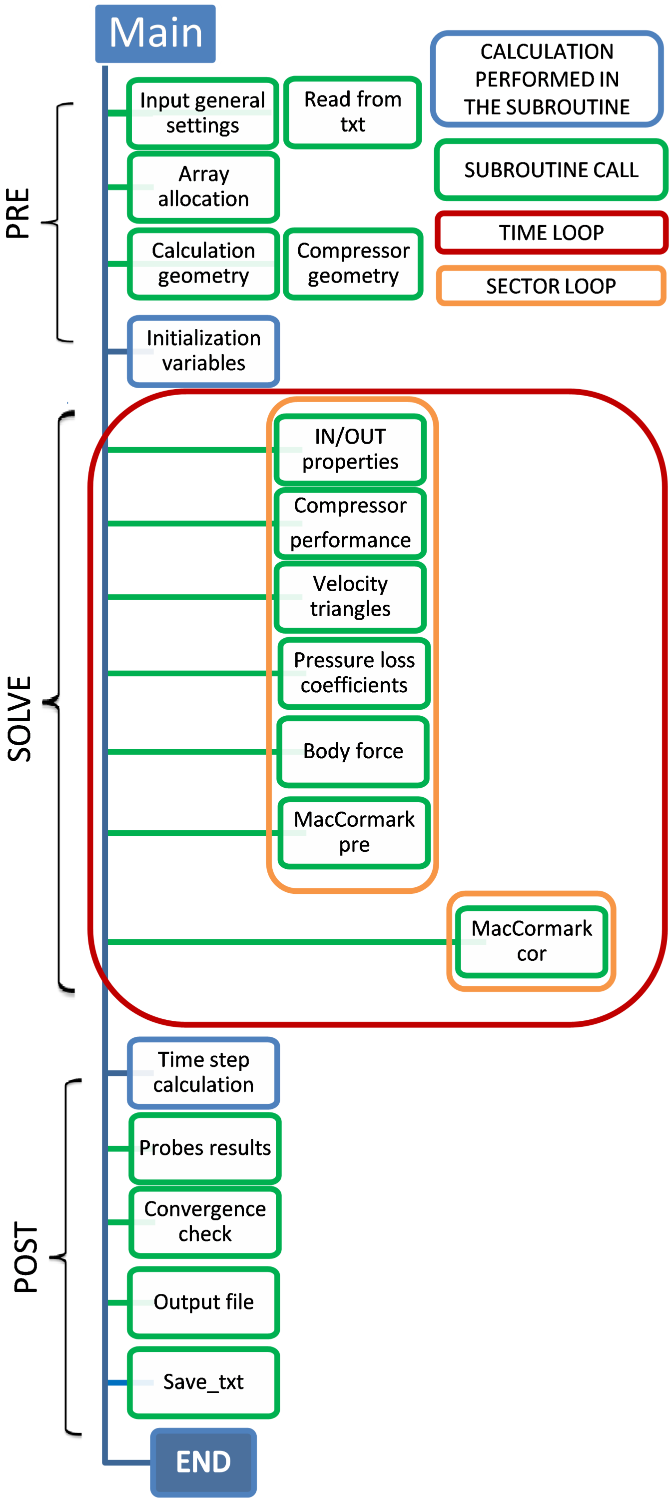

Figure 3.19: Main program structure.

3.7 Summary

The literature review carried out on compressor models and computational tools led to the development and implementation of a through-flow solver based on the Euler equations which relies on semi-empirical correlations and models to account for viscous features of the flow. A major requirement of this research was, in fact, the development of a tool able to provide an accurate prediction of the complete compressor map relying only on geometrical information. Other important requirements taken into consideration concern the reliability, robustness and efficiency of the tool since the aim was to provide a good alternative to 3D CFD simulations which are particularly expensive in terms of computational time and power required.

This chapter has provided a detailed description of the methodology followed for the tool's implementation, highlighting both assumptions and limitations, along with implementation details. The developed tool, named by the author as FENICE, is a solver which offers the user the choice between two slightly different approaches to solve the flow field: a quasi-2D solver which relies on the 'parallel compressors' technique to deal with asymmetric flow field and a real 2D solver which solves the 2D Euler equations.

The research focus was mainly on the modeling of rotating stall and surge events and therefore particular attention was devoted on the modeling of selected key-features of both phenomena such as pressure loss, deviation, stall cell growth and so on. Nonetheless, the developed tool can easily be used for other scenarios. In this regards, the next chapter provides some example of the wide applicability of the tool. As a matter of fact, the following chapter reports on investigations performed in all the three regions (forward, stalled and reverse flow) for different case-studies of inlet flow distortion and variable throttle settings.

Chapter 4

Results and verification

The first part of the present chapter deals with the results regarding the preliminary work described in Section §3.1. At this point it is worthy highlighting that this numerical investigation was performed in order to decide between Eulerian and Lagrangian modeling and to gain confidence in solving a generic unsteady flow field. The verification performed with the final tool FENICE-PC/2D is reported starting from Section §4.2.

4.1 Lagrangian solver and Euler solver in comparison

4.1.1 Verification

The comparison between the Lagrangian and Eulerian quasi-1D solver and their verification was carried out adopting the same geometry and case-study already mentioned in Section §3.1 and described in [7].

The domain is a simple straight empty duct which is suddenly indented as shown below in Figure 4.1. The aim of this simulation was, in fact, the modeling of the propagation's waves involving the main flow properties due to a sudden change of the axial cross section.

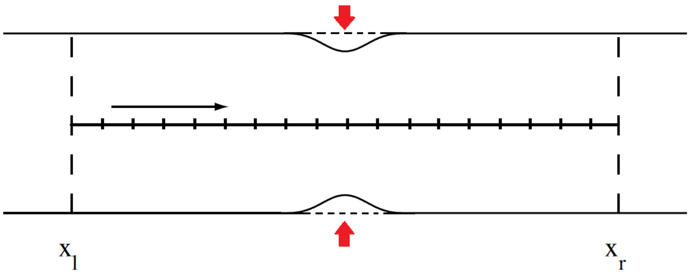

Figure 4.1: Lagrangian case study: straight duct with sudden change in cross section.

The choice of this particular case study was mainly related to the available results from the work of Bernard described in [7] and the possibility of solving the same case study analytically.

For what concerned the duct geometry, as can be found in [7], a straight empty duct from x_l equal to -1 to x_r equal to 1 was implemented. The cross section, that is a function of the axial position, was defined using the following equation.

$$A(x) = \begin{cases} \left[1 - \frac{\beta}{4}\left\{\cos\left(\pi\left(1+2X\right)\right) - 1\right\}^2\right]^2 & |x| \leq 0.5 \\ 1 & |x| > 0.5 \end{cases} \tag{4.1}$$

where β is a shape parameter used to defined the level of indentation. The comparison and verification were carried out with β equal to 0.05.

The verification was performed comparing the exact steady solution obtained through ODE45[1] of MATLAB (red line) and the steady solution reached by the quasi-1D Euler solver (black circles) and the quasi-1D Lagrangian solver (light blue circles). The graphical comparison is shown below in Figure 4.2. For the following graph and each graphical representation reported in this section, flow and geometrical properties have been non-dimensionalized as reported in Section §3.1.

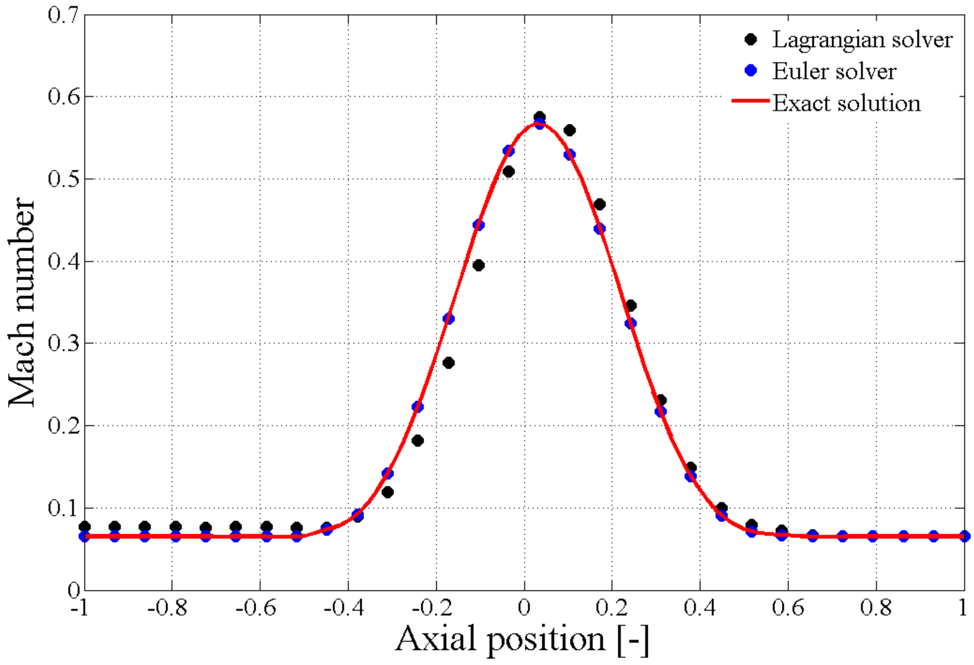

Figure 4.2: Comparison of steady solutions.

---

[1] ODE45 is a MATLAB algorithm based on an explicit Runge-Kutta(4,5), it is a one-step solver which needs only the solution at the preceding time point.

From a visual analysis, the finite difference approach appears clearly more accurate. For both solvers, the convergence criterion was the mass conservation along the domain. The steady solution was reached for both solvers after 4800 iterations which corresponds to 2.4 s. In order to check the stability of the two solvers, after convergence, the simulation was let to run until 9000 iterations (4.5 s); Figure 4.2 shows the Lagrangian and the Eulerian solution after 4.5 s and highlights how the Lagrangian version tends to deviate slightly from the exact solution. In terms of real simulation time, although both methods proved able to provide a converged solution in few minutes, the Euler solver proved to be more computationally efficient (about 10% faster). The complex procedure performed in the Lagragian method to estimate the second derivative of the temperature and the treatment of the boundary conditions are in fact computational expensive.

Grid independence study Having assessed that the Euler approach is more accurate and also computationally faster, a further study was carried out for this approach in order to evaluate the dependency of the final solution on the axial discretization. Table 4.1 reports the results obtained during the grid independence investigation. The first column reports the number of axial nodes tested while the second and third column provides the maximum percentage errors[2] evaluated respectively for the axial velocity and the static temperature.

Axial nodes	Max $V_{err}[\%]$	Max $T_{err}[\%]$
200	0.058	0.032
300	0.072	0.031
600	0.077	0.031
1200	0.077	0.031

Table 4.1: Grid independence study and related maximum percentage error relative to the exact analytical solution.

As it is possible to observe from Table 4.1, for this relatively simple case-study, above 300 axial nodes, the influence of the axial discretization is negligible. On the other hand, an axial grid of 600 nodes was selected in order to be consistent in the comparison against the study carried out by Bernard and Shen [7, 66].

---

[2] For each axial element, an error relative to the exact analytical solution is calculated. The table reports the maximum relative error.

Velocity and temperature disturbances

At the beginning of this subsection, the aim of the investigation of this particular case-study was justified as the intention of reproducing the axial propagation of a disturbance caused by a sudden change in cross section. After the comparison of the Lagrangian method against the Eulerian one and their verification in respect to the exact analytical solution, this section continues reporting on the transient capabilities of the Eulerian method, which was selected as more accurate and computationally efficient.

In particular, the results reported below were obtained initializing the flow field with a previous converged solution for the simple straight duct and letting the solver run until convergence imposing a sudden change in cross section as shown above in Figure 4.1. The first set of plots represents the effect of the disturbance propagation on the velocity field through a representation of the Mach number. In the second set, the effect of the disturbance on the static temperature field can be appreciated.

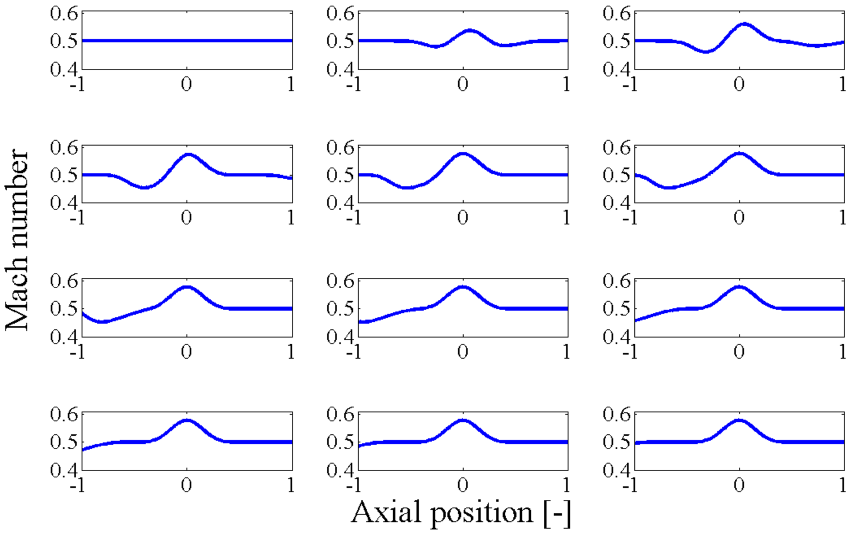

Figure 4.3: Propagation of the velocity disturbance from t=2s to t=2.4s (left to right and top to bottom).

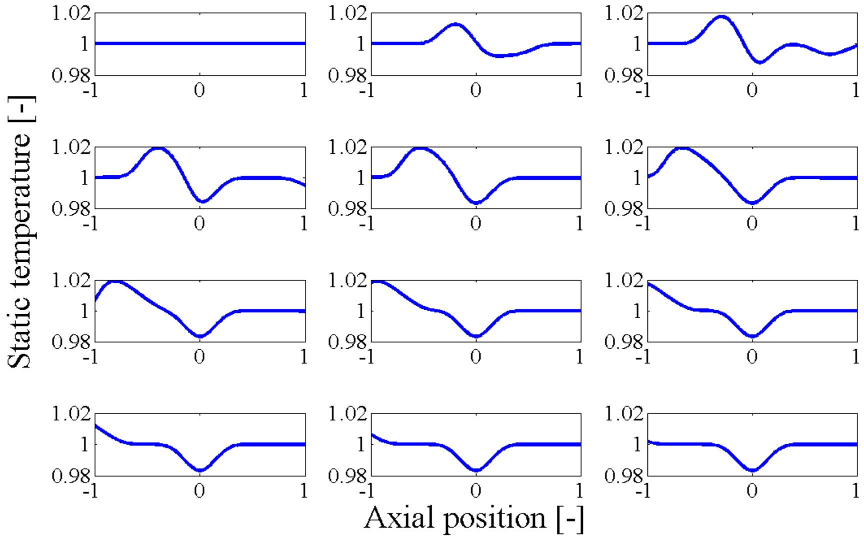

Figure 4.4: Propagation of the temperature disturbance from t=2s to t=2.4s (left to right and top to bottom).

As a second verification that the Euler approach captures the correct behavior, the results obtained by Bernard and Shen for the same case study are reported below.

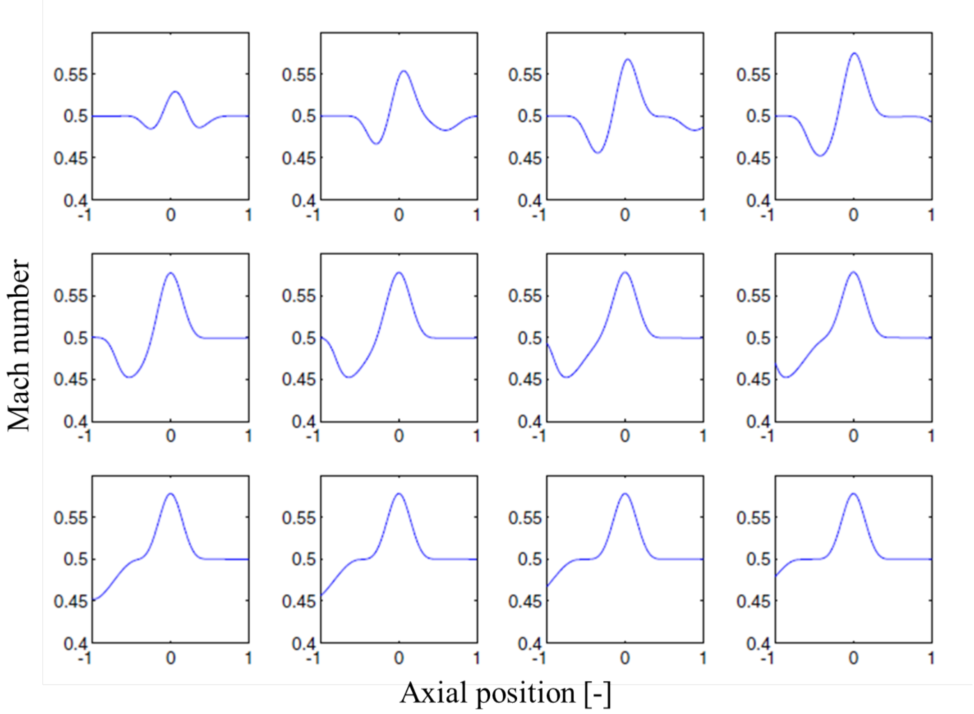

Figure 4.5: Propagation of the velocity disturbance predicted using the Lagrangian solver by Shen [66, 7].

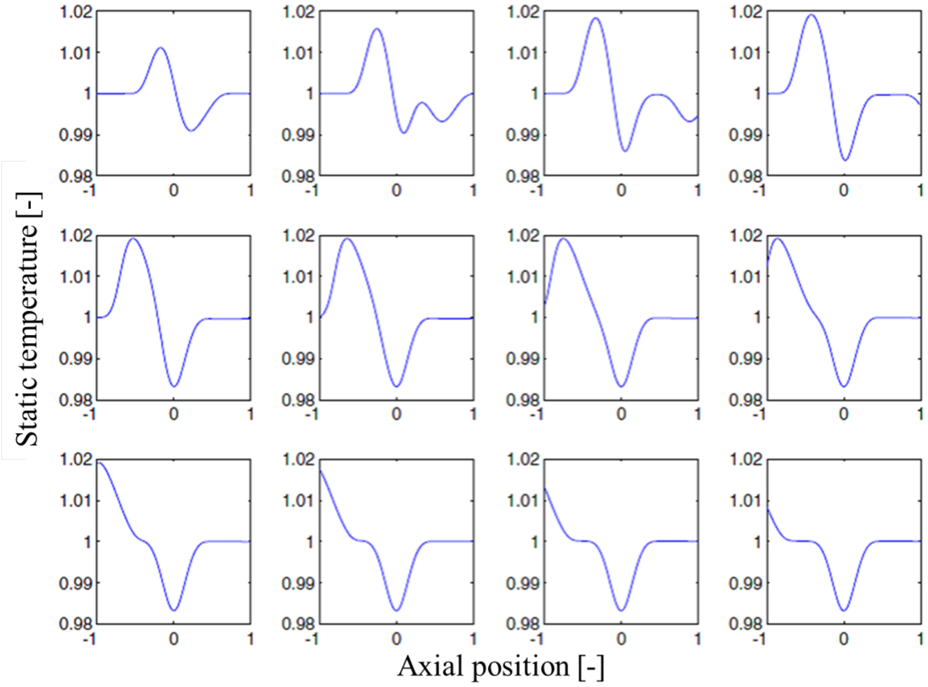

Figure 4.6: Propagation of the temperature disturbance predicted using the Lagrangian solver by Shen [66, 7].

Time wise cross section change

The solver behavior when subjected to a time-dependent cross section variation was also analyzed. The importance of this feature is related to the modeling of a nozzle with variable cross section and in particular to the modeling of a throttle which is a key element in compressor modeling. Examples of similar modeling techniques for the throttle of a compressor can be found in the work of Cherrett, Adam and Chima [14, 1, 15].

A test was performed considering a time wise sinusoidal change in the cross section as sketched out in Figure 4.7. The top graph of Figure 4.7 reports the variation in time of the cross section at half duct (A' indentation) while the bottom graph shows the axial distribution of the cross section at three different instants. The variable cross section was implemented using again equation (4.1) modifying in time the β parameter as follows:

$$\beta(t) = 0.05 sin\left(\pi\left(N_{step} - t\right)N_{step}/3\right) \tag{4.2}$$

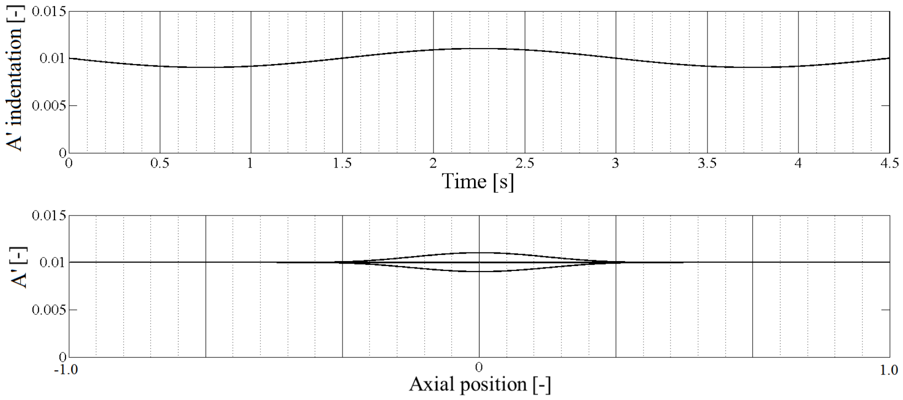

Figure 4.7: Time-wise sinusoidal cross section variation: (top graph) cross section of the middle of the duct against time, (bottom graph) axial distribution of the cross section respectively at zero, positive and negative indentation.

Figures 4.8 and 4.9 compare the propagation of the velocity disturbance produced by a sudden change against the one generated by a continuous sinusoidal change in cross section. The different colors correspond to different instants in time; as it is clear from Figure 4.9, a continuous change in cross section does not lead to a converged steady solution but only to a periodic solution.

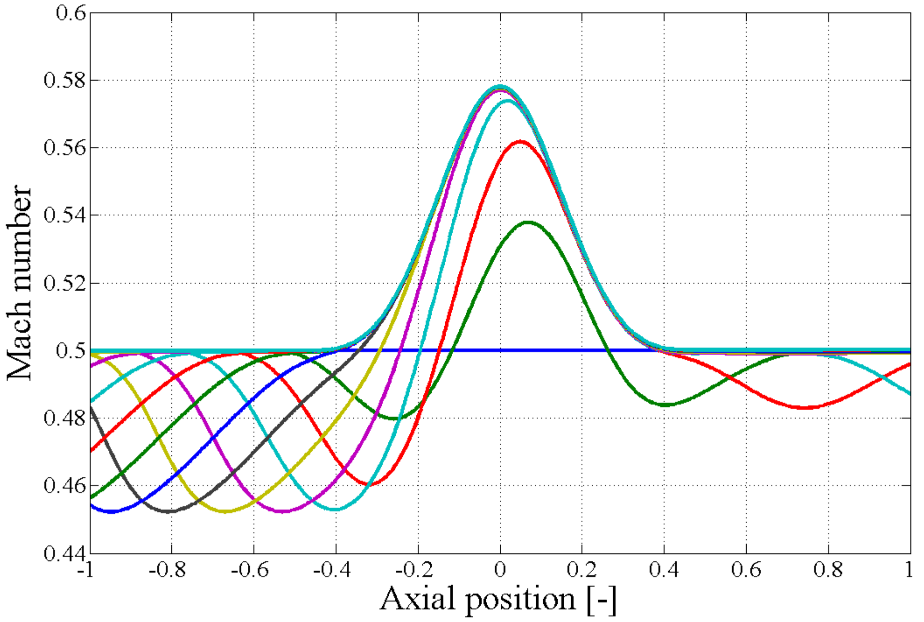

Figure 4.8: Propagation of a velocity disturbance produced by a sudden change in the cross section.

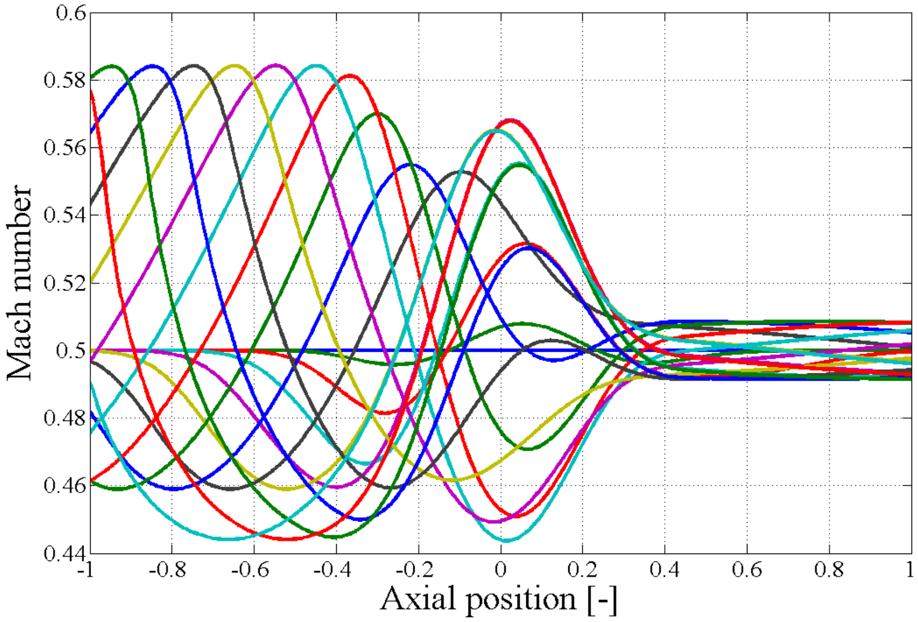

Figure 4.9: Propagation of a velocity disturbance produced by a sinusoidal time wise change in the cross section.

To conclude this section on the preliminary work carried out, the different verifications performed with the quasi-1D Euler solver proved this numerical approach suitable for this research. As a matter of fact, the author was looking for a computationally efficient and robust method of tracking transient changes in the flow field as well as time-variant changes of the flow path geometry.

4.2 Quasi-2D unsteady Euler solver

The verification of the quasi-2D unsteady Euler solver, which represents the " backbone" of FENICE-PC, was performed mainly adopting two compressors geometries: the two-stage NASA TP 1493 [76] and the four-stage low speed compressor C106 [18]. Due to the differences in the availability of the experimental data, in the current and following chapter, the compressor performance for the NASA TP 1493 is reported in terms of total pressure ratio versus equivalent mass flow while total to static pressure rise and flow coefficient are adopted for the compressor C106.

The solver's verification, reported in this section, is divided into three subsections that correspond to the three possible operating regions, forward, stalled and reverse flow. The detailed geometry of both compressors is reported in Appendix B.

4.2.1 Forward flow

The simulations in this operating region were performed adopting for both geometries the configuration CN (compressor followed by a con-di nozzle). The aim was, in fact, the tuning of the pressure loss models for this region in order to establish a good agreement between the predicted steady forward flow compressor characteristic and the experimental one.

When studying a new compressor geometry, a certain procedure should be followed; indeed the first solution has to be obtained running the solver after having initialized the flow field with a generic-user-defined flow field. The initial flow field does not need to be close to the final solution, however a good guess of the final solution will reduce the convergence time. At convergence, a check in terms of compressor performance is carried out to calibrate the pressure loss and deviation models. It is necessary to determine an initial calibrated operating point on the forward flow characteristic before running the solver changing the throttle setting to get different operating points on the same speed line. Further adjustments might be necessary after the first derivation of the curve in order to properly align the curve with the experimental one.

After the calibration, a grid independence study was carried out in order to determine the minimum number of elements necessary for an accurate solution of the flow field. The grid independence study was performed for an operating point close to the design condition for both compressors. Table 4.2 reports the results of this study. The solution was considered grid independent once it was showing an asymptotic behaviour. For all the simulations reported in this chapter a final grid of 600 and 1000 axial elements was selected respectively for the compressor NASA TP 1493 and the compressor C106. Considering Table 4.2, the four-stage low speed compressor C106 is more sensitive to the discretization than the NASA TP 1493. The explanation of the necessity of a finer grid for the compressor C106 can be found bearing in mind that this particular compressor is characterized by a straight duct, a low rotational speed and therefore low Mach number and mass flow. These features when combined with time-marching techniques, as the one adopted in this research, generate an ill-condition problem which is therefore prone to poor convergence [45].

Axial nodes	**C106**		**NASA**	
	ϕ	ψ	ϕ	ψ
600	0.5600	1.3935	0.5441	1.2549
800	0.5595	1.3653	0.5441	1.2545
1000	0.5594	1.3575	0.5441	1.2540
1500	0.5594	1.3527	0.5441	1.2539
2000	0.5593	1.3510	0.5441	1.2537
2500	0.5593	1.3510	0.5441	1.2536
3000	0.5590	1.3510	0.5441	1.2536

Table 4.2: Grid independence study for the compressor C106 and the compressor NASA TP 1493.

NASA TP 1493

The first compressor that was tested is the two-stage fan with low aspect-ratio described in the NASA TP 1493. As test-case, the 50% NRT speed line which corresponds to a rotational speed of 8035 rpm, was selected. Figure 4.10 provides a cross-sectional view of the compressor. Since this research focused mainly on the rotating stall region, the most important target during the verification of the forward flow region of the compressor map was to obtain an accurate prediction of the last stable point on the forward characteristic (point 0 in Figure 4.11). Point 0 was in fact used to initialize the solver in order to investigate the rotating stall region. For this purpose the tuning of pressure loss and deviation models was performed only for this operating point, while the remaining points were just obtained by changing the throttle settings.

Quantitatively speaking, considering again Figure 4.11, it is worth highlighting that the agreement with the experimental curve is quite good. In terms of pressure ratio, the percentage error for all the operating points predicted is below 3% and it decreases moving towards lower mass flow. In particular point 0 is predicted with a percentage error in equivalent mass flow and pressure ratio respectively of 0.3% and 0.2%. Further tuning of the pressure loss and deviation models could improve the overall matching.

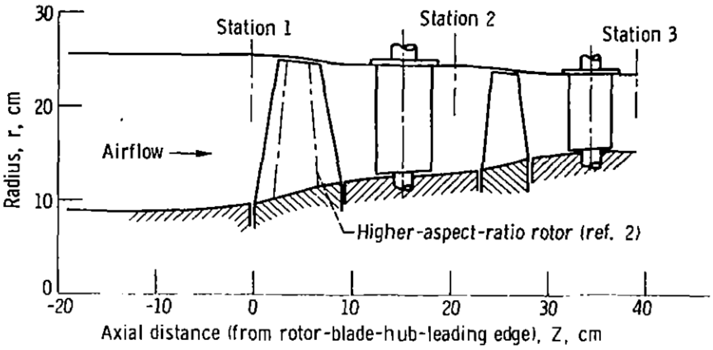

Figure 4.10: Cross section of the two/stage compressor NASA TP 1493 [76].

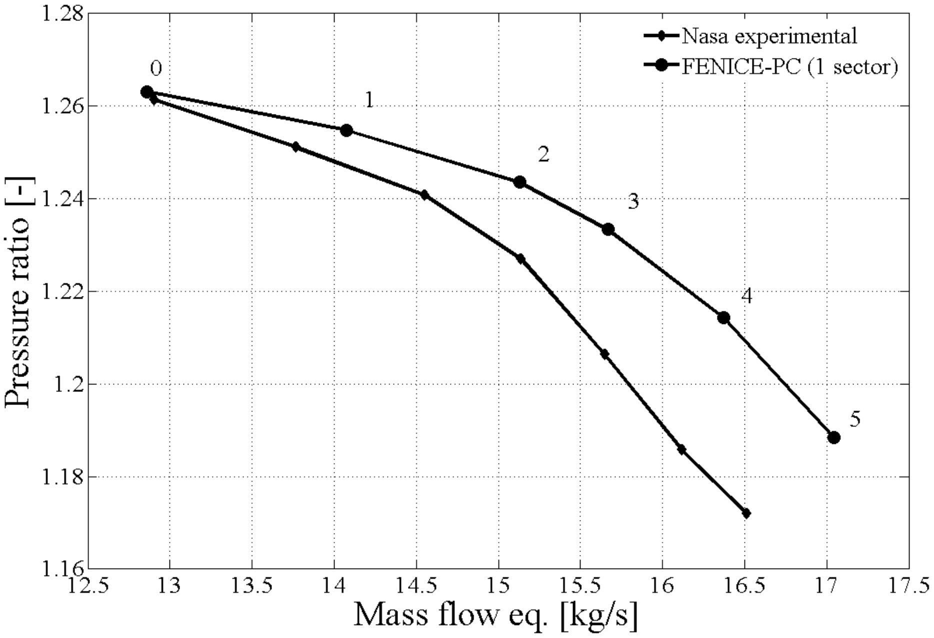

Figure 4.11: Comparison against experimental data of the predicted forward flow characteristic for the NASA TP 1493.

C106

As previously mentioned, another compressor geometry adopted during this research is the compressor C106, a four-stage compressor characterized by a straight annulus and a much lower rotational speed than the NASA TP 1493, 3000 rpm. Figure 4.12 shows a cross sectional view of the compressor.

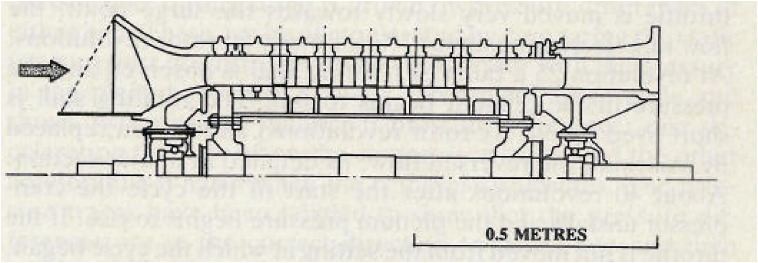

Figure 4.12: Cross sectional view of the compressor C106 [18].

In the following two sections, the focus will move to this compressor since, in the past years, several experimental investigations for what concerns the rotating stall and reverse flow regions were carried out with this compressor.

For the same reasons mentioned above, the effort during the investigation of the forward flow region was devoted to the tuning of the pressure loss and deviation models in order to predict accurately the last stable operating point. As seen previously, the tool's prediction of the forward flow characteristic is very promising. Point 0 is predicted with a percentage error in total to static pressure rise which is below 0.6%. For the other operating points, again the error is generally lower than 5%.

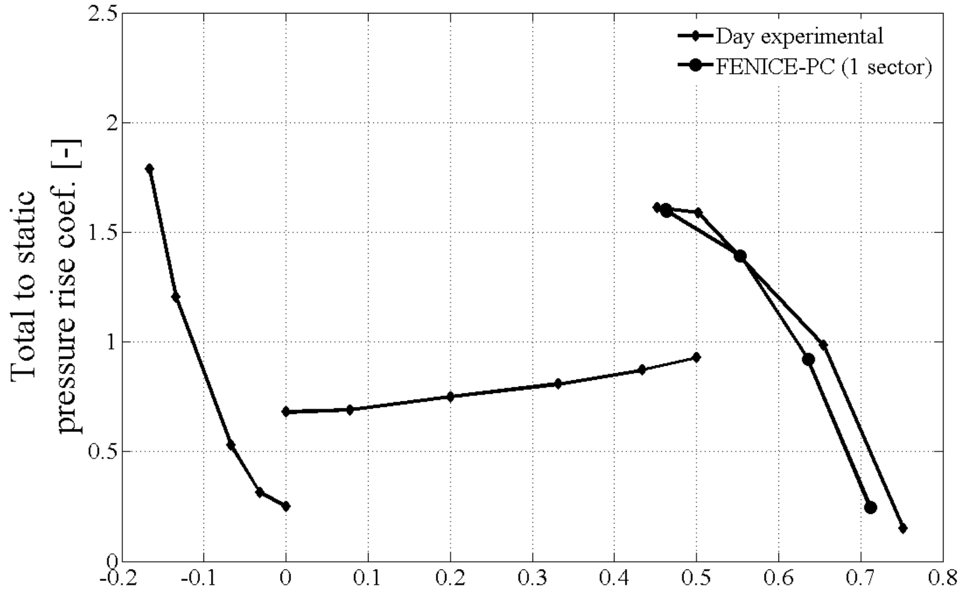

Figure 4.13: Comparison against experimental data of the predicted forward flow characteristic for the NASA TP 1493.

4.2.2 Stalled flow

The verification of the stalled flow region of the compressor map was mainly performed with the four-stage low speed compressor C106 since the complete experimental compressor characteristic was available. On the other hand, different transient and steady behavior can be observed changing the compressor geometry therefore some results obtained with the NASA TP 1493 are also reported for completeness.

4.2.2.1 Influence of the time delay constant

As explained in the methodology 3.3.2, during stall operation an important role is played by the two models adopted for pressure loss and deviation (Moses and Thomason and Tauveron) and by the time delay parameter τ which is necessary to account for the stall cell growth rate. A first investigation was performed to establish the influence of the time delay in terms of transient behavior and final steady solution.

Starting from the last stable operating point on the forward flow characteristic the compressor was pushed into an axis-symmetric stall decreasing the nozzle area (configuration CN and imposition of a 20% throttle closure). Figure 4.14 shows the transient path followed by the operating point until convergence on the experimental stalled curve for three different values of τ.

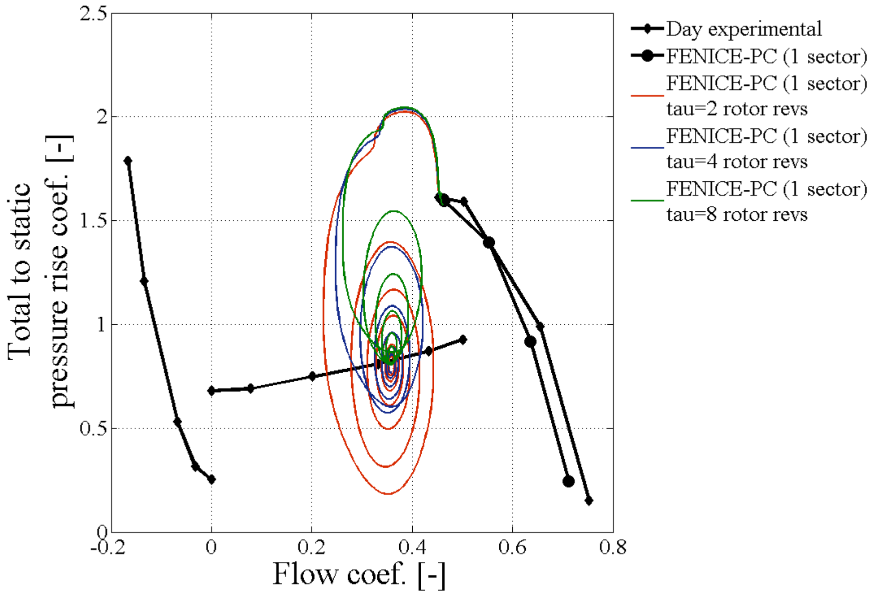

Figure 4.14: Influence of the delay parameter τ for a constant throttle setting.

The “loops” performed by the operating point before convergence are typically observed during rotating stall; examples of this transient behaviour can be found in

Paduano[57] or Gamache [28]. Regarding value assigned to the delay parameter, in the public domain several references can be found. The chosen value for this parameter is usually in a range between 2 and 3 rotor revolutions [18, 20, 19, 28, 1, 17]. On the other hand, higher values have been tested to assess its effect on the transient performance.

The first thing that can be observed is that the τ parameter only influences the transient trend whilst the final stable point in stalled condition is just governed by the throttle setting. For what concerns the initial increase in pressure rise, it is due to the configuration type adopted, the absence of the plenum chamber allows the static pressure wave produced by the reduction of the throat area to propagate upstream very quickly without any damping.

Figure 4.15 presents the same set of simulations, the total to static pressure rise is plotted against time which is expressed for convenience in rotor revolutions. From this perspective the real effect of the τ becomes clear, this parameter regulates the speed of the pressure rise drop. The τ parameter is in fact linked with the stall cell growth. A small τ parameter relates to a fast stall cell growth. A value of 2.5 rotor revolutions was adopted as suggested by Adam [1], who developed an unsteady model based on the same compressor.

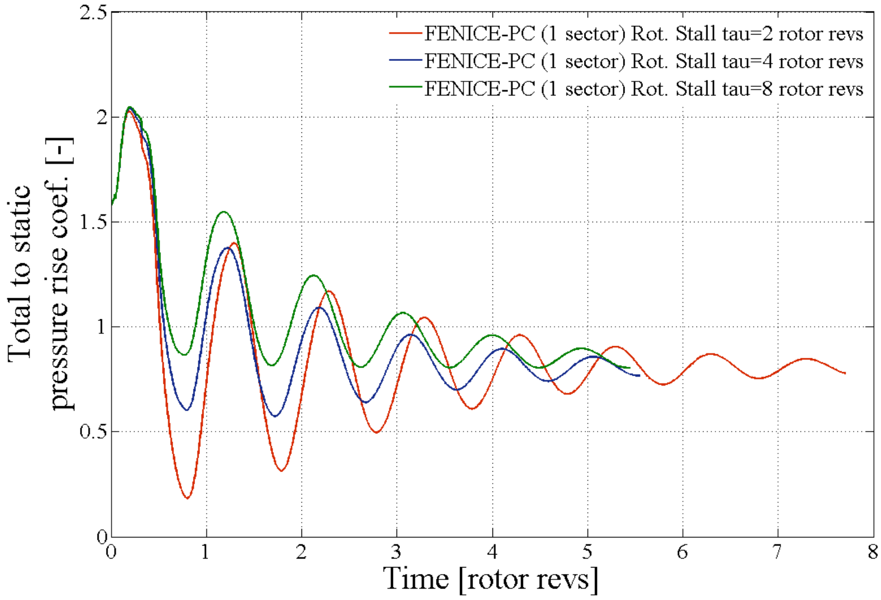

Figure 4.15: Total to static pressure rise versus rotor revolutions for different values of τ.

Similarly to the procedure adopted for the forward flow characteristic, the compressor map in rotating stall can be obtained imposing different throttle settings. The next figure is a collection of consecutive simulations obtained from the previous converged solution closing and opening the throttle.

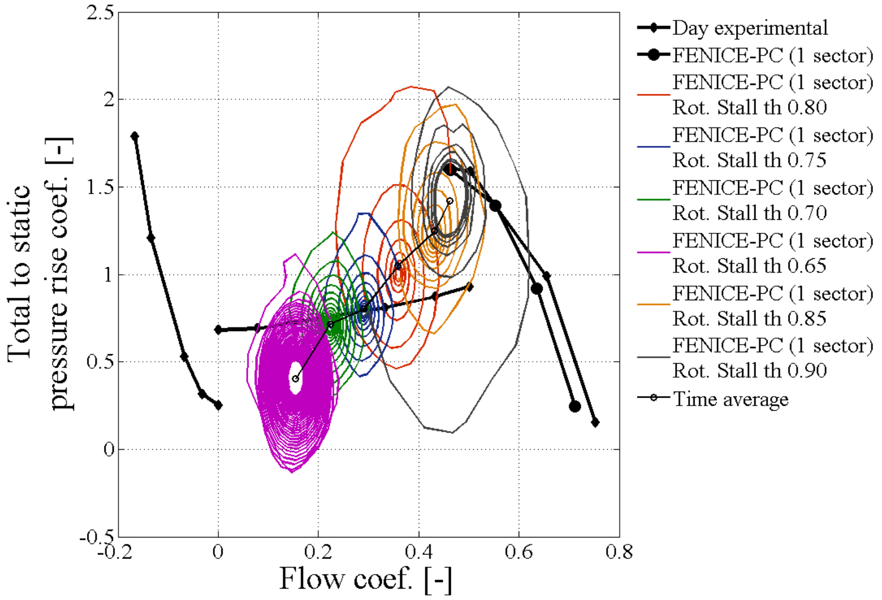

Figure 4.16: FENICE-PC (1 sector) prediction of the axis-symmetric rotating stall characteristic.

The compressor rotating stall characteristic obtained from these simulations appeared to be on a diagonal line, as it basically represents operation on a throttle line with axis-symmetric stall. In order to predict a more realistic rotating stall curve, it was necessary to force the compressor into an asymmetric stall which means growth of asymmetric instabilities that can propagate circumferentially around the annulus. This was achieved by later work and is reported in Chapter 5.

4.2.3 Reverse flow

The reverse flow regime is an extreme condition during which the compressor discharges air from the inlet, the losses are much higher compared to those commonly encountered in stalled or forward flow conditions. Very little experimental data can be found in the public domain; the cost and difficulties involved in carrying out experimental investigations in this extreme condition is prohibitive. However a considerable amount of work on this topic was carried out and published by Gamache [28] who reported some useful information about the overall performance characteristic and stage by stage flow properties of a compressor in reverse flow.

At Cranfield University, during the last few years, a lot of effort was devoted to model this particular flow regime using 3D CFD since it was found that the common 2D analytical models, such as the one developed by Koff and Greitzer [41], are unable to capture important radial flow and compressibility effects. A stage stacking technique enhanced with correlations derived from the 3D CFD simulations was found to be very effective in providing a good prediction of the reverse flow condition (see the work of Soria [70]).

The tool developed within this research, as previously mentioned, relies on Longley's model to predict the pressure loss during reverse flow. A future substitution of the Longley's model with the one developed at Cranfield [70] is envisaged since this could drastically improve the tool's prediction capabilities in this region.

Initially, to verify the correct implementation of the reverse flow regime, several simulations were run in steady reverse flow adopting the geometry of the four-stage C106 compressor. This choice was again related to the availability of the complete compressor map from experimental observation.

In order to run the compressor geometry in reverse flow, the boundary conditions of inlet and outlet had to be reversed: static pressure was applied at inlet while total pressure, total temperature and flow direction were applied at the outlet. For this specific task the configuration C (compressor only) was used.

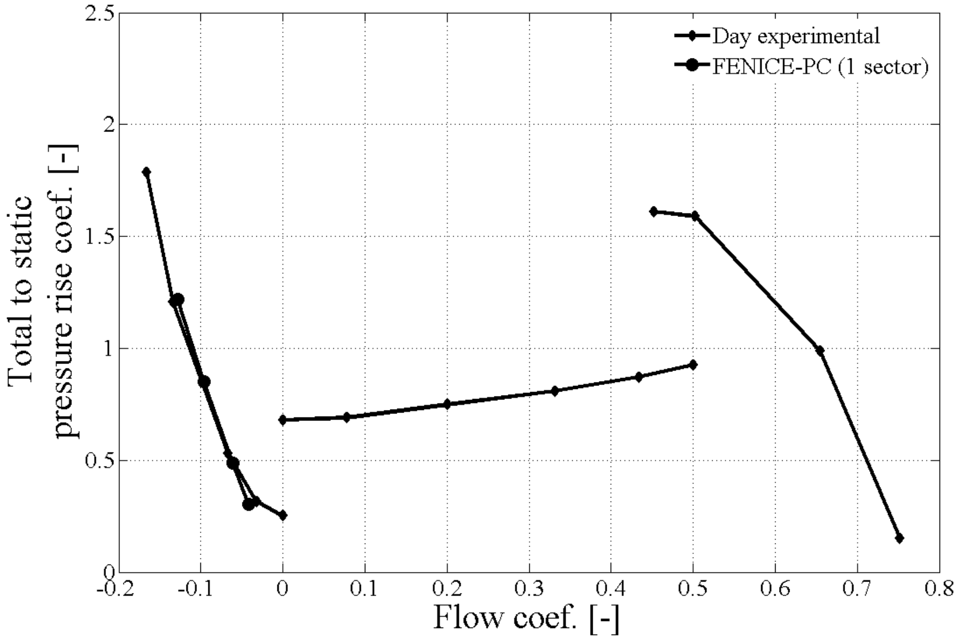

Figure 4.17: Comparison between the reverse flow characteristic predict by the Euler solver against the experimental one.

Convergence in this flow regime proved to be very difficult and some considerable tuning of the pressure loss and deviation model was required. On the other hand, the final agreement achieved with the experimental data was considered more than acceptable being within a 5% error.

4.2.3.1 Influence of the plenum size

In the introduction the differences between rotating stall, classic and deep surge were extensively described. An investigation in this context was performed and linked to the well-known Greitzer's parameter. The B parameter is basically the ratio of the stored energy over the inertia and it is directly linked with the plenum volume as described in section 2.4.2 by the equation (2.10).

For all the results presented in this subsection, until the end of this section, the configuration C with plenum and nozzle modeled as boundary conditions (see section 3.2.2) was adopted in order to save computational time. Figure 4.18 sketches out the configuration adopted and the concept behind this campaign.

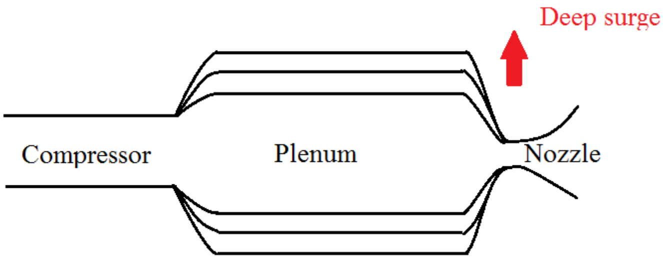

Figure 4.18: Sketch of the adopted configuration.

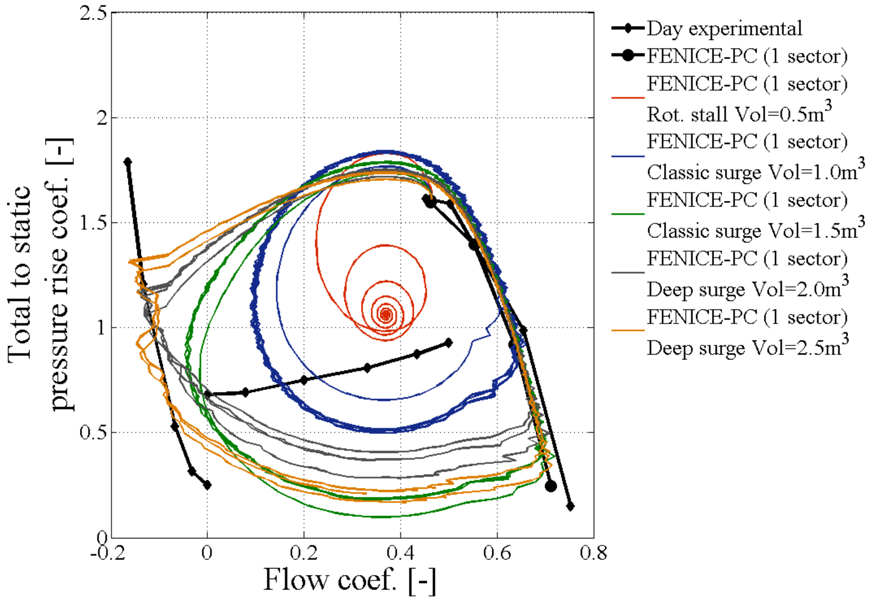

Figure 4.19: Influence of the plenum size beyond the surge line.

Figure 4.19 shows the transient performance obtained starting from the last stable point on the forward flow characteristic and imposing a 20% reduction in throttle area. The three different transient behaviors are due to the effect of the plenum volume. The simulations were in fact run for five different plenum sizes: 0.5 m^3, 1.0 m^3, 1.5 m^3, 2.0 m^3 and 2.5 m^3. As it was expected, increasing the plenum volume, the transient phenomenon changes from rotating stall to classic surge and finally deep surge for the bigger volume. From a different perspective, considering Figure 4.20 which shows the total to static pressure rise versus rotor revolutions, it is worth highlighting how the oscillation frequency decreases going from rotating stall to deep surge.

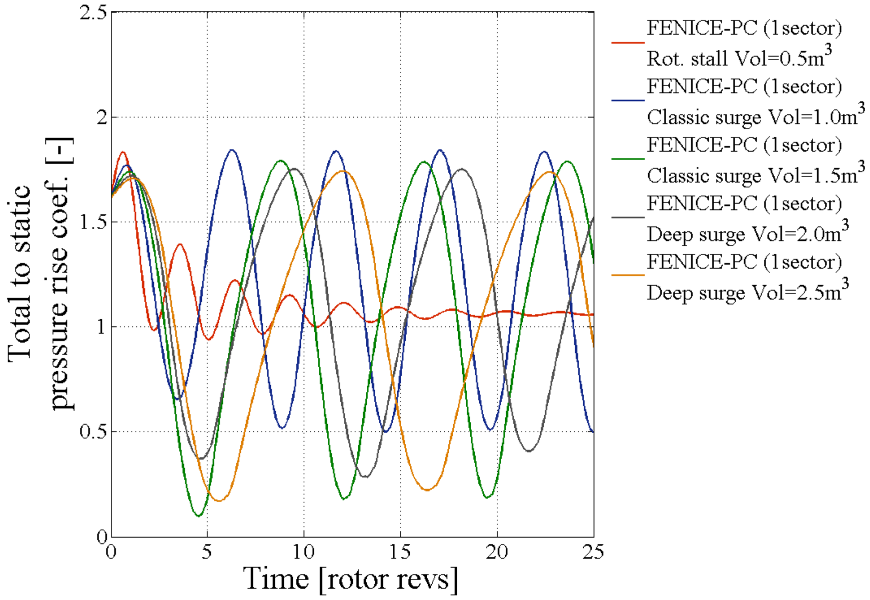

Figure 4.20: Plenum size effect on the frequency of oscillation: from rotating stall to deep surge.

4.2.3.2 Influence of the stall inception model

The same case-studies reported for the plenum investigation were performed changing the stall inception model. As reported in 3.3.2, the user can choose between three possible stall inception models. The flow coefficient approach which was used to obtained the results reported up to this point requires the a priori knowledge of the forward flow characteristic. The verification reported in this section was carried out in order to assess that more physically based models such as the Aungier criterion based on the diffusion factor and the Bloch and O'Brien's correlation provide similar predictions of the transient performance. The collection of graphs that follows, highlights the major differences in transient trends obtained choosing among the three possible stall detection techniques.

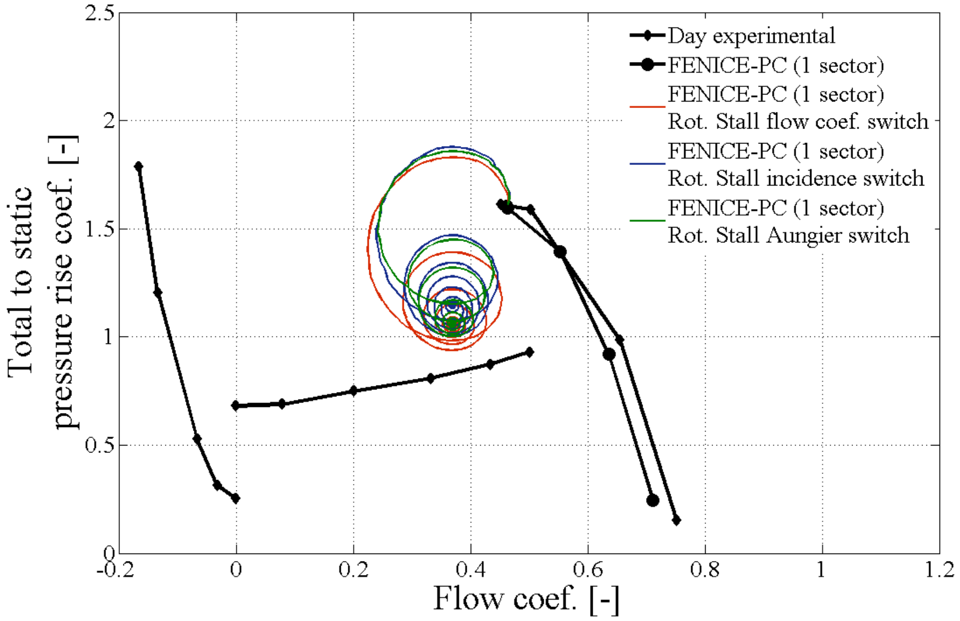

Figure 4.21: Comparison of the three blade stall inception models for a plenum volume of 0.5 $m^3$and a throttle closure of 20%.

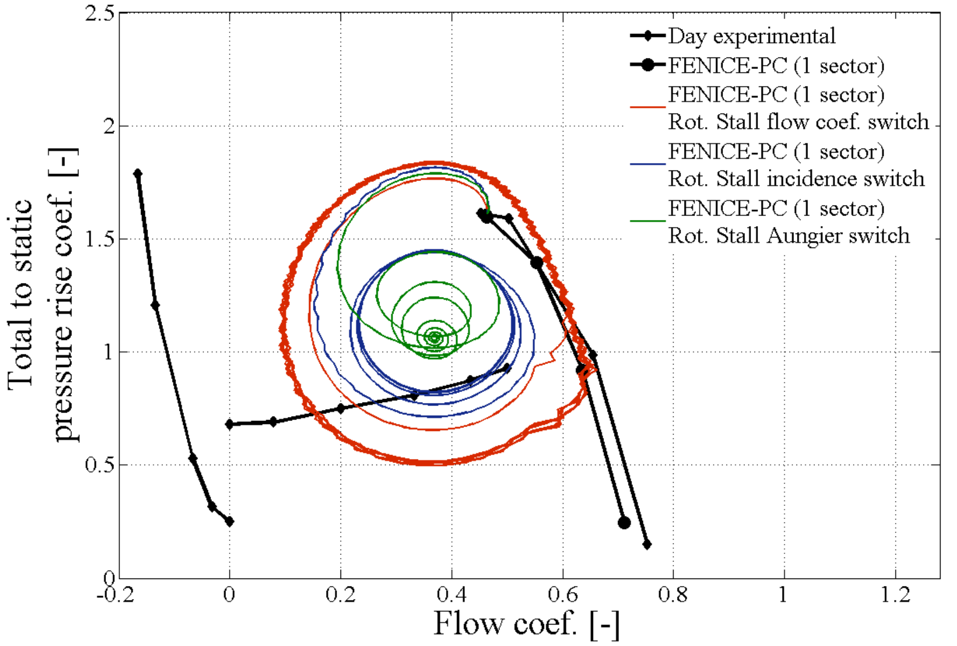

Figure 4.22: Comparison of the three blade stall inception models for a plenum volume of 1.0 m^3 and a throttle closure of 20%.

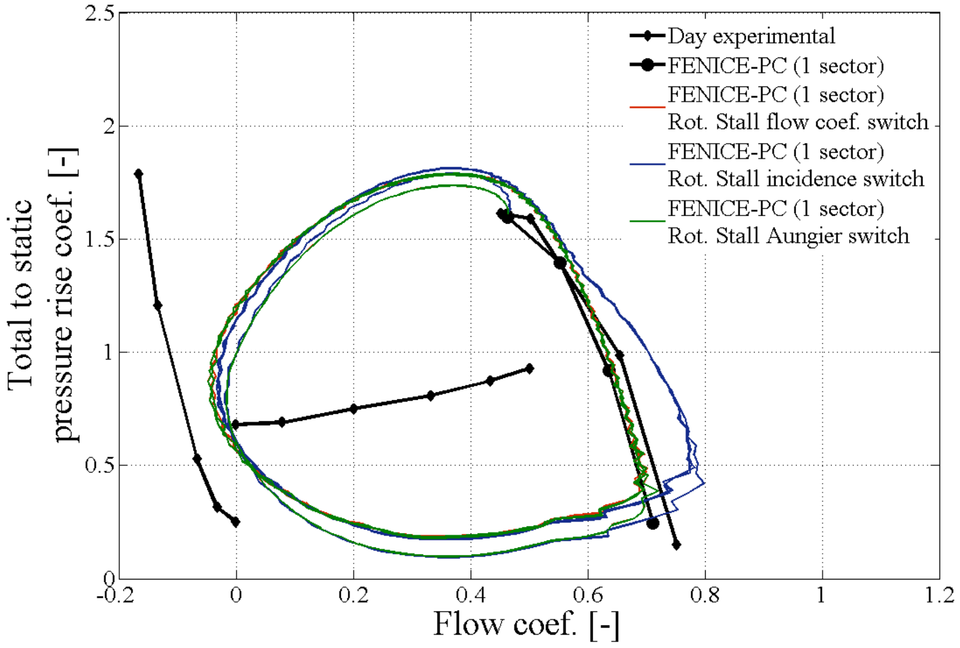

Figure 4.23: Comparison of the three blade stall inception models for a plenum volume of 1.5 m^3 and a throttle closure of 20%.

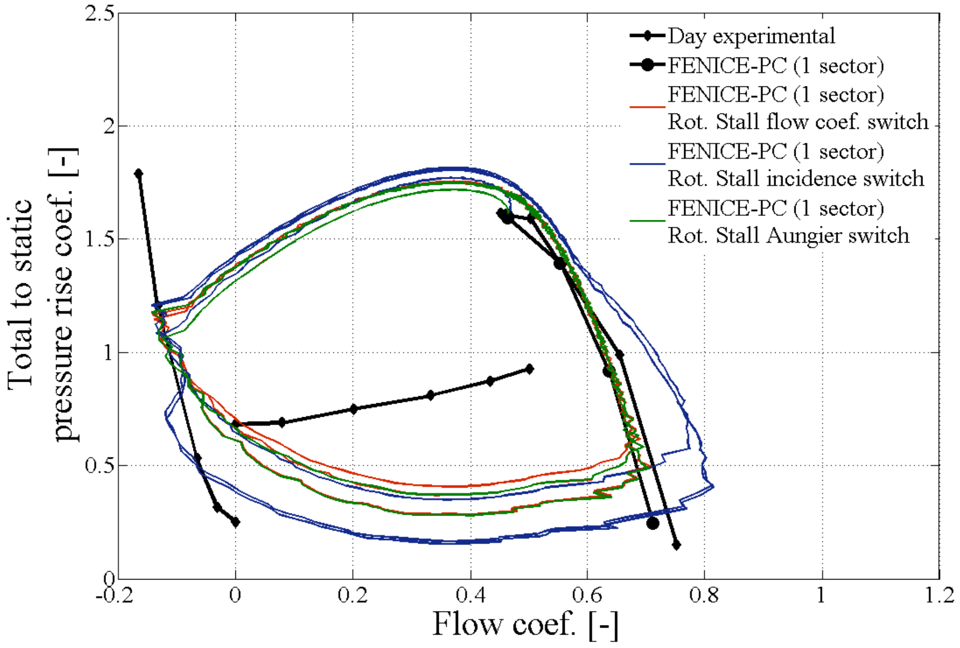

Figure 4.24: Comparison of the three blade stall inception models for a plenum volume of 2.0 m^3 and a throttle closure of 20%.

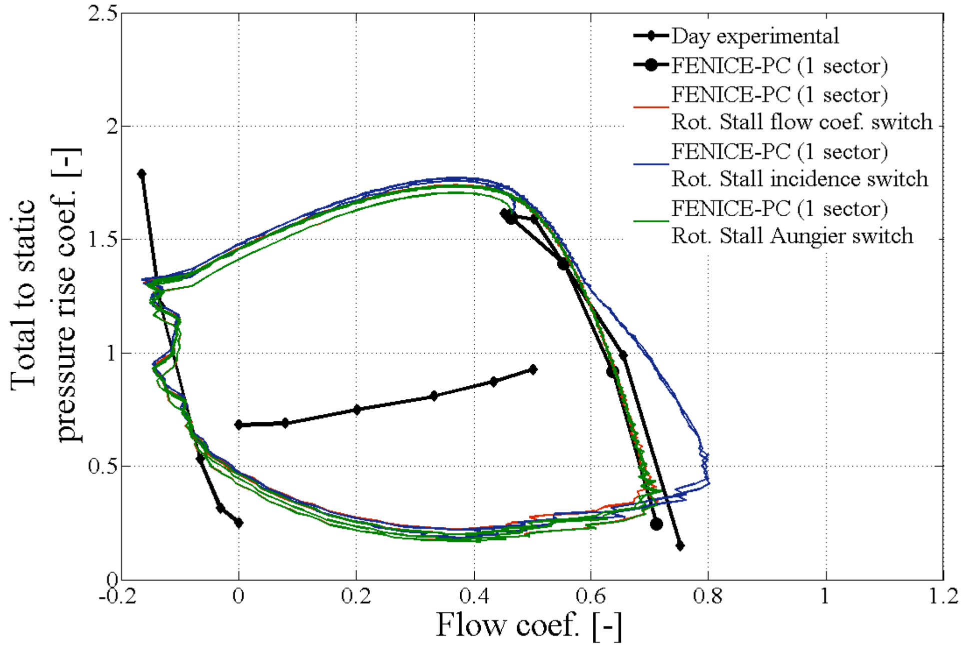

Figure 4.25: Comparison of the three blade stall inception models for a plenum volume of 2.5 m^3 and a throttle closure of 20%.

Analyzing the graphs included above, it becomes clear that the three models do not provide the same transient behavior; the same answer can be obtained only in terms of a time-average compressor performance. For the rotating stall case the final stable condition in “locked-in” stall is just governed by the throttle setting. It is interesting to note that for a plenum volume of 1.0 m^3, only the flow coefficient switch predicts a classic surge trend while for the incidence and Aungier switches the compressor exhibits the typical rotating stall behavior.

For the cases with larger plenum volumes, the major difference was observed for the case with the incidence switch. Considering Figures 4.23 and 4.25, it is clear how in these three cases the operating point during its transient trajectory, overshoots the forward flow characteristic in the recovery part. A possible explanation for this behavior might be related to the fact that the application of the time delay in the recovery region is determined only by the average flow coefficient (see 3.3.2).

For completeness, the same analysis was performed for the compressor NASA TP 1493 [76]. The simulations were performed initializing the flow field with the solution obtained for the last stable point on the forward flow characteristic. The same range of plenum volumes was tested, from 0.5 m^3 to 2.5 m^3 and the compressor was pushed towards the stalled condition imposing a 20% reduction in throttle area. The stall inception switch used for all these simulations was the flow coefficient. Figure 4.26 shows the transient performance of the compressor, as expected, the behavior is close to the one previously obtained with the compressor C106.

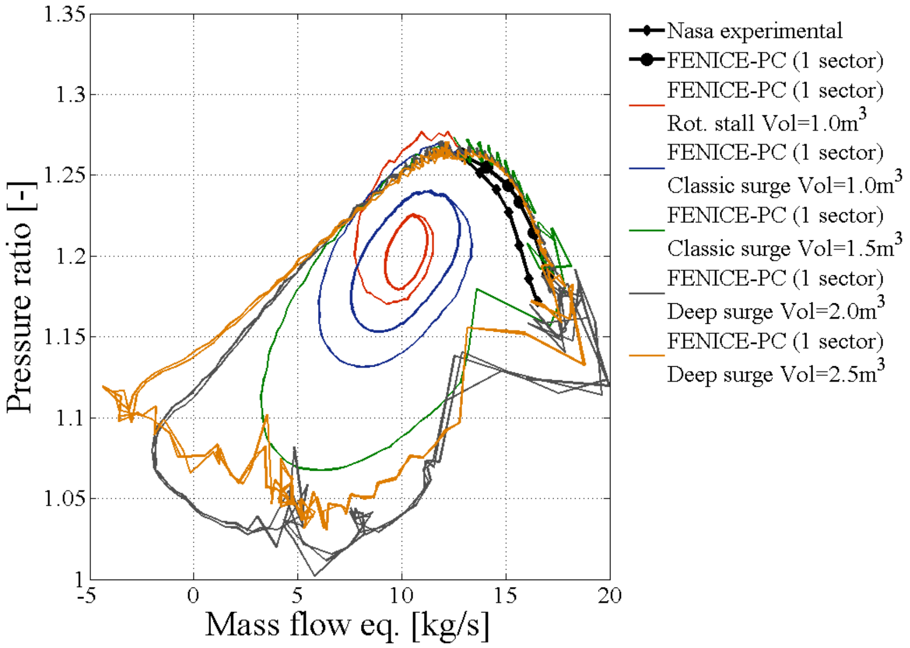

Figure 4.26: Plenum size investigation for the NASA TP 1493 compressor.

4.3 Quasi-2D unsteady Euler + 'parallel compressors' (FENICE-PC)

The motivation that led to the choice of applying the quasi-2D unsteady Euler solver together with the 'parallel compressors' approach was the requisite of developing a tool able to tackle asymmetric phenomena, as broadly explained in Section §3.4. This section describes the verification of the quasi-2D solver carried out after the extension to the circumferential direction (i.e. FENICE-PC). A first verification was performed assessing the tool's ability to tackle inlet flow distortion, more in detail, the tool was tested with different distorted inlet conditions to check if the expected trends were obtained. The objectives of this section along with the following remaining sections of this chapter were:

- Implementation check (boundary conditions, mass redistribution and circumferential discretization);
- Verification of the tool's ability to deal with asymmetric phenomena;
- Assessment of the rotating stall phenomena.

To run the first two sets of simulations, the tool was set up with configuration C; each simulation was run initializing the solver with a previously converged solution on the forward flow characteristic and imposing a certain stationary inlet distortion until convergence. All the results reported in this section, with exception of those simulations where information on the circumferential number of sectors is provided, were obtained adopting a very coarse grid of only 4 sectors with equal circumferential extent, the purpose was in fact the checking of the correct behavior of the solver and not the accurate prediction of the compressor performance.

Total pressure distortion

NASA TP 1493 50% NRT

As a first verification, the solver was run adopting the original 'parallel compressors' approach (without cross flow between sectors); the first two graphs below show the effect of a 5% and 2.5% inlet total pressure drop that covers half the annulus for three different operating points ("initial points" in Figure 4.27).

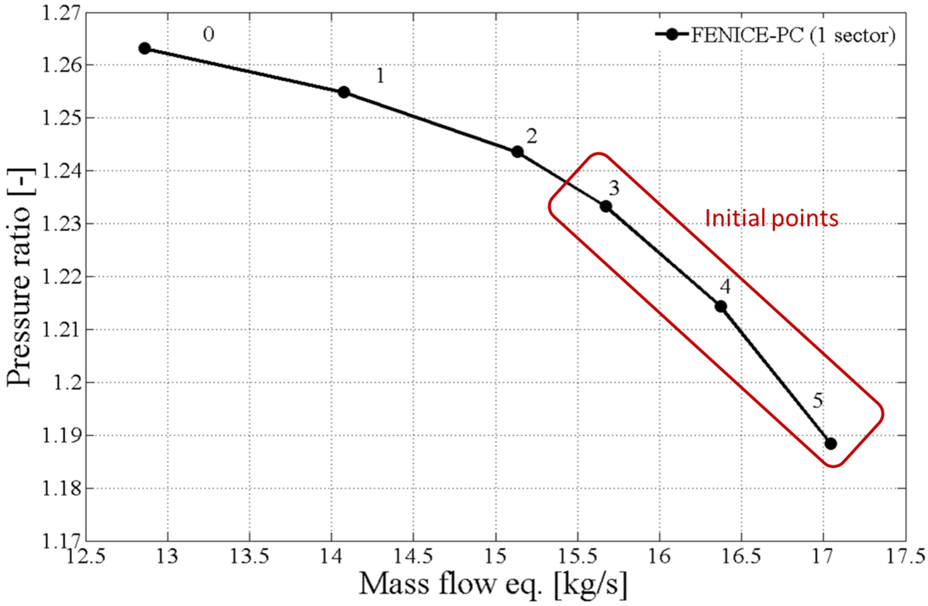

Figure 4.27: Clean operating points used as starting condition for inlet flow distortion investigations.

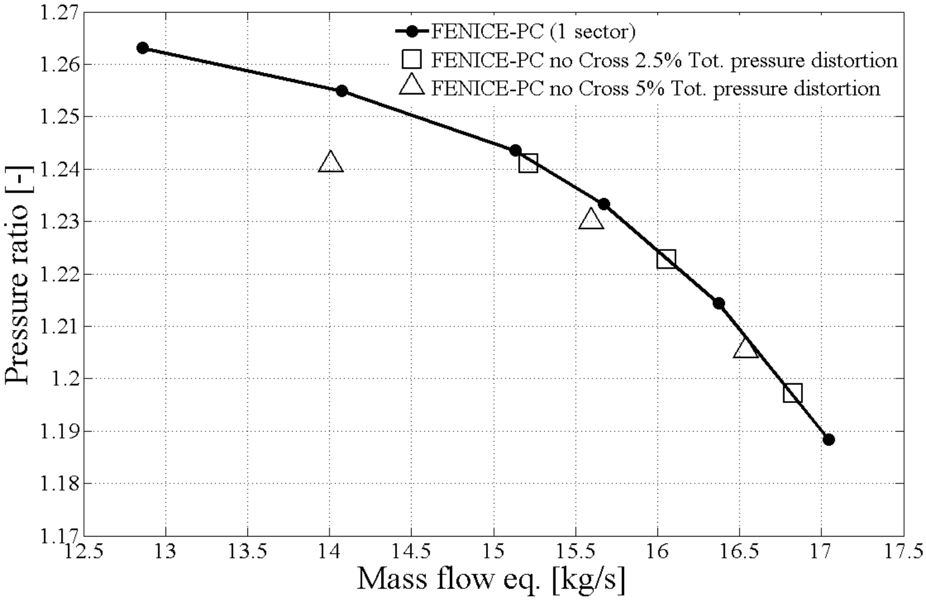

Figure 4.28: Compressor performance prediction for a total pressure drop of 2.5% and 5% imposed on half annulus adopting the original 'parallel compressors' approach.

As expected, the distortion moves the operating point towards a higher overall pressure ratio and a lower equivalent mass flow. The effect is more important in the case of a larger distortion. As stated in the methodology section, one of the basic assumptions behind the 'parallel compressors' technique is that all the "parallel sectors" operate at the same rotational speed discharging to the same plenum which means the same exit static pressure is applied to all the sectors.

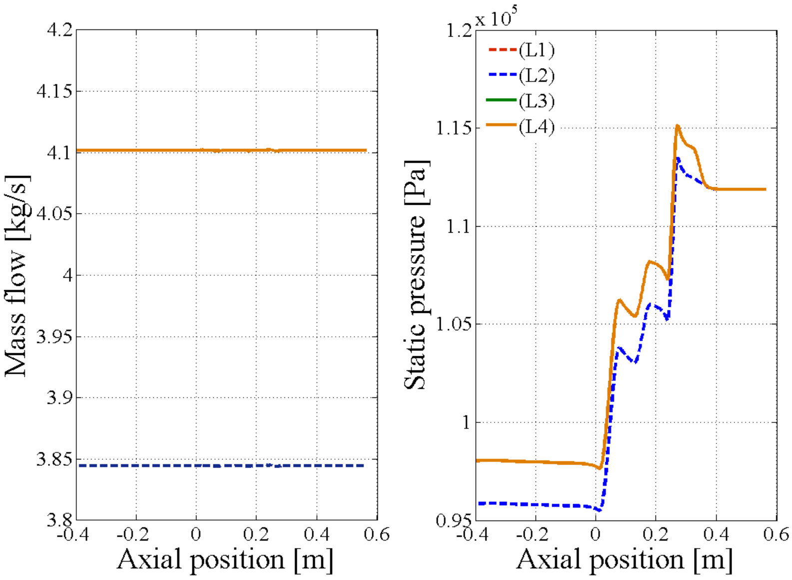

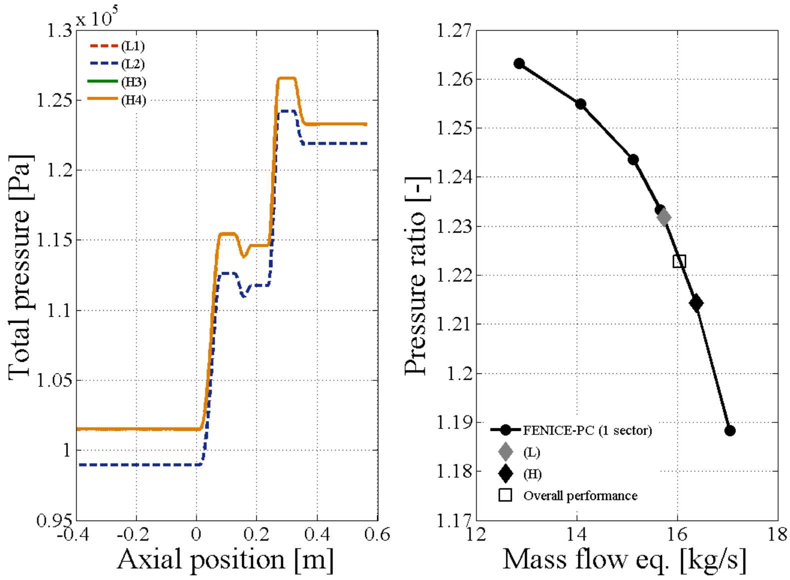

Figure 4.29: Flow properties along the compressor obtained with the original 'parallel compressors' approach for the case of inlet total pressure drop of 2.5%.

The different operation of the clean (H) and distorted (L) sectors can be better visualized through the flow properties along the axial direction; mass flow, static pressure and total pressure as shown in Figure 4.29. Besides, Figure 4.29 shows the compressor performance of the two 'parallel compressors' together with the overall operating point that is obtained from a mass flow average.

Analyzing the graphs from left to right and from top to bottom of Figure 4.29, it is clear how the two halves of the compressor, operate at two distinct mass flows which are determined by the two different values of inlet total pressure. The imposition of a unique static pressure and therefore the adaption of both halves to its value can be visualized from the third graph which highlights how the two static pressure fields overlap at the exit of the domain. Regarding the overall performance of the distorted compressor, the last plot shows the location on the compressor map of the clean half (H), of the distorted half (L) and their average. The locations on the map of the clean and distorted compressors halves, are determined considering the compressor as operating subjected to a full annulus clean inlet (H) or a full annulus distorted inlet (L). The performance plot can be compared with a generic prediction of the performance of a total pressure distorted compressor (see Figure 2.14 in section 2.4.1) proving the correct implementation of the solver.

Mass redistribution

The same case-studies were then performed allowing cross flow between 'parallel compressors'. At this point it is worth to highlight the reasons behind this modification; through experimental observations and comparison with the parallel method prediction, it was found that the mass redistribution in the circumferential direction plays an important role in the assessment of the overall performance of a compressor subjected to distorted inlet conditions. Basically the standard 'parallel compressors' technique tends to over-predict the loss in surge margin [74].

As a first attempt the cross flow was allowed only in the rotor-stator gaps (Gap Cross) as suggested by Kimzey [40]. In reality the higher redistribution, occurs in the duct before the first rotor, therefore all the cases were also run allowing mass flow exchange everywhere excluding blade components (Full Cross) [71]. For both, "Gap/Full Cross" the C_{xflow} coefficient of equation (3.104) was set equal to 1.0 (maximum flow exchange).

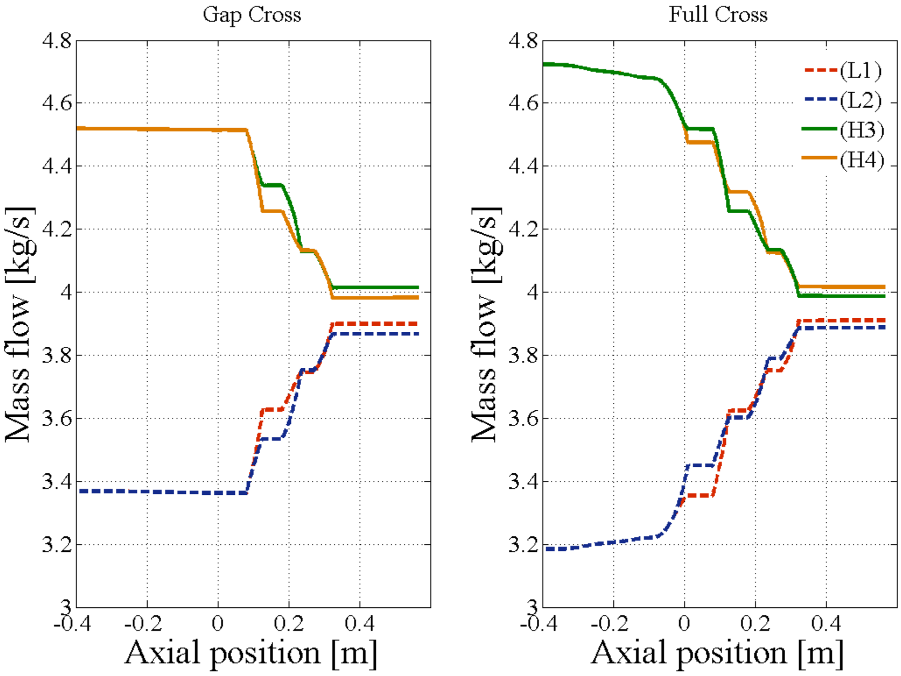

Figure 4.30: Mass flow exchanges between clean and distorted sectors. Comparison Gap and Full cross prediction for a 2.5% total pressure drop on half annulus.

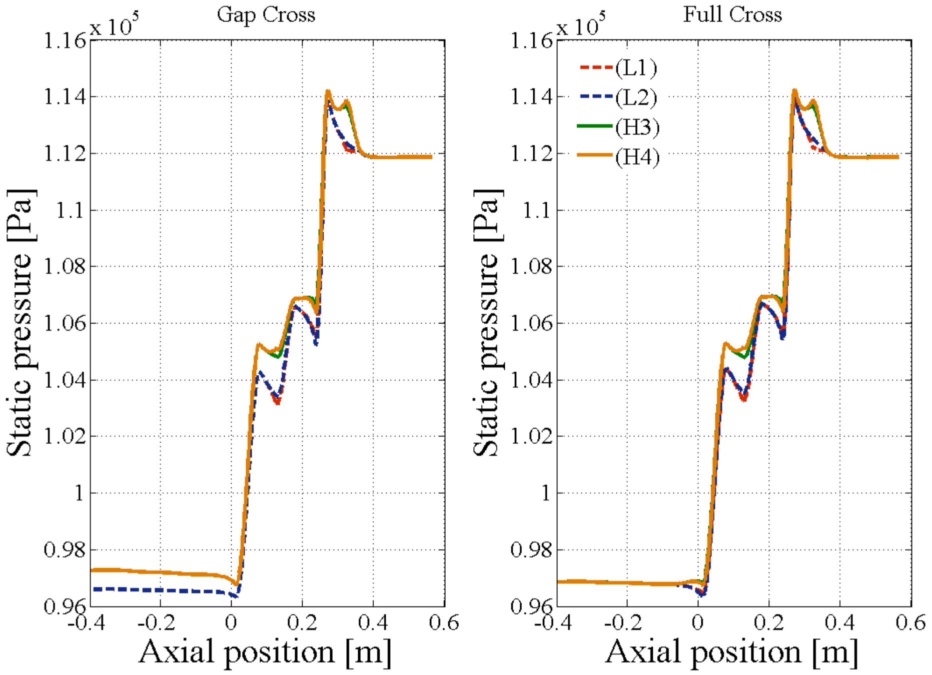

Figure 4.31: Static pressure trend along the axial direction for clean and distorted sectors. Comparison Gap and Full cross prediction for a 2.5% total pressure drop on half annulus.

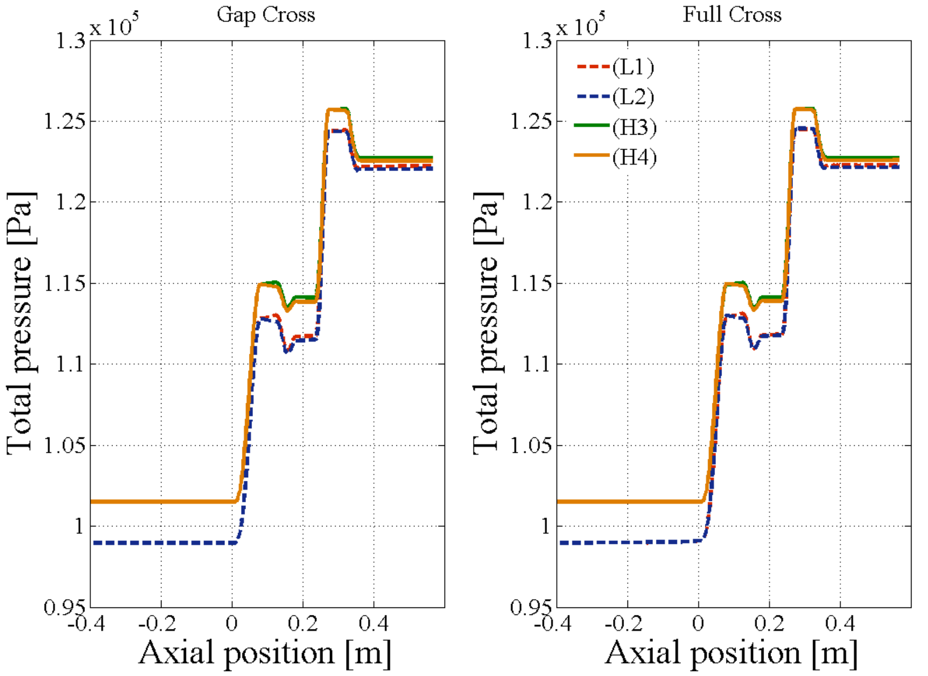

Figure 4.32: Total pressure trend along the axial direction for clean and distorted sectors. Comparison Gap and Full cross prediction for a 2.5% total pressure drop on half annulus.

The collection of graphs reported in Figures 4.30-4.32 compare the flow field obtained allowing the mass redistribution only in the rotor-stator gap, against the one obtained allowing cross flow also in the duct-components.

In both cases the distorted sectors are receiving mass flow from the clean sectors (the mass flow of the distorted sectors increases moving from inlet to outlet along the axial direction). The trends despite being similar, they highlight how the redistribution of mass flow which occurs in the duct before the first rotor is quite relevant and cannot be neglected. The major differences between Gap/Full Cross and the basic 'parallel compressors' technique with no cross flow can be observed in terms of mass flow. For what regards the other properties, the differences are less relevant. For all the sectors a uniform static pressure is still imposed as can be seen from the axial static pressure trend which shows a unique exit static pressure for all the four sectors. Besides, for this particular flow property, it is worth noting how the Full Cross predict a unique static pressure also along the inlet duct while a clear difference between distorted and clean sectors is predicted by both FENICE-PC Gap Cross and no cross. This prediction of a unique inlet static pressure is quite odd and related to the approach followed to estimate the amount of cross flow. In Section §4.5 two comparisons against 3D CFD for inlet total pressure distortion are reported showing how in reality a distorted static pressure field should be observed near the inlet of the domain. The prediction of FENICE-PC Full Cross can be improved reducing the amount of cross flow which means decreasing the C_{xflow} coefficient. Further details on this regard are provided in the following sections.

Total temperature distortion

NASA TP 1493 50%NRT

The effect of inlet total temperature distortion was also investigated following the same procedure previously presented for inlet total pressure distortion. To investigate a real scenario a higher inlet total temperature was imposed on half annulus. As previously shown for inlet total pressure distortion, Figure 4.33 shows the effect of a 2.5% and 5% increase in inlet total temperature for four different operating points. Again the trend is the one expected since it follows what is usually found through experimental observation or 3D CFD simulations [16]. Indeed, an increase in inlet total temperature moves the operating point towards lower mass flows with a decrease in pressure ratio that is proportional to the amount of distortion imposed.

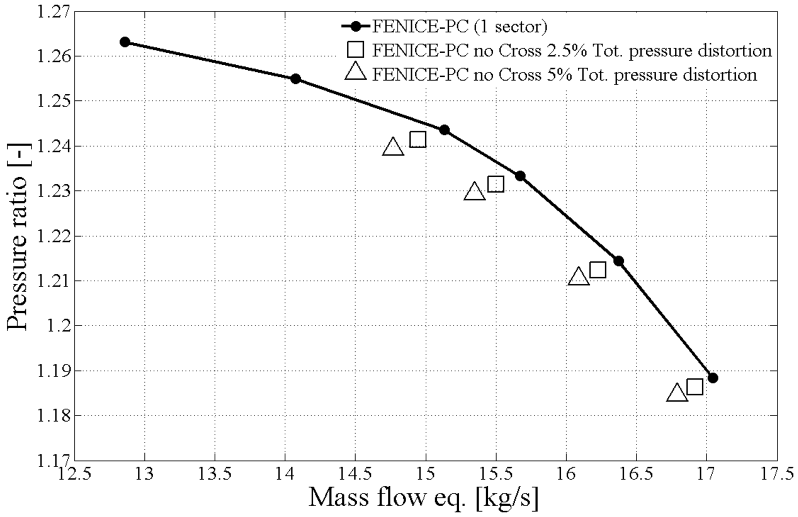

Figure 4.33: Compressor performance prediction for a total temperature increase of 2.5% and 5% on half annulus adopting the original 'parallel compressors' approach.

Mass redistribution As reported for the investigation of the total pressure distortion, the effect of the mass redistribution on the overall compressor performance was assessed allowing mass flow exchange within sectors. Both 'Gap Cross' and 'Full Cross' cases were performed for the case-study of a total temperature increase of 2.5% on half compressor.

For this case-study, it was observed that a 10% total temperature drop on half compressor produced a mass redistribution which is negligible compared to that occurring when the same deficit is applied to the total pressure. A good agreement between the predictions of FENICE-PC with and without cross flow was expected. Figure 4.34 below, compares the prediction of the overall performance obtained with the three possible set ups of FENICE-PC. The maximum difference between the three predictions in terms of mass flow and pressure ratio of the final predicted operating point is below 0.1% which is found for the operating point at the highest pressure ratio.

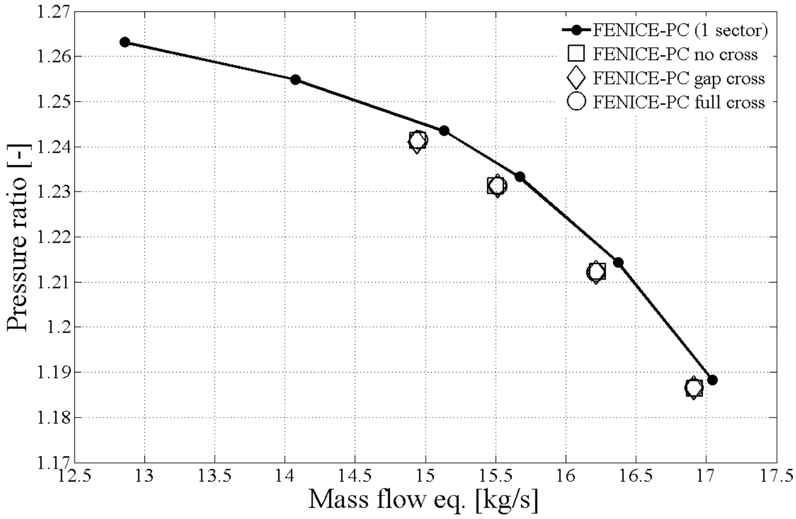

Figure 4.34: Effect of the amount of cross flow on the compressor performance.

4.4 FENICE-2D verification

Section §3.5 has provided a detailed description of the reasons behind the implementation of a 2D tool and the technical modifications involved. The following sections report the results obtained during the verification of FENICE-2D.

4.4.1 Comparison between FENICE-2D and FENICE-PC (1 sector)

In order to check the correct behavior of the solver after the upgrade in the treatment of the circumferential direction, some simulations previously run in the stalled flow region were replicated using different levels of circumferential discretization. The main purpose of this study was to check the correct modification of the main governing equations. As a matter of fact, no differences were expected between the prediction of FENICE-PC considering one compressor only (which means running the solver as a quasi-2D) and FENICE-2D since this particular investigation was performed pushing the compressor into an axis-symmetric stall. All the simulations were run starting from the last stable point on the forward flow characteristic; plenum and throttle were modeled as boundary condition, in particular for this set of simulations, a 20% throttle closure was imposed and a plenum volume of 0.5 m^3 was adopted.

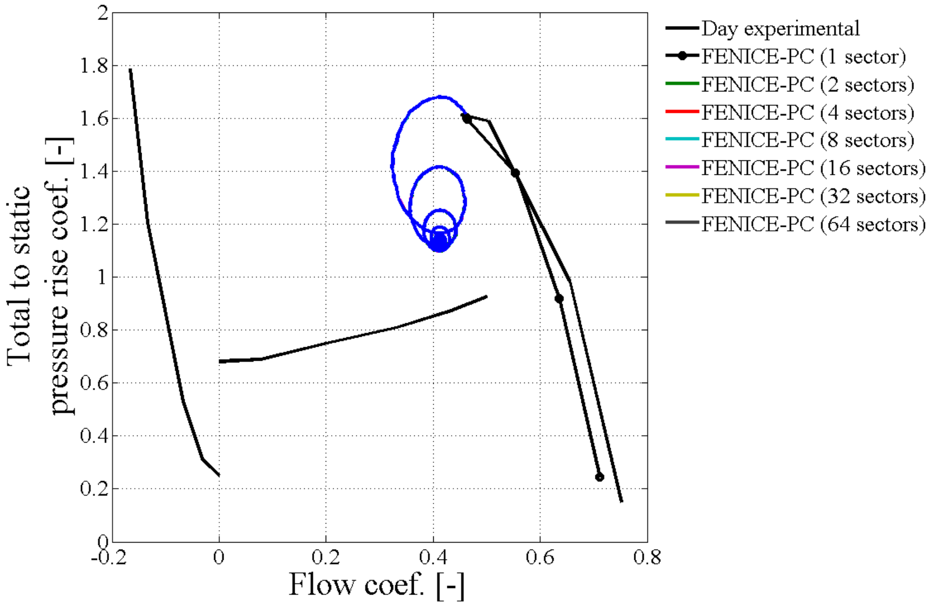

Figure 4.35: Circumferential discretization effect for an axis-symmetric stall.

Figure 4.35 compares the transient performance predicted by FENICE-PC (1 sector) and by FENICE-2D with different levels of circumferential discretization; as expected all the transient trajectories fall on top of each other. Indeed, the circumferential terms (“G” of equations (3.116)-(3.118)) cancel each other in the circumferential integration.

4.4.2 FENICE-2D and inlet distortion

The investigation presented in Section §4.2 was performed also with the 2D version of the tool in order to verify the implementation of both versions and to assess the pros and cons of both of them. For the purpose of this investigation, the results reported below are compared to those previously obtained with and without mass redistribution.

Total pressure distortion

The first comparison was performed against the original ’parallel compressors’ approach (FENICE-PC no Cross) previously reported in Section §4.2. The FENICE-2D was run considering 4 sectors and imposing a total inlet pressure drop of 2.5% on half compressor. Figure 4.36 shows the comparison in terms of compressor performance. As it is clear from the plot, the differences are negligible. The reason of this behavior is hidden in the mass redistribution effect and can be clarified considering the collection of graphs included in Figures 4.37-4.39.

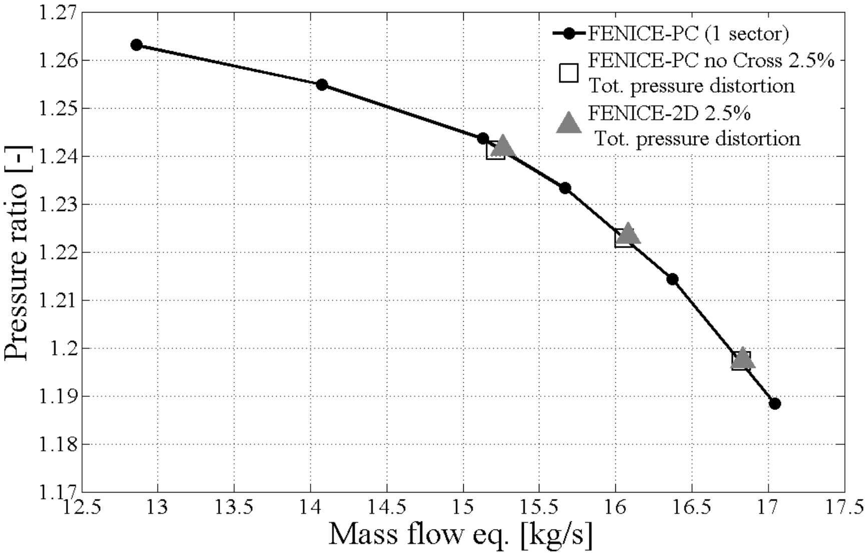

Figure 4.36: Comparison of compressor performance prediction with FENICE-PC no cross and FENICE-2D.

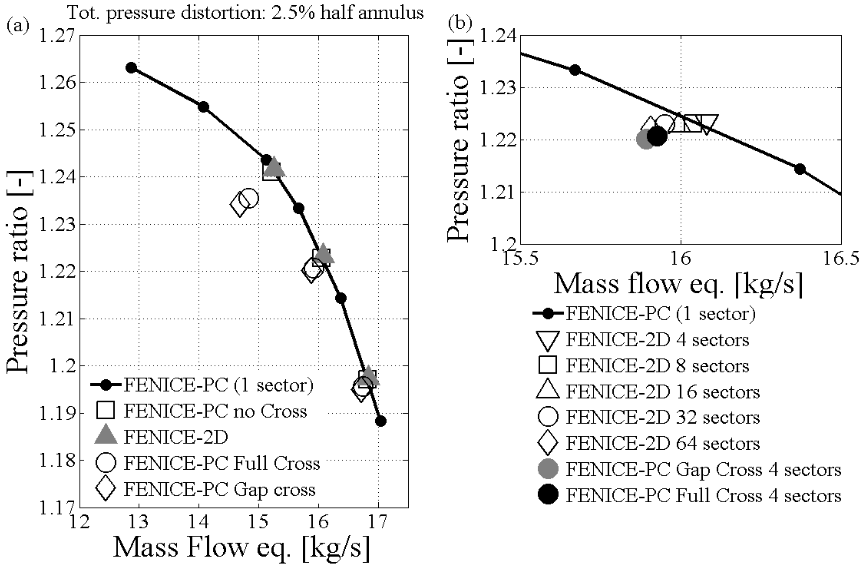

Figure 4.37: Comparison of the predictions obtained with all the different tool's set ups for the case of a 2.5% total pressure deficit on half annulus. (a) Comparison for different outlet conditions. (b) Effect of the circumferential resolution on the performance prediction of FENICE-2D.

Considering the collection of graphs from Figure 4.37 to Figure 4.39, the first two graphs of Figure 4.37 display the compressor performance. The first graph (a) shows the different predictions obtained with all the available options of the developed tool. The mass redistribution tends to move the operating points towards lower mass flows;

the second graph (b), shows a grid independence study performed to assess the influence of the circumferential discretization. This study highlighted how the FENICE-2D requires a circumferential grid of at least 32 nodes in order to achieve an amount of cross flow similar to the one occurring in the FENICE-PC with 4 circumferential sectors.

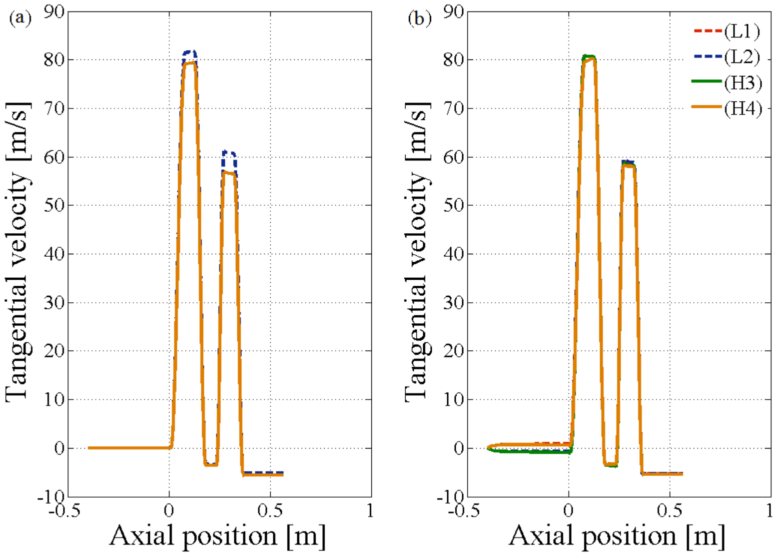

Figure 4.38: Comparison between axial trends of the tangential velocity. (a) FENICE-PC no Cross and (b) FENICE-2D.

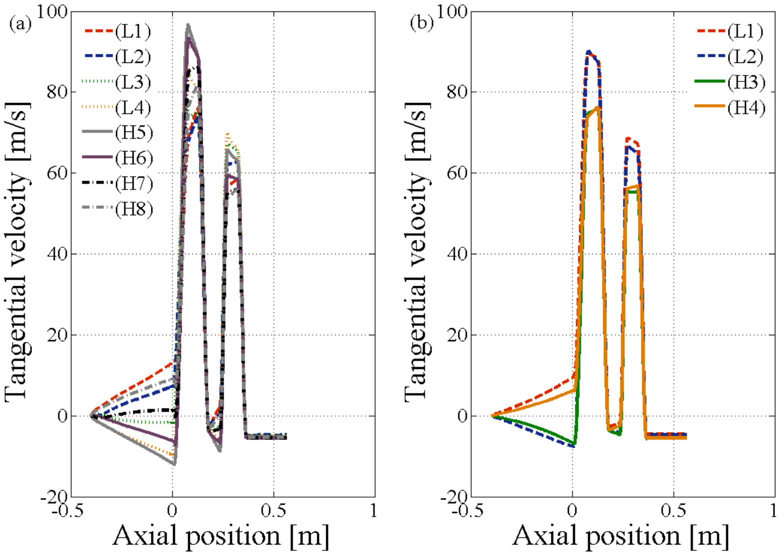

Figure 4.39: Comparison between axial trends of the tangential velocity. (a) FENICE-2D with a circumferential grid of 8 sectors, (b) FENICE-PC Full Cross with a C_{xflow} coefficient equal to 0.2.

The same conclusions can be drawn observing the flow field along the axial direction; the flow property chosen for this analysis is the tangential velocity since this property is directly linked with the mass redistribution. Both FENICE-PC and 2D were run dividing the compressor into 4 sectors and imposing a 2.5% deficit in total pressure on half annulus. Graphs (a) and (b) of Figure 4.38 show the trend of tangential velocity obtained respectively with FENICE-PC no Cross and FENICE-2D, highlighting how the mass redistribution which should be taken into account by FENICE-2D is almost absent due to the coarse grid. Graphs (a) and (b) of Figure 4.39 demonstrate how the two solvers predict very similar trends when the circumferential discretization of FENICE-2D is increased from 4 to 8 sectors and the amount of cross flow allowed between parallel sectors in FENICE-PC Full Cross is decreased. In particular, graph (a) was obtained running FENICE-PC Full Cross with a C_{xflow} coefficient reduced from 1 to 0.2 (equation (3.104)). From this analysis two key messages can be drawn. Firstly, FENICE-2D requires a minimum level of circumferential discretization to properly solve the flow filed. Indeed, a circumferential grid of 4 sectors is too coarse to account for the mass flow redistribution occurring in the circumferential direction providing a flow solution very close to that obtained with the original 'parallel compressors' technique. Secondly, in FENICE-PC the amount of cross flow can be regulated through the C_{xflow} coefficient avoiding the need of fine circumferential grids.

Total temperature distortion

In a similar manner to the analysis reported above, an investigation was performed in the case of total temperature distortion. Having already observed in the previous section that the mass redistribution does not play an important role for this type and amount of distortion, a complete agreement in terms of prediction of the overall compressor performance was expected from all the tool's set ups.

The graph of Figure 4.40 shows the compressor performance obtained with all the possible options, imposing on half compressor annulus an increase of 2.5% of inlet total temperature. Each simulation was run starting from the clean operating points on the forward characteristic highlighted before by Figure 4.28.

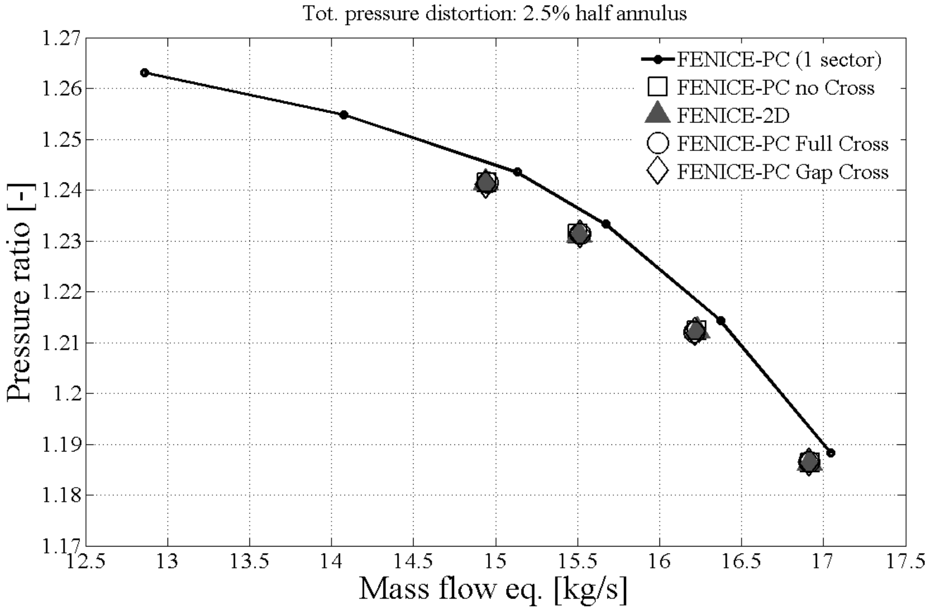

Figure 4.40: Compressor performance prediction in the case of a total temperature increase of 2.5% on half annulus.

4.5 Verification against 3D CFD models

To further verify the tool developed, the author also compared the predictions of FENICE-PC/2D against the predictions of a full 3D CFD model for two slightly different geometries: a convergent duct and the NASA rotor 37. To simulate the convergent duct, the geometry adopted was the same of the rotor 37 which is reported in 6.3 considering the component “rotor” as a simple “duct” (i.e body forces were set to zero).

Before presenting the results obtained, it is worthy clarifying how this comparison was performed and the angle used during the analysis. For both geometries, the comparison was carried out investigating cases of inlet flow distortion. The aim of this study was, in fact, the verification of the capability of FENICE-PC/2D to capture the correct circumferential trend of each flow property when dealing with asymmetric flow fields. Although experimental results for the case-studies reported in this section were not available, the comparison being performed against the commercial 3D CFD tool ANSYS CFX was considered reliable and sufficient to verify the capabilities of FENICE-PC/2D.

Convergent duct

A first comparison was carried out for the case of a convergent duct. The main purpose of this comparison was to verify the tool's implementation particularly in terms of sign conventions and the correct treatment of the reference system. The check was performed imposing a 10% total inlet pressure drop on a 90 degrees sector and comparing the circumferential trends of the flow properties at convergence. Figure 4.41 shows the 3D geometry of the convergent duct, the extent of the distorted region imposed at the inlet of the domain and the location of the plane at which the information was collected to carry out the comparison (at 20% of the axial length). Both, FENICE-PC/2D consider the flow radially uniform, therefore, from the 3D solution, the circumferential trends were extracted at mean radius.

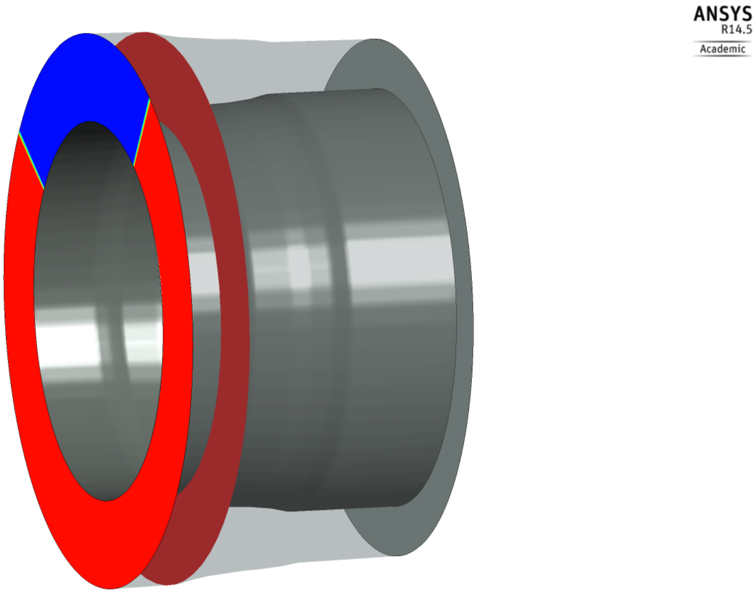

Figure 4.41: Convergent duct with total pressure distortion on a 90 degrees sector.

Since this simple case-study allows the adoption of a quite coarse grid also for the 3D model, the same axial and circumferential discretization was used for the 3D model and the FENICE-2D. Table 4.3 provides all the information regarding discretizations and boundary conditions adopted. Total inlet pressure and temperature as well as outlet static pressure are expressed as a ratio to the atmospheric conditions (101.3 kPa and 288.15 K were selected as reference values for the atmospheric pressure and temperature). The coarser circumferential discretization adopted for the FENICE-PC simulations is related to a limitation of this technique which will be clarified at the end of this subsection.

For the 3D model, only RANS simulations were carried out since the main purpose was the comparison of the final steady solution. Regarding the turbulence model, the k-epsilon model with scalable wall functions, which combines accuracy and computational efficiency, was adopted along with a second order advection scheme. The CFD results which are used in this section as a reference for the comparison, were obtained running 5 simulations; the first three simulations were required to obtain a good prediction of the clean solution while the last two simulations provided the distorted case. The set of 5 simulations was run using 64 CPUs for an overall running time of 30 min.[3].

Solver	**Axial nodes**	**Circumferential nodes**	**Radial nodes**
FENICE-PC	100	48	-
FENICE-2D	100	288	-
ANSYS CFX	100	288	50
Boundary Conditions			
α^0=0 degrees			
Clean inlet	P'^0=1	T'^0=1	
Distorted inlet	P'^0=0.9	T'^0=1	
Outlet	P'=0.87		

Table 4.3: Discretizations adopted by the different solvers and boundary conditions for the convergent duct's case study.

From a physical perspective, the distorted region is expected to receive mass flow from the clean region. This mass flow exchange induces a swirl in the flow which can be visualized through the tangential velocity. The induced swirl which is located at the interfaces between clean and distorted region provides an indication of the reference system adopted. Indeed, the induced swirl has opposite sign at the two interfaces as shown by the contour in Figure 4.42.

The first comparison which is reported, is in terms of tangential velocity. All the flow properties, henceforth, are non-dimensionalized respect to their value in clean condition. The tangential velocity being null in clean condition, is non-dimensionalized dividing each circumferential value by the value of the clean axial velocity. The capability of capturing this property is relevant since it verifies the correct implementation of the reference system and the consistency of the sign convention adopted. Figure 4.43 proves the correct implementation of the reference system, both FENICE-PC and FENICE-2D capture the correct trends; a better agreement (within 10%) is achieved by FENICE-2D pointing out a limitation of FENICE-PC which will be de-

---

[3] A proper comparison with FENICE-PC/2D is not available since FENICE-PC/2D was run on an office computer with Intel i7 2.98GHz CPU. Around 15 min were necessary for FENICE-2D to reach the converged solution. It is also worthy underlining that FENICE-PC/2D is a "work-in-progress" solver that still need to be optimized.

scribed, as previously mentioned, at the end of this subsection.

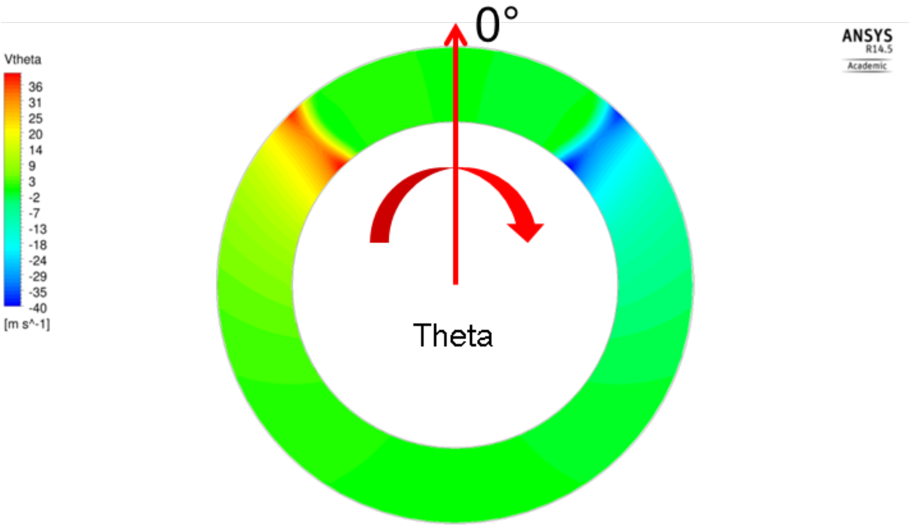

Figure 4.42: Contour of the tangential velocity obtained with ANSYS CFX.

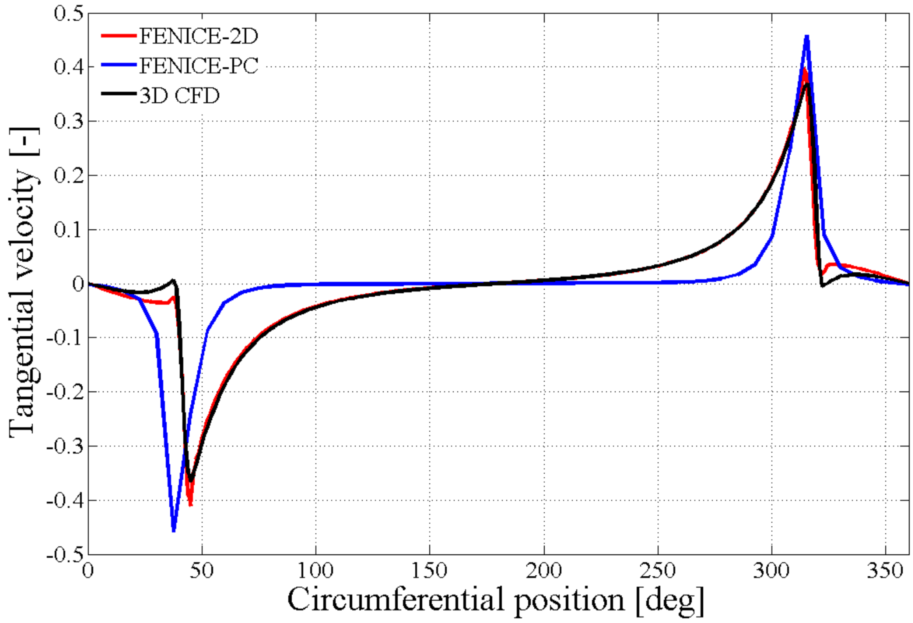

Figure 4.43: Comparison of the circumferential trends of the tangential velocity.

A second comparison is performed for the total pressure property. Figure 4.44 below reports the total pressure contour highlighting the clean and distorted region. The circumferential trend is provided in Figure 4.45 which shows that both, FENICE-PC and FENICE-2D, match properly the 3D solution; the better match obtained by FENICE-2D regarding the transition between the clean and distorted region is again related to the higher discretization of the 2D model. Considering again the transition regions, the two picks which appear for the 2D solution are purely numerical and due to the finite difference technique adopted for the spatial integration. The imposition of a smooth transition from clean to distorted region as boundary condition eliminates these numerical overshoots. The agreement for this flow property is within 1% excluding the zones of transition.

Figure 4.44: Contour of the total pressure obtained with ANSYS CFX.

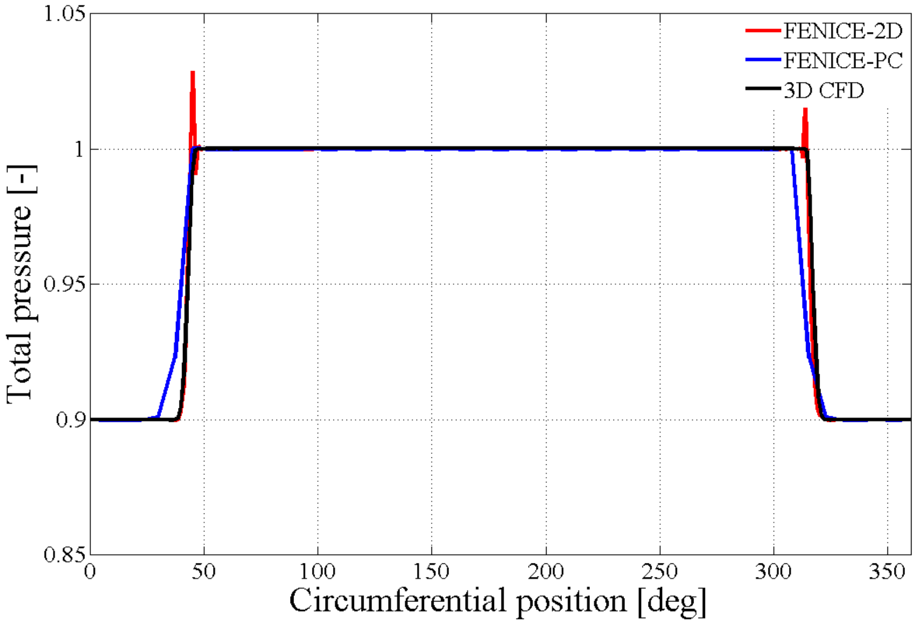

Figure 4.45: Comparison of the circumferential trend prediction of the total pressure.

The following four graphs report the comparison of the axial velocity and the static pressure circumferential trends. The contour of the axial velocity predicted by the 3D CFD is reported in Figure 4.46 while the following graph, Figure 4.47 displays the comparison of the circumferential trend of the axial velocity for all the three solvers.

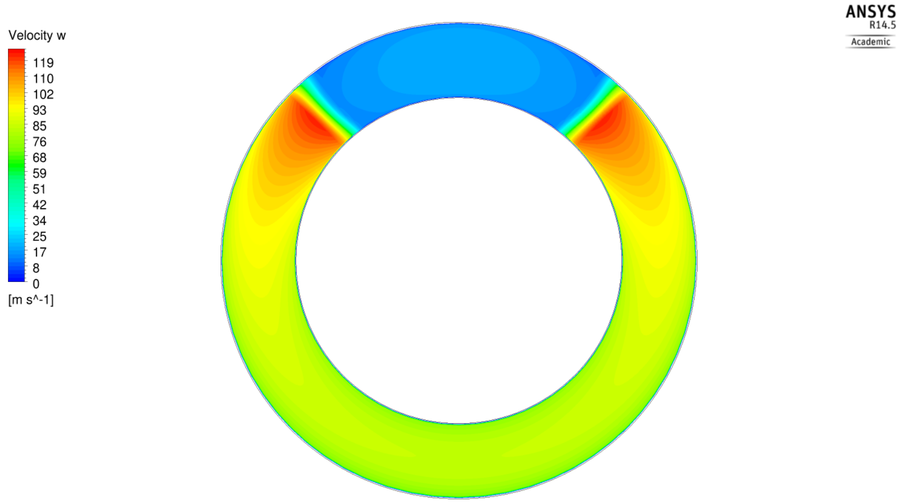

Figure 4.46: Contour of the axial velocity obtained with ANSYS CFX.

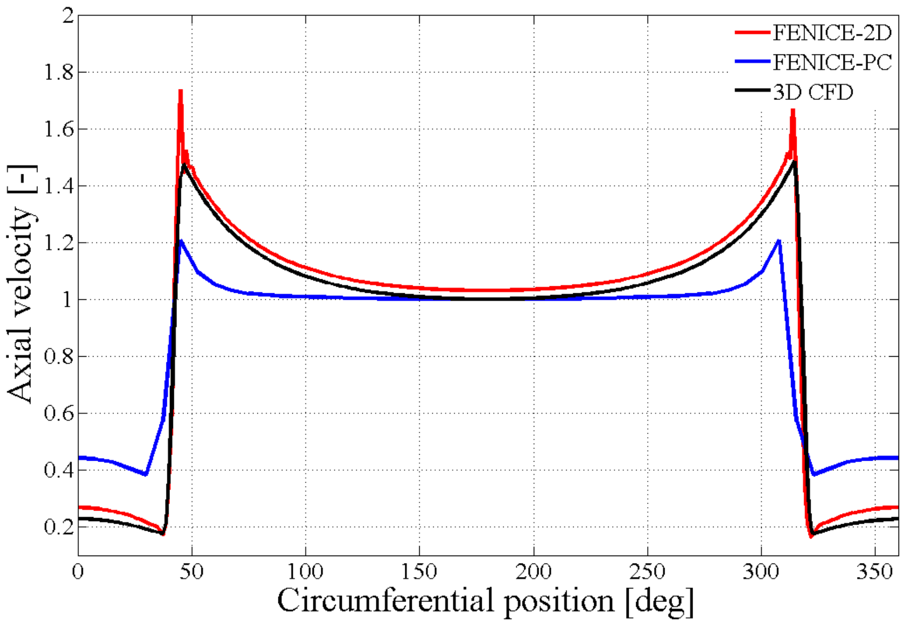

Figure 4.47: Comparison of the circumferential trend prediction of the axial velocity.

The axial velocity plot reported above and the static pressure one which follows, discloses a limitation of FENICE-PC. From the visual analysis of Figure 4.47 and Figure 4.49 is clear that a quite good agreement is obtained between 3D CFD and FENICE-2D; the agreement is indeed below 10% error in the clean region and slightly above in the distorted one for the axial velocity. Considering the below figure, reporting the static pressure field, the agreement is within 1% along the all circumference. For what concerns FENICE-PC, there is a clear mismatch which is most probably due to the lower discretization and the amount of mass exchange.

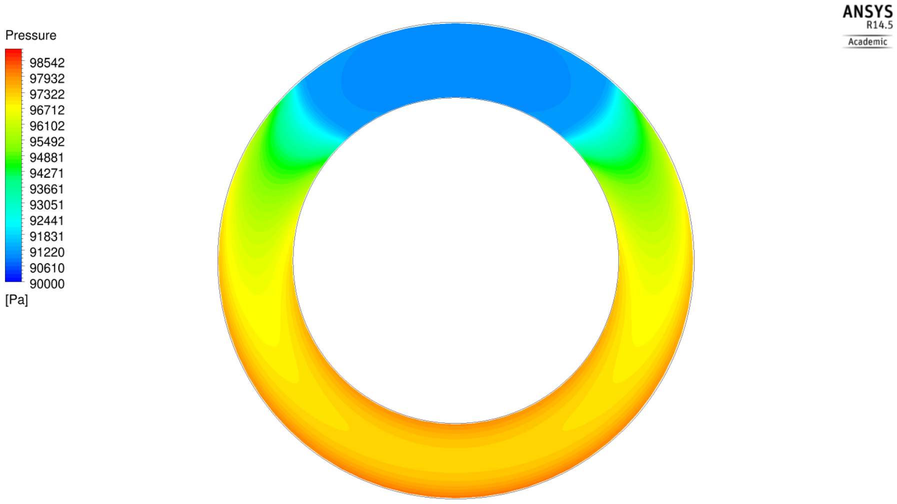

Figure 4.48: Contour of the static pressure obtained with ANSYS CFX.

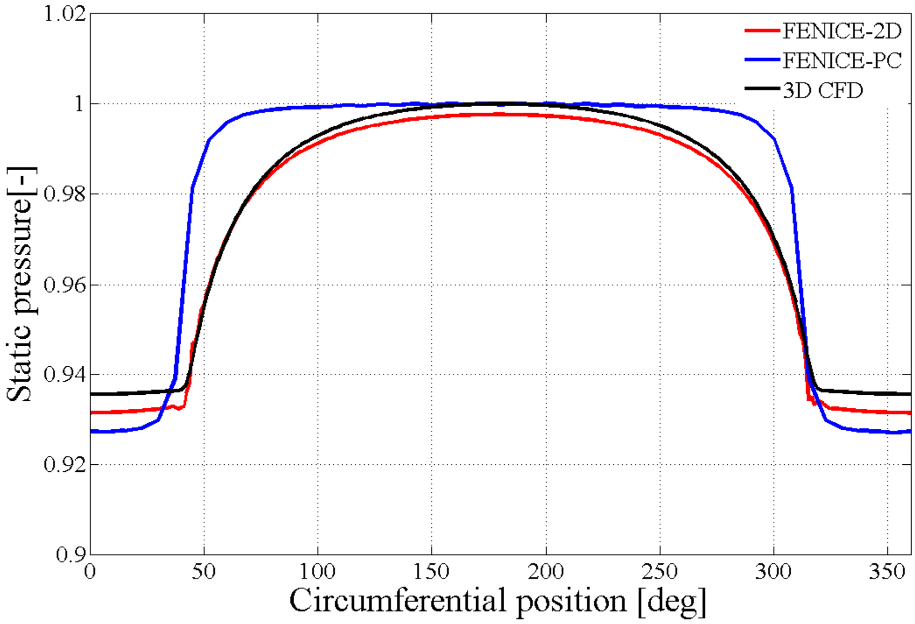

Figure 4.49: Comparison of the circumferential trend prediction for the static pressure.

The author believes that this mismatch, together with the limitation of FENICE-PC in adopting high levels of circumferential discretization, are due to the procedure followed to determine the amount of mass redistribution. Therefore, a parametric study was carried out in order to investigate the influence of the circumferential discretization and the C_{xflow} coefficient which can be used to regulate the amount of mass flow exchange between parallel segments.

For clarity, the equation used to determine the mass flow exchange which contains the C_{xflow} coefficient, is reported again below:

$$\dot{m}_{cross} = \pm C_{xflow} \rho_{cross} V_{cross} A_{gap} \tag{4.3}$$

For what concerns the circumferential discretization, as already mentioned at the beginning of this section, for this particular case-study the finer grid adopted consisted on 48 circumferential nodes, indeed higher levels of discretization had been tested and led to the divergence of the solver. The procedure adopted for the estimation of the mass flow exchange between 'parallel compressors' is quite simple and based on strong assumptions as it was explained in section 3.4.2. This simplistic procedure introduces unphysical oscillations which become more relevant increasing C_{xflow} or increasing the discretization. A higher discretization is in fact equivalent to lower mass flows across each 'parallel compressors' which means cross terms and main flows become of the same order of magnitude.

The role played by the C_{xflow} coefficient becomes clear considering Figure 4.50 below. The first plot on the left of Figure 4.50 shows the effect of an increasing C_{xflow} coefficient and therefore of an increasing mass flow exchange between parallel segments. The right plot of Figure 4.50 displays the effect in comparison with the 2D and the 3D model prediction of the static pressure distribution. As this second graph emphasizes, the prediction obtained with the higher C_{xflow} is closer to those obtained by the 2D and the 3D models. On the other hand, the increase amount of mass flow exchange introduces quite relevant unphysical oscillations. The comparison previously reported was therefore obtained running FENICE-PC with a coarse grid of only 48 circumferential nodes and a C_{xflow} coefficient equal to 0.2.

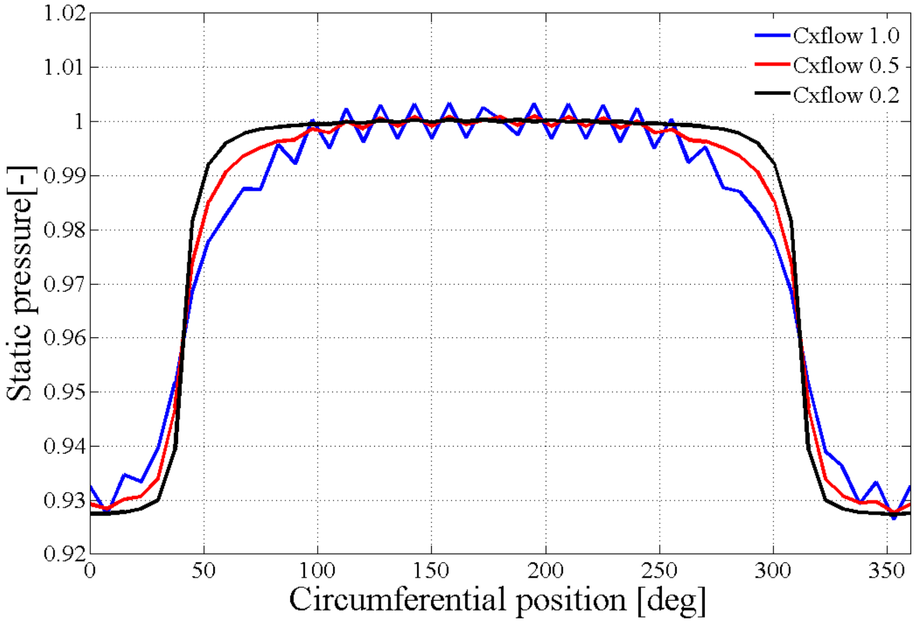

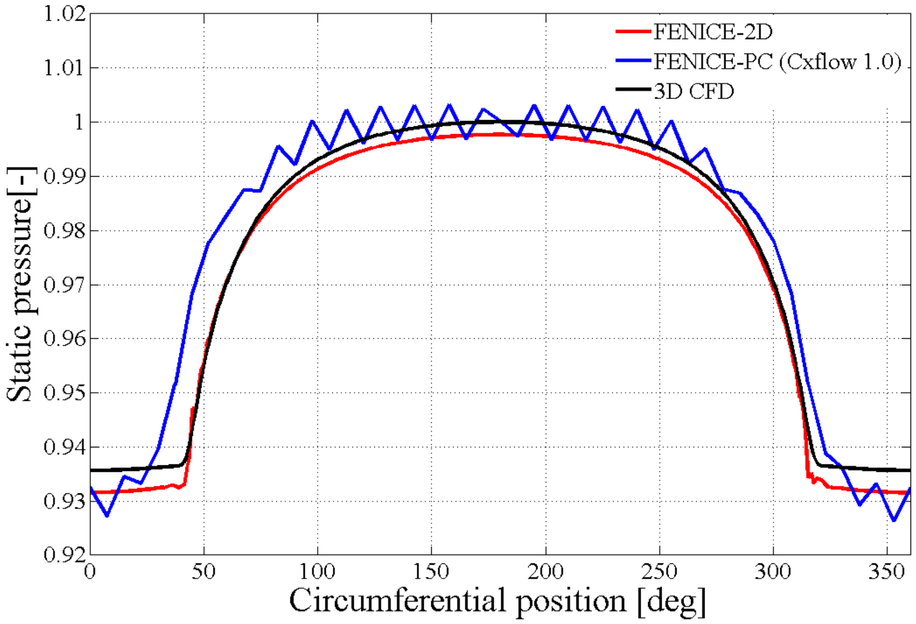

Figure 4.50: Influence of the amount of mass flow exchange.

NASA Rotor 37

This subsection reports the comparison performed against the NASA Rotor 37. The choice of this particular geometry was driven by the fact that at Cranfield University a lot of research was carried out, in recent years, on inlet flow distortion using the NASA Rotor 37 as a model. Several CFD data and models were therefore available for this comparison as reported for instance in [11].

Figure 4.51 shows the experimental map of NASA Rotor 37. The characteristic at 60%NRT was selected for this comparison to avoid losses due to supersonic flow (a shock loss model to account for supersonic flow has not been implemented yet).

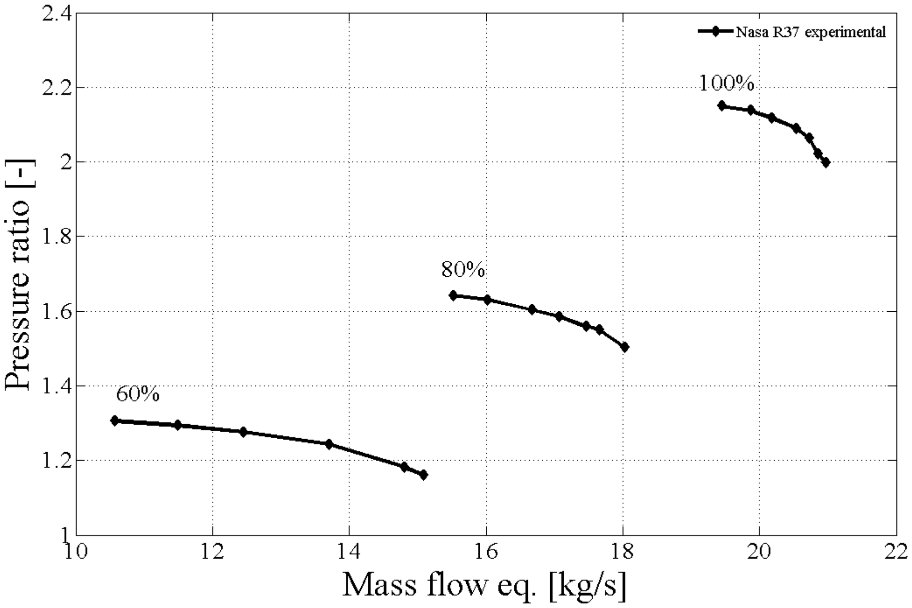

Figure 4.51: Experimental map of NASA Rotor 37.

Regarding the 3D CFD simulations, since the aim was the comparison of the converged distorted solution, to save computational time, only RANS simulations were carried out. In terms of mesh, a grid of about 11 millions nodes was adopted along with the k-epsilon turbulence model with scalable wall function. As seen for the previous comparison, this turbulence model offers both accuracy and low computational cost. The 3D CFD simulations were run using a workstation of 64 CPUs and each simulation needed about a day especially near the stall region. Further details regarding the CFD simulations and verifications can be found in [11, 9]. As reported in [11] a proper grid verification was performed for the 100% speed line. Although for this case study a 60% rotational speed was adopted, the same grid (named in the cited thesis as “medium with lower y_{plus}”) was chosen without carrying out a proper grid independency. The agreement with the experimental character

istic shown below in Figure 4.52 was considered sufficient for this investigation.

The first campaign of simulations using FENICE-PC/2D and ANSYS CFX were run in order to obtained the clean forward flow characteristic. The same procedure, previously described in section 4.2.1 was followed. The predicted forward flow characteristics were then compared against the experimental one as displayed below in Figure 4.52.

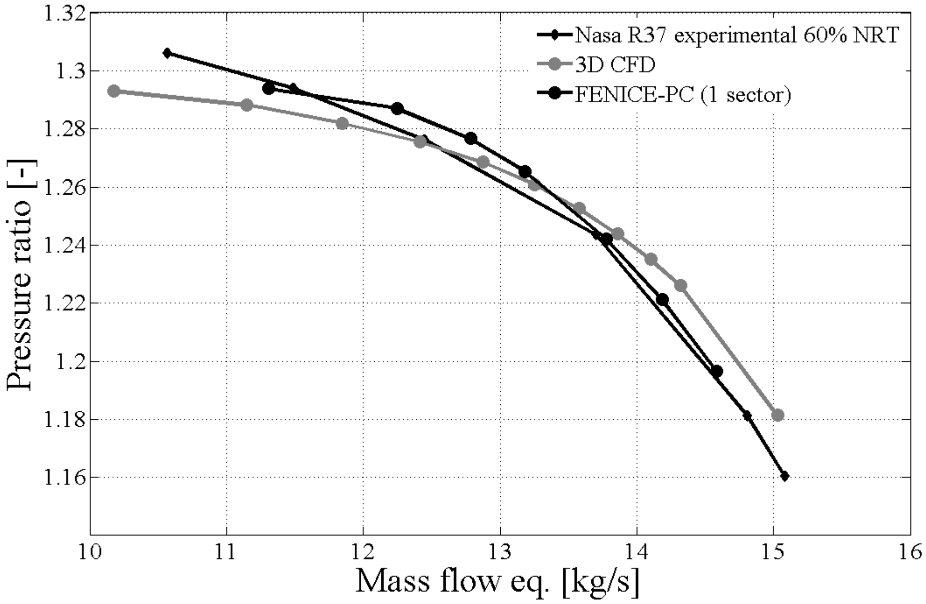

Figure 4.52: Comparison of the predicted forward flow characteristic obtained with 3D CFD and FENICE-2D/PC against the experimental data for the NASA Rotor 37.

Considering Figure 4.52, the agreement with the experimental characteristic is within a 2% error for both equivalent mass flow and pressure ratio. An agreement within a 2% error was considered acceptable since the purpose was to investigate the capability of the tool to properly capture the right trends in terms of flow properties and not a perfect match. Therefore no further alignment of both 3D CFD and FENICE-PC/2D models was attempted.

The comparison was then performed in terms of total pressure and total temperature distortion for two different values of outlet static pressure; the two clean operating points were chosen respectively near chocking and stalling which are the most critical conditions.

The table below reports the details of the simulations performed in terms of boundary conditions and discretizations adopted.

	Axial nodes	**Circumferential nodes**	**Radial nodes**
FENICE-PC/2D	100	36	-
ANSYS CFX	$\backsim$100	$\backsim$1100	$\backsim$50
Boundary Conditions			
Total pressure case study			
α^0=0 degrees			
Clean inlet	P'^0=1	T'^0=1	
Distorted inlet	P'^0=0.9	T'^0=1	
Total temperature case study			
α^0=0 degrees			
Clean inlet	P^0=1	T^0=1	
Distorted inlet	P^0=1	T^0=0.9	
Outlet	P'=0.87 and 0.96		

Table 4.4: Discretizations adopted by the different solvers and boundary conditions for the convergent duct's case study.

The set of results presented below in this section, regards the specific case-study of total pressure and total temperature distortion for the relative outlet static pressure of 0.87. The set of results for the higher outlet static pressure (P' equal to 0.96) are reported only in terms of overall compressor performance since for these the same consideration for the lower outlet static pressure can be applied. The results were obtained running both 3D CFD and FENICE-PC/2D imposing a stationary inlet total pressure deficit of 10%, on a 120° sector and a relative outlet static pressure of 0.87 .

For FENICE-PC/2D a grid consisting on 100 elements in the axial direction and 36 in the circumferential direction was used as reported in Table 4.4. The comparison presented below is in terms of flow properties distribution in the circumferential direction. Information was collected from both 3D CFD and FENICE-PC/2D at two locations, plane 1 and plane 2, respectively at 1 and 0.5 chords upstream and downstream of the rotor. Figure 4.53 shows the 3D domain adopted and the location of the planes for the flow field comparison in the circumferential sense.

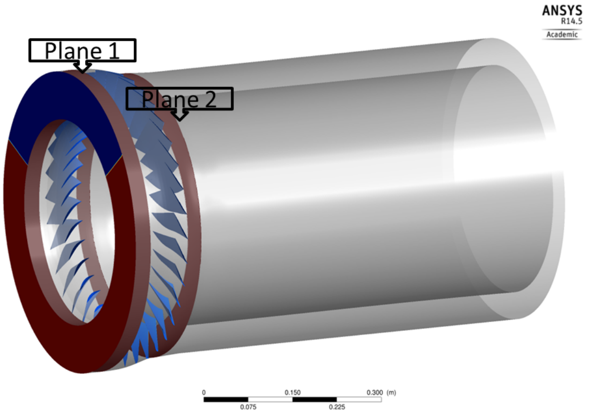

Figure 4.53: Rotor 37 3D domain adopted for the CFX simulations.

For the 3D CFD, all the flow properties reported in Figures 4.55-4.58 were extracted at mid span for each circumferential position and non-dimensionalized with their respective clean value. Before considering the graphs, it is worth remembering that the main aim was to check the capability of FENICE-PC/2D to capture the right circumferential trends; a perfect agreement was not expected since FENICE-PC/2D does not consider any radial variation of the flow properties, blades are modeled in terms of body forces and several flow features are accounted through semi-empirical models and correlations.

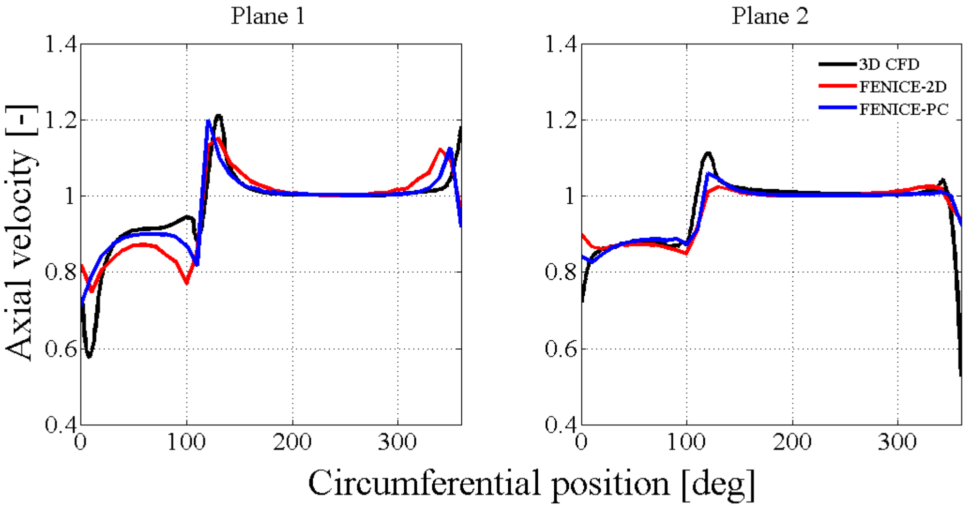

Figure 4.54: Circumferential trend of the axial velocity before and after the rotor for the case of total pressure distortion.

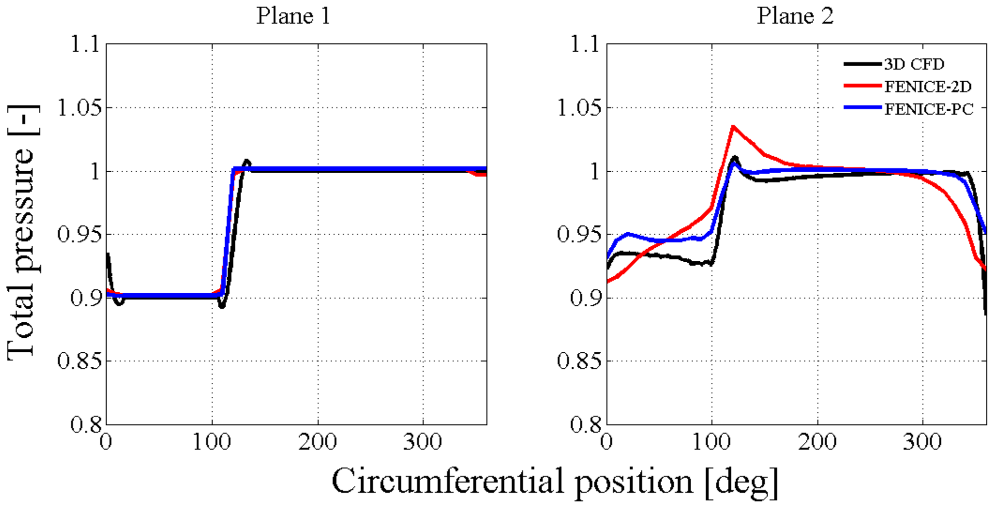

Figure 4.55: Circumferential trend of the total pressure before and after the rotor for the case of total pressure distortion.

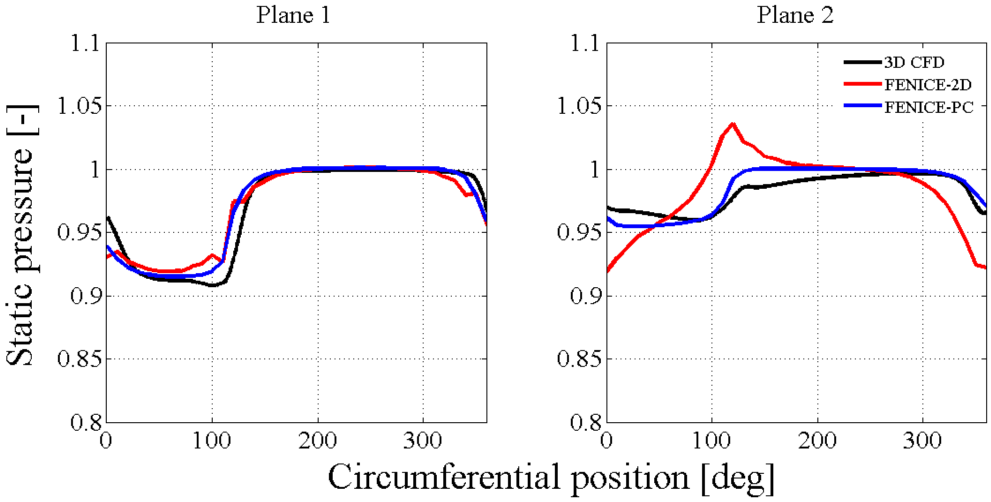

Figure 4.56: Circumferential trend of the static pressure before and after the rotor for the case of total pressure distortion.

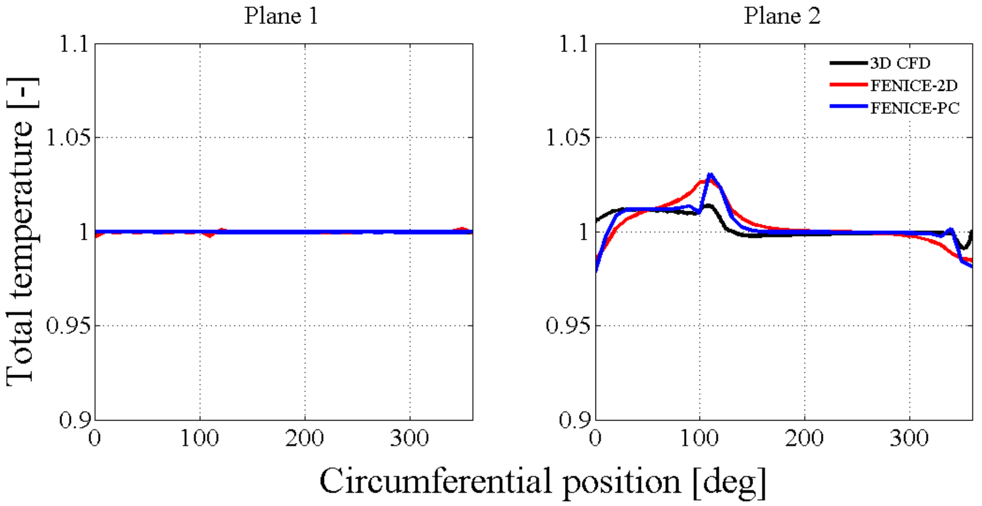

Figure 4.57: Circumferential trend of the total temperature before and after the rotor for the case of total pressure distortion.

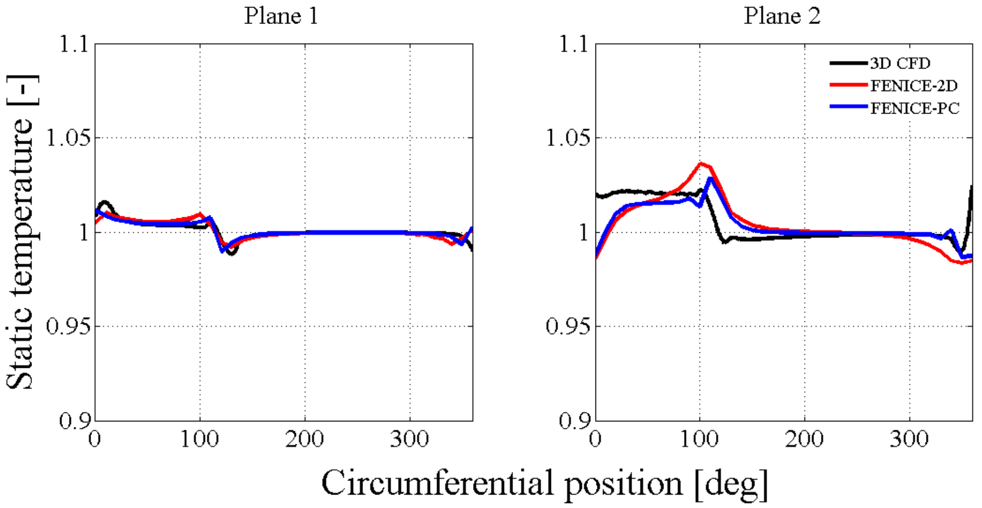

Figure 4.58: Circumferential trend of the static temperature before and after the rotor for the case of total pressure distortion.

Considering all the properties reported above and keeping in mind that this is a comparison between a 3D CFD simulation and a 2D one, it is worth pointing out that the tool developed shows promising capabilities. Both FENICE-PC/2D capture the right trends upstream and downstream of the blade row. Analyzing the flow properties one by one, as it was expected the total pressure distortion produces an increase in axial velocity (Figure 4.55) in the direction of rotation (circumferential position equal to 120 degrees) and a decrease in the opposite direction (circumferential position equal to 0 degrees). In terms of total pressure itself, a similar behavior was expected and found downstream of the blade Figure 4.55.

As explained in the section 3.4.1, a distorted sector works at a higher temperature ratio than the respective clean one and Figure 4.57 shows how FENICE-PC/2D captures again the right behavior upstream and downstream the rotor blade. For all the properties described, excluding the transition's regions between clean and distorted flow for the axial velocity, FENICE-PC/2D provides always a solution within the 5% error.

As anticipated at the beginning of this section, the same analysis was carried out for a case of total temperature distortion. The collection of graphs reported below compares the prediction of the circumferential trend of the main flow properties at plane 1 and 2, at steady condition. As previously seen in this chapter, the flow field distortion produced by the imposition of a 10% total temperature distortion is less severe than that occurring when the same amount is imposed to the total pressure. As a matter of fact, less marked differences between clean and distorted region can be observed.

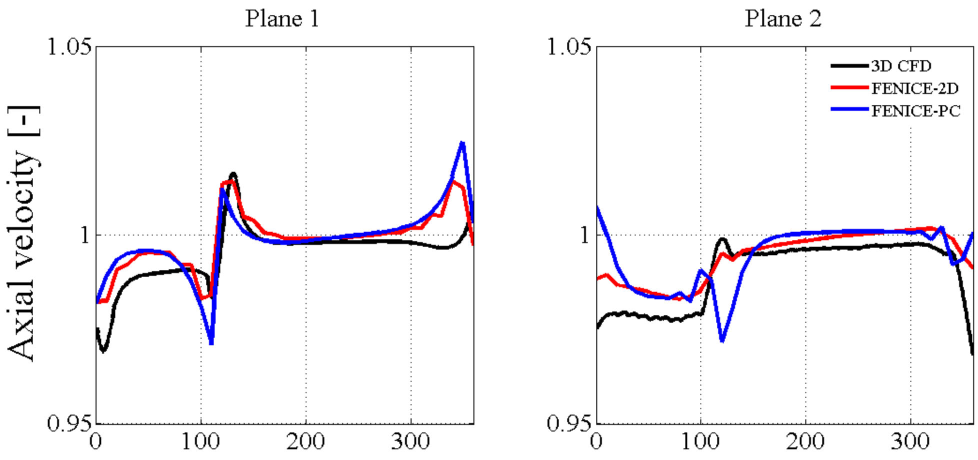

Figure 4.59: Circumferential trend of the axial velocity before and after the rotor for the case of total temperature distortion.

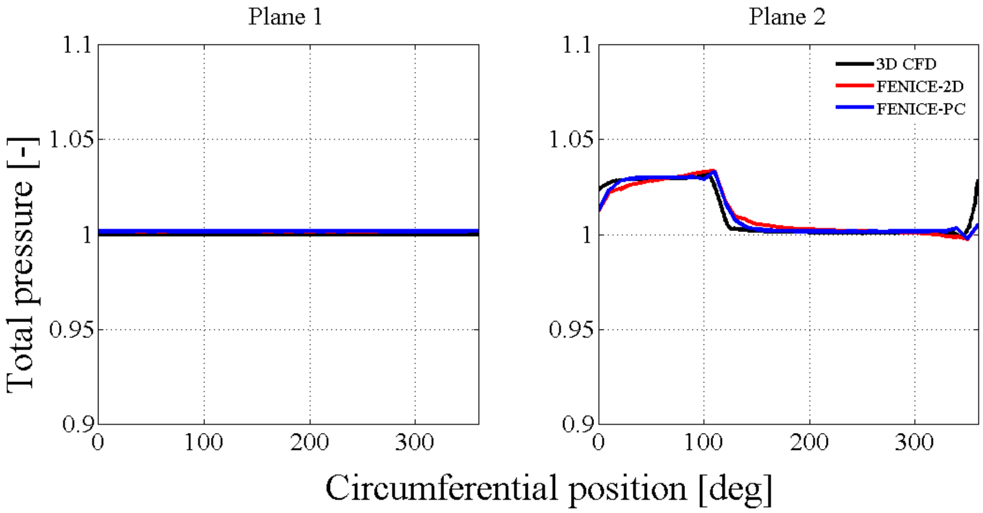

Figure 4.60: Circumferential trend of the total pressure before and after the rotor for the case of total temperature distortion.

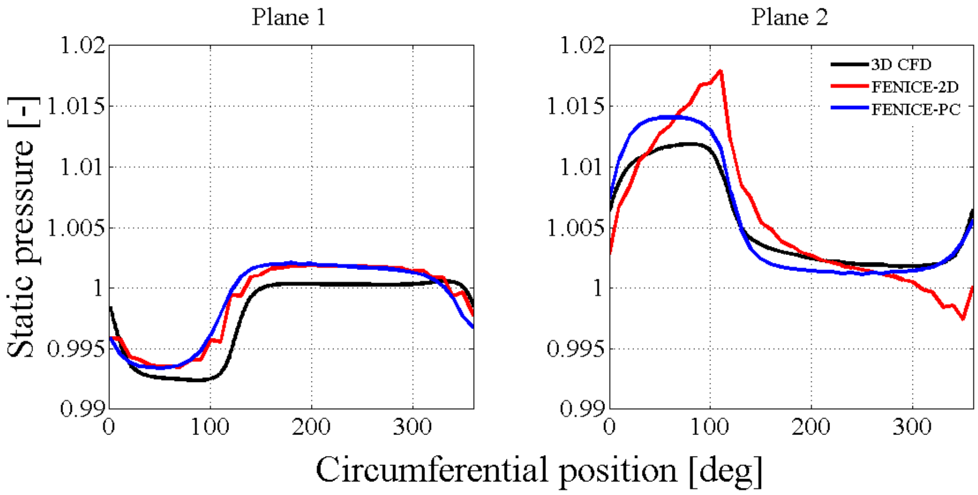

Figure 4.61: Circumferential trend of the static pressure before and after the rotor for the case of total temperature distortion.

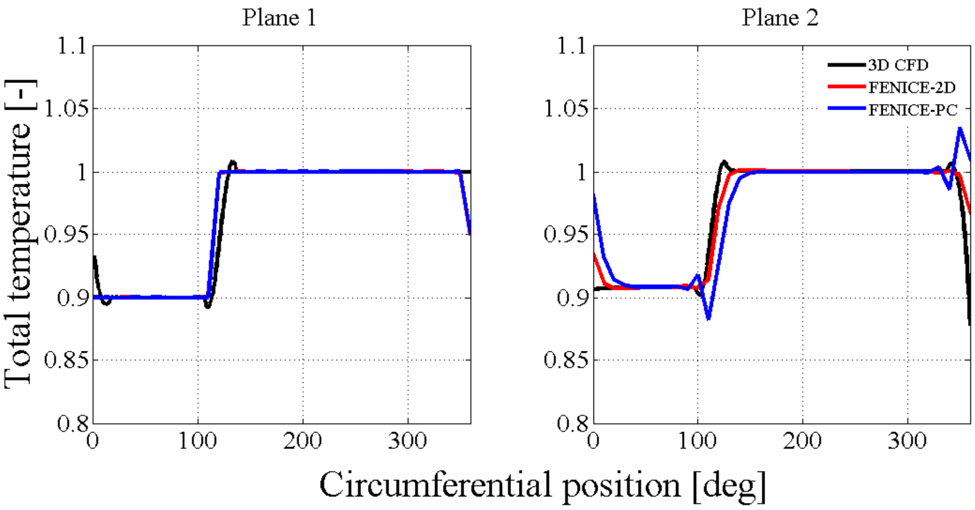

Figure 4.62: Circumferential trend of the total temperature before and after the rotor for the case of total temperature distortion.

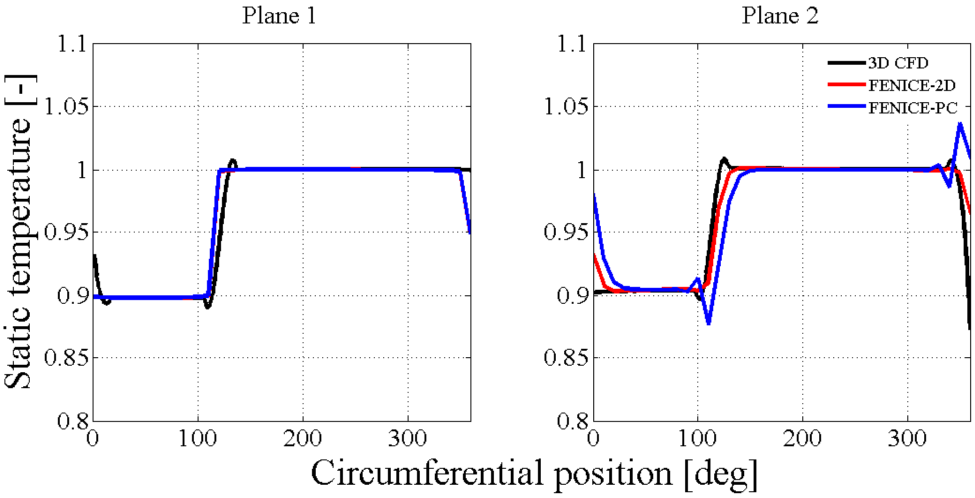

Figure 4.63: Circumferential trend of the static temperature before and after the rotor for the case of total temperature distortion.

As shown for the case of total pressure distortion, the agreement between 3D CFD and FENICE-PC/2D is very good and with a percentage error consistently below 5%.

Analyzing the flow properties reported, it is worthwhile highlighting that before the rotor blade row, as expected, the total pressure is perfectly uniform, while after the blades the distorted region is operating at a slightly higher total pressure Figure 4.60. Considering the total temperature, Figure 4.62, it is possible to observe clearly the 120 degrees distorted sector at the inlet (before the blade plane1) and its reduction passing across the rotor blade row. Comparing the capabilities of FENICE-PC and FENICE-2D, both versions of the solver seems to agree and provide very similar predictions, the only exception can be pointed out for the case of FENICE-PC in determining the axial velocity trend in the transition between clean and distorted region after the rotor blade as shown by Figure 4.59. A possible explanation for this different behavior could be related to the technique adopted to determine the flow property exchange between parallel sectors. Indeed, for FENICE-PC the mass flow redistribution and therefore the redistribution of the other flow properties is strongly dependent on the difference of static pressures which is not particularly marked for this case of total temperature distortion and on the calibration of the C_{xflow} coefficient.

In terms of overall compressor performance, Figure 4.64 and 4.65 below, compare the prediction of FENICE-PC/2D against the 3D CFD one for the two outlet static pressures reported in Table 4.4.

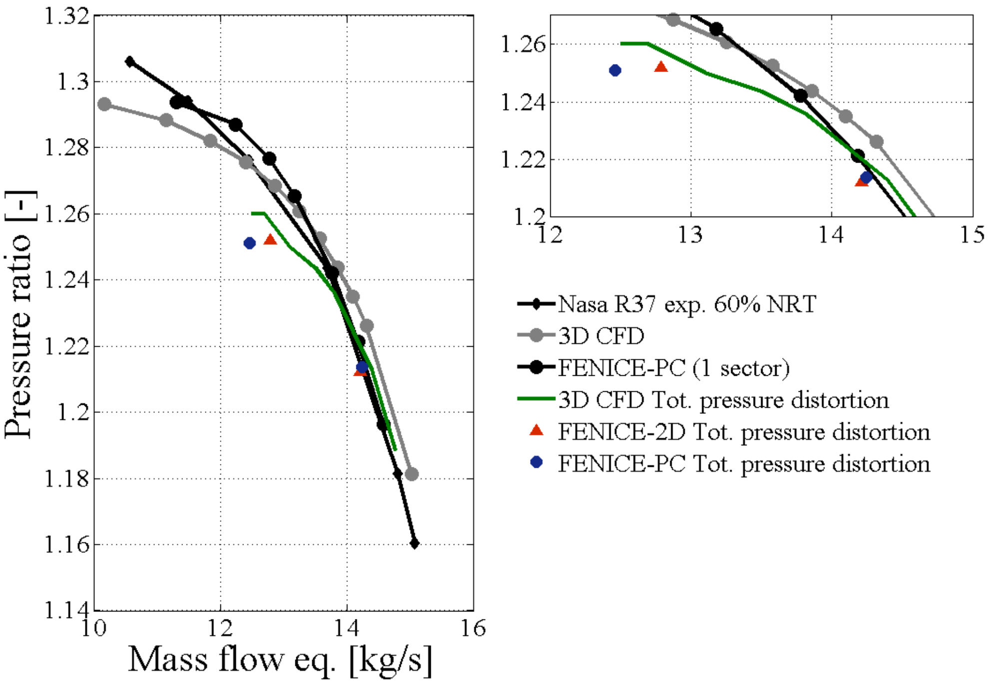

Figure 4.64: Overall compressor performance predictions for the case of total pressure distortion.

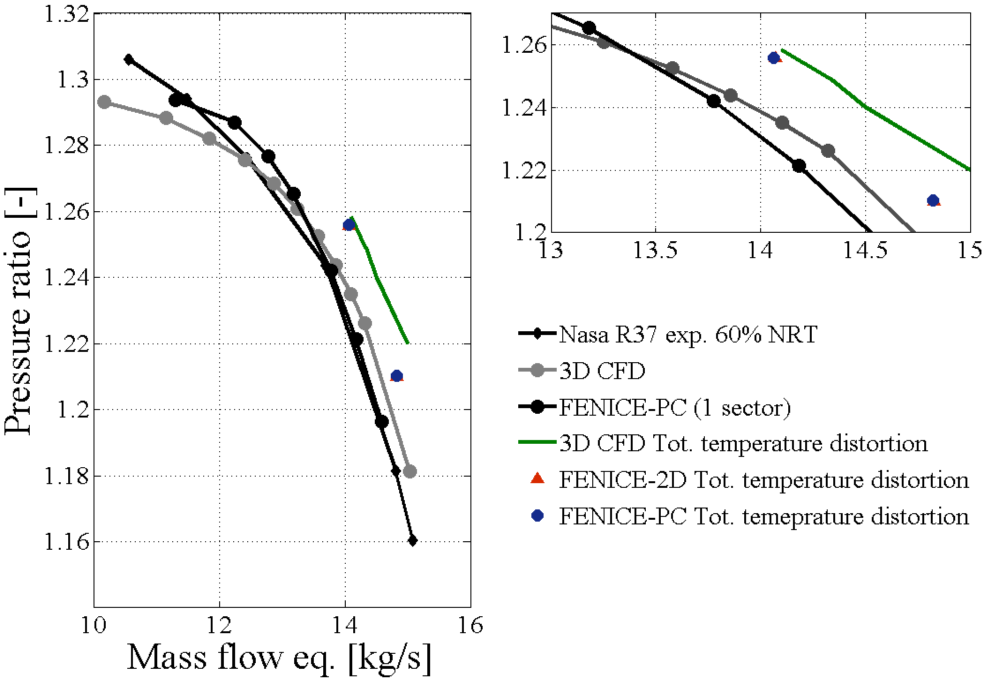

Figure 4.65: Overall compressor performance predictions for the case of total pressure distortion.

The left graph of Figure 4.64 and Figure 4.65 reports all the predicted compressor forward characteristics, clean and distorted and the experimental clean characteristic; on the right a “zoom in” is provided for clarity. In this graph, the experimental curve has been removed to focus the attention on the distorted curves. Analyzing this comparison it is important to bear in mind that 3D CFD and FENICE-PC/2D do not provide exactly the same prediction of the forward flow characteristic therefore a certain mismatch was expected also for the distorted curves. On the other hand the agreement can be considered very good, for both case studies and both outlet static pressure the error is within 0.5% in terms of pressure ratio and within 1% in terms of equivalent mass flow.

Concluding, both case studies proved the capability of the tool of dealing with asymmetric flow fields which is a key feature when modeling the rotating stall phenomenon. The tool is in fact able to model the transient axial and circumferential propagation of a disturbance.

The rationale behind the focus on inlet flow distortion was mainly driven by two reasons; firstly inlet flow distortion is an asymmetric phenomenon which has been intensively studied. Indeed, a large amount of data and information are available in the public domain identifying inlet flow distortion as an interesting case study for verification purposes; secondly it represents a useful technique to force the compressor into stall and study the inception and development of asymmetric flow instabilities (see following chapter).

4.6 FENICE-PC/2D Capabilities assessment

So far in this chapter, several results have been reported for both versions of the solver to provide evidence that the solver was verified adopting different compressors' geometries, configurations (isolated compressor, compressor with con-di nozzle, and compressor with a plenum and a con-di nozzle) and conditions such as changes in throttle settings, total pressure and total temperature distortions.

Particular effort was devoted to seek similarities and differences between the two methodologies, pros and cons and possible improvements. This section aims to provide a breakdown of the FENICE-PC and FENICE-2D methodologies highlighting again in some cases features that have been already mentioned.

To start this discussion, it is important to bear in mind that the only difference between FENICE-PC and FENICE-2D relates to how the circumferential direction and therefore the flow field along it, is modeled. Figure 4.66 below sketches out the differences under investigation and introduces the comparison between circumferential terms which follows. On the left side of Figure 4.66 there are the equations used to estimate the source terms which appear in equation (3.104) when the option FENICE-PC is selected (see section 3.6.2); on the right side there are the G terms which are used by FENICE-2D to model the circumferential direction when dealing with a "DUCT" component as it was explained in Section §3.5. The comparison is performed only for "DUCT" components since in FENICE-PC, the cross flows are determined for each axial element excluding those within blade rows.

$$\begin{bmatrix} \dot{m}_{cross} \\ Mom_{xcross} \\ Mom_{tcross} \\ E_{cross} \end{bmatrix} = \begin{bmatrix} \mp C_{xflow}\rho_{cross}v_{cross}A_{gap} \\ \dot{m}_{cross}V_x \\ \dot{m}_{cross}(\mp v_{cross} + V_t) \\ \dot{m}_{cross}c_p T^0 \end{bmatrix} \overset{?}{=} \frac{1}{r}\frac{\partial}{\partial\theta}\begin{bmatrix} G_1 \\ G_2 \\ G_3 \\ G_4 \end{bmatrix} = \frac{1}{r}\frac{\partial}{\partial\theta}\begin{bmatrix} \rho V_t A \\ \rho V_t V_x A \\ \rho A V_t^2 + PA \\ \rho V_t A H^0 \end{bmatrix}$$

Figure 4.66: The differences behind FENICE-PC and FENICE-2D.

The case study selected for the comparison between the "cross" terms and the "G" terms is the convergent duct already presented in Section §4.5, since for this particular investigation a very good agreement has been obtained between FENICE-2D and 3D CFD. For completeness, the case study is briefly described before continuing the discussion on the treatment of the circumferential direction by the two methodologies.

The results previously presented and those which are going to follow, were obtained imposing a stationary 90 degrees 10% total pressure deficit at the inlet and keeping fixed and uniform the outlet static pressure (which means the static pressure value of the clean starting solution). Section §4.5 already reported further information regarding this particular case-study, such as the required coarser circumferential discretization for FENICE-PC due to numerical stability and the influence of the C_{xflow} parameter (Figure 4.50). This section provides a proof that the technique adopted to account for the circumferential direction within FENICE-PC is actually very close to the proper 2D discretization of FENICE-2D. On the other hand, this comparison also states the relevance of the C_{xflow} parameter to tune the amount of mass flow exchange.

The following four graphs compare the four "cross" terms of Figure 4.66 and their equivalent for FENICE-2D which are obtained from the average of the circumferential derivative of the "G" terms. Since the numerical technique adopted for integrating the governing equations is the MacCormark scheme (described in section 3.6.1), the circumferential derivative is estimated as the average of the forward derivative and rearward one as reported below for the term G_1 which refers to the mass flow exchange (same concept is applied to the other "G" terms).

$$Mass_{exchange2D} = \frac{1}{2}\left(-\frac{1}{r}\frac{G_1(pc+1)-G_1(pc)}{\triangle\theta} - \frac{1}{r}\frac{G_1^{Prov}(pc)-G_1^{Prov}(pc-1)}{\triangle\theta}\right) \tag{4.4}$$

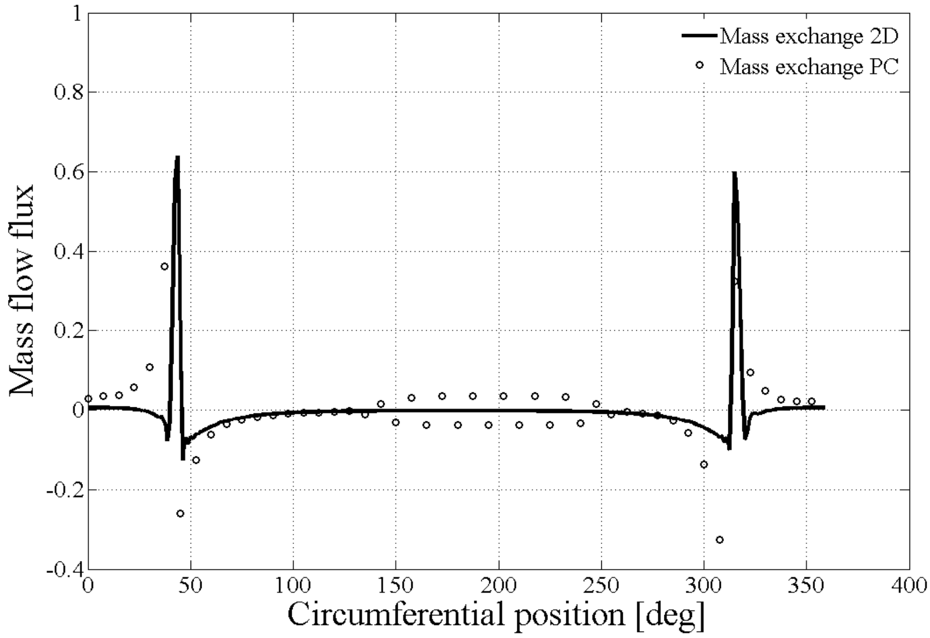

Figure 4.67: Comparison mass flow exchange: W_{cross} and G_1.

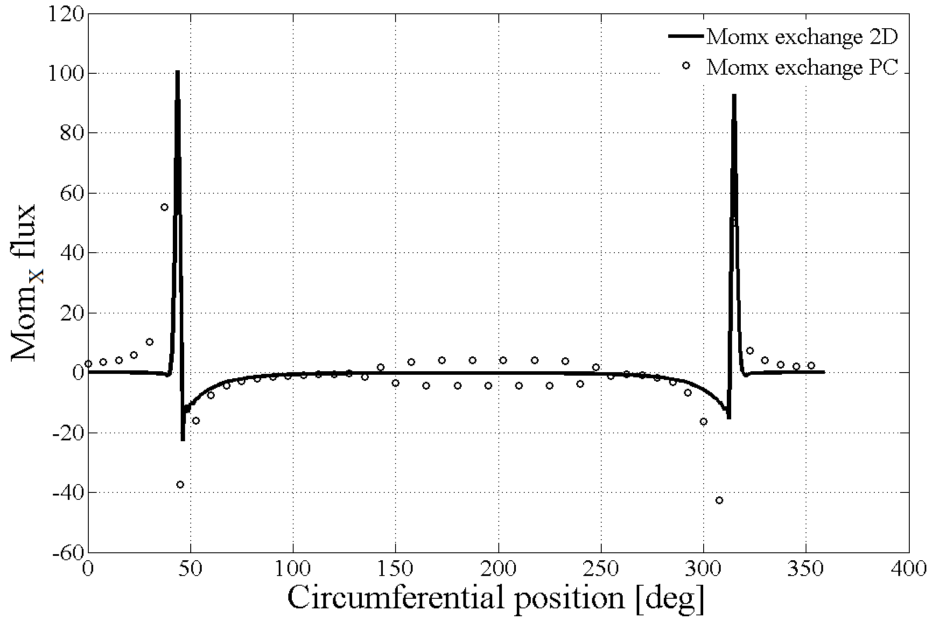

Figure 4.68: Comparison axial momentum exchange: Mom_{xcross} and G_2.

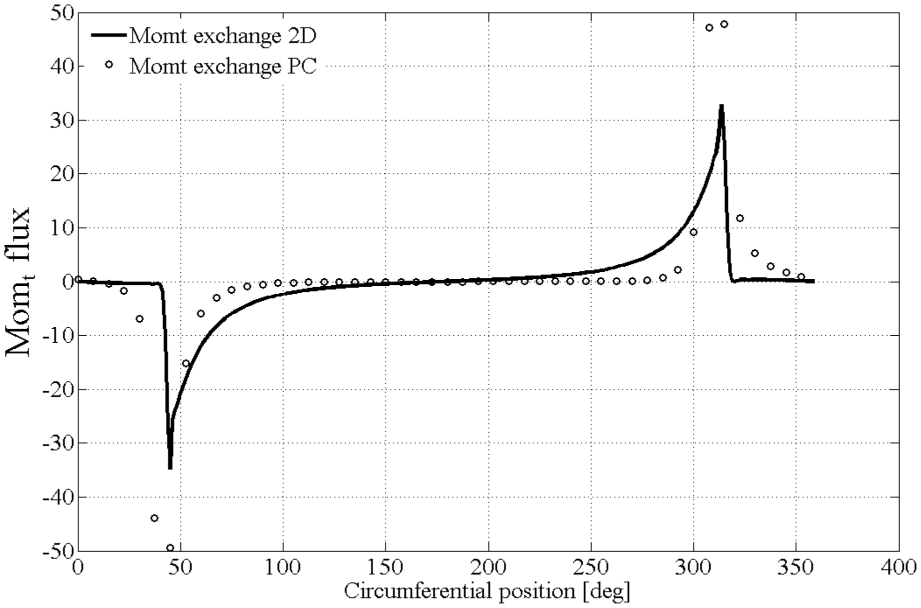

Figure 4.69: Comparison tangential momentum exchange: Mom_{tcross} and G_3.

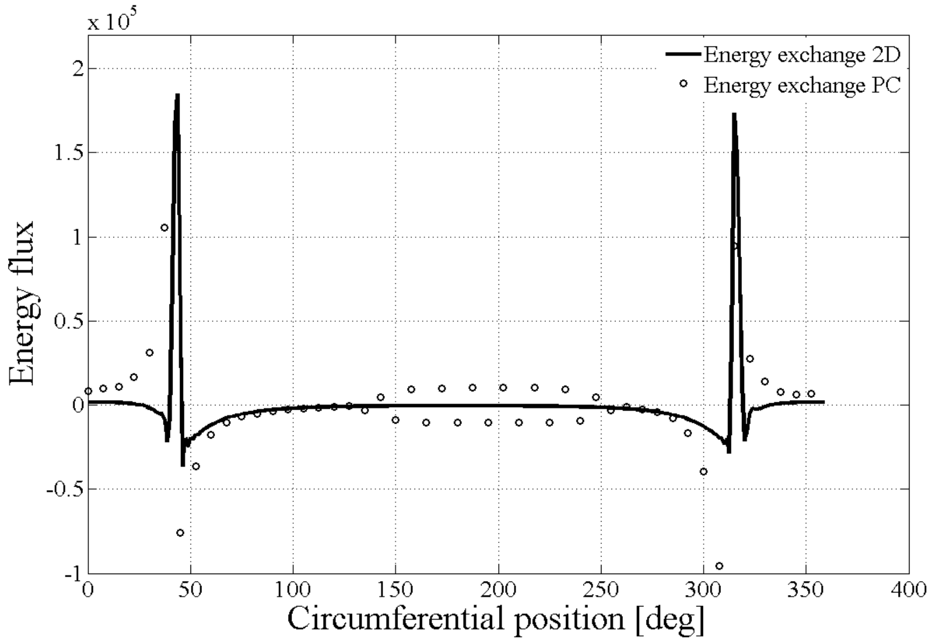

Figure 4.70: Comparison total enthalpy exchange: E_{cross} and G_4.

Analyzing the four pictures above it is possible to see that the modeling of the circumferential trend by the two versions of FENICE, is very similar. As previously mentioned, FENICE-PC is limited in terms of circumferential discretization by the occurrence of non-physical oscillations; small oscillations are already visible in the middle of the clean region in three of the four exchanges. The major differences between the two techniques can be observed around 0 and 90 degrees, that correspond with the transition regions between distorted and clean flow. A particular effort in order to reduce the differences between FENICE-PC and FENICE-2D was not devoted by the author due to time constraint. On the other hand, it would be interesting to see if improving the agreement between the circumferential treatment of FENICE-PC and FENICE-2D, improves the prediction of FENICE-PC.

Considering pros and cons, it has already been mentioned that FENICE-PC is limited in terms of circumferential discretization which is a drawback when an accurate circumferential solution is required. On the other hand, a lower number of circumferential nodes also required less computational time. Another limitation of FENICE-PC, which is described in the following chapter, regards the behavior in the rotating stall region; indeed FENICE-PC is not able to capture the typical rotating stall transient trend already presented in section 4.2.2 or reported by [28, 17]. The author believes that the cause of these limitations is the methodology behind the evaluation of the cross terms and in particular the assumptions involved such as the modeling of the “giving” sector (high static pressure) as a reservoir.

As far as FENICE-2D is concerned, the tool has proved to overcome the main limitations encountered with FENICE-PC. FENICE-2D provided a prediction of the flow field which is in very good agreement with the 3D CFD solution (see Section §4.5); moreover, FENICE-2D simulated the expected transient trends in terms of performance and flow fields in the rotating stall region as described in Chapter 5.

In general both versions assuming the flow radially uniform, cannot tackle phenomena which involve strong radial redistribution. In terms of computational time, the same time is required by both versions when the same grid is adopted. As already mentioned (see section 4.4.2), FENICE-PC can model the same amount of mass redistribution with a coarser grid and therefore it can be considered a more appropriate technique for investigations of asymmetric phenomena along the forward characteristic.

To conclude this section, the author believes that both versions of FENICE could be used successfully as an alternative to more complex and computationally expensive solvers for a quick assessment of compressor performance, bearing in mind their limitations and range of applicability.

Chapter 5

Parametric study in the rotating stall region

In the previous chapter several tests were reported in order to prove the correct implementation of FENICE-PC/2D and present its capabilities. The tool has proved to be able to tackle both steady and transient phenomena and to provide a quite accurate prediction of the compressor performance in all the three possible regions of operation: forward, stalled and reverse flow. This chapter reports on the parametric study that was run with FENICE-2D in the rotating stall region; a campaign of simulations was performed focusing on obtaining one or more regions of low flow (stall cell) rotating around the annulus. To push the compressor into the rotating stall region, two types of forcing were taken into consideration: inlet total pressure distortion and axial force pulse. For what concerns the pressure distortion, particular attention was paid to the investigation of the effect of the magnitude of distortion and to its time of application. For the axial force, only the amplitude of the pulse was taken into account.

This chapter is subdivided into three main sections; the first two sections correspond to the two types of triggers adopted while the last section reports on the procedure followed to derive the rotating stall curve.

The parametric study was carried out adopting the four-stage low speed compressor C106 already adopted in previous investigations as reported in Chapter 4. The compressor was discretized into 1000 axial and 36 circumferential elements. This coarse circumferential grid was selected for mainly two reasons. At first, as it was clearly explained in the previous chapter, the solution of FENICE-PC is subjected to numerical oscillations when fine circumferential grids are adopted; besides as reported in section 3.3.1 the compressor C106 requires already a fine axial grid, this coarse circumferential grid was found to offer a good trade-off between resolution of the flow field and computational time.

Before reporting on the results obtained during the parametric study, it is worth to mention, that few case-studies were run also with FENICE-PC; however the results obtained were quite bizarre and not consistent with the known rotating stall behavior. It was found that the overall compressor performance was dropping down excessively without showing the common oscillatory trend. The author believes that this limitation is once again due to the methodology followed to account for the exchanges in the circumferential direction. As a matter of fact, the calculation of the “cross” terms is based on the analytical solution of steady equations as it was extensively described in the methodology chapter. For these reasons the results presented hereafter were obtained running the tool as FENICE-2D.

5.1 Inlet total pressure distortion

During this first campaign of simulations, the effect of inlet total pressure distortion on the turbo-machine was exploited specifically to trigger the rotating stall phenomenon. The results presented in this section were obtained with a plenum volume of 0.5 $m^3$and a value of the delay parameter of 2.5 rotor revolutions. These particular values of plenum chamber and delay parameter were chosen in relation to the focus of this campaign of simulations that was the investigation of the rotating stall region. As highlighted in section 4.2.2.1, a plenum chamber of 0.5 m^3 determines a typical rotating stall behavior for the compressor C106. In terms of time delay, 2.5 rotor revolutions was selected as already adopted for testing the quasi-2D Euler solver and also suggested by other researchers [1, 23].

5.1.1 Effect of the amount of inlet total pressure distortion

The aim of this study was the investigation of the effect of a stationary deficit in inlet total pressure, concentrated on a sector of two different circumferential extents, respectively 60 and 90 degrees. The two figures below present the results obtained with FENICE-2D for three different amounts of total pressure drop, 2.5%, 5% and 10%. All the simulations were run initializing the flow field with the solution obtained for the last stable point on the forward flow characteristic and imposing after 50 time steps the stationary distortion. An important aspect that has to be highlighted, regards the boundary conditions adopted; indeed, all these simulations were carried out adopting the configuration type C (compressor only) while plenum and nozzle were modeled with equation (3.48), (3.49) and (3.50).

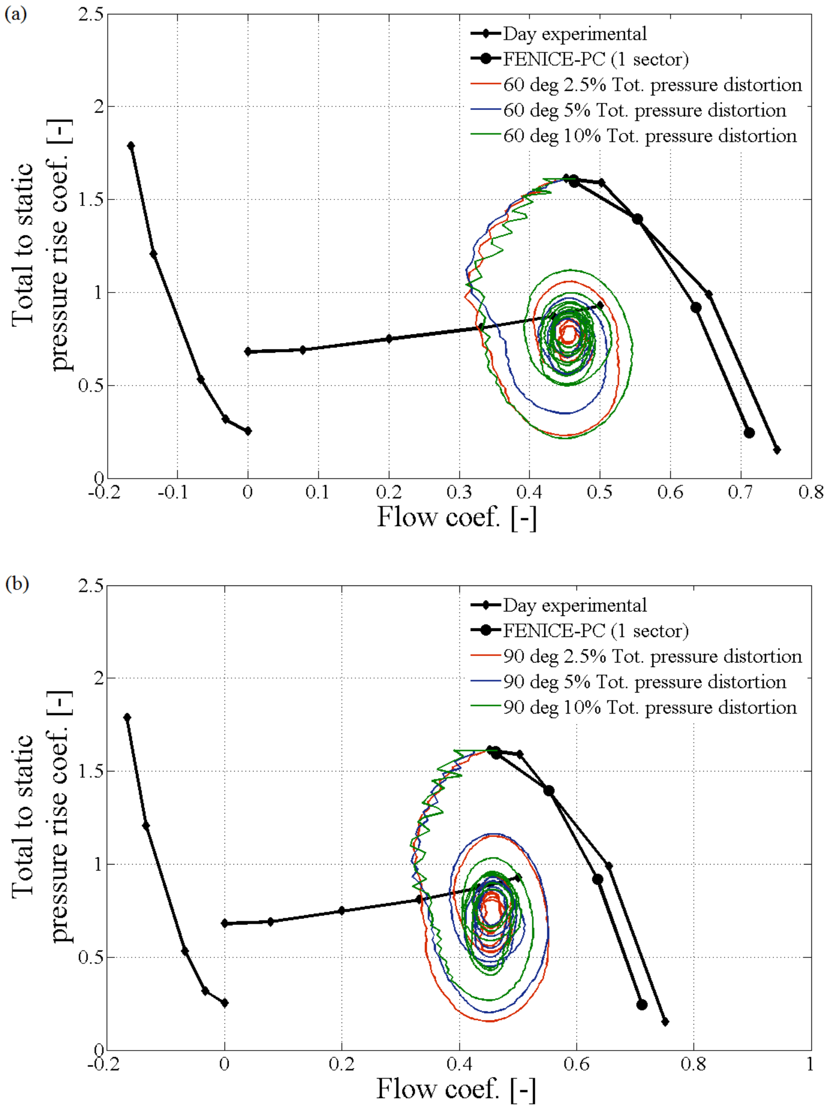

Figure 5.1: Effect of different amounts of total pressure distortion on a sector of 60 degrees and 90 degrees on the performance of the compressor C106.

Considering both compressor maps reported in Figure 5.1, it is clear that neither the intensity of the distortion or the circumferential extent affects the final operating point; once again, it can be stated that the final operating point is determined only by the throttle setting. What can be appreciated is that an increase in the circumferential extent reflects in an increase of the amplitude of the oscillations while an increase of pressure deficit shows slightly different trends comparing the case with a 60 degrees extent against the one with a 90 degrees extent.

5.1.2 Effect of the circumferential extent of the distorted region

This section considers the effect of the circumferential extent of the distorted region, from a different perspective. The focus of these simulations is on the transient behavior and final overall compressor performance as for the previous case-study. The results presented were obtained once again using the configuration C (compressor only) with plenum and throttle modeled as boundary conditions (see section 3.2.2). Following the same approach adopted for the previous case-study, the throttle setting was kept fixed and equal to the setting of the last stable operating point on the forward characteristic.

The case-study presented in this section is still related to the circumferential extent of the distortion; in this case-study three different simulations were carried out. The three simulations were performed applying the same amount of total pressure deficit respectively over one, two and three regions conserving the overall circumferential extent. Figure 5.2 below sketches out the investigation performed.

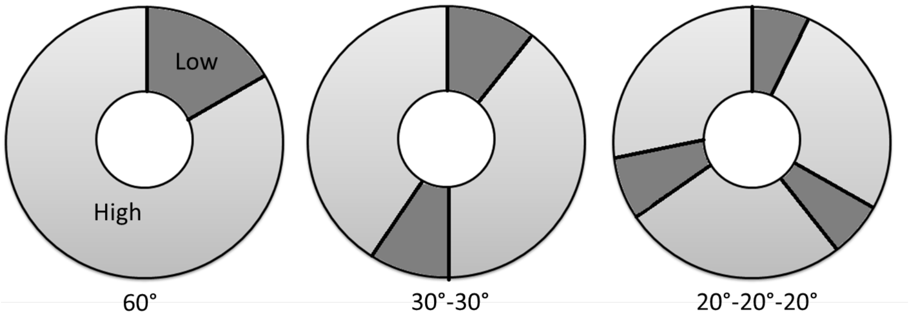

Figure 5.2: Multiple regions of total pressure distortion.

The first comparison is reported in Figure 5.3 . The first graph on the left of Figure 5.3 shows the already seen transient trend for the case of a 5% total pressure deficit concentrated on a 60 degrees sector. The right plot shows the transient trend of the compressor performance for a 5% total pressure deficit distributed over two opposite-facing sectors of 30 degrees (middle case of Figure 5.2).

From a qualitative perspective, looking at the trajectory of the operating point, it is clear that the case 30-30 degrees has a stronger effect on the compressor pushing it to experience larger oscillations before converging in a stalled condition. The distribution of the distorted region over more regions of smaller extent changes the transient behavior of the compressor from classic rotating stall to classic surge.

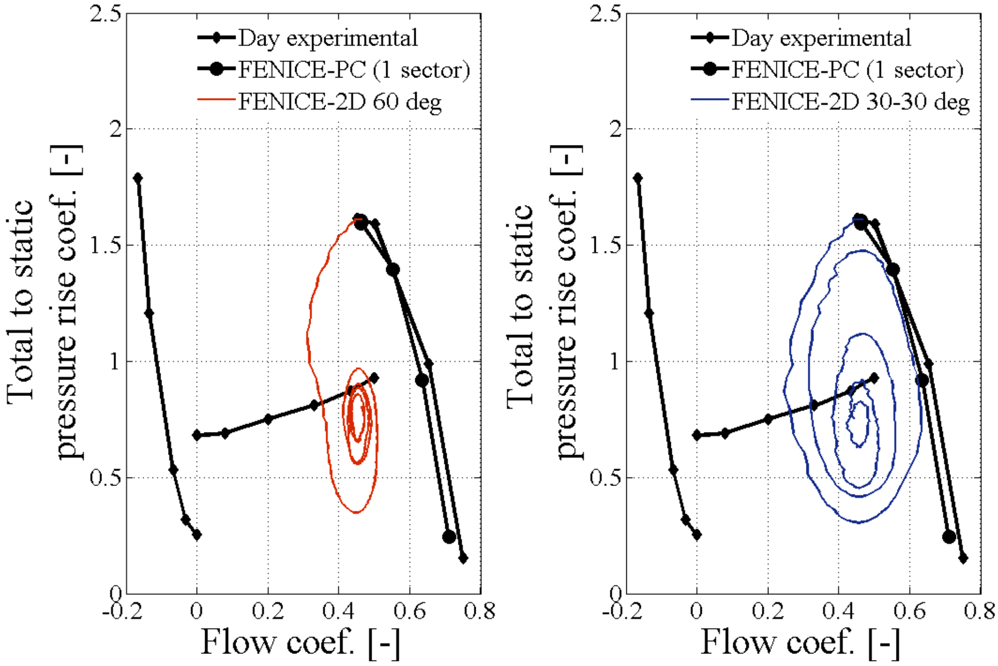

Figure 5.3: Comparison between the effect of a 5% total pressure deficit distributed over a 60 degrees sectors against the effect of the same amount of distortion distributed over two 30 degrees opposite-facing sectors.

Having observed this tendency of changing from typical rotating stall to classic surge simply distributing the same amount of distortion on two smaller regions, for the third case which distributes the distortion over three sectors of 20 degrees equally distributed around the annulus, a classic surge behavior was expected.

For the third case sketched out in Figure 5.2, two different case-studies were carried out: stationary and temporary. Where the term stationary refers to a distortion which is imposed at the inlet of the domain and kept until the end of the simulation. While the term temporary corresponds to the case of a distortion imposed for a certain amount of rotor revolutions and then removed. So far, only the effect of stationary distortions have been investigated and a proper investigation on the effect of the time-wise extent of the distorted boundary is reported in the following section. As expected a stationary three-region distortion pushes the compressor into a classic surge transient as shown in the left plot of Figure 5.4. On the right side of Figure 5.4, the case of a temporary 5% distortion distributed over three regions with a 20 degrees circumferential extent is reported. The three distorted regions are imposed after few iterations from the starting of the simulation and removed after 5000 iterations which corresponds to a physical time lower than a rotor revolution (about a third of rotor revolution). From the overall performance plot, it appears clearly how the removal of the distortion forces the compressor to change from classic surge to a typical rotating stall transient.

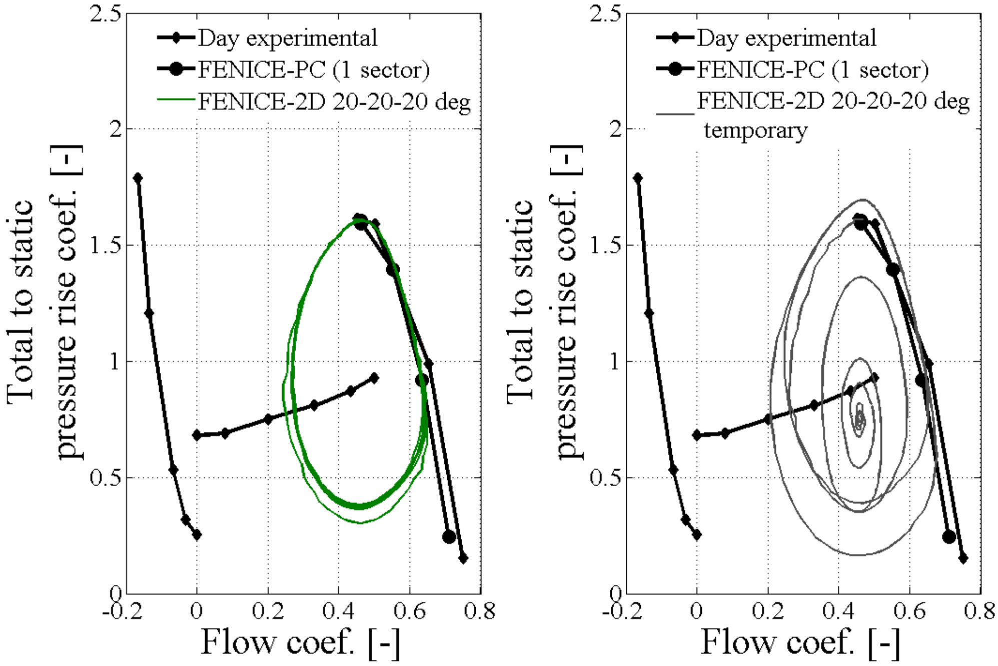

Figure 5.4: Comparison between the effect of a stationary and a temporary three-region 5% total pressure deficit.

A more clear picture of the physical phenomenon occurring after the removal of the distorted regions, can be obtained analyzing the flow coefficient traces. Indeed, Figure 5.5 and Figure 5.6 report the evolution in time of the flow coefficient respectively for the stationary and temporary case; on the x-axis the time is reported in terms of rotor revolutions, while the y-axis reports the flow coefficient of each circumferential sector. For visualization purposes a constant value proportional to the circumferential position was added to the flow coefficient. For what concerns the axial position, both figures report the flow coefficient collected at the inlet of the IGV.

Analyzing both plots, it appears evident how for the stationary case the three distorted regions remain distinct and fixed at the same circumferential location for the entire simulation. While for the temporary case it is possible to observe how for the first 6 rotor revolutions, the flow field is characterized by the three distinct regions of low flow seen for the stationary case even if the imposed distortion is removed before the first revolution. After the sixth revolution, the distorted regions merge into two and then one with a consistent reduction in rotational speed[1] and an increase in circumferential extent.

---

[1] The rotational speed of the disturbance is determined in respect to the rotor speed and it is a function of the time required by the disturbance to cover the whole annulus.

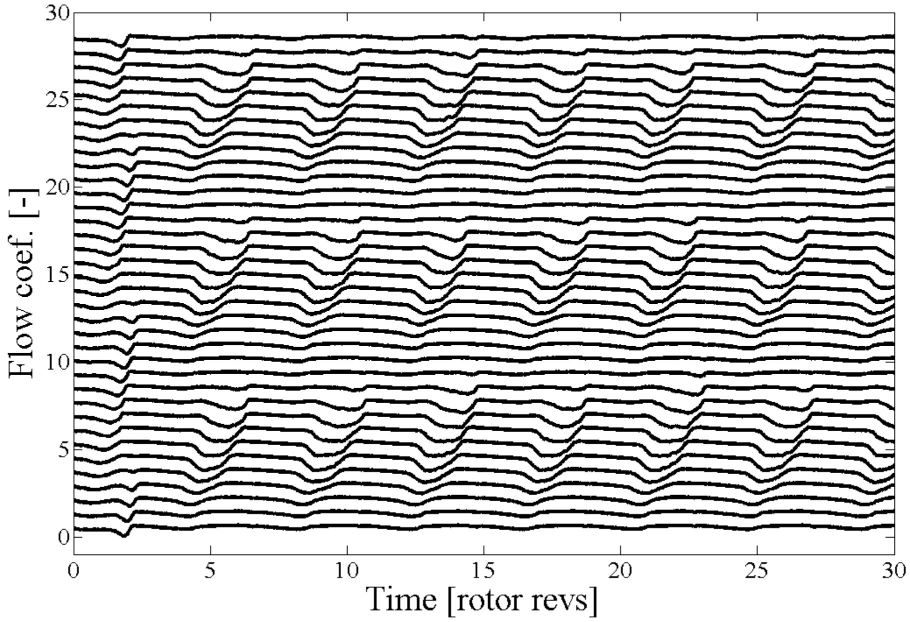

Figure 5.5: Flow coefficient traces at the IGV's inlet for a three-region stationary total pressure distortion.

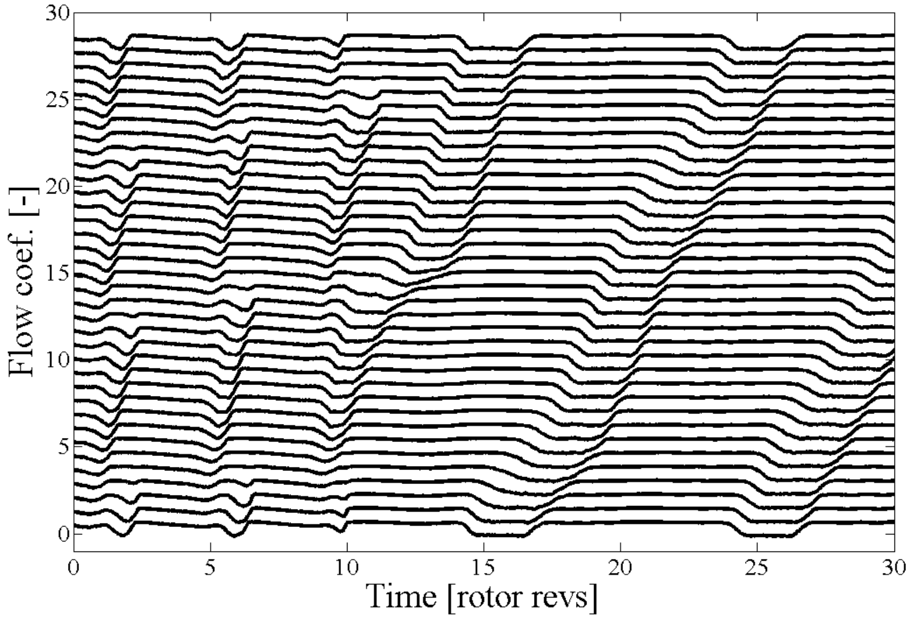

Figure 5.6: Flow coefficient traces at the IGV's inlet for a three-region temporary total pressure distortion.

5.1.3 Temporary and stationary distortion

Up to this point, all the cases presented can be classified under the label "stationary distortion" with the only exception presented in the previous section regarding a temporary distortion split over three sectors. Indeed, for the previous cases, the low pressure region was imposed as boundary condition and kept until the end of the transient simulation. This section aims to address a very important question which arises when dealing with rotating stall and surge phenomena, that is, under which circumstances the compressor is able to recover.

As described in Chapter 2, inlet flow distortion can be a transient event, for instance when due to wind gusts, and therefore not enough to lead the compressor into locked-in stall or surge. On the other hand, in some cases after the inception of stall, the removal of the inlet distortion is not sufficient to recover the compressor and the opening of the throttle is necessary.

The collection of graphs reported in this subsection, shows the transient behavior of the compressor C106 when subjected to a temporary inlet pressure deficit of 10% with a circumferential extent of 60 degrees. As for the previous case-studies each simulation was initialized utilizing the clean solution of the last stable point on the forward flow characteristic. After few time steps (50 iterations), a distortion was imposed and removed after three different time extents: 1, 0.5 and 0.25 rotor revolutions.

Figure 5.7 shows that for all the three cases, the compressor does not recover converging at the same "locked-in" stall operating point. The first case, with a distortion imposed for one rotor revolution and then removed, was repeated twice adding respectively a 10% and a 20% throttle opening after removing the distorted boundary conditions in order to further investigate the recovery capability. The transient performance of the compressor for this particular case is reported in Figure 5.8.

Figure 5.8 highlights how a 10% (throttle setting th 1.1) opening of the throttle is still not enough to recover the compressor. The operating point in fact converges on the right extreme of the stall characteristic while with a 20% (th 1.2) opening the compressor recovers from the stall condition as described by the trajectory of the operating point which converges on the forward flow characteristic.

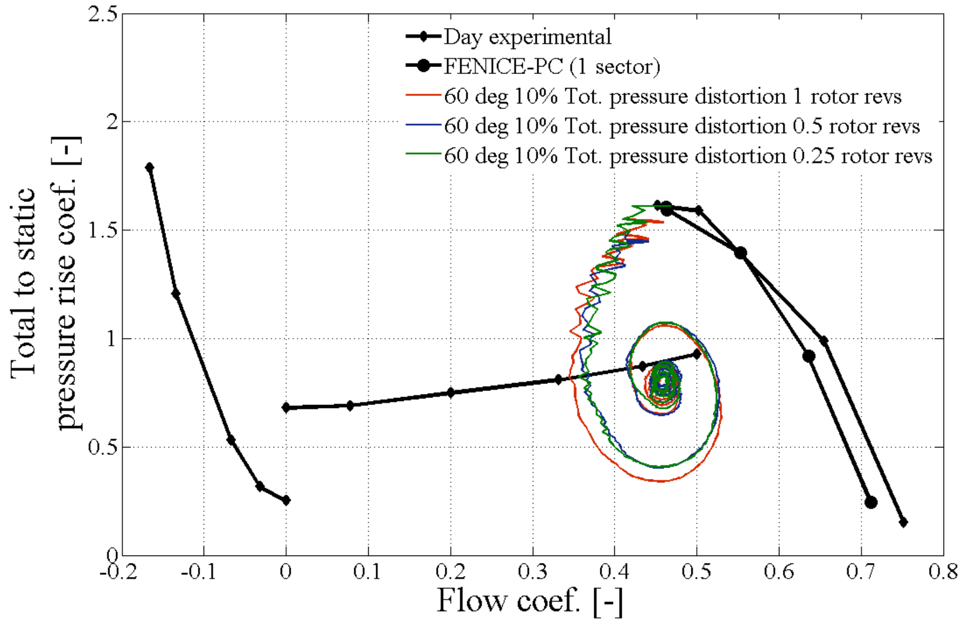

Figure 5.7: Temporary and stationary inlet total pressure distortion for the compressor C106.

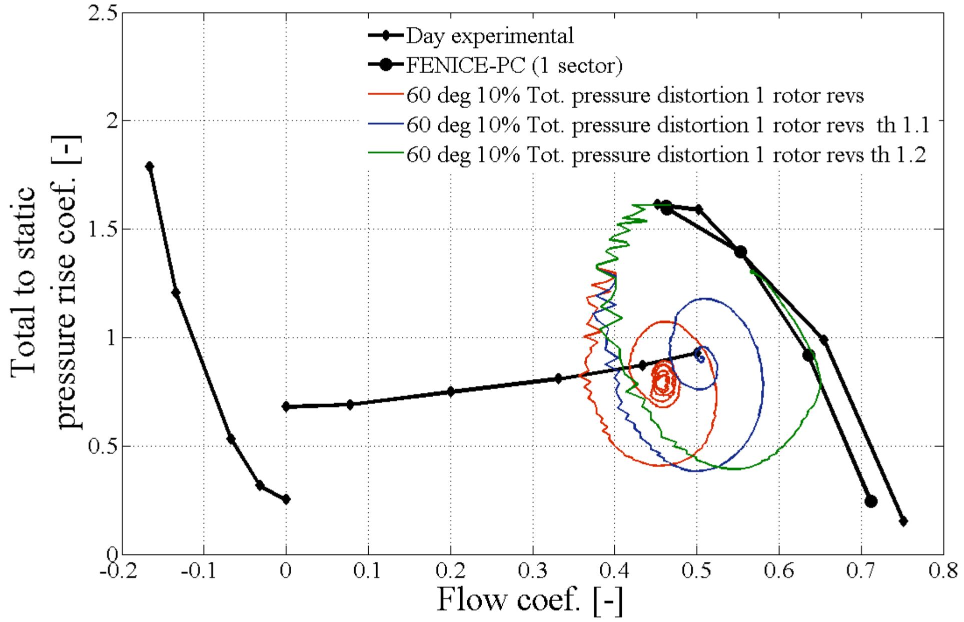

Figure 5.8: Transient performance obtained combining a temporary distortion and a change in throttle settings.

Concluding, the compressor C106 requires a substantial opening of the throttle to recover even after the removal of the distorted inlet. The capability of recovering is a feature that changes from one compressor to the other and that is strongly linked with the events occurring in the compressor's surroundings. The "recovery feature", in fact, represents a key point when studying rotating stall and surge phenomena. An example of its importance was provided in the section 1.1.1 of Chapter 1 for the particular case of a shaft failure event. Although the prediction of the recovery phenomenon is quite important, the prediction of the compressor recovery from stall/surge conditions is nowadays still very difficult. The verification against available experimental data or other sources and the improvement of tools such the one developed in this work are therefore of fundamental importance.

In this context, few investigations were carried out also with the two-stage compressor NASA TP 1493 in order to check the differences in terms of transient phenomena experienced by this compressor when subjected to the same conditions of the C106. As already mentioned, for the NASA TP 1493, experimental data in the stalled and reverse flow region are not available therefore a proper investigation of these unstable regions, was not carried out.

In this regards, Figure 5.9 shows that the NASA TP 1493 is able to recover once the distortion is removed without the necessity of a change in the throttle settings; indeed for the temporary case, the operating point goes back to the forward characteristic and converges to the last stable point on the forward characteristic which was used to initialize the simulation.

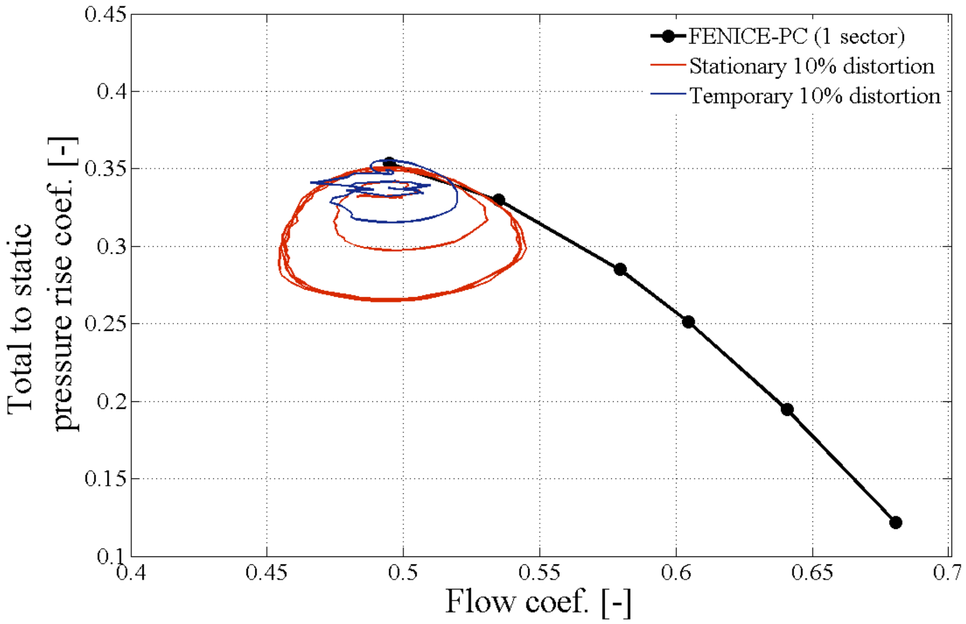

Figure 5.9: Comparison of the transient performance for a stationary and a temporary inlet total pressure deficit for the NASA TP 1493.

The different transient trend between the stationary and temporary case can be better visualized considering the trend of the total to static pressure rise coefficient versus rotor revolutions as shown below in Figure 5.10.

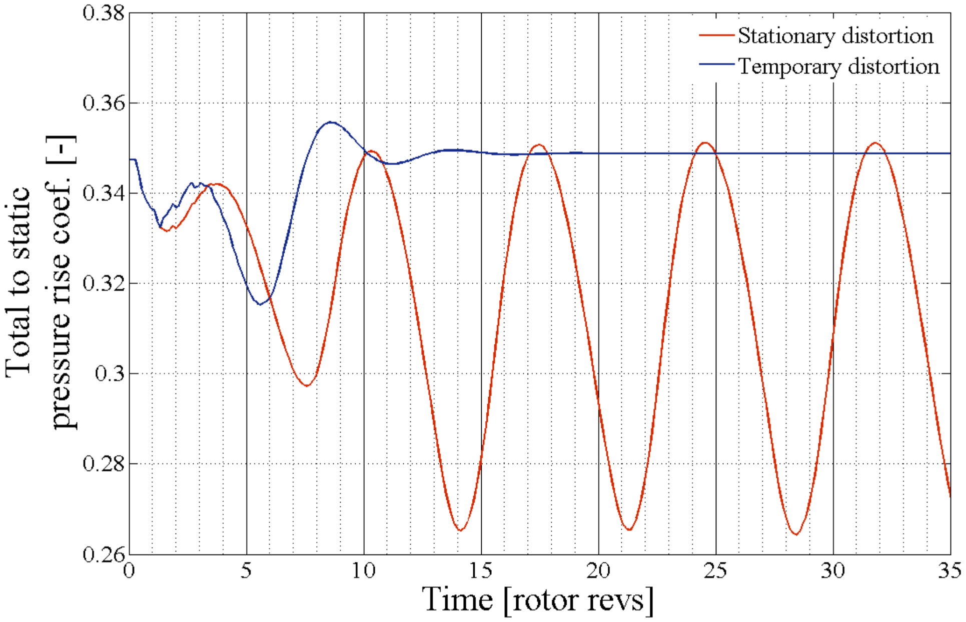

Figure 5.10: Transient behavior of the total to static pressure rise coefficient for a temporary and a stationary case of inlet total pressure distortion for the compressor NASA TP 1493.

Looking at Figure 5.10, it is possible to notice how the temporary case deviates from the stationary after the distortion is removed (1 rotor revolution); it is interesting to highlight how the temporary and stationary case overlap for slightly more than 1 rotor revolution, this behavior is due to the inertia of the flow which is modeled through the time lag law as previously explained in 3.3.2.

5.2 Modeling of spike-type disturbance through axial force pulses

Chapter 2, and particularly section 2.2.1 described how stall onset can occur following two routes: growth of modal long length and/or growth of local short length disturbances. The former is known as modal-type inception while the second is commonly addressed as spike-type inception.

The author is aware that spike-type disturbances are usually localized in few blade pitches and that a more appropriate modeling would be achieved with a 3D solver. On the other hand it was considered worth investigating the transient behavior of the compressor when subjected to spikes since this type of inception is quite common for modern high-speed multistage compressors. In order to model a spike inception, a localized axial force pulse having a constant frequency was adopted as suggested also by Gong [82].

The results presented in this section were obtained imposing, once per revolution, a force pulse on the third rotor over a circumferential extent of 40 degrees. Basically the axial force applied on the third rotor was multiplied by a chosen factor; four different values, both positive and negative, were tested: 1.05, 1.10, 1.20 and 1.50.

In terms of boundary conditions, plenum and throttle were adopted as seen in the previous section with a plenum volume of 0.5 m^3. For all the simulations reported in this section, the throttle setting and the rotational speed were kept constant determining the final average operating point.

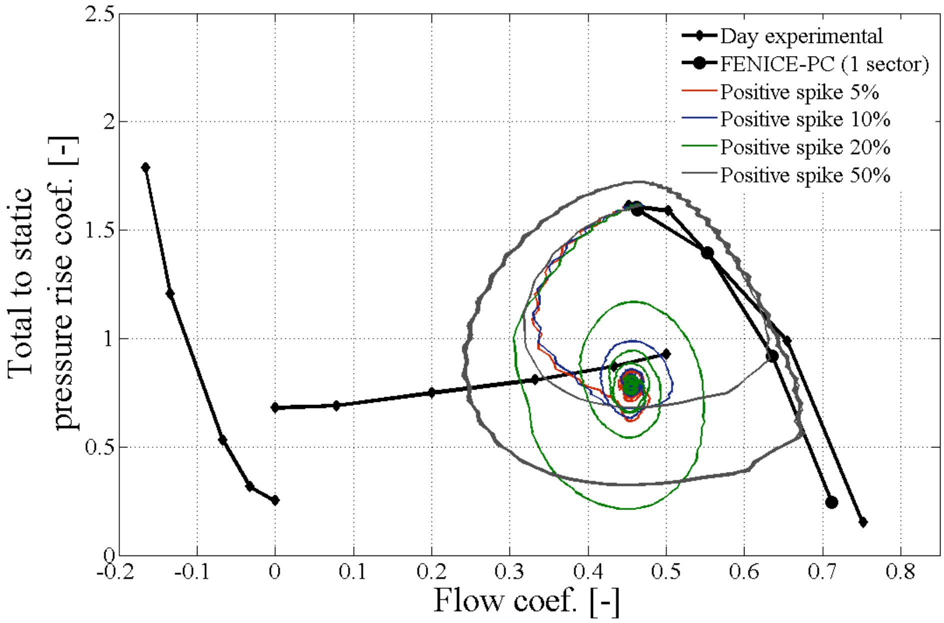

Figure 5.11: Positive axial force spike on the third rotor of the compressor C106.

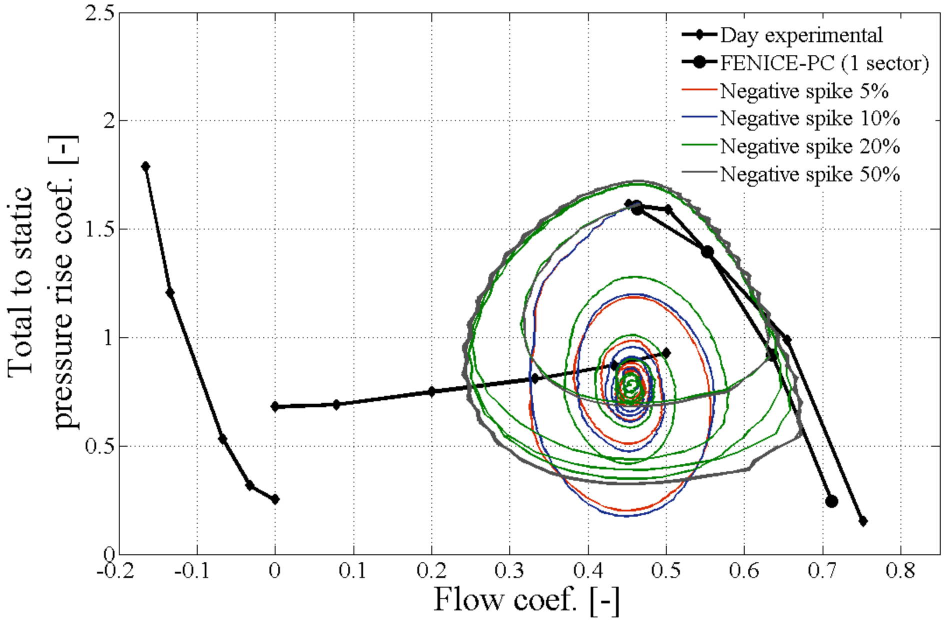

Figure 5.12: Negative axial force spike on the third rotor of the compressor C106.

Analyzing Figures 5.11 and 5.12, it appears clear that starting from the very last stable position on the forward flow characteristic, even the smallest pulse (±5%) in the axial force can push the compressor into stall. On the other hand increasing the amplitude, the compressor shows different transient behaviors; considering as first the positive pulse, Figure 5.11, two different transients can be observed. Indeed increasing the pulse amplitude from 5% to 20%, the amplitude of oscillations in total to static pressure rise coefficient increases up to the point of switching from a typical rotating stall behavior to a classic surge for a 50% pulse.

Similar considerations can be derived from Figure 5.12; on the other hand, as expected, a negative pulse has a much stronger effect since it does not only amplify the axial force but it changes the direction of its application. While a negative pulse of 5% and 10% lead the compressor into typical rotating stall transient, the negative 20% induces the compressor into a pair of classic surge cycles before entering in pure rotating stall mode. The negative 50% pulse similarly to the positive case forces the compressor into classic surge.

The flow coefficient traces versus time are shown below for two case-studies: the negative spike of 5% and the negative spike of 20% amplitude. As it was expected from the visual analysis of Figure 5.12 the region of low flow increases in size and slows down in terms of rotational speed in both cases, but the all process appears to be slightly faster for the negative spike of 5%.

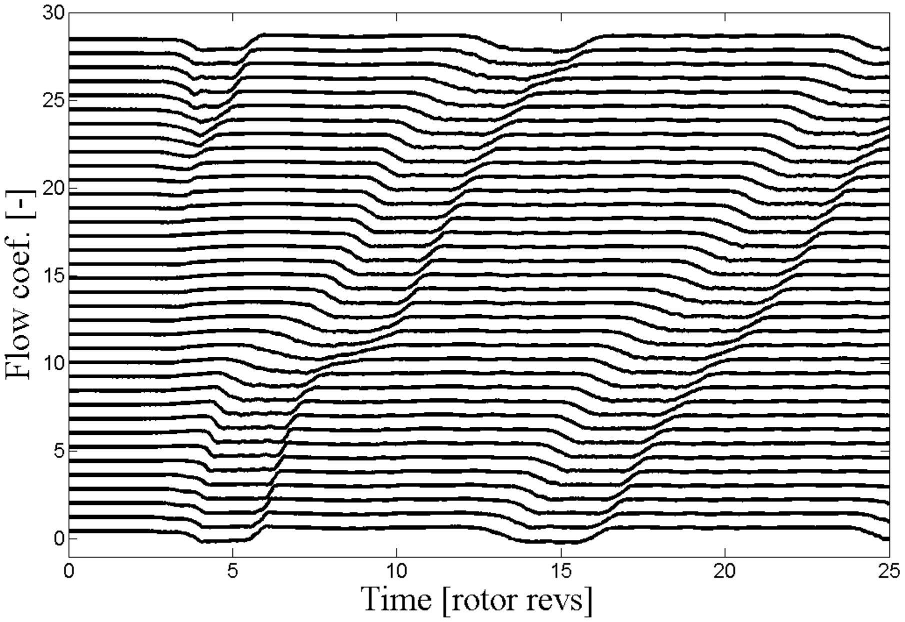

Figure 5.13: Flow coefficient traces at the inlet of the IGV for a negative spike of 1.05.

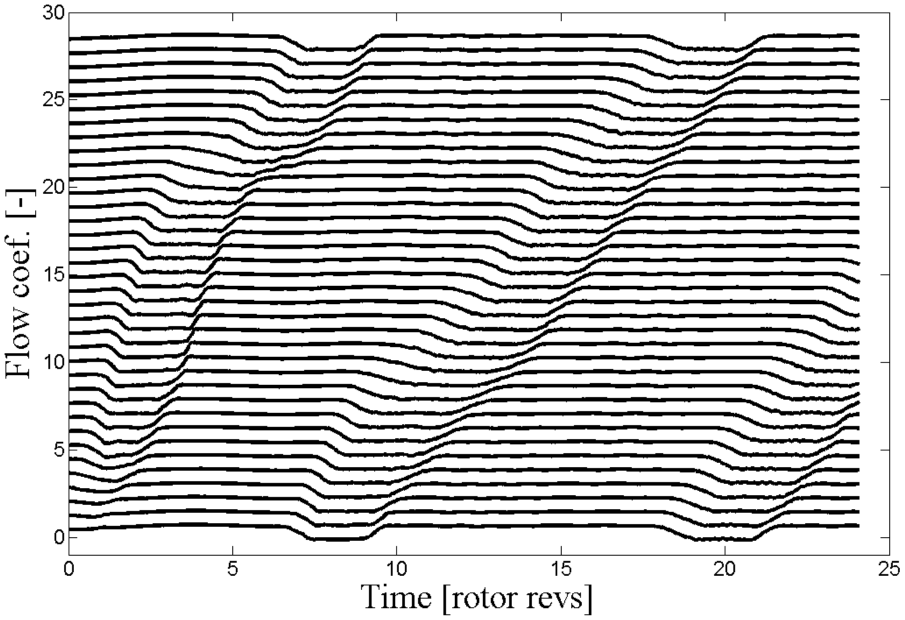

Figure 5.14: Flow coefficient traces at the inlet of the IGV for a negative spike of 1.2.

5.3 Derivation of the rotating stall characteristic

In the previous sections of the present chapter, the effect of the intensity, circumferential extent and time extent of the inlet distortion were extensively described along with an attempt to model spike-type inception.

This section shows how inlet distortion or spikes can be used in combination with variable throttle settings to obtain a prediction of the rotating stall characteristic; two slightly different procedures were adopted.

The first set of results, reported in Figure 5.15, was obtained imposing a stationary 5% total pressure deficit on a 60 degrees sector and three different throttle settings. All the simulations were obtained initializing the flow field with the last stable solution on the forward characteristic; indeed, the first transient performance displayed in Figure 5.15 shows the transient trajectory followed by the operating point imposing the stationary distortion without any change in throttle setting. The second and third simulations, instead, correspond respectively to a throttle closure equal to 20% (th 0.8) and 30% (th 0.7). This transient behavior is the typical trend of the rotating stall phenomenon; the main purpose of these simulations was to check the final operating point in stalled conditions to assess the capability of the tool of providing a prediction of the stall curve. In this context, the results obtained are really impressive since all the three simulations ended up very close to the experimental stall curve.

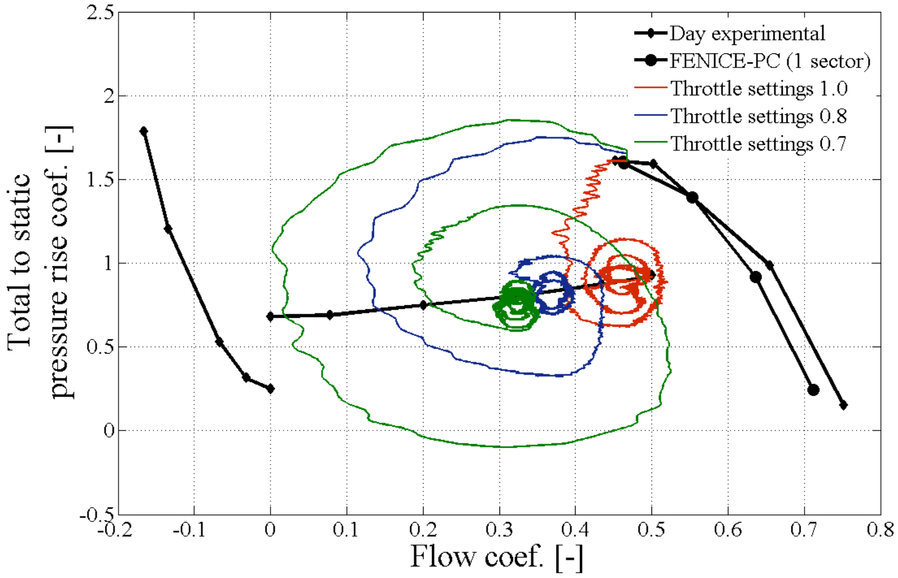

Figure 5.15: Rotating stall characteristic combining inlet total pressure distortion and throttle settings.

The good agreement with the experimental stall characteristic can be better appreciated from Figure 5.16 which reports the respective time average compressor performance of the above simulations. Indeed, the three final operating points lying on the experimental stall charecteristic demonstrate that the tool can predict the stall characteristic within a 5% percent error.

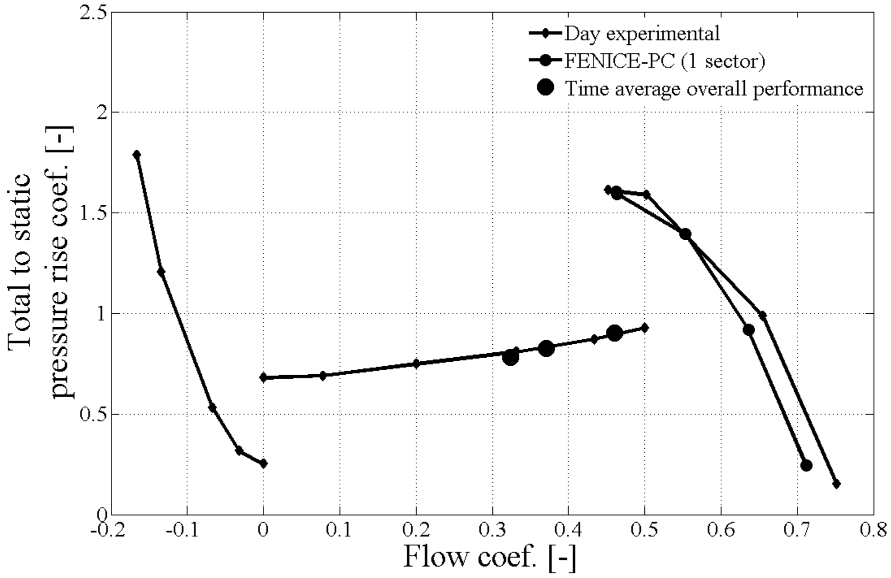

Figure 5.16: Time average of the compressor performance for three different throttle setting and stationary 5% total pressure distortion on a 60 degrees sector.

The second technique applied to investigate the rotating stall region combining distortion and throttle settings, led to the results reported in Figure 5.17 below.

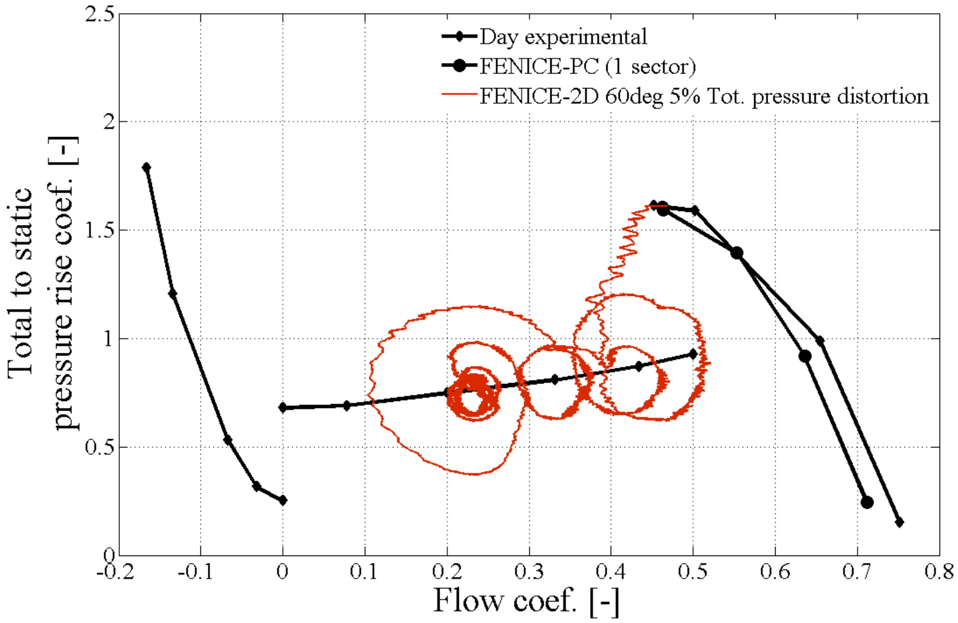

Figure 5.17: Rotating stall characteristic obtained combining inlet flow distortion and throttle changes.

In this second case, the throttle was changed three times within the same simulations without letting the simulation converging in stalled and then starting again from the last stable clean solution. The purpose of this investigation was the verification that the transient trajectory is confined in a region which revolves around the experimental stall characteristic. Besides, it was important to verify the capability of the tool to converge in stalled condition when no further changes are applied to the throttle settings.

Considering Figure 5.18, which reports the flow coefficient against time, expressed in rotor revolutions, it is possible to appreciate when the different throttle setting was imposed and its effect on the transient trend. Starting from a throttle setting equal to 1.0 which means the throttle setting of the last operating point on the forward flow characteristic which was used to initialize the solution, the throttle is progressively reduced by 10% every 6 rotor revolutions.

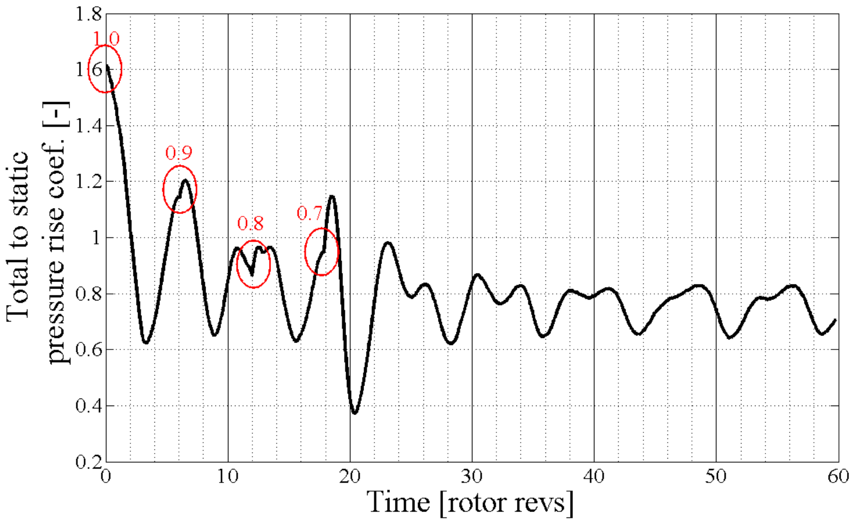

Figure 5.18: Total to static pressure rise coefficient versus time with throttle settings highlighted.

This second procedure was also applied in combination with axial force pulses. As presented previously in this chapter, an axial force pulse of 5% amplitude was applied to the last rotor over a circumferential extent of 20 degrees. In terms of throttle settings, again a three-step change was performed during the simulation. Figure 5.19 reports the transient performance obtained proving once again that the operating point keeps on revolving around the experimental stalled characteristic and than converges very close to it when the throttle stabilizes.

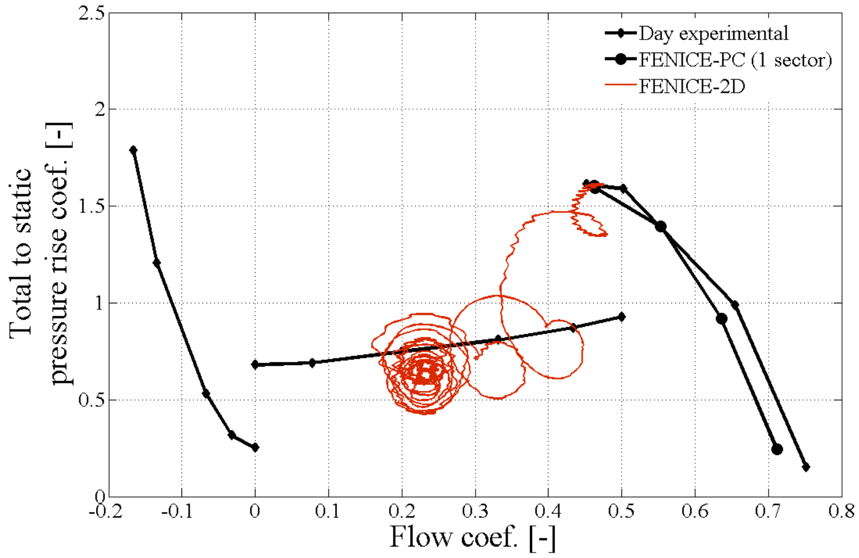

Figure 5.19: Rotating stall characteristic obtained combining spikes and throttle changes.

Figures 5.15, 5.17 and 5.19 represent the most important milestone of this research proving that FENICE-2D can be successfully adopted to assess the compressor performance in the rotating stall region. Figure 5.17 shows how the transient trajectory of the operating point is, indeed, confined around the experimental stalled curve. As a matter of fact, the transient operating point keeps on revolving around the experimental stalled characteristic moving towards lower flow coefficients, and therefore lower mass flows due to the closure of the throttle.

Chapter 6

Conclusions and recommendations

6.1 Summary

In the introductory part of this document, the main objectives of this research were outlined; the aim of this research was the investigation of the rotating stall phenomenon through the development and implementation of a tool which allows the capturing of the transient flow field across multi-stage axial compressor. A particular attention was devoted to the selection of an appropriate methodology in order to develop a tool that could be used as a successful alternative to the common 3D CFD especially during the preliminary design phase to assess geometry trade offs and their effect on the unsteady behavior of the compressor.

Accuracy, reliability and computational efficiency were the key requirements of this project. The literature review carried out at the beginning of this research led the author to the selection of a through-flow approach based on the inviscid Euler equations. The modeling of compressor blades and the annulus geometry was left to the appropriate calculation of source terms while flow features such as effect of viscosity and deviation were introduced through semi-empirical models and correlations. The accuracy and reliability of tools, such the one developed, are strongly determined by the selection of these semi-empirical correlations; for this reason particular care was dedicated in their implementation and calibration.

Initially, a quasi-2D Euler solver, based on the assumption of uniform tangential velocity, was implemented using FORTRAN. On the other hand the nature of the stall and surge phenomena requires the capability of modeling both asymmetric and axis-symmetric flow fields. In order to properly model asymmetric phenomena, a modified ’parallel compressors’ technique was introduced (FENICE-PC).

To verify the methodology, FENICE-PC was tested for inlet total pressure and inlet total temperature distortion. In both cases the tool demonstrated the capability of correctly capturing the overall compressor performance and the right axial trend of all the flow properties. FENICE-PC proved to be a computationally efficient tool to assess compressor performance under non-uniform inlet conditions. On the other hand, some limitations were found during the parametric study; when testing the tool in terms of circumferential discretization, FENICE-PC proved to be unstable for high numbers of circumferential nodes (this limitation depends on the compressor adopted, for instance for the convergent duct, 48 circumferential nodes is the finer grid that allowed converged solutions). The stability could be improved reducing the amount of cross flow through the C_{xflow} coefficient. Another limitation was encountered when adopting the tool in the rotating stall region. Most probably the limitation in this region is due to the assumptions behind the derivation of the cross flow between parallel compressors.

A second version of the tool was also implemented and named as FENICE-2D, since it relies on the fully 2D Euler equations. This second version of the solver was verified against the same case-studies performed with FENICE-PC. Particularly relevant is the comparison of both versions of the tool against the 3D CFD model of the NASA Rotor 37 and of a convergent duct subjected to inlet total pressure and temperature distortion. The main purpose of this comparison was to check the capability of properly modeling asymmetric flow fields, therefore the check was performed in terms of circumferential trends of each flow property, such as axial and tangential velocities, total and static pressures and temperatures. In this verification, FENICE-2D showed a better agreement with the 3D model since this second version of the solver allows finer circumferential grids and does not require any unphysical calibration of the amount of mass flow exchange in the circumferential direction.

Regarding the rotating stall region, a parametric study was conducted with only FENICE-2D, since FENICE-PC proved unable to properly capture the flow behavior in this region. The campaign of simulations performed in the stall region, relied on the adoption of two types of triggers to push the compressor into stall: inlet total pressure distortion and axial force pulses. The investigation was carried out focusing on the capability of the tool to capture the right trends in terms of overall compressor performance. As reported in Chapter 5, several aspects were investigated, such as the role played by the circumferential extent or by the amount of total pressure deficit. The outcomes proved, as expected, that only the transient trajectory of the operating point is affected while the final converged “in stalled” solution is just determined by the throttle setting. A study was also carried out to assess the capability of the compressor to recover from the stall condition, testing the compressor C106 and the NASA TP 1493 with temporary distortions. The analysis of transient performance for a compressor subjected to a temporary distortion, highlighted how the capability of recovering changes from one compressor to the other. On this regards, the NASA compressor proved to be able to recover after the removal of the distorted inlet condition, while the compressor C106, although subjected to a temporary distortion for only a quarter of rotor revolution, required a 20% throttle opening to go back to the forward characteristic and stabilize. The inlet total pressure distortion was also used combined with different throttle settings, as a trigger for rotating stall in order to obtain an estimation of the trend of the rotating stall characteristic. As described in Chapter 5, two different procedures were tested; as first a set of three simulations were carried out imposing three different throttle settings with the same level and circumferential extent of total pressure deficit. These simulations were all initialized with the last stable solution on the forward characteristic and let them run until convergence. The main objective was in fact to check how close the final "in stalled" operating point was to the experimental stall characteristic. The second procedure adopted was again to combine the inlet total pressure distortion and the use of throttle settings to get an estimation of the stall characteristic; the difference for this second study, relates to the fact that the throttle was progressively closed during the simulation. The aim of this particular study was in fact the verification that the operating point revolves around the experimental rotating stall curve moving towards lower mass flow if the throttle is continuously closed and converges on it if no further throttle changes are imposed.

Concluding, the work carried out during this doctoral research has led to the development of a tool that contributes to the understanding of the rotating stall phenomenon through analytical modeling. Although the author recognizes that many steps are still needed to use FENICE-PC/2D as an alternative to standard 3D CFD tools. This research has contributed developing a robust methodology, implementing and verifying the building blocks of a through-flow time marching solver which allows the quick assessment of compressor performance under different conditions requiring only geometrical information.

6.2 Conclusions

While the previous section has provided a quite detailed summary of the overall doctoral research, this section focus on the contributions and scientific achievements.

- This research has provided a methodology and a solver which allows the investigation and assessment of multistage axial flow compressors perfomance under several different operating conditions: reverse flow, rotating stall, inlet flow distortion etc. In comparison with others tools available in the public domain the solver does not rely on steady state characteristics as input. Indeed, the complete compressor map is one of the output of the tool.

- To allow the prediction of the complete compressor characteristic (forward flow, stalled flow and reverse flow) the research has focused also on modelling aspects such as stall inception, pressure loss evaluation, techniques to trigger asymmetric disturbances etc. In this regards, different parametric studies have been carried out to test the models implemented proving a good agreement with the experimental data.
- A quasi-2D Euler solver was also developed, FENICE-PC. Indeed, this solver can be considered as a smart alternative to FENICE-2D when investigations of asymmetric flow field within the forward flow region are under consideration. Whitin FENICE-PC the capability of capturing asymmetric flow field was incorporated through a novel mass redistribution technique which showed very promising results.
- The different parametric studies carried out, highlighted how geometry, type of disturbance (temporary, stationary) and intensity can change the transient behavior of the axial compressor from typical rotating stall to classic or deep surge. For instance it has been shown for the compressor C106 that a change from stationary to transient distortion of the same amount and distribution, leads to a change from classic surge to typical rotating stall behaviour. In terms of geometry, the different test-cases have shown how the C106 compressor being characterized by a low rotational speed (3000 rpm) and a straight annulus is more likely to stall compare to the NASA TP 1493 which has a convergent annulus and higher rotational speed (8035 rpm). The geometry seems to play an important role also in terms of recovery. Indeed the NASA TP 1493 after being subjected to the same conditions of the C106 recovers as soon as the distorted inlet condition is removed, while the C106 required also a 20% opening of the throttle to fully recover. In terms of triggering techniques, an extended investigation of the rotating stall region was carried out using FENICE-2D and different methods to trigger the inception of asymmetric instabilities. In this document several cases have been reported showing the possibility of using inlet flow distortion or axial force pulses combined with different throttle settings to derive the rotating stall characteristic.

6.3 Recommendations for future work

This section provides some suggestions for future work that the author did not endeavor due to time constraints. Indeed, the following list of suggestions aims to both provide some guidance to tackle some of the tool's limitations and to highlight few key area of investigation. Therefore, the list was divided into two categories: "implementation" and "investigation".

Starting from "implementation", there are several aspects which could improve FENICE-PC/2D:

- The requirement of high discretization when tackling low Mach number problems, due to the ill-condition of the system could be overcome by the implementation of alternative numerical techniques for the time and space integration of the Euler equations. The investigation and implementation of alternative techniques could also improve the overall robustness and computational efficiency of the tool;
- The application of strong variations of the throttle settings or the direct imposition of high changes in outlet static pressure can lead to unphysical numerical reflections and to the divergence of the solution. The suggested solution is the implementation of non-reflecting boundary conditions to avoid numerical oscillations when dealing with abrupt changes in the compressor's surroundings;
- The current tool is limited in terms of investigation to axial compressors which operate at low Mach number due to the lack of a complete set of pressure loss models and deviations. The implementation and verification of alternative models for the prediction of pressure losses and deviation would enlarge the range of applicability of the tool and improved its accuracy. Particular attention should be devoted also to the identification of a more physically based deviation model for the stalled region;
- All the case studies reported in this doctoral thesis regard single-spool low speed axial compressor, however the tool can be easily set up for receiving a multi-spool geometry. This modification together with previously suggested work on pressure losses and deviation models would allow the investigation of multistage high-speed modern compressors;
- The developed tool, considering the flow uniform along the radial direction, does not allow the modeling of part-span stall or other phenomena which involve re-distribution of flow properties along the span. Moreover, the campaign of simulations carried out adopting axial force pulses in order to trigger a spike-type stall

onset would provide a more realistic prediction adding to the tool the capability of handling the radial direction. A possibility considered is the combination of FENICE-PC/2D with SOCRATES, a steady 2D solver based on the Streamline Curvature method. The idea behind this methodology is to couple the two solvers and exchange information at each iteration exploiting the capability of solving the radial equilibrium of SOCRATES;

- Although, the efficiency of the tool is already competitive in comparison with common 3D CFD, further improvement could be achieved optimizing each iterative loop and in particular the process adopted to save the results in txt files.

As far as the “investigation” is concerned, the following list suggests few key area of investigation which the author considers valuable for further development of the tool:

- Following the adaptation of the FENICE-PC/2D to receive multi-spool configurations, a proper investigation of all the three regions should be carried out. The tool should be tested in order to ensure the correct capturing of the flow field under different boundary conditions: throttle closure, inlet distortion and spikes;
- Throughout this research the flow inertia was taken into account applying a time delay to the calculation of the axial blade force. The value of the lag constant τ was decided on the basis of what suggested by other researchers. A proper investigation should be carried out in order to assess a more physical way of accounting for the flow inertia or a proper procedure to determine the value of the lag parameter;
- FENICE-PC/2D was verified against 3D CFD for an empty convergent duct and for the NASA Rotor 37. The comparison was performed in terms of converged solution for cases of total pressure and total temperature distortion. A comparison in terms of transient solution is envisaged in order to verify the correct modeling of the transient flow field especially in rotating stall condition.

References

[1] O. Adam and O. Leonard. A quasi-one dimensional model for axial compressors. In *17th, International symposium on air breathing engines*, pages 1–12, Munich, Germany, 4-9 September 2005. International Society of Air-Breathing Engines.

[2] J. D. Anderson. *Computational fluid dynamics: the basics with applications*. McGraw-Hill Education, 1th edition, 1995.

[3] J. D. Anderson. *Fundamentals of Aerodynamics*. McGraw-Hill Education, 3rd edition, 2001.

[4] Anonymous. American aviation historical society. `http://www.aahs-online.org/centennialofflight.net/essay/Theories_of_Flight/Skin_Friction/TH11G3.htm`. (Online; accessed 14 December 2012).

[5] R. H. Aungier. *Centrifugal compressors: a strategy for aerodynamic design and analysis*. American Society of Mechanical Engineers, 1st edition, 1999.

[6] R. H. Aungier. *Axial flow compressors: a strategy for aerodynamic design and analysis*. ASME Press and Professional Engineering Publishing, 1st edition, 2003.

[7] P. S. Bernard and J. Shen. A grid-free dilatation element method for quasi-one-dimensional gas dynamics. *Journal of Computational Physics*, 199(1):41–65, 2004.

[8] M. P. Boyce. *Gas turbine engineering handbook*. Butterworth-Heinemann Ltd, 4th edition, 2011.

[9] M. Cailler. Inlet flow distortion modelling using cfd. Technical report, Cranfield University, Cranfield, Bedfordshire, U.K. (unpublished report), 2013.

[10] T. R. Camp and I. J. Day. A study of spike and modal stall phenomena in a low-speed axial compressor. *Journal of Turbomachinery*, 120(3):393–491, 1998.

[11] Mehdi A. Di Cugno D. Castaneda, J. and V. Pachidis. A preliminary numerical cfd analysis of transonic compressor rotors when subjected to inlet swirl distortion. In *ASME 2011 Turbo Expo: Turbine Technical Conference and Exposition*, volume 7, pages 417–429, Vancouver, British Columbia, Canada, 6-10 June 2011 2011. ASME.

[12] D. Cenciotti. F-18c compressor surge. `http://theaviationist.com/tag/compressor-surge/`. (Online; accessed 3 December 2010).

[13] Lyes P. A. Longley J. P. Cherrett, M. A. and A. A. J. Demargne. *Measurement and calculation of instability inception in a high-speed multi-stage compressor*. Unsteady flows in turbomachines. Von Karman Institute Lecture Series, Von Karman Institute, Belgium, 1996.

[14] Lyes P. A. Longley J. P. Cherrett, M. A. and A. A. J. Demargne. *Multistage environment, modelling approaches*. Unsteady flows in turbomachines. Von Karman Institute Lecture Series, Von Karman Institute, Belgium, 1996.

[15] R. V. Chima. A three-dimensional unsteady cfd model of compressor stability. Technical Report TM-2006-214117, National Aeronautics and Space Administration, Cleveland, U.S.A., 2006.

[16] W. T. Cousins and W. D. Milt. Evaluating complex inlet distortion with a parallel compressor model: part 1 - concepts, theory, extensions and limitations. In *ASME Turbo Expo 2011: Turbine Technical Conference and Exposition*, pages 1–12, Vancouver, British Columbia, Canada, 6-10 June 2011 2011.

[17] C. Cravero and A. Massardo. A gas turbine compressor simulation model for inclusion of active control strategies. Technical Report ADPO11157, Defense Technical Information Center, Genova, Italy, 2010.

[18] I. J. Day. Axial compressor performance during surge. *Journal of Propulsion and Power*, 10(3):329–336, 1994.

[19] I. J. Day and N. A. Cumpsty. The measurement and interpretation of flow within rotating stall cells in axial compressors. *Journal of Mechanical Engineering Science*, 20(2):101–114, 1978.

[20] I. J. Day and C. Freeman. The unstable behavior of low and high-speed compressors. *Journal of Turbomachinery*, 116(2):194–201, 1994.

[21] B. De Jager. Rotating stall and surge control: a survey. *Decision and Control*, 2(1):1857–1862, 1995.

[22] S. L. Dixon and C. A. Hall. *Fluid mechanics and thermodynamics of turbomachinery*. Elsevier, Kidlington, U.K., 6th edition, 2010.

[23] W. Du and O. Leonard. Numerical simulation of surge in axial compressor. *International Journal of Rotating Machinery*, 2012(1):1–10, 2012.

[24] Pearson C. E. Emmons, H. W. and H. P. Grant. Compressor surge and stall propagation. *Transaction of the ASME*, 77(1):455–469, 1955.

[25] J. Fabri and R. Siestrunck. Rotating stall in axial flow compressors. *Journal of the Aeronautical Sciences*, 1(1):805–812, 1957.

[26] N. J. Fredrick. Investigation of the effects of inlet swirl on compressor performance and operability using a modified parallel compressor model. Master's thesis, University of Tennessee, Knoxville, U.S.A., 2010.

[27] L. Gallar. *Gas turbine shaft over-speed / failure performance modelling*. PhD thesis, Cranfield University, Cranfield, Bedfordshire, U.K., 2011.

[28] R. N. Gamache. *Axial compressor reversed flow performance*. PhD thesis, Massachusetts Institute of Technology, Cambridge, U.S.A., 1985.

[29] J. T. Gravdahl. *Modelling and control of surge and rotating stall in compressors*. PhD thesis, Norwegian University of Science and Technology, Trondheim, Norway, 1998.

[30] E. M. Greitzer. Review - axial compressor stall phenomena. *Journal of Fluids Engineering*, 102(1):134–151, 1980.

[31] E. M. Greitzer and H. R. Griswold. Compressor-diffuser interaction with circumferential flow distortion. *Journal of Mechanical Engineering Science*, 18(1):25–38, 1976.

[32] R. Groh. Bio-mimetic drag reduction part 2: Aero-and hydrodynamics. `http://aerospaceengineeringblog.com/bio-mimetic-drag-reduction-2/`. (Online; accessed 15 December 2012).

[33] Fiola R. Haake, M. and S. Staudacher. Multistage compressor and turbine modeling for the prediction of the maximum turbine speed resulting from shaft breakage. *Journal of Turbomachinery*, 133(2):1–12, 2011.

[34] C. Hirsch and J. D. Denton. Through flow calculations in axial turbomachinery. In *AGARD Propulsion and Energetics Panel*, pages 1–238, Koln, Germany, 20-21 May 1976 1976.

[35] R. Hofs. Picture of the boeing 767-2b7/er aircraft. `http://www.airliners.net/photo/US-Airways/Boeing-767-2B7-ER/0963368/`. (Online; accessed 22 November 2010).

[36] J. H. Horlock. *Axial flow compressors*. Butterworths Scientific Publications, London, U.K., 1 edition, 1958.

[37] J. H. Horlock and J. D. Denton. A review of some early design practice using computational fluid dynamics and a current perspective. *Journal of Turbomachinery*, 127(5):5–13, 2005.

[38] Belytschko T. Fern S. Huerta, A. and T. Rabczuk. *Meshfree methods*. University of Canterbury, Upper Riccarton, New Zealand, 1 edition, 2004.

[39] I. A. Johnsen and R. O. Bullock. Aerodynamic design of axial-flow compressors. Technical Report NASA SP-36, National Advisory Committee for Aeronautics, Washington, D.C., U.S.A., 1965.

[40] W. F. Kimzey. An analysis of the influence of some external disturbances of the aerodynamic stability of turbine engine axial flow fans and compressors. Technical Report AEDC-TR-77-80, Arnold Engineering Development Center, Arnold Air Force Station, Tennessee, U.S.A, 1977.

[41] S. G. Koff. Stalled flow characteristics for axial compressors. Master's thesis, Massachusetts Institute of Technology, Cambridge, U.S.A., 1983.

[42] J. A. Korn. Compressor distortion estimates using parallel compressor theory and stall delay. *Journal of Aircraft*, 11(9):584–586, 1974.

[43] M. Lecht. Improvement of the parallel compressor model by consideration of unsteady blade aerodynamics. Technical Report AD-P005 467/6, Defense Technical Information Center, Germany, 1987.

[44] H. Li and S. S. Mulay. *Meshless methods and their numerical properties*. CRC Press, 1st edition, 2013.

[45] F. E. Lima de Medeiros and L. Santos de Brito Alves. Preconditioning reconditioning methods for low mach number compressible flow simulations with

an optimized pseudo speed of sound. In *13th Brazilian Congress of Thermal Sciences and Engineering*, Uberlandia, Brazil, 5-10 December 2010 2010.

[46] J. P. Longley. Calculating stall and surge transients. In *ASME Turbo Expo 2007: Power for Land, Sea and Air*, pages 1–12, Montreal, Canada, 4-17 May 2007 2007.

[47] J. P. Longley and E. M. Greitzer. *Inlet distortion effects in aircraft propulsion system integration*, pages 1–182. Fundamentals and special problems of synthetic aperture radar (SAR). AGARD Lecture Series, Bad Neuenahr, Germany, 1992.

[48] J. P. Longley and T. P. Hynes. Stability of flow through multistage axial compressor. *ASME Journal of Turbomachinery*, 112(1):126–132, 1990.

[49] Shin H. W. Plumbey R. E. Silkowski P. D. Day I. J. Greitzer E. M. Tan C. S. Longley, J. P. and D. C. Wisler. Effects of rotating inlet distortion on multistage compressor stability. *Journal of Turbomachinery*, 118(1):181–188, 1996.

[50] J. S. Marshall and J. R. Grant. A lagrangian vorticity collocation method for viscous, axisymmetric flows with and without swirl. *Journal of Computational Physics*, 138(2):302–330, 1997.

[51] R. S. Mazzawy. Multiple segment parallel compressor model for circumferential flow distortion. *ASME Journal of Engineering for Power*, 99(1):288–296, 1977.

[52] Cumpsty N. A. McDougall, N. M. and T. P. Hynes. Stall inception in axial compressors. *Journal of Turbomachinery*, 112(1):116–125, 1990.

[53] D. Morales Molinero. Rotating stall inception prediction in axial compressors. Master's thesis, Cranfield University, Cranfield, Bedfordshire, U.K., 2013.

[54] H. L. Moses and S. B. Thomason. Approximation for fully stalled cascades. *Journal of Propulsion and Power*, 2(2):188–189, 1986.

[55] Palomba C. Nurzia, F. and P. Puddu. Some considerations about the rotating cell structure. *International Journal of Rotating Machinery*, 2009(1):1–7, 2009.

[56] W. F. O'Brien. Dynamic simulation of compressor and gas turbine performance. Technical Report ADP007894, Virginia Polytechnic Institute and State University, Blacksburg, Virginia, U.S.A., 1992.

[57] J. D. Paduano. *Analysis of compression system dynamics*. PhD thesis, Brussels, 2001. Von Karman Institute Invited Lecture.

[58] H. Pearson and A. B. McKenzie. Wakes in axial compressors. *Journal of the Royal Aeronautical Society*, 63(1):415–416, 1959.

[59] Wiedermann A. Petrovic, M. V. and M. B. Banjac. Development and validation of a new universal through flow method for axial compressors. In *ASME Turbo Expo 2009: Power for Land, Sea, and Air*, volume 7, pages 579–588, Orlando, Florida, U.S.A., 8-12 June 2009 2009.

[60] P. Pilidis. *Gas-turbine theory and performance*. PhD thesis, Cranfield, Bedfordshire, U.K., 2010. Gas Turbine Performance Course Note.

[61] C. Reid. The response of axial flow compressors to intake flow distortion. Technical Report 69-GT-29, The American Society of Mechanical Engineers, New York, U.S.A., 1969.

[62] A. L. Rowe. Shaft failure review - large fan engines. Technical Report DHC127683, Rolls-Royce plc, Derby, U.K., (unpublished report), 2003.

[63] Ginter F. Ruprecht, A. and R. Neubauer. Numerical simulations of unsteady flow instabilities (rotating stall) in pumps. Technical report, Institute for Fluid Mechanics and Hydraulic Machinery, University of Stuttgart, Stuttgart, Germany, 2005.

[64] F. J. Sayas. *A gentle introduction to the Finite Element Method*. PhD thesis, University of Minnesota, Minneapolis, U.S.A., 2008. FEM Course Note.

[65] M. Schobeiri. *Turbomachinery flow physics and dynamic performance*. Springer, 1st edition, 2005.

[66] J. Shen. *A grid-free Lagrangian dilatation element method with application to compressible flow*. PhD thesis, University of Maryland, College Park, MD, U.S.A., 2005.

[67] H. Shu. Nonlinear instability behavior of a high speed multistage compressor. Master's thesis, Massachusetts Institute of Technology, Cambridge, U.S.A., 1997.

[68] J. F. Simon. *Contribution to throughflow modelling for axial flow turbomachines*. PhD thesis, University of Liège, Liege, Belgium, 2007.

[69] K. Simpson A. and J. P. Longley. An experimental study of the inception of rotating stall in a single-stage low-speed axial compressor. In *ASME Turbo Expo 2007: Power for Land, Sea and Air*, pages 1–29, 14-15 May 2007 2007.

[70] C. Soria. Compressor reverse flow performance prediction using a stage stacking technique. Technical Report UTC TR 2011-1, Cranfield University, Cranfield, Bedfordshire, U.K. (unpublished report), 2011.

[71] W. G. Steenken. Modelling compression component stability characteristics - effects of inlet distortion and fan bypass duct disturbances. *AGARD Conference Proceedings*, 24(324):1–15, 1983.

[72] Day I. Morris S. Tan, C. S. and A. Wadia. Spike-type compressor stall inception, detection, and control. *Annual Review of Fluid Mechanics*, 42(1):275–300, 2010.

[73] Saez M. Ferrand P. Tauveron, N. and F. Leboeuf. Axial turbomachine modelling with a 1d axisymmetric approach. application to gas cooled nuclear reactor. *Nuclear Engineering and Design*, 237(15):1679–1692, 2007.

[74] Moszee R. H. Tesch, W. A. and W. G. Steenken. Linearized blade row compression component model stability and frequency response analysis of a j85-13 compressor. Technical Report CR-135162, National Aeronautics and Space Administration, Lewis Research Center, Cleveland, Ohio, U.S.A., 1976.

[75] G. A. Tibboel. Modification of a one-dimensional dynamic compression system model to calculate stage characteristics internally. Master's thesis, University of Tennessee, Knoxville, U.S.A., 2003.

[76] Gorrell W. T. Urasek, D. C. and W. S. Cunnan. Performance of two-stage fan having low-aspect-ratio, first-stage rotor blading. Technical Report NASA-TP-1493, National Aeronautics and Space Administration, Springfield, Virginia, U.S.A., 1979.

[77] H. D. Vo. *Role of tip clearance flow on axial compressor stability*. PhD thesis, Massachusetts Institute of Technology, Cambridge, U.S.A, 2001.

[78] Tan C. S. Vo, H. D. and E. M. Greitzer. Criteria for spike initiated rotating stall. *Journal of Turbomachinery*, 130(1):1–8, 2008.

[79] S. A. Weichert. *Tip clearance flows in axial compressors: stall inception and stability enhancement*. PhD thesis, Cambridge University, Cambridge, U.K., 2011.

[80] F. Willems. Modeling and control of compressor flow instabilities. *Control Systems, IEEE*, 9(5):8–18, 1999.

[81] C. Wu. A general theory of three-dimensional flow in subsonic and supersonic turbomachines of axial-, radial-, and mixed-flox types. Technical Report NACA TN 2604, National Advisory Committee for Aeronautics, Lewis Flight Propulsion Laboratory Cleveland, Ohio, U.S.A., 1952.

[82] G. Yifang. *A computational model for rotating stall and inlet distortions in multistage compressors*. PhD thesis, Massachusetts Institute of Technology, Cambridge, U.S.A., 1999.

[83] A. M. Yocum. *An experimental and numerical investigation of performance of compressor cascades with stalled flow*. PhD thesis, Virginia Polytechnic Institute and State University, Blacksburg, VA., U.S.A., 1988.

Bibliography

H. Abdi. *Partial Least Squares (PLS) regression*, pages 792–795. Encyclopedia for research methods for the social sciences. SAGE, Thousand Oaks, California, U.S.A., 2003.

A. J. Al-Daini. Loss and deviation model for a compressor blade element. *International Journal of Heat and Fluid Flow*, 7(1):69–78, 3 1986.

W. Antwerpen. *Multi-quadrant performance simulation for subsonic axial flow compressors*. PhD thesis, North-West University Potchefstroom Campus, Potchefstroom, South Africa, 2007.

A. Bergara. Finite difference numerical methods of partial differential equations in finance with matlab. `http://www.ehu.es/aitor/irakas/fin/apuntes/pde.pdf`. (Online; accessed 5 May 2013).

G. S. Bloch. A wide-range axial-flow compressor stage performance model. Technical Report ADA251937, Wright Lab Wright-Patterson, Wright-Patterson Air Force Base, OHIO, U.S.A., 1992.

K. M. Boyer. *An improved streamline curvature approach for off-design analysis of transonic compression systems*. PhD thesis, Virginia Polytechnic Institute, Blacksburg, Virginia, U.S.A., 2001.

J. D. Denton. *Cambridge Turbomachinery Course*. Whittle Laboratory, University of Cambridge, U.K., 2004.

J. D. Denton. Some limitations of turbomachinery cfd. In *Proceedings of ASME Turbo Expo 2010: Power for Land, Sea and Air*, pages 735–745, Glaslow, U.K., 14-18 June 2010 2010.

S. L. Dixon. *Fluid mechanics: thermodynamics of turbomachinery*. Butterworth-Heinemann Ltd, Oxford, U.K., 4th edition, 2008.

R. P. Dring and H. D. Joslyn. Throughflow analysis of a multistage compressor operating at near-stall conditions. *Journal of Turbomachinery*, 109(4):483–491, 1987.

N. Falck. Axial flow compressor mean line design. Master's thesis, Lund University, Sweden, 2008.

Calcagni C. Llorens C. Gallar, L. and V. A. Pachidis. Time accurate modelling of the secondary air system response to rapid transients. *Journal of Aerospace Engineering*, 225(8):946–958, 2011.

Burguburu S. Leboeuf F. Gourdain, N. and G. Michon. Simulation of rotating stall in a whole stage of an axial compressor. *Computers and Fluids*, 39(9):1644–1655, 10 2010.

S. Gray. Stage matching, stall, and surge in multi-stage axial flow compressors. In *Proceedings of the Institution of Mechanical Engineers*, volume 184, pages 49–56, 1969.

N. Grech. *Gas turbine sub-idle performance modelling; groundstart, altitude relight, and windmilling*. PhD thesis, Cranfield University, Cranfield, Bedfordshire, U.K., 2013.

E. M. Greitzer. Surge and rotating stall in axial flow compressors - part i: Theoretical compression system model. *Journal of Engineering for Power*, 98(1):190–198, 1976.

Feng J. Somlyo A. P. Ho, R. and Z. Shao. Optimizing the window size for multiple least squares fitting of electron energy loss spectra. *Journal of microscopy*, 197(1):46–51, 2000. Cited By (since 1996): 1.

J. S. Howard. Improved methods for modelling dynamic stage characteristics. Master's thesis, Virginia Polytechnic Institute and State University, Blacksburg, Virginia, U.S.A., 1999.

Tan C. S. Huu D. V. Hoying, D. A. and E. M. Greitzer. Role of blade passage flow structurs in axial compressor rotating stall inception. *Journal of Turbomachinery*, 121(4):735–742, 1999.

Ou-Yang H. Ch ZHu X. Qiang X. Q. Hu, J. F. and Z. H. Du. An improved streamline curvature approach for transonic axial compressor performance prediction. *Journal of Aerospace Engineering*, 225(5):575–584, 2011.

Peters T. Hu, J. and L. Fottner. Numerical simulation of flow instabilities in high speed multistage compressors. *Journal of Thermal Science*, 8(1):23–31, 1999.

A. Huang. Loss mechanisms in turbine tip clearance flows. Master's thesis, Massachussetts Institute of Technology, Cambridge, U.S.A., 2011.

M. F. Huber and U. D. Hanebeck. Progressive gaussian mixture reduction. In *2008 11th International Conference on Information Fusion*, pages 1–8, Cologne, France, 30 June - 3 July 2008 2008.

J. Iatrou. Compressor performance modelling during rotating stall. Master's thesis, Cranfield University, Cranfield, Bedfordshire, U.K., 2012.

M. Ismail. Rotating stall in axial flow compressors. In *7th National Aeronautical Conference*, pages 3295–3300, PAF Academy, Risalpur, Pakistan, 26-27 March 1995 1995.

A. D. Jackson. Stall cell development in an axial compressor. *Journal of Turbomachinery*, 109(4):492–498, 1987.

Hall-C. A. Jerez Fidalgo, V. and Y. Colin. Circumferential flow distortion inlet distortion axial compressors model components field. In *Proceedings of ASME TurboExpo 2010: Power for Land, Sea and Air*, pages 369–380, Glaslow, U.K., 14-18 June 2010.

Basa M. Lastiwka, M. and N. J. Quinlan. Permeable and non-reflecting boundary conditions in sph. *International Journal for Numerical Methods in Fluids*, 61(7):709–724, 2009.

Li M. Lin, F. and J. Chen. Long-to-short length-scale transition: a stall inception phenomenon in an axial compressor with inlet distortion. *Journal of Turbomachinery*, 128(1):130–140, 2005.

J. W. Lindau and A. K. Owen. Nonlinear quasi-three-dimensional modeling of rotating stall and surge. In *33rd Joint Propulsion Conference and Exhibit*, pages 1–10, Seattle, WA, U.S.A., 06-09 July 1997 1997. American Institute of Aeronautics and Astronautics.

J. P. Longley. A review of nonsteady flow models for compressor stability. *Journal of Turbomachinery*, 116(2):202–215, 1994.

E. I. Mahiques. Study on flow separation and blockage in a compressor at locked rotor conditions. Master's thesis, Cranfield University, Cranfield, Bedfordshire, U.K., 2012.

D. J. Mehta. Inlet swirl distortion: the ground vortex on rotor 67. Master's thesis, Cranfield University, Cranfield, Bedfordshire, U.K., 2011.

N. A. Mitchell. A time marching method for unsteady two-dimensional flow in a blade passage. *International Journal of Heat and Fluid Flow*, 2(4):205–220, 1980.

J. C. Montes. Modelling inlet swirl distortion using cfd. Master's thesis, Cranfield University, Cranfield, Bedfordshire, U.K., 2010.

F. K. Moore and E. M. Greitzer. A theory of post-stall transients in multistage axial compressor systems. *Journal of Engineering for Gas Turbines and Power*, 108(1):68–76, 1986.

T. Nakano and A. Breeze-Stringfellow. A method for evaluating the aerodynamic stability of multistage axial-flow compressors. *Journal of Turbomachinery*, 133(3), 2010.

H. G. Neuhoff and K. G. Grahl. Numerical simulation of rotating stall in axial compressor blade rows and stages. In *ASME International Gas Turbine Conference and Exhibit*, pages 1–8, Duesseldorf West Germany, 8-12 June 1968 1968.

V. A. Pachidis. *Gas turbine advance performance simulation*. PhD thesis, Cranfield University, Cranfield, Bedfordshire, U.K., 2006.

A. A. Patel. Assessment of a body force representation for compressor stability estimation. Master's thesis, Massachusetts Institute of Technology, Cambridge, U.S.A., 2009.

J. D. Pelegrin Garcia. Compressor modelling using parallel compressor theory. Master's thesis, Cranfield University, Cranfield, Bedfordshire, U.K., 2013.

Sacco R. Quarteroni, A. and F. Saleri. *Numerical mathematics*. Springer, New York, U.S.A., 2 edition, 2007.

Jackson-R. J. Robbins, W. H. and S. Lieblein. Aerodynamic design of axial-flow compressors. vii - blade-element flow in annular cascades. Technical Report RM E55G02, National Advisory Committee for Aeronautics, Lewis Flight Propulsion Laboratory, Cleveland, Ohio, U.S.A., 1955.

Ma Y. Rong, J. and L. Wu. Gradual transition detection using em curve fitting. In *MMM '05 Proceedings of the 11th International Multimedia Modelling Conference*, pages 364–369, Washington, DC, U.S.A., 12-14 January 2005 2005.

Vigilante E.-De Cesare N. Perillo E. Rosato, M. and G. Spadaccini. Weighted fit by orthonormal polynomials. *Computer Physics Communications*, 22(2):311–315, 1981.

P. B. Salunkhe and A. M. Pradeep. Stall inception mechanism in an axial flow fan under clean and distorted inflows. *Journal of Fluids Engineering*, 132(12):1–14, 2010.

Rogers G. F. C. Cohen H. Saravanamuttoo, H. I. H. and P. Straznicky. *Gas turbine theory*. Prentice Hall, 6th edition, 2008.

Saxer A. P. Inderbitzin A. Saxer-Felici, H. M. and G. Gyarmathy. Prediction and measurement of rotating stall cells in an axial compressor. *Journal of Turbomachinery*, 121(2):365–375, 1999.

H. Schonenborn and T. Breuer. Aerodynamic and mechanical vibration analysis of a compressor blisk at surge. In *Proceedings of ASME Turbo Expo 2004 Power for Land, Sea, and Air*, pages 517–526, Vienna, Austria, 14-17 June 2004.

K. A. Shahrokhi. Application of a modified dynamic compression system model to a low-aspect-ratio fan: effects of inlet distortion. Technical Report AEDC-TR-95-16, Sverdrup Technology, Inc., AEDC Group, Arnold AFB, U.S.A., 1995.

Kim T. S. Kim J. H. Song, T. W. and S. T. Ro. Performance prediction of axial flow compressors using stage characteristics and simultaneous calculation of interstage parameters. *Journal of Power and Energy*, 215(1):89–98, 2001.

M. Soundranayagam and R. L. Elder. A study of stall in a low hub tip ratio fan. *Journal of Turbomachinery*, 115(1):10–16, 1993.

A. Spurr. The prediction of 3d transonic flow in turbomachinery using a combined throughflow and blade-to-blade time marching method. *International Journal of Heat and Fluid Flow*, 2(4):189–199, 1980.

E. G. Steven. An experimental study of exit flow patterns in a multistage compressor in rotating stall. Technical Report WRDC-TR-90-2083, Sverdrup Technology, Inc., AEDC Group, Wright-Patterson AFB, U.S.A., 1990.

R. Vepa. Modelling and quasilinear control of compressor surge and rotating stall vibrations. *Mathematical Problems in Engineering*, 2010(1):1–21, 2010.

A. N. Vishwanatha Rao and O. N. Ramesh. The dynamics of surge in compression systems. *Sadhana*, 32(1-2):43–49, 04/01 2007. J2: Sadhana.

Tourlidakis A. White, N. M. and R. L. Elder. Axial compressor performance modelling with a quasi-one-dimensional approach. *Proceedings of the Institution of Mechanical Engineers, Part A: Journal of Power and Energy*, 216(2):181–193, 2002.

F. Willems. Modeling and control of compressor flow instabilities. *Control Systems, IEEE*, 19(5):8–18, 1999.

D. G. Wilson and T. Korakianitis. *The Design of high-efficiency turbomachinery and gas turbines*. Prentice Hall, Cambridge, Massachusetts, U.S.A., 2nd edition, 1998.

Tan C. S. Montgomery M. Islam T. Zlatinov, M. B. and M. Harris. Turbine hub and shroud sealing flow loss mechanisms. *Journal of Turbomachinery*, 134(6):061027–061027–12, 2012.

Appendix A

FENICE-PC/2D inputs and outputs

This appendix describes in details inputs and outputs of FENICE. The aim is, in fact, to provide the reader with enough information to set and run a simulation. Inputs and outputs, as mentioned at the end of Chapter 3, are exchanged between the user and the solver through .TXT files, a quite detailed description is provided below.

Inputs All the information to start a simulation are provided through two .TXT files:

- Euler_GeneralSettings.txt
- Flow_properties_restart.txt

The Euler_General_Settings.txt contains the following information:

- GEOM_INDX: This index allows the user to choose which configuration to run. A generic con-div nozzle as well as a plenum chamber are implemented and can be combined with all the available compressor geometries. An index equal to "1" should be used to run a compressor followed by a nozzle, "2" if the user wants to run only the compressor and "3" for the combination of a compressor, a plenum and a nozzle;
- NELEMENTS: Number of elements in the axial direction;
- NSTEP: Maximum number of time steps;
- DT: Initial time step;
- BETA: This variable plays a role when running the configurations CN and CPN, that is, Geom_indx equal to "1" or "3". Beta allows the user to control the geometry of the nozzle and adjust in this way the throttle setting;
- NST: Number of elements in the circumferential direction/ parallel compressors;
- CX: Damping factor for artificial viscosity, this coefficient is usually set to a value between 0.5-0.8;

- NCOMP: Total number of turbo-components, the solver recognizes six different turbo-components;
- COMPRESSOR_NAME: The user can choose one of the three compressor geometries already implemented writing the name of the subroutine containing the geometrical information (for instance ROTOR_37);
- MODE: this option can be set to “STEADY” or “TRANSIENT”. “STEADY” is a useful option only when running the solver from an initial constant solution far from the final converged solution. This option is convenient since it forces the solver to use only forward flow empirical models speeding up the convergence.
- STALL INCEPTION: The user can choose between three criteria, flow coefficient (FLOW_COEF), incidence (INCIDENCE) and Aungier (AUNGIER);
- PARALLEL: Flag (Y or N) to decide if running the solver as PC or 2D;
- THROTTLE_PAR: Parameter that can be adjusted to impose the desired throttle settings when using the boundary conditions as defined in section 3.2.2;
- USER_THROTTLE_CHANGE: this logical parameter can be set to TRUE or FALSE. If TRUE, the throttle can be changed during the simulation;
- FLAG: TRUE or FALSE to start from a previous converged solution or from a constant general initialization, if this logical parameter is set as TRUE, the flow field is initialized reading the information from FLOW_PROPERTIES_Restart.txt;
- BC_OUTLET: the user can easily decide which type of boundary conditions to apply. If the user is running the configuration C, three possibilities are available. Setting the BC_OUTLET as “TANK”, the solver will apply the boundary conditions describes in section 3.2.2, if the user needs to impose a fixed value of static pressure, BC_OUTLET should be set as “P_OLD” (the outlet static pressure correspond to the value of static pressure of the last element which could have been read from the restart process or imposed as a generic constant initial solution) or “P_NEW” (if a new value of static pressure need to be imposed);
- NELEMENTS_RES: Number of elements in the axial direction of the restarting solution;
- NST_RES: Number of elements in the circumferential direction of the restarting solution.

- DISTORTION: This and the following variable are important only when running inlet flow distortion investigations; a distorted case is run if the flag is equal to "Y".
- DIST_EXTENT: When running inlet flow distortion investigations, a distortion extent need to be provided, this is an integer number and it refers to the number of circumferential sectors subjected to distorted inlet boundary condition.

The Flow_properties_restart.txt is a file saved when the solver converges and exits. The following flow properties are saved for each axial element (each row corresponds to an axial element and each column to a different property); the circumferential position is identified as a streamtube number.

- Axial velocity;
- Static temperature;
- Density;
- Tangential velocity;
- Absolute velocity;
- Total absolute pressure;
- Total absolute temperature;
- Mass flow;
- Absolute Mach number;
- Axial coordinate.

Outputs Several .TXT files are saved using the subroutine "Probes_results". Saving .TXT is quite time consuming, therefore this subroutine should be called the least possible. The user can decide to call the subroutine every tot seconds through the variable PROBES_TIME (which can be found in the main program).

When the subroutine "Probes_results" is called, the .txt reported below are saved:

- Flow_propertiesXXX.txt: where XXX correspond to the actual iteration number, this file is structured as the previously described Flow_properties_restart;
- Overall_map.txt: this .TXT file contains all the information in terms of compressor performance, each row corresponds to a different time and each column to a different performance parameter:

  - Iteration number
  - Physical time
  - Mass flow average
  - Mass flow equivalent
  - Average flow coefficient
  - Total to static pressure rise
  - Pressure ratio
  - Temperature ratio
  - Plenum pressure

- Static_pressure.txt: this .TXT contains time-wise information on static pressure and axial velocity at different axial locations (outlet of each turbo-component) and at different circumferential position around the annulus. This collection of data allow the plot of static pressure and flow coefficient traces against rotor revolutions.

Appendix B

Compressors' geometrical information

This appendix provides the geometrical information at meanline along with the rotational speed of the three compressors adopted in this work.

COMPRESSOR NASA TP 1493												
Components	R^{in}_{hub} [m]	R^{out}_{hub} [m]	R^{in}_{tip} [m]	R^{out}_{tip}[m]	X_{in}[m]	X_{out}[m]	γ[rad]	β'_{in} [rad]	β'_{out}[rad]	σ	c [m]	t_{blade}/c
Duct	0.089	0.089	0.257	0.257	-0.4	-0.31	-	-	-	-	-	-
Duct	0.09	0.09	0.256	0.256	-0.263	-0.171	-	-	-	-	-	-
Duct	0.09	0.091	0.255	0.254	-0.127	-0.035	-	-	-	-	-	-
Rotor	0.96	0.119	0.253	0.246	0.11	0.081	-0.718	-0.904	-0.522	1.91	0.093	0.061
Stator	0.122	0.132	0.242	0.242	0.126	0.181	-0.261	0.672	-0.152	1.781	0.057	0.068
Rotor	0.133	0.146	0.238	0.234	0.237	0.273	-0.772	-0.914	-0.619	1.765	0.052	0.064
Stator	0.15	0.154	0.234	0.234	0.323	0.366	0.256	0.673	-0.162	1.637	0.044	0.067
Duct	0.154	0.154	0.234	0.234	0.40	0.434	-	-	-	-	-	-
Duct	0.154	0.154	0.234	0.234	0.466	0.50	-	-	-	-	-	-
Duct	0.154	0.154	0.234	0.234	0.532	0.566	-	-	-	-	-	-
Rot. Speed [rpm]	8035											

Table A1: Mean line geometry for each turbo-component of the NASA TP 1493 at 50% NRT.

COMPRESSOR C106												
Components	R_{hub}^{in} [m]	R_{hub}^{out} [m]	R_{tip}^{in} [m]	R_{tip}^{out}[m]	X_{in}[m]	X_{out}[m]	γ[rad]	β'_{in} [rad]	β'_{out}[rad]	σ	c [m]	t_{blade}/c
Duct	0.191	0.191	0.254	0.254	0	0.5	-	-	-	-	-	-
Igv	0.191	0.191	0.254	0.254	0.513	0.54	0.166	0.314	0.017	1.20	0.027	0.112
Rotor	0.191	0.191	0.254	0.254	0.553	0.579	-0.771	-0.876	-0.527	1.47	0.036	0.11
Stator	0.191	0.191	0.254	0.254	0.592	0.625	0.405	0.883	0.174	1.56	0.036	0.11
Rotor	0.191	0.191	0.254	0.254	0.638	0.663	-0.771	-0.876	-0.527	1.47	0.036	0.11
Stator	0.191	0.191	0.254	0.254	0.676	0.709	0.405	0.883	0.174	1.56	0.036	0.11
Rotor	0.191	0.191	0.254	0.254	0.723	0.748	-0.771	-0.876	-0.527	1.47	0.036	0.11
Stator	0.191	0.191	0.254	0.254	0.761	0.794	0.405	0.883	0.174	1.56	0.036	0.11
Rotor	0.191	0.191	0.254	0.254	0.807	0.833	-0.771	-0.876	-0.527	1.47	0.036	0.11
Stator	0.191	0.191	0.254	0.254	0.846	0.79	0.405	0.883	0.174	1.56	0.036	0.11
Duct	0.191	0.191	0.254	0.254	0.891	1.192	-	-	-	-	-	-
Rot. Speed [rpm]	3000											

Table A2: Mean line geometry for each turbo-component of the C106 at 100% NRT.

NASA Rotor 37												
Components	R_{hub}^{in} [m]	R_{hub}^{out} [m]	R_{tip}^{in} [m]	R_{tip}^{out}[m]	X_{in}[m]	X_{out}[m]	γ[rad]	β'_{in} [rad]	β'_{out}[rad]	σ	c [m]	t_{blade}/c
Duct	0.175	0.176	0.257	0.255	-0.07	-0.011	-	-	-	-	-	-
Rotor	0.176	0.179	0.255	0.252	-0.009	0	-0.866	-0.977	-0.672	1.477	0.057	0.06
Duct	0.179	0.18	0.252	0.251	0	0.01	-	-	-	-	-	-
Duct	0.18	0.181	0.251	0.25	0.01	0.013	-	-	-	-	-	-
Duct	0.181	0.182	0.25	0.249	0.014	0.018	-	-	-	-	-	-
Duct	0.182	0.186	0.249	0.246	0.018	0.054	-	-	-	-	-	-
Duct	0.186	0.187	0.246	0.245	0.057	0.071	-	-	-	-	-	-
Duct	0.187	0.189	0.245	0.243	0.073	0.093	-	-	-	-	-	-
Duct	0.189	0.193	0.243	0.24	0.094	0.109	-	-	-	-	-	-
Duct	0.193	0.193	0.24	0.238	0.111	0.211	-	-	-	-	-	-
Rot. Speed [rpm]	10313											

Table A3: Mean line geometry for each turbo-component of the NASA Rotor 37 at 60% NRT.